Title
Deciphering structural heterogeneity in metal-organic frameworks towards an understanding of structure-property relationships

Author
Trickett, Christopher Andrew

Publication Date
2017

Peer reviewed|Thesis/dissertation

Deciphering structural heterogeneity in metal-organic frameworks towards an understanding of structure-property relationships

By

Christopher Andrew Trickett

A dissertation submitted in partial satisfaction of the

requirements of a doctoral degree of

Doctor of Philosophy

in

Chemistry

in the

Graduate Division

of the

University of California, Berkeley

Committee in charge:

Professor Omar M. Yaghi, Chair

Professor Kenneth N. Raymond

Professor Bryan D. McCloskey

Spring 2017

Abstract

Deciphering Structural Heterogeneity in Metal-Organic Frameworks Towards an Understanding of Structure-Property Relationships

by

Christopher Andrew Trickett

Doctor of Philosophy in Chemistry

University of California, Berkeley

Professor Omar M. Yaghi, Chair

The work presented herein describes the relevance and study of structural heterogeneity in the porous crystalline metal-organic framework (MOF) materials. These frameworks, which consist of metal clusters bridged by organic linking units, frequently contain defects or other components that are not described simply by the unit cell of the framework. Intriguingly, even if the features make up a small part of the overall structure, these can dominate a given material's properties. This is evidenced in Chapters 2 and 3, which focus on characterizing the structural heterogeneity on a molecular level, specifically of the 'missing linker' defects in UiO-66 and the origin of superacidity in sulfated MOF-808 respectively. The former displays Lewis acidic sites and different protonation states while the latter has superacidic Brønsted acid sites following exchange of sulfuric acid into the pristine MOF-808 framework. These sites are dependent on the post-synthetic treatment of the material, and are a direct result of the heterogeneous chemical features that are not necessarily ordered in a long-range manner. Chapter 4 extends the characterization of sulfated MOF-808 by investigating other oxides that may be incorporated into the framework, focusing on their structural characterization.

The concept of structural heterogeneity is not limited to defects and other features that are not ordered over long-range. MOFs can be developed into smart solid-state materials by incorporating multiple types of functional groups with the capacity for different reactivity and chemistry within the same material. This is the focus of Chapter 5, which discusses the synthesis and characterization of MOFs containing phosphonate groups with multiple binding modes and protonation states, carboxylate-based MOFs with disulfide units, and the incorporation of peptide units into the MOF linker to stabilize alkali metal-based clusters.

Finally, the full potential of these materials with complex structural landscapes can only be realized through careful structural characterization and analysis. Chapter 6 highlights the case study of fifteen mixed-linker zeolitic imidazolate frameworks (ZIFs) and how their single crystal structures are characterized from low resolution data. While the information at low resolution is clearly less than what can be uncovered at high resolution, there is still much structural information to be gained. The procedures to obtain the data and model the structures, the limitations and methods used, are described.

Table of Contents

Acknowledgements

During the course of my Ph.D., I was fortunate to have been surrounded and have the opportunity to learn from exceptional people. This has been both in a scientific context and in my personal life. I have so many people to thank, and it's because of them that I have kept going, who have motivated and supported me throughout my Ph.D.

I would like to thank Professor Omar Yaghi first, who gave me the opportunity to work under his mentorship in the first place. He has shaped my scientific career and taught me so much, and I'm so grateful for his support. I also want to thank my other mentors, including Professor Hans-Beat Bürgi, Dr. Kevin Gagnon, Dr. Felipe Gándara, Dr. Simon Teat, Kyle Cordova, Dr. Hiroyasu Furukawa and Dr. Peter Siman. There is no doubt I would not be writing this if it had not been for the help, support and advice each of you have given me. Your mentorship has involved all sorts of things, ranging from writing reports, grants, papers and how to mentor others through to X-ray diffraction, synthesis and wet chemistry. Whatever it was, you have been inspirations on both a personal and scientific level, and you have all shaped my outlook on research and life.

I'd also like to thank the entire Yaghi group, past and present, who have given me a rich environment for scientific discussion and a melting pot of cultures and viewpoints have only enhanced the environment I have been a part of for the past four years. These include Jayeon, Farhad, Markus, Longyu, Philipp, Noelle, Christian, Eugene, Robinson, Xiang, Lei, Zhe, Philjun, Seungkyu, Yuzhong, Steven, Hao, Xiaokun, Tom, Bunyarat, Peter, Wentao, Jingjing, Bing, Yingbo, Salman, Yasmeen and Maureen from current members. Past members include Abdul, Muataz, JJ, Travis, Peter K, Caitlin, Leela, Kyungmin, Alejandro, Hyungmo, Alex, Xixi, Jian, Yue-Biao and Michael. Beyond the Yaghi group, I have learnt so much from collaborators in other research groups and fields that are too numerous to list, and it is my interactions with all of these people that keep me moving forward, motivated and interested in research.

Outside of research, I cannot forget my friends and family who support me through thick and thin, and keep me sane. Thanks to Mum and Dad, Jayne, Amélie, Grannie, Maia and my extended family who have always been there for me, even though they live 5,000-odd miles away. Thanks to my friends, especially from the tennis community: my doubles partners Khoa and Vicky for sticking with me even when I play badly. Duc, Christie, David, Michelle, Lawrence, Kenneth, Phil, Meg, among many others have reminded me to enjoy life. And, of course, Alice.

I would never have made it to pursuing my Ph.D. in chemistry without the early guidance in chemistry and research from Mrs. Taylor and Mr. Robinson at Heart of England School, and then later Professor Vas Stavros, Professor Dr. ir. Stefan Bon, Professor Richard Walton and Dr. Ross Hatton from the University of Warwick, Professor Michael Breadmore and Dr. Rosanne Guijt at the University of Tasmania and others.

During the course of my studies, I have completely changed as a person and as a researcher. Looking back, it has been the people and their influence that have enriched my life and made it all worth it. You all are my inspiration, and I am grateful to have known all of you.

Vita

September 20, 1991	Born Newport, Wales, United Kingdom
October 2009 – June, 2013	MChem Chemistry University of Warwick Coventry, United Kingdom
August 2013 – May 2017	Graduate Student Instructor and Researcher Department of Chemistry University of California, Berkeley Berkeley, California, United States

Publications

(1) Yang, J.; Zhang, Y.-B.; Liu, Q.; Trickett, C. A.; Gutierrez-Puebla, E.; Monge, M. Á.; Cong, H.; Aldossary, A.; Deng, H.; Yaghi, O. M. *J. Am. Chem. Soc.* **2017**, *Just Accepted*, DOI:10.1021/jacs.7b02272.

(2) Choi, K.; Kim, D.; Rungtaweevoranit, B.; Trickett, C. A.; Barmanbek, J. T. D.; Alshammari, A.; Yang, P.; Yaghi, O. M. *J. Am. Chem. Soc.* **2017**, *139* (1), 356–362.

(3) Catarineu, N. R.; Schoedel, A.; Urban, P.; Morla, M. B.; Trickett, C. A.; Yaghi, O. M. *J. Am. Chem. Soc.* **2016**, *138* (34), 10826–10829.

(4) Nguyen, N. T. T.; Furukawa, H.; Gándara, F.; Trickett, C. A.; Jeong, H. M.; Cordova, K. E.; Yaghi, O. M. *J. Am. Chem. Soc.* **2015**, *137* (49), 15394–15397.

(5) Siman, P.; Trickett, C. A.; Furukawa, H.; Yaghi, O. M. *Chem. Commun.* **2015**, *51* (98), 17463–17466.

(6) Trickett, C. A.; Gagnon, K. J.; Lee, S.; Gándara, F.; Bürgi, H.-B.; Yaghi, O. M. *Angew. Chem. Int. Ed.* **2015**, *54* (38), 11162–11167.

(7) Trickett, C. A.; Henderson, R. D.; Guijt, R. M.; Breadmore, M. C. *Electrophoresis* **2012**, *33* (21), 3254–3258.

Chapter 1: An Introduction Structural Heterogeneity in Metal-Organic Frameworks

The structural characterization of metal-organic frameworks (MOFs), which are porous crystalline frameworks consisting of metal oxide clusters bridged with organic linking units, is the cornerstone of understanding and applying their chemistry.[1,2] Indeed, the structural characterization of MOFs has grown into its own discipline, requiring a myriad of techniques to effectively describe it. This has included diffraction techniques which increasingly blur the boundaries between small-molecule and protein crystallography to identify topology and connectivity, through to more subtle details such as defective sites and structural heterogeneity, which includes crystallographically disordered functional groups and other disruptions to the repeat unit of the framework which can drastically alter the properties of MOFs.[2,3] While crystallography is most often the starting point for MOF structure elucidation, this is insufficient on its own to understand and full characterize the frameworks as crystallography does not probe the local environment. Instead, a holistic view of the average unit cell of the crystal being studied is obtained.[4] The local environment is especially relevant for heterogeneous MOFs or those where defects are prominent, since these features are poorly represented by the average repeating unit (Figure 1.1).

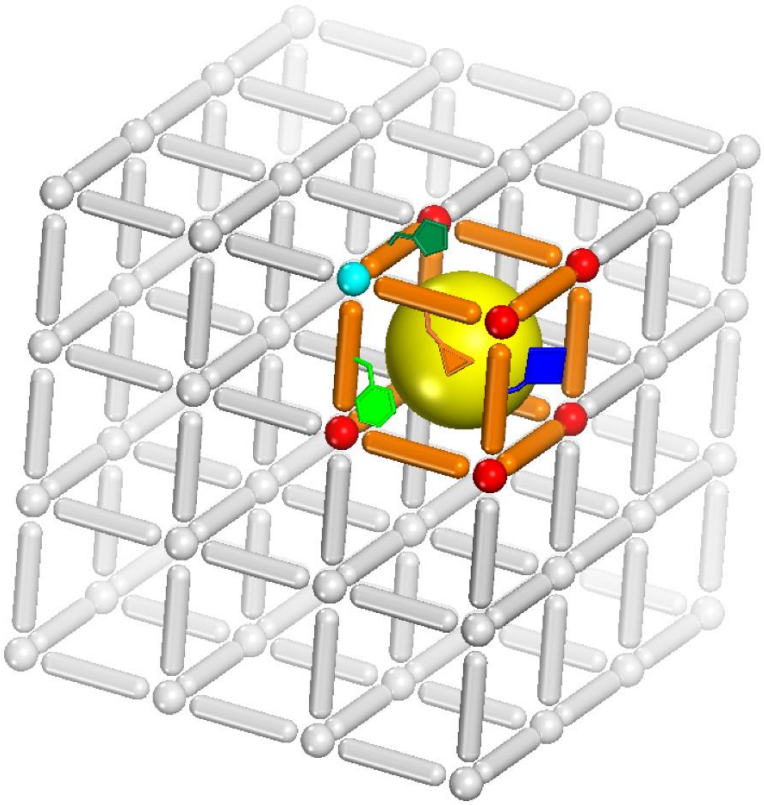

Figure 1.1. A representation of an extended framework is shown with a unit cell highlighted in color. Some of the linking units display different functional groups, which would be superimposed on top of one another crystallographically. However, their local and medium-range ordering may have a dramatic influence on the resulting structural properties.

An increasing number of studies are reporting on such heterogeneity within MOFs.[5–11] Of the most commonly studied structures, the zirconium-based framework known as UiO-66 stands out in this regard. First invented in 2008, and found to contain missing linkers, this MOF has been extensively studied, initially for its chemical and thermal stability but later for its defects and their influence on the material's properties.[12] These included investigations into its CO_2 uptake performance,[13,14] Lewis acid catalytic activity[15–17] and overall surface area.[11,13] The chemical formula of defect-free UiO-66 is $Zr_6O_4(OH)_4(BDC)_6$ (BDC = 1,4-benzenedicarboxylate), and has an octahedral arrangement of zirconium atoms bridged by alternating μ^3-oxo and -hydroxy groups. The metal oxide cluster is completed by the bridging carboxylate groups that are part of the BDC linker, which connect the zirconium-based clusters together. Each cluster is 12-coordinate. This is how the framework is commonly described, and is certainly representative of the average repeating unit. However, if the structure was fully defined from this summary, there would be no Lewis acid sites or defects, and modifications to the synthetic conditions, as long as UiO-66 is the sole product, should theoretically make no difference to the material's properties. However, this is clearly not the case, and the previously mentioned reports have studied these discrepancies with a strong correlation between the quantities of defects and the output properties. Further work was directed towards understanding the nature of these defects, yet conclusively identifying the defects, their molecular origin and how they could be manipulated post-synthetically were still open questions.

While more work has been carried out to follow this up, the focus of Chapter 2 is the identification of the chemical species that replace the linkers at these defect sites. The former were further investigated to determine how these can be manipulated by tuning the synthesis conditions and controlling their nature following pore evacuation at different temperatures. The project is expected to contribute to the understanding of how such defect sites arise, and knowledge of their chemical nature will allow for rational and systematic control over the type and ratio of defects in the material. This in turn will enable the design of materials with the desired properties. The techniques involved for studying such defects in porous crystalline materials, particularly the use of the environment cell for probing the structure under non-ambient conditions, may pave the way for other similar investigations.

The importance of studying MOFs in the environment they are applied in is highlighted in Chapter 3. Herein, the first and to date only known superacidic MOF, known as the zirconium-based sulfated MOF-808 (S-MOF-808), was examined to identify the origins of Brønsted superacidity.[18] This property was previously identified in the original work on S-MOF-808, yet its structural and chemical nature remained elusive. During the course of this investigation, it was found that the coordination mode of sulfate converts from primarily bridging between two zirconium atoms in the cluster to being exclusively chelating to a single zirconium atom upon evacuation under dynamic vacuum. This shift in configuration, along with a portion of the terminal water molecules that are not removed from the framework upon pore evacuation, is revealed to be crucial in displaying superacidic properties. Indeed, both too much and too little moisture precludes superacidity. Therefore, an understanding of the material is only possible by probing the structure and local environment of the framework under non-standard conditions.

As with the defects in UiO-66, the work discussed in Chapter 3 allows for control and manipulation of the material's properties, in this case superacidity, by understanding the nature of the activity and the required chemical features for the material to exhibit this property. While

this study focuses on S-MOF-808 specifically, parallels can be drawn between the MOF and its inspiration, sulfated zirconia (SZ). SZ has also been found to display superacidic properties by Hammett indicator tests, and is also zirconium-based with sulfate groups post-synthetically functionalized on the surface of the material. The precise properties of this solid vary substantially depending on the synthesis conditions.[19–22] SZ is prepared from ZrO_2 or $Zr(OH)_4$, calcined at elevated temperatures of around 500 – 700 °C in the presence of moisture. This material has been extensively studied, yet no direct structural proof for superacidity had been found despite a number of models being proposed (Figure 1.2).[23–29] However, SZ has also been found to possess both Brønsted and Lewis acidity, with Brønsted acidity only occurring if the material is exposed to some degree of moisture.[23] While the properties, notably acid strength and catalytic performance, of SZ depend strongly on the synthesis conditions, these features are thought to be common to the superacidic forms of SZ. The chemical features of combining zirconium oxide units with sulfate and moisture, identified in both SZ and S-MOF-808 as being needed for Brønsted superacidity, hint at the possibility that superacidic SZ may adopt a similar structural configuration as S-MOF-808. Direct structural confirmation by probing SZ itself would provide stronger evidence, but the structure-property relationship between S-MOF-808 and its superacidity that this work has identified has the potential to inform researchers on materials beyond just the MOF itself.

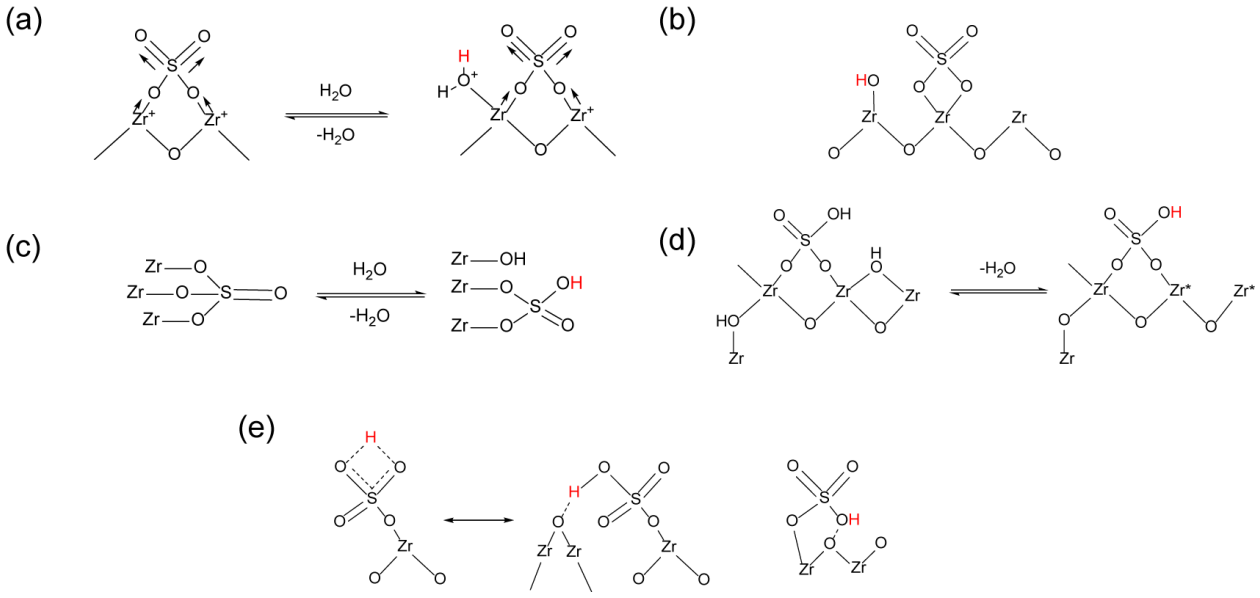

Figure 1.2. Some of the proposed models for the superacidic Brønsted acid sites in sulfated zirconia are shown above.[22-28] The proton in question is highlighted in red. Many reports discuss the effect of moisture on superacidity, and discuss the equilibrium between the hydrated and dehydrated frameworks.

Sulfate groups are not the only strongly acidic and catalytically active species that have been incorporated into solid-state materials. Indeed, molybdate and tungstate have also found useful for acid catalysis, although have not been included within MOF-808.[30] With the success of modifying this framework with sulfate groups, further investigation into incorporating other oxide-containing compounds such as chromate, molybdate, tungstate and selenate were carried

out and reported in Chapter 4. The structures of the post-synthetically functionalized MOFs were characterized by a variety of techniques in order to understand the binding mode and environment of the oxides. Ultimately, the goal of this work is to test and compare different materials for their catalytic activity, and relate this activity to the underlying structure. This investigation, combined with the thorough characterization of S-MOF-808 in Chapter 3, encompasses the wider goal of characterizing structural heterogeneity in MOFs. Further, my ultimately aim is to establish methods for systematically modify and tune porous frameworks to rationally design a material with the desired properties, rather than by attempting trial-and-error iterations to develop functional catalysts.

The possibilities offered by structural heterogeneity offer exponentially more possibilities for developing the chemistry of materials simply due to the added complexity. This has been taken advantage by Nature in many forms. This is perhaps most notable in DNA, whereby the backbone of phosphate groups and the four nucleotides which combine together to code for the genetic make-up of living organisms.[31] In a continuation of this theme of heterogeneity and how it can be exploited, Chapter 5 focuses on the structural characterization of frameworks containing multiple kinds of chemical functional groups whose chemistry can be utilized for a variety of applications. Specifically, by employing linkers containing both carboxylate and disulfide groups, not only can this facilitate the design of new MOF structures, this approach has the potential to synthesize metal clusters that cannot be realized by solvothermal methods including chains, sheets or other 3D materials. This can be achieved by taking advantage of the different chemical reactivity of the incorporated functional groups. In this case, disulfide moieties are susceptible to reduction under mild conditions which would be unreactive towards carboxylate functional groups.[32–34] Conversely, acid-base chemistry that would cleave metal-oxygen bonds will leave disulfide bonds intact. By exploiting these differences, it should be possible to selectively modify and rebuild the original frameworks, as is common in chemical transformations by organic synthetic methods.

The synthesis of MOFs containing alkali metals such as sodium have been limited, with a lack of porosity due to structural collapse often observed.[35–40] The use of linkers containing a high density of coordinating groups on the organic linker can offer a solution to this by minimizing solvent coordination, and maximizing linker-SBU interactions. This was achieved in the synthesis of two isoreticular sodium-based MOFs using a linker based on L-aspartate. This linker of 16.5 Å in length has a total of four carboxylate groups and two amide units that provide rigidity and many coordinating groups within a relatively small area to link up with the sodium-based SBU, leading to both air stability and preventing framework collapse on pore evacuation under dynamic vacuum.

Phosphonate-based MOFs also offer a similar potential of heterogeneity, even with only one type of functional group as part of the linker. This is because there are many possible coordination modes for phosphonate, ranging from monodentate through to tridentate.[41] Since each phosphonate moiety has two hydroxyl groups with vastly different pK_a values, different protonation states can exist, even in the same framework. This is in contrast to the more traditional carboxylate-based linkers, which are fully deprotonated when coordinating to metals. In the work described, three phosphonate-based MOFs were synthesized and these features

identified and compared. Additionally, the syntheses were performed in the presence of an ionic liquid, and charged frameworks for all three were observed. This structural analysis, combined with preliminary characterization of the properties of one of the frameworks, demonstrates their potential use for proton conduction applications.

As the field of MOFs develops and matures, there is an ever increasing need to characterize the structure of frameworks with disorder and heterogeneity with care to take full advantage of the information available from crystallographic studies. This also may demand the ability to obtain structural information from low resolution data. Such information can of course never be as detailed or informative as high resolution data, as is typical in small molecule crystallography. However, there is still much value to be gained from meticulous study and analysis of these data sets. The connectivity and topological structural information are particularly relevant in the context of MOF structures. Chapter 6 addresses this in the context of mixed linker zeolitic imidazolate frameworks (ZIFs). These materials are zeolite-like frameworks which could be designed semi-empirically to contain large voids by incorporating up to three imidazolate linkers. A total of fifteen ZIFs were characterized by SXRD, though the resolution obtained for these materials ranged from 1.0 Å to 1.7 Å, which is in the range of macromolecular crystallography. The process and methodology, as well as the data analysis, are discussed in this Chapter, demonstrating both the relevance and limitations of characterizing disordered and heterogeneous structures at low resolution.

Bibliography

(1) Furukawa, H.; Cordova, K. E.; O'Keeffe, M.; Yaghi, O. M. *Science* **2013**, *341* (6149), 1230444.

(2) Furukawa, H.; Müller, U.; Yaghi, O. M. *Angew. Chem. Int. Ed.* **2015**, *54* (11), 3417–3430.

(3) Deng, H.; Doonan, C. J.; Furukawa, H.; Ferreira, R. B.; Towne, J.; Knobler, C. B.; Wang, B.; Yaghi, O. M. *Science* **2010**, *327* (5967), 846–850.

(4) Kong, X.; Deng, H.; Yan, F.; Kim, J.; Swisher, J. A.; Smit, B.; Yaghi, O. M.; Reimer, J. A. *Science* **2013**, *341* (6148), 882–885.

(5) Fang, Z.; Bueken, B.; De Vos, D. E.; Fischer, R. A. *Angew. Chem. Int. Ed.* **2015**, *54* (25), 7234–7254.

(6) Aoki, T.; Chang, Y.; Badano, G.; Zhao, J.; Grein, C.; Sivananthan, S.; Smith, D. J. *J. Cryst. Growth* **2004**, *265* (1–2), 224–234.

(7) Ameloot, R.; Vermoortele, F.; Hofkens, J.; De Schryver, F. C.; De Vos, D. E.; Roeffaers, M. B. J. *Angew. Chem. Int. Ed.* **2013**, *52* (1), 401–405.

(8) Rickman, R. H.; Dunstan, P. R. *J. Raman Spectrosc.* **2014**, *45* (1), 15–21.

(9) Stammer, X.; Heißler, S. *Nachr. Chem.* **2013**, *28* (8), 22–27.

(10) Petkov, P. St.; Vayssilov, G. N.; Liu, J.; Shekhah, O.; Wang, Y.; Wöll, C.; Heine, T. *Chem. Phys. Chem.* **2012**, *13* (8), 2025–2029.

(11) Cliffe, M. J.; Wan, W.; Zou, X.; Chater, P. A.; Kleppe, A. K.; Tucker, M. G.; Wilhelm, H.; Funnell, N. P.; Coudert, F.-X.; Goodwin, A. L. *Nat. Commun.* **2014**, *5*, 4176–4183.

(12) Cavka, J. H.; Jakobsen, S.; Olsbye, U.; Guillou, N.; Lamberti, C.; Bordiga, S.; Lillerud, K. P. *J. Am. Chem. Soc.* **2008**, *130* (42), 13850–13851.

(13) Wu, H.; Chua, Y. S.; Krungleviciute, V.; Tyagi, M.; Chen, P.; Yildirim, T.; Zhou, W. *J. Am. Chem. Soc.* **2013**, *135* (28), 10525–10532.

(14) Liang, W.; Coghlan, C. J.; Ragon, F.; Rubio-Martinez, M.; D'Alessandro, D. M.; Babarao, R. *Dalt. Trans.* **2016**, *45* (11), 4496–4500.

(15) Vermoortele, F.; Vandichel, M.; Van De Voorde, B.; Ameloot, R.; Waroquier, M.; Van Speybroeck, V.; De Vos, D. E. *Angew. Chem. Int. Ed.* **2012**, *51* (20), 4887–4890.

(16) Vermoortele, F.; Bueken, B.; Le Bars, G.; Van de Voorde, B.; Vandichel, M.; Houthoofd, K.; Vimont, A.; Daturi, M.; Waroquier, M.; Van Speybroeck, V.; Kirschhock, C.; De Vos, D. E. *J. Am. Chem. Soc.* **2013**, *135* (31), 11465–11468.

(17) Vandichel, M.; Hajek, J.; Vermoortele, F.; Waroquier, M.; De Vos, D. E.; Van Speybroeck, V. *CrystEngComm.* **2015**, 20–27.

(18) Jiang, J.; Gándara, F.; Zhang, Y.-B.; Na, K.; Yaghi, O. M.; Klemperer, W. G. *J. Am. Chem. Soc.* **2014**, *136* (37), 12844–12847.

(19) Bolis, V.; Magnacca, G.; Cerrato, G.; Morterra, C. *Langmuir* **1997**, *13* (5), 888–894.

(20) Hino, M.; Kurashige, M.; Matsuhashi, H.; Arata, K. *Thermochim. Acta* **2006**, *441* (1), 35–41.

(21) Arata, K. *Green Chem.* **2009**, *11* (11), 1719–1728.

(22) Yadav, G. D.; Nair, J. J. *Microporous Mesoporous Mater.* **1999**, *33* (1), 1–48.

(23) Song, X.; Sayari, A. *Cat. Rev. - Sci. Eng.* **1996**, *38* (3), 329–412.

(24) Clearfield, A.; Serrette, G. P. D.; Khazi-Syed, A. H. *Catal. Today* **1994**, *20* (2), 295–312.

(25) Arata, K. *Adv. Catal.* **1990**, *37*, 165.

(26) Ward; D. A.; Ko, E. I. *J. Catal.* **1994**, *150* (1), 18–33.

(27) Bensitel, M.; Saur, O.; Lavalley, J.-C.; Morrow, B. A. *Mater. Chem. Phys.* **1988**, *19* (1–2), 147–156.

(28) Kustov, L. M.; Kazansky, V. B.; Figueras, F.; Tichit, D. *J. Catal.* **1994**, *150* (1), 143–149.

(29) Adeeva, V; Dehaan, J. W.; Janchen, J; Lei, G. D.; Schunemann, V.; Vandeven, L. J. M.; Sachtler, W. M. H.; Vansanten, R. A. *J. Catal.* **1995**, *151* (2), 364–372.

(30) Reddy, B.; Patil, M. *Curr. Org. Chem.* **2008**, *12* (2), 118–140.

(31) Osborn Popp, T. M.; Yaghi, O. M. *Acc. Chem. Res.* **2017**, *50* (3), 532–534.

(32) Fritze, U. F.; von Delius, M. *Chem. Commun.* **2016**, *52* (38), 6363–6366.

(33) Yan, G.; Yang, M.; Wu, X. *Org. Biomol. Chem.* **2013**, *11*, 7999–8008.

(34) Jiang, Y.; Qin, Y.; Xie, S.; Zhang, X.; Dong, J.; Ma, D. *Org. Lett.* **2009**, *11* (22), 5250–5253.

(35) Tominaka, S.; Henke, S.; Cheetham, A. K. *CrystEngComm* **2013**, *15* (45), 9400–9407.

(36) Reger, D. L.; Leitner, A.; Smith, M. D.; Tran, T. T.; Halasyamani, P. S. *Inorg. Chem.* **2013**, *52* (17), 10041–10051.

(37) Raja, D. S.; Luo, J. H.; Yeh, C. T.; Jiang, Y. C.; Hsu, K. F.; Lin, C. H. *CrystEngComm* **2014**, *16* (10), 1985–1994.

(38) Raja, D. S.; Luo, J.-H.; Wu, C.-Y.; Cheng, Y.-J.; Yeh, C.-T.; Chen, Y.-T.; Lo, S.-H.; Lai, Y.-L.; Lin, C.-H. *Cryst. Growth Des.* **2013**, *13* (8), 3785–3793.

(39) Choi, A.; Kim, Y. K.; Kim, T. K.; Kwon, M.-S.; Lee, K. T.; Moon, H. R. *J. Mat. Chem. A* **2014**, *2* (36), 14986.

(40) Thuéry, P. *CrystEngComm* **2014**, *16* (9), 1724.

(41) Gagnon, K. J.; Perry, H. P.; Clearfield, A. *Chem. Rev.* **2012**, *112* (2), 1034–1054.

Chapter 2: Definitive Molecular Level Characterization of Defects in UiO-66 Crystals

Introduction

While crystalline materials contain a periodic array of atoms, no real crystal could ever be described as perfectly ordered in all directions, as they are typically modeled. In reality, the models presented to describe the structures of crystals are only approximations of reality, since any given crystal must have a surface where terminating groups differ from the bulk interior, even for the most well-ordered and carefully grown crystals. However, far from being problematic, structural defects in solids have a well-established role in enhancing and controlling the properties of materials, most notably in heterogeneous catalysis and band-gap tuning of semiconductors.[1–5] Unfortunately, by their very nature defects are typified by disorder and low concentration compared to the bulk of a material, so studying them is a challenging undertaking. Given the effect they can have on the properties of a material however, their characterization is necessary in order to be able to manipulate and rationalize material design towards a given application.

There are a number of different classifications of crystallographic defects that have been identified, based on their dimensionality. The first set, known as point defects, are located at a single site as opposed to being extended in any direction – in other words, they are 0-dimensional. These can be as a result of a vacancy, where an atom or molecule in an otherwise ordered array is simply not present, and is known as a Schottky defect. Interstitial defects, called Frenkel defects, also exist, where an atom is dislocated onto a site that would not otherwise be occupied in a crystal. One-dimensional line defects are linear misalignments of atoms, and exist as either edge or screw dislocations, though may contain some character of both. Edge dislocations are formed from the abrupt termination of a plane of atoms within a crystal, forcing adjacent planes to bend around it. A screw dislocation, which may result from shear stress, is characterized by a helical path about a dislocation line. Planar, two-dimensional defects subsist as grain or twin boundaries resulting from the joining of two crystals growing separately. Finally, three-dimensional bulk defects may also exist in crystals, which include macroscopic cracks and imperfections as well as the clustering of atoms into a second phase inside the main phase. While all types of defects will affect the material properties, this chapter will focus on understanding and characterizing point defects on the molecular level.

The characterization of such defects is very much possible however, especially when one is aware of their potential presence. This often involves a combination of techniques, including but not limited to electron[6] and fluorescence microscopy,[7] Raman,[8] infrared[9] and X-ray photoelectron spectroscopy,[10] powder X-ray diffraction combined with density functional theory calculations,[11] and single crystal X-ray diffraction (SXRD).[12,13] Indeed, MOFs are increasingly found to have defective structures, even in the specific kind of point defect of missing linkers,[14–17] a situation which is unique to these extended organic-containing frameworks. For example, three MOF structures, MOF-5, HKUST-1 and UiO-66, have been identified to contain defect sites.[7,10,18,19] However, in both the established inorganic solids mentioned above and MOFs, the molecular level determination of the nature of these sites is not easily elucidated because of the ambiguities associated with deciphering low concentrations of electron density. The porous nature of MOFs allows chemical modification of defect sites without changing the underlying

connectivity of the overall structure, and thus provides definitive means of achieving molecular-level characterization of defects.

Defects are no exception in the MOF field, although it is only in the past few years that the importance of defects is really being recognized and investigated. As an illustrative example, the zirconium-based MOF called UiO-66 [$Zr_6O_4(OH)_4(C_8H_4O_4)_6$], first reported in 2008,[20] has a structure that is replete with missing organic linker point defects. Despite these previously reported sites in the structure, which were identified first by powder neutron diffraction[21] and later SXRD,[22] with approximately 1 in 12 of the BDC linkers are replaced by another species, UiO-66 stands out amongst MOFs for its exceptional thermal and chemical stability, along with its excellent mechanical properties.[23] It has been shown that these defects may be converted into Lewis acid sites by heating the MOF under dynamic vacuum, and these sites can be used for catalysis.[24] This would be impossible with a 'perfect' structure which has no linkers missing since there would be no open metal sites to act as Lewis acids. This work demonstrates how only small changes, with as little as 5 to 10% missing linkers, can dramatically alter the performance of the framework, while being a small enough structural difference that it may be overlooked by common material characterization techniques such as X-ray diffraction, elemental analysis and surface area analysis.

For this reason, the structure and properties of UiO-66 have been heavily studied. The identity of this defect has been the subject of intense scrutiny, with contradictory reports postulating the species replacing the linker to be water, hydroxide,[25,26] chloride,[27] modulators such as formate and acetate,[21] or solvent molecules such as *N*,*N*-dimethylformamide.[25] Additionally, it was recently found that under certain synthesis conditions, primitive nanodomains form within hafnium-based UiO-66, likely related to the defects.[11] Besides the uncertainty of the molecular identity of these defects, there has been no indication of what causes the relatively large percentage of missing linkers in an otherwise highly crystalline material. Gaining such knowledge is imperative in light of the utility of this MOF in catalysis, adsorption and its thermally and chemically robust structure.[23] This importance is underlined by the large number of studies (287 papers on UiO-66 from 2008 to 2014) focused on its chemistry.

The structure of UiO-66 consists of an octahedron of square antiprismatic zirconium atoms capped by μ^3-oxo and hydroxyl groups in an alternating fashion, each bridged by carboxylates from the benzenedicarboxylate (BDC) linker (Figure 2.1) to form a 12-connected zirconium oxide cluster, which extends into a face-centered cubic array. This report shows for the first time how the precise structure of defects in MOFs can be determined from SXRD data.

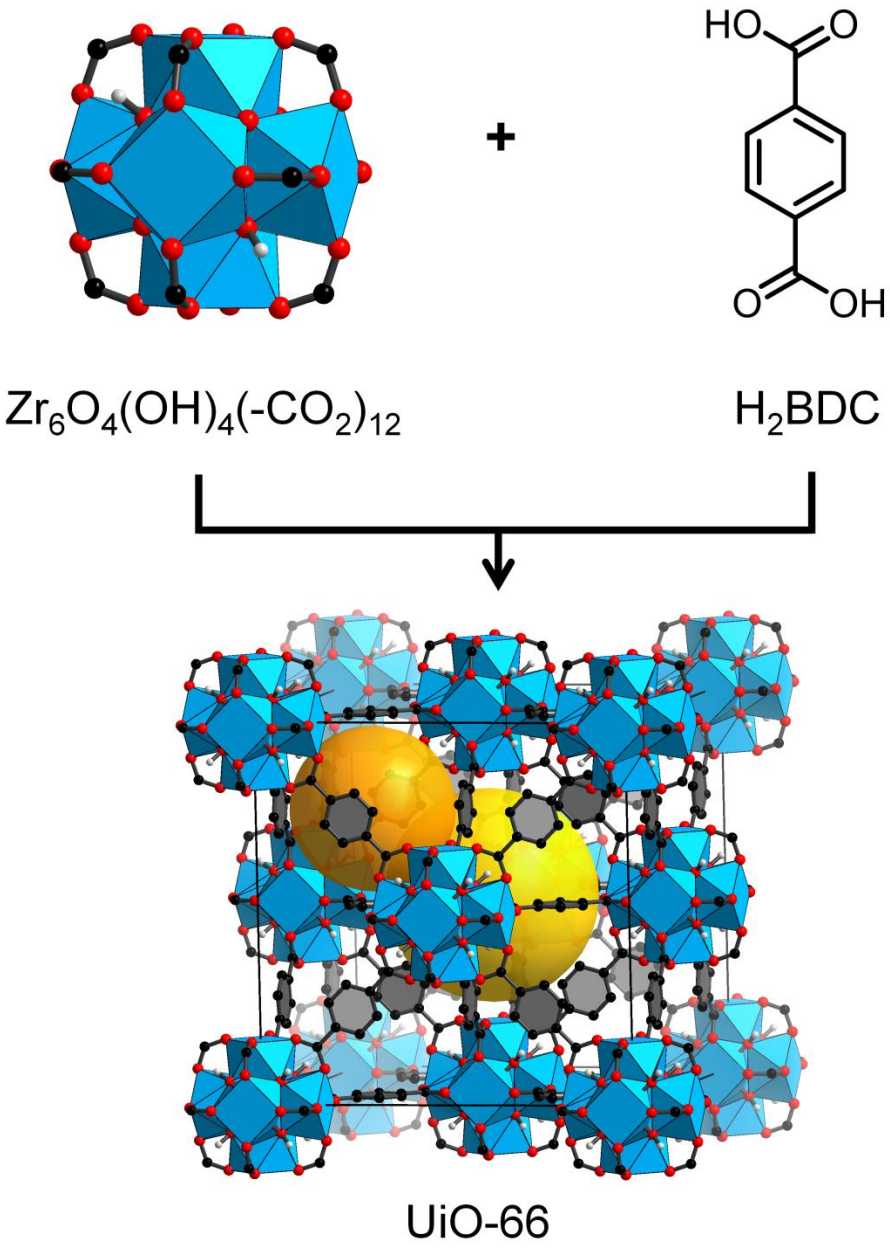

Figure 2.1. The defect-free SXRD structure of UiO-66 with 12-coordinated Zr-based metal clusters interconnected by benzenedicarboxylate (BDC) linkers in a face-centered cubic array. Atom labeling scheme: C, black; O, red; Zr, blue polyhedra; H, white; tetrahedral cavity, orange; octahedral cavity, yellow. Hydrogen atoms on the BDC link have been omitted for clarity.

Experimental

A new synthesis was developed for making previously unnatainable large single crystals of UiO-66. It uses a combination of N,N-diethylformamide (DEF) and formic acid, with the optimal ratio of 1:1 by volume, and produces the largest crystals (Figure 2.2) with the least number of defects. The starting salts of $ZrOCl_2 \cdot 8H2O$ (0.037 mmol) and H_2BDC (0.03 mmol) were dissolved in DEF prior to mixing and addition of formic acid. The resulting solution was placed in the oven for 2 days at 408 K. Further, it was found these conditions could be extended to a variety of zirconium salts and functionalized linkers. This includes $ZrCl_4$, $ZrBr_4$, $Zr(OPr)_4$, 2-bromobenzenedicarboxylic acid (H_2BDC-Br), 2-aminobenzenedicarboxylic acid (H_2BDC-NH_2), 2-nitrobenzendicarboxylic acid (H_2BDC-NO_2) and 2,5-dimethylbenzendicarboxylic acid (H_2BDC-Me_2), all of which contain similar 'missing linker' point defects, but the ability to use such a wide array of starting materials demonstrates the versatility of these synthetic conditions .

Chemicals used in this work. *N*,*N*-dimethylformamide (DMF) was obtained from Fisher Scientific. Formic acid (purity >98%) and anhydrous methanol were obtained from EMD Millipore Chemicals. *N*,*N*-Diethylformamide (DEF) was purified with activated charcoal and molecular sieves before passing them through the columns of a PS-MD-7 solvent purification system made by Inert Technology. Zirconium oxychloride octahydrate (>99.5%), zirconium(IV) chloride (>99.5%), hydrofluoric acid (aqueous, 48%), benzenedicarboxylic acid (98%), 2-bromobenzenedicarboxylic acid, 2-nitrobenzendicarboxylic acid and 22-aminobenzenedicarboxylic acid were all purchased from Sigma-Aldrich. Zirconium(IV) propoxide (70 wt% in 1-propanol) was purchased from Alfa Aesar, zirconium(IV) bromide (99%) was obtained from VWR International and 2,5-dimethylbenzendicarboxylic acid was purchased from TCI America. All starting materials and solvents, unless otherwise specified, were used without further purification.

Analytical techniques. SXRD data for UiO-66 environment cell stages 1 – 4, NH_2-, NO_2-, DiMe- and Br-UiO-66 were collected on beamline 11.3.1 at the Advanced Light Source, Lawrence Berkeley National Lab. Samples were mounted on MiTeGen® kapton loops and placed in a 100(2) K nitrogen cold stream provided by an Oxford Cryostream 700 Plus low temperature apparatus on the goniometer head of a Bruker D8 diffractometer equipped with a PHOTON100 CMOS detector operating in shutterless mode. For the environment cell measurements, a quartz cell connected to a vacuum line and integrated gas loading manifold was used. The sample was evacuated at 298(2) K overnight, and data was continuously collected whilst heating to 500(2) K. This was then cooled to 200(2) K for a more accurate structure determination, then warmed to 298(2) K and exposed to the atmosphere. Heating and cooling rates of 200 K per hour and 360 K per hour were used respectively. Diffraction data were collected using synchrotron radiation monochromated using silicon(111) to a wavelength of 0.7749(1)Å, except Br-UiO-66 which was measured with 0.6880(1)Å. An approximate full-sphere of data was collected using a combination of phi and omega scans with scan speeds of 1 second per degree for the phi scans, and 1 and 3 seconds per degree for the omega scans at $2\theta = 0$ and -45, respectively.

Data for the remaining samples were collected using a Bruker D8-Venture diffractometer equipped with Mo-(λ= 0.71073 Å) and Cu-target (λ= 1.54184 Å) micro-focus X-ray tubes and a PHOTON 100 CMOS detector, operated at 50 kW and 1 mA. In all case, the structures were

solved by intrinsic phasing (SHELXT) and refined by full-matrix least squares on F^2 (SHELXL-2014). All non-hydrogen atoms were refined anisotropically unless otherwise specified. Hydrogen atoms were geometrically calculated and refined as riding atoms.
Powder X-ray diffraction patterns (PXRD) were recorder using a Bruker D8 Advance diffractometer (Göbel-mirror monochromated Cu Kα radiation λ= 1.54056 Å). Elemental microanalyses (EA) were performed at Atlantic Microlab, Inc. Thermogravimetric analysis coupled to mass spectrometer (TGA-MS) curves were recorded with a SDT Q600 (TA Instruments) coupled with a Thermostar QMS200 M3 quadropolar mass spectrometer, under a 100 ml min^{-1} Ar flow at a heating rate of 10 K min^{-1}. Solution ^1H NMR spectra were acquired on a Bruker AVB-400 NMR spectrometer. FTIR spectra were collected in-house using a Bruker ALPHA Platinum ATR-FTIR Spectrometer equipped with a single reflection diamond ATR module. N_2 sorption isotherms were measured on a Quantachrome Quadrasorb at 77 K.

The permanent porosity of activated UiO-66 synthesized with a variable amount of formic acid was proven by N_2 sorption analysis at 77 K. The Brunauer-Emmett-Teller (BET) surface areas were 1212.2, 1238.4, 1095.9, 1104.4, 1216.6 m^2 g^{-1} for 0.5:1, 0.75:1, 1:1, 1.25:1 and 2:1 formic acid:DEF, following the same general trend of a higher percentage of defects resulting in a higher surface area, as determined from SXRD. The BET of the sample activated at 573 K and the least number of defects is 1066.3 m^2 g^{-1}.

UiO-66 and functionalized UiO-66 syntheses. In a 20 mL vial, 12 mg (0.037 mmol) zirconium oxychloride octahydrate was dissolved in 1 mL DEF. Separately, 5 mg (0.03 mmol) H_2BDC was dissolved in 1 mL DEF. The solutions were mixed together and 2 mL formic acid was added. The resulting solution was shaken and placed in the oven at 408 K for 2 days. Block crystals were obtained in 69% yield. This synthesis route has been employed to obtain single crystals using an equimolar amount of $ZrCl_4$, $ZrBr_4$, $Zr(SO_4)_2$ and $Zr(OPr)_4$. Additionally, an equimolar amount of functionalized BDC linker also yields single crystals of the respective functionalized versions. Evacuated samples were prepared by washing twice a day for three days with DMF, the same again with methanol, then activated under vacuum at 423 K. Unless otherwise specified, UiO-66 single crystals were synthesized from the standard conditions with zirconium oxychloride octahydrate as described here.

FTIR of native UiO-66 (4000 – 400 cm^{-1}): 3219 (br), 3929 (m). 2907 (w), 1651 (m), 1579 (s), 1504 (s), 1306 (s), 1157 (m), 1104 (w), 1018 (m), 819 (m), 742 (s), 701 (m), 661 (s), 551 (s), 472 (s)

E.A. (wt%): C: 31.11; H: 2.24; N: <1.0; Cl: <1.0

Silver chloride test. 57.6 mg of UiO-66 was solvent exchanged and activated at 423 K before being digested in aqueous HF. The organic components are insoluble and were filtered. To the supernatant, 2 ml of 1 M $AgNO_3$ (2 mmol) was added.

Effect of varying the amount of formic acid on defect percentage. By varying the amount of formic acid used in the synthesis (Table 1), keeping other variables constant, a ratio of 1:1 ratio of formic acid:DEF is optimal to reduce the defects was observed, with less formic acid in the synthesis resulting in poorer crystal quality and more defects. More formic acid results in a slight increase in the number of defects, with some variation from sample to sample expected.

Additionally, the electron density at O3 is correlated with the number of defects in the structure, as evidenced in Table 2.1.

Table 2.1. The variation of formic acid in the synthesis affects the crystal size, quality and number of defects as determined from SXRD data.

Formic acid:DEF volume ratio	Linker occupation /%	O3 site occupation /%
0.5 : 1	82 ±1.8	35.0 ±3.1
0.75 : 1	83 ±1.2	25.5 ±2.4
1 : 1	90 ±0.9	19.1 ±1.4
1.25 : 1	93 ±1.2	20.7 ±1.3
2:1	85 ±1.1	21.5 ±2.3

Included below (Figure 2.2) are some optical microscope images of the single crystals obtained with the different ratio of formic acid to DEF. Qualitatively, the size of the crystals relates to the amount of defects, with larger crystals containing fewer defects.

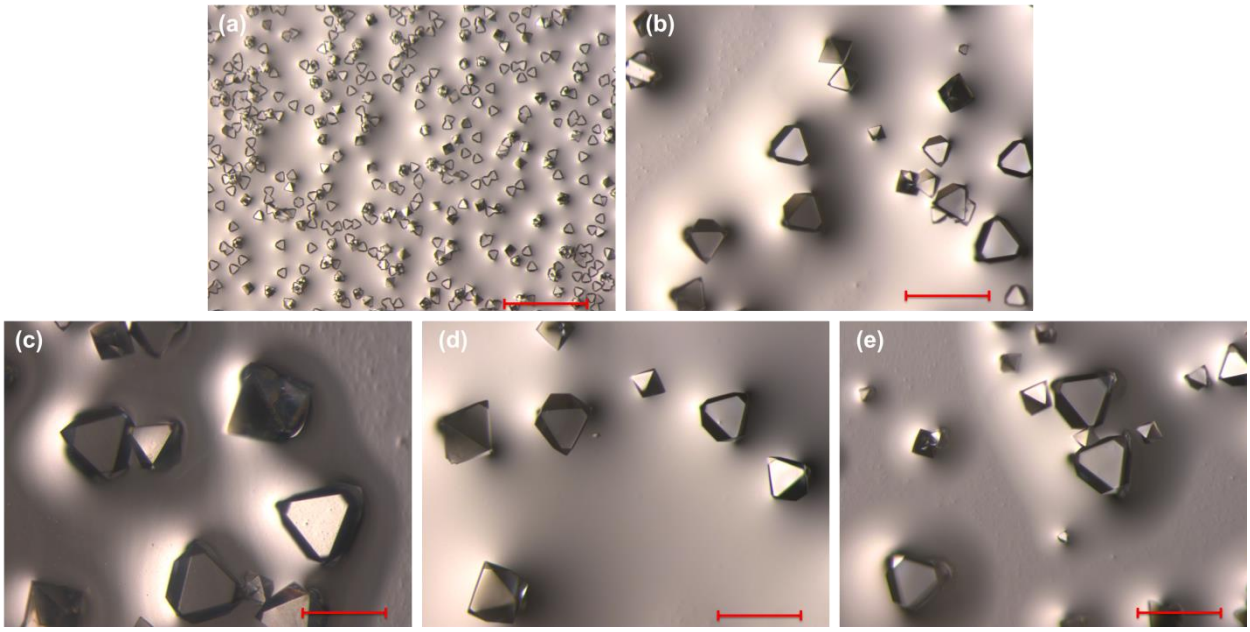

Figure 2.2. Optical microscope images of typical UiO-66 crystals synthesized from varying the ratio of formic acid to DEF: (a) 1:4 formic acid:DEF; (b) 1:2; (c) 1:1; (d) 5:4; (e) 2:1. Crystal size peaks at a 1:1 ratio of DEF to formic acid. Scale bar on each image is 300 μm.

Results and Discussion

A significant limitation in conclusively identifying the defect species has been the microcrystalline nature of UiO-66, with the largest crystals reaching only 10 μm.[22] The identity origins of the defects in the structure are determined and postulated in this study. This was facilitated by our development of a highly versatile synthesis of large single crystals up to 300 μm in diameter (Figure 2.2) that is achievable from a variety of zirconium salts and functionalized linkers. In this study species at the defect site is identified as a water molecule, with the charge-balancing achieved by a hydroxide counterion located at hydrogen-bonding distance to the μ^3-OH group on the cluster. In some cases there is also an excess of oxide over hydroxide in the metal-oxide cluster.

Since the starting salt, $ZrOCl_2 \cdot 8H_2O$, is in reality a cluster of four zirconium atoms that are eight-coordinated, with bridging hydroxides and terminal water molecules, the charge in this salt is compensated by hydrogen-bonded chloride counterions.[28] Combined with experimental evidence for the water and hydroxide species, both the counterion species and the coordinated water are hypothesized to be displaced during the synthesis by the negatively charged BDC linker in order to maintain charge neutrality, yet not all species are displaced prior to the crystallization of the structure.

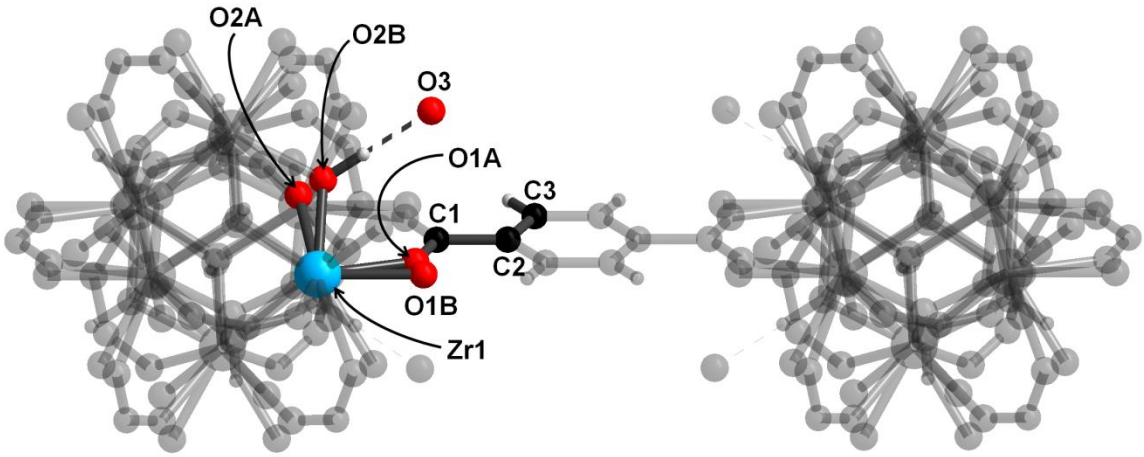

Figure 2.3. The asymmetric unit of UiO-66 is highlighted with zirconium (blue), oxygen (red), carbon (black) and hydrogen (white) in color.

The asymmetric unit of UiO-66 synthesized from zirconium oxychloride octahydrate is shown in Figure 2.3. In the following discussion, the defect site will be referred to as O1B, and the position at a hydrogen bonding distance to μ^3-OH (O2B) on the zirconium cluster is designated O3. The structure was found to be identical to that reported by the previous single crystal study[22] save for the linker occupancy, which has previously been shown to be variable dependent on synthetic conditions.[11,21] Two notable bond lengths for this study are zirconium to O1B of 2.24(3) Å, and O2B to O3 of 2.730(6) Å, the latter corresponding to a hydrogen-bonding distance. The values quoted are for the optimal synthesis conditions as discussed below.

In order to investigate the effect of sample activation on the defect site, an environment cell was used to study the structure *in-situ* in real-time under vacuum. The results are shown in Figure 2.4 and Tables 2-5. A single crystal of UiO-66, synthesized using the optimal ratio of 1:1 formic acid: *N*,*N*-diethylformamide (DEF), was glued to a 10 μm Kapton MiTeGen loop with a minimum amount of epoxy resin. This was mounted on a custom goniometer head affixed with gas-inlet and a 3 mm diameter capillary cover. The sample was then placed under vacuum overnight at room temperature (stage 1), then heated at a rate of 200 K per hour up to 500 K where the sample was kept at this temperature for 1 hour (stage 2). To reduce thermal motion and obtain a more accurate structure, the sample was then cooled to 200 K (stage 3) at 360 K per hour. Finally, the cell was warmed to room temperature, also at 360 K per hour, and the crystal exposed to the atmosphere (stage 4).

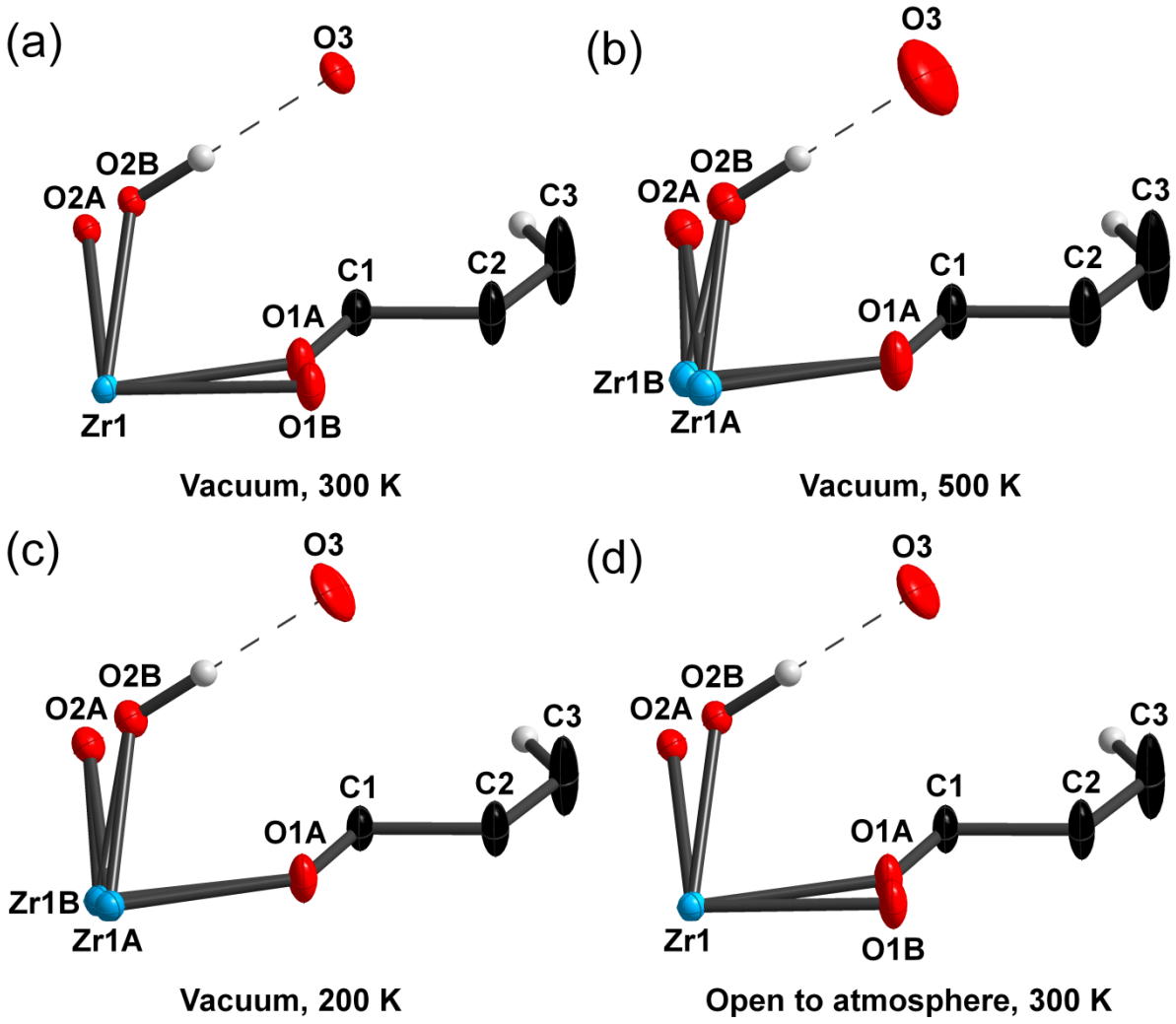

Figure 2.4. Asymmetric unit of UiO-66 measured in the environment cell. The measurement begins at room temperature under vacuum (a), then heated to 500 K at 200 K per hour, (b), during which the water molecules replacing the linker are removed to leave an open metal site on Zr. The crystal was then cooled to 200 K, (c), for a more accurate structure determination. Finally, the crystal was warmed to room temperature, (d), where the water molecules are once again coordinated to Zr. Ellipsoids are shown at 50% probability.

After stage 1, structure refinement reveals the electron density at O1B is reduced compared to the as-synthesized sample, converging to 5.0 ±1.0% of the oxygen atom O1B, 92 ±0.9% linker, with O1B still located at 2.27(6) Å from zirconium. The refinement was performed by allowing the occupancies of both O1A, C1, C2 and C3 to refine freely but constrained to the same value, while the occupancy of O1B was refined separately and freely, apart from the constraint that the anisotropic thermal ellipsoid parameters must be identical to O1A. From solving the structure during heating, it was found that at just above room temperature, all electron density at this site is removed, while an oxygen atom of 11.3% occupancy is modeled at O3, located at 2.85(2) Å from O2B.

Stage 2 still shows no density at O1B, but intriguingly, there is still 11.3% of an oxygen atom at position O3, suggesting the hydrogen-bonded species present here are strongly bound to the metal cluster. As confirmation at lower temperature, the structure at stage 3 does not change except the thermal ellipsoids shrink, as expected. The relatively short hydrogen-bonding O2B-O3 distance combined with the consistent observation of electron density at this position, even at high temperature, strongly indicate the presence of anions.

This is also necessary considering the negative charge lost from the missing BDC must be accounted for. The oxo and hydroxyl (O2A and O2B respectively) occupancies converge to 50.7 ±0.5% and 49.3 ±0.5% respectively, so another species must counterbalance the charge. This can be achieved by O3 if this species is anionic, further corroborating these findings.

The only other structural change at this point is brought about by the loss of the water molecule, producing a coordinatively unsaturated site at zirconium. This results in a shift of the affected zirconium ions towards the center of the metal oxide cluster, so now zirconium is disordered over two positions. This is not surprising as the coordination number is reduced while maintaining the Zr^{4+} charge, meaning zirconium binds more tightly to the remaining atoms in the coordination sphere.

Upon warming to room temperature and exposure to the atmosphere at stage 4, the density at O1B returns and the zirconium atom is no longer disordered, as is expected when O1B is coordinated. The bond length is 2.21(3) Å, identical to the as-synthesized sample. Since the source of O1B at this stage is from the atmosphere, this must be either water or hydroxide originating from deprotonated atmospheric water. A search through the Cambridge Structural Database consistently puts Zr-OH_2 distances around 2.2 Å, while Zr-OH is approximately 2.0 Å. This matches the evidence at stage 3 that anions are responsible for charge-balancing the structure, not at the defect site itself. Indeed, the cause of defect formation of defects is postulated to arise from the strong hydrogen bonding interactions of these counterions to the metal cluster, since the negatively charged BDC linker must substitute these anions in order to coordinate to the structure for charge-balancing reasons. This may be a result of an ion mobility issue once the framework begins to crystallize, preventing hydroxide from replacing water bound to zirconium. Similarly, the lack of space in the crystallized structure would prevent the BDC linker from coordinating.

Table 2.2. Crystallographic data for UiO-66 measured in the environment cell from stage 1.

Sample	**UiO_GC1**
chemical formula	$C_{44.16}H_{26.02}O_{32.18}Zr_6$
formula mass	1618.87
crystal system	cubic
space group	*Fm*-3*m*
λ (Å)	0.77490
a (Å)	20.7570(7)
Z	4
V (Å^3)	8943.2(9)
temperature (K)	298(2)
density (g/cm^{-3})	1.202
measured reflections	8290
unique reflections	1081
parameters	33
restraints	0
R_{int}	0.0496
θ range (deg)	2.14-39.48
R_1, wR_2	0.0357, 0.1454
S (GOF)	1.302
max/min res. dens. (e/Å^3)	0.89/-0.87

Table 2.3. Crystallographic data for UiO-66 measured in the environment cell during stage 2.

Sample	**UiO_GC2**
chemical formula	$C_{44.16}H_{26.02}O_{30.99}Zr_6$
formula mass	1599.67
crystal system	cubic
space group	*Fm*-3*m*
λ (Å)	0.77490
a (Å)	20.7192(7)
Z	4
V (Å^3)	8894.4(9)
temperature (K)	500(2)
density (g/cm^{-3})	1.195
measured reflections	49181
unique reflections	1389
parameters	32
restraints	0
R_{int}	0.0328
θ range (deg)	2.14-43.92
R_1, wR_2	0.0302, 0.1183
S (GOF)	1.266
max/min res. dens. (e/Å^3)	01.04/-0.84

Table 2.4. Crystallographic data for UiO-66 measured in the environment cell during stage 3.

Sample	**UiO_GC3**
chemical formula	$C_{44.16}H_{26.02}O_{30.99}Zr_6$
formula mass	1599.67
crystal system	cubic
space group	*Fm*-3*m*
λ (Å)	0.77490
a (Å)	20.7239(8)
Z	4
V (Å^3)	8900.5(10)
temperature (K)	200(2)
density (g/cm^{-3})	1.194
measured reflections	48278
unique reflections	1388
parameters	32
restraints	0
R_{int}	0.0355
θ range (deg)	2.14-43.91
R_1, wR_2	0.0312, 0.1191
S (GOF)	1.252
max/min res. dens. (e/Å^3)	1.14/-0.82

Table 2.5. Crystallographic data for UiO-66 measured in the environment cell during stage 4.

Sample	**UiO_GC4**
chemical formula	$C_{44.16}H_{26.02}O_{32.18}Zr_6$
formula mass	1618.87
crystal system	cubic
space group	*Fm*-3*m*
λ (Å)	0.77490
a (Å)	20.7574(7)
Z	4
V (Å^3)	8943.7(9)
temperature (K)	298(2)
density (g/cm^{-3})	1.202
measured reflections	48357
unique reflections	1396
parameters	33
restraints	0
R_{int}	0.0305
θ range (deg)	2.14-43.90
R_1, wR_2	0.0300, 0.1243
S (GOF)	1.202
max/min res. dens. (e/Å^3)	1.34/-0.96

Confirmation of the presence of anions came from the synthesis of UiO-66 starting from zirconium(IV) propoxide, where a propoxide counterion is cleanly refined within hydrogen-bonding distance to the metal cluster (Figure 2.5a). Upon activation at 423 K under vacuum, propoxide is still present (Figure 2.5b), suggesting this is strongly bound and charge-balancing the cluster. Propoxide is favored in this position over hydroxide presumably because the former is in excess and a slightly stronger base than hydroxide, which is present in trace amounts. However, activation at 573 K successfully removes the propoxide ion, and after exposure to the atmosphere the crystal structure is indistinguishable from UiO-66 synthesized from zirconium oxychloride (Figure 2.5c). Indeed, the entirely air-free crystal structure of UiO-66 synthesized from the zirconium oxychloride salt after activation at 573 K reveals the loss of the counterion. As confirmation of the propoxide model, refinements using the propoxide model were performed against the reflection data for other starting salts as well as the sample activation at 573 K, which failed to converge. This treatment at 573 K correspond to the 'dehydroxylated' structure of UiO-66, previously reported as containing inorganic clusters of Zr_6O_6.[21] The results from this study indicate this conversion is partial, however based on the percentage of μ^3-oxo groups, only the

μ^3-hydroxy groups with counterions are deprotonated. Charge-balancing is now achieved from 60.0 ±3.7% μ^3-oxo and 39.0 ±3.7% μ^3-hydroxy groups bound to the zirconium cluster, from occupancy refinement (Figure 2.5e). Interestingly, upon exposure to water the structure reverts to 50.4 ±1.8% oxo, 49.6 ±1.8% hydroxyl, and charge-balancing achieved by the return of a counterion (Figure 2.5f). This agrees with the previous observation of structural reversibility from neutron powder refinement.[21] Since this process occurs upon simple atmospheric exposure, it is postulated that moisture is sufficient to protonate some of the μ^3-oxo groups to form μ^3-hydroxy groups, leaving the charge-balancing hydroxide ions in the pore and hydrogen-bonding to the clusters.

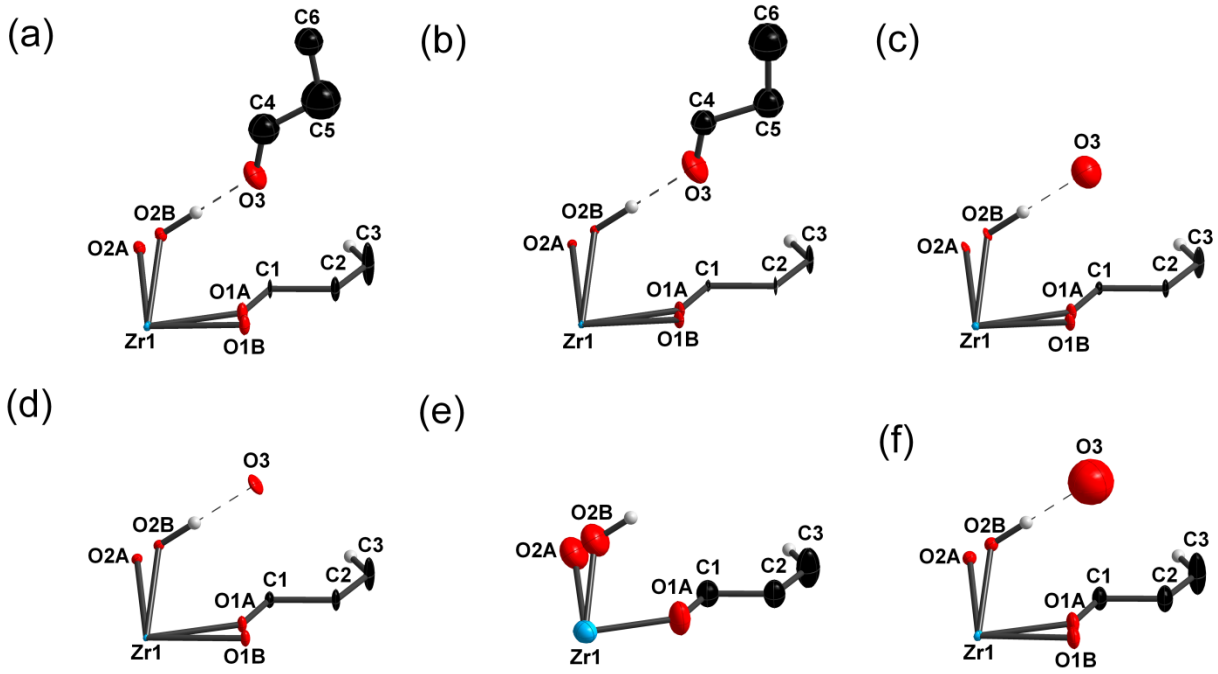

Figure 2.5. The asymmetric unit of UiO-66 of the as-synthesized propoxide (a) shows propoxide anions hydrogen-bonded to the cluster. This propoxide anion is not removed upon evacuation at 423 K for 24 hours (b), but is removed under vacuum at 573 K for 24 hours (c). Both (b) and (c) were exposed to atmosphere after evacuation. Structure (d) is as-synthesized from $ZrOCl_2$ for comparison with the air-free structure of UiO-66, (e), also synthesized from $ZrOCl_2$ but evacuated at 573 K for 24 hours. In (e) hydroxide anion has been removed and the adjacent μ^3-hydroxy groups are deprotonated, converting some portion to μ^3-oxo groups to achieve charge balance. Finally, (f) is the rehydrated sample by exposure to the atmosphere following activation at 573 K.

In syntheses starting from halide salts such as $ZrCl_4$, the as-synthesized anion identity required further investigation: no density beyond O3 can be modeled and make reasonable chemical sense, suggesting O3 is either hydroxide or chloride. There are reports of UiO-66 containing varying amounts of chloride, thus indicating the species present may be dependent on synthesis conditions.[11,22,27] Elemental analysis of the samples in this investigation reveal an average of 0.6% chlorine present after solvent exchange followed by activation at 423 K of UiO-66. With an error of 0.3% in both accuracy and precision, this amount of chloride cannot be

considered significant. With a defect percentage of 10% and no further density in the pores, 2.6% chloride by weight would be expected.

As another test for chloride, silver nitrate was added to the digested supernatant of UiO-66, but no immediate precipitation was observed. After leaving overnight, a dark brown solid formed which is likely due to silver oxide formation.

The anion identity was further investigated from the synthesis of UiO-66 from zirconium(IV) bromide with a trace amount of added water. If bromide was hydrogen bonding to the cluster, a large increase in electron density and a longer hydrogen bond length would be expected. SXRD reveals comparable electron density in the as-synthesized samples, with an oxo:hydroxyl occupancy of 50.1 ±1.2% to 49.9 ±1.2%, and a hydrogen bond length of 2.718(18) Å, indicating bromide ions are not present in that position. It was also found that saturating the solution with alkali halide salts such as NaCl, KCl, NaBr and KBr did not result in a significant increase in electron density or number of defects.

Another possibility is that the counterions are formates due to the large amount incorporated during the synthesis. However, ^{1}H NMR digestion of UiO-66 shows there is no formate present, and it is not possible to model density beyond O3. Evidence in support of hydroxide counterions is that the hydrogen bonding distance in the as-synthesized sample is very similar to that of the 'dehydroxylated' and rehydrated sample. Since this species can only come from the atmosphere in the rehydrated sample, O3 must be hydroxide originating from deprotonated atmospheric water. Bringing the evidence together strongly indicates the identity of O3 is a hydroxide ion.
Thermogravimetric analysis coupled to a mass spectrometer shows three steps during the decomposition of UiO-66 under an argon atmosphere. The first step, beginning around 323 K confirms the loss of water molecules from the defect position. The second step at 573 to 723 K reveals the loss of the hydroxide counterion as water, corresponding to the dehydroxylation step. The final step from 723 to 923 K is the decomposition of the BDC linker, with loss of CO_2 and aromatic species. No HCl gas was found to be released during this decomposition process, as would be expected is chloride was present as the counterion.

Scanning electron microscopy images show well-defined single crystals that show no obvious surface defects (Figure 2.6). Additionally energy-dispersive X-ray spectroscopy showed no amount of chloride, even in the samples with the highest number of defects.

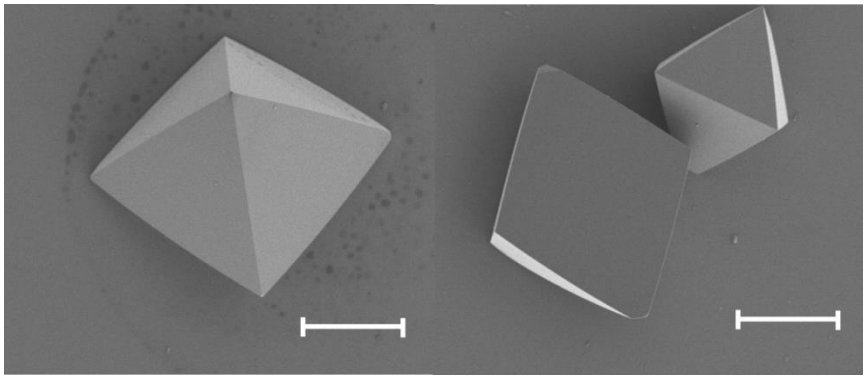

Figure 2.6. Scanning electron microscopy images of single crystal UiO-66 showing no obvious signs of a defective structure. Scale bar 100 μm.

Conclusion

In summary, the linker defect has been definitively identified to be water, with charge neutrality maintained by hydroxide anions hydrogen-bonding to the metal cluster, in the well-known and important crystal structure of UiO-66 (Figure 2.7). This is a rare study in the field of solid-state chemistry and MOFs in which defects were successfully identified with molecular level precision. This study opens up the possibility to study point defects in other similar porous systems such as a comparison with UiO-67, and to design *in-situ* studies following the cluster growth formations in order to confirm the hypotheses put forward on defect formation.

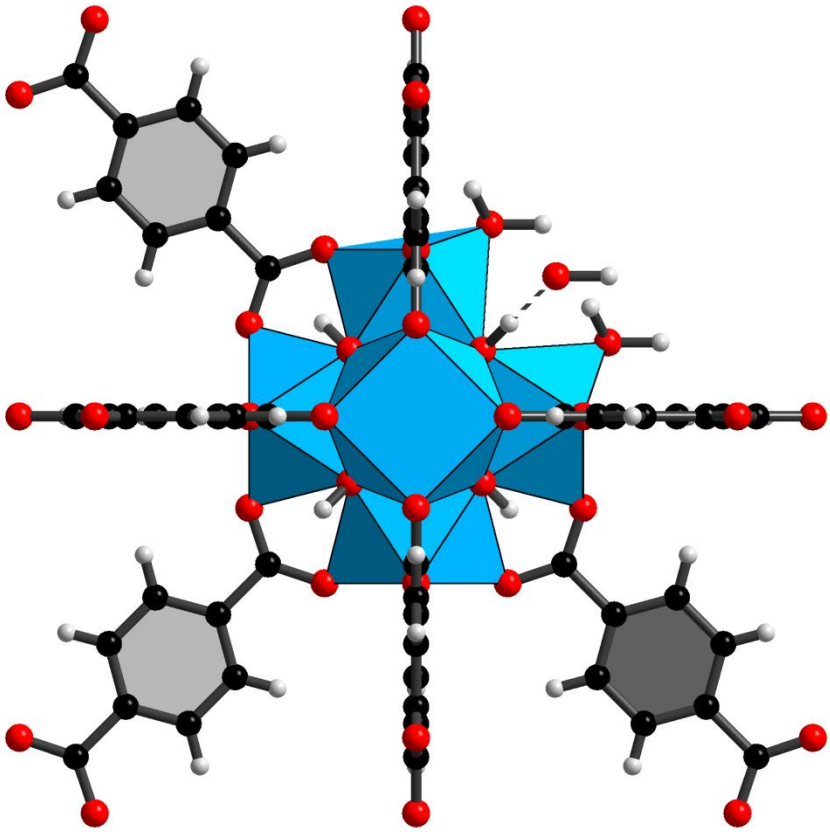

Figure 2.7. View of one metal cluster in UiO-66 with a defect site where BDC is replaced by water, with the resulting loss in charge counterbalanced by a hydroxide anion.

Appendices and Notes

Acknowledgements. This work, including synthesis, characterization and crystal structure analysis was funded by BASF SE (Ludwigshafen, Germany) and the U.S. Department of Defense, Defense Threat Reduction Agency (HDTRA 1-12-1-0053). Work performed at the Advanced Light Source is supported by the Director, Office of Science, Office of Basic Energy Sciences, of the U.S. Department of Energy under Contract No. DE-AC02-05CH11231. I acknowledge Dr. Kevin J. Gagnon for support with the environment cell experiment, assistance with the crystallography and discussions, Seungkyu Lee for the synthesis of large UiO-66 crystals, Professor Hans-Beat Bürgi and Dr. Felipe Gándara for help with crystallography. I also acknowledge Yingbo Zhao for his assistance with electron microscopy, Dr. Peter Siman for discussions; and Dr. Simon Teat for the synchrotron X-ray diffraction data acquisition support at the beamline 11.3.1 (Advanced Light Source, Lawrence Berkeley National Laboratory).

X-ray Diffraction Analyses

Table 2.6. SXRD data for UiO-66 synthesized with 0.5:1 formic acid:DEF.

Sample	**UiO66_0.5:1_formic: DEF**
chemical formula	$C_{39.36}H_{23.52}O_{34.80}Zr_6$
formula mass	1600.54
crystal system	cubic
space group	Fm-3m
λ (Å)	0.71073
a (Å)	20.7343(11)
Z	4
V (Å^3)	8913.9(14)
temperature (K)	100(2)
density (g/cm^{-3})	1.193
measured reflections	6409
unique reflections	499
parameters	32
restraints	0
R_{int}	0.1223
θ range (deg)	2.78-26.04
R_1, wR_2	0.508, 0.1955
S (GOF)	1.243
max/min res. dens. (e/Å^3)	0.78/-0.53

Table 2.7. SXRD data for UiO-66 synthesized with 0.75:1 formic acid:DEF.

Sample	**UiO66_0.75:1_formic: DEF**
chemical formula	$C_{39.84}H_{23.92}O_{34.04}Zr_6$
formula mass	1594.55
crystal system	cubic
space group	*Fm*-3*m*
λ (Å)	0.71073
a (Å)	20.7425(9)
Z	4
V (Å^3)	8824.5(12)
temperature (K)	100(2)
density (g/cm^{-3})	1.187
measured reflections	8151
unique reflections	745
parameters	32
restraints	0
R_{int}	0.0762
θ range (deg)	2.78-30.47
R_1, wR_2	0.0488, 0.1867
S (GOF)	1.279
max/min res. dens. (e/Å^3)	0.91/-0.52

Table 2.8. SXRD data for UiO-66 synthesized with 1:1 formic acid:DEF.

Sample	**UiO66_1:1_formic: DEF**
chemical formula	$C_{43.20}H_{25.60}O_{33.53}Zr_6$
formula mass	1628.40
crystal system	cubic
space group	*Fm*-3*m*
λ (Å)	0.71073
a (Å)	20.7366(9)
Z	4
V (Å^3)	8916.9(12)
temperature (K)	100(2)
density (g/cm^{-3})	1.213
measured reflections	8152
unique reflections	745
parameters	32
restraints	0
R_{int}	0.0552
θ range (deg)	2.78-30.48
R_1, wR_2	0.0356, 0.1278
S (GOF)	1.320
max/min res. dens. (e/Å^3)	0.94/-0.56

Table 2.9. SXRD data for UiO-66 synthesized with 1.25:1 formic acid:DEF.

Sample	**UiO66_1:1.25_DEF: formic**
chemical formula	$C_{44.64}H_{26.24}O_{33.66}$ Zr_6
formula mass	1648.37
crystal system	cubic
space group	*Fm*-3*m*
λ (Å)	0.71073
a (Å)	20.7366(9)
Z	4
V (Å^3)	8916.9(12)
temperature (K)	100(2)
density (g/cm^{-3})	1.228
measured reflections	8134
unique reflections	744
parameters	32
restraints	0
R_{int}	0.0662
θ range (deg)	2.78 – 30.48
R_1, wR_2	0.0392, 0.1424
S (GOF)	1.302
max/min res. dens. (e/Å^3)	1.16/-0.60

Table 2.10. SXRD data for UiO-66 synthesized with 2:1 formic acid:DEF.

Sample	**UiO66_2:1_formic: DEF**
chemical formula	$C_{40.80}H_{24.32}O_{33.72}Zr_6$
formula mass	1601.36
crystal system	cubic
space group	Fm-3m
λ (Å)	0.71073
a (Å)	20.7366(9)
Z	4
V (Å^3)	8916.9(12)
temperature (K)	100(2)
density (g/cm^{-3})	1.193
measured reflections	7967
unique reflections	743
parameters	32
restraints	0
R_{int}	0.0524
θ range (deg)	2.78-30.48
R_1, wR_2	0.0438, 0.1712
S (GOF)	1.323
max/min res. dens. (e/Å^3)	0.84/-0.50

Table 2.11. SXRD data for UiO-66 synthesized from $Zr(OPr)_4$.

Sample	**UiO66-propoxide**
chemical formula	$C_{44.38}H_{23.47}O_{34.47}Zr_6$
formula mass	1655.50
crystal system	cubic
space group	*Fm*-3*m*
λ (Å)	0.71073
a (Å)	20.7570(11)
Z	4
V (Å^3)	8943.2(14)
temperature (K)	100(2)
density (g/cm^{-3})	1.230
measured reflections	16715
unique reflections	745
parameters	41
restraints	3
R_{int}	0.0864
θ range (deg)	2.78-30.45
R_1, wR_2	0.0387, 0.1432
S (GOF)	1.259
max/min res. dens. (e/Å^3)	1.56/-0.62

Table 2.12. SXRD data for UiO-66 synthesized from $Zr(OPr)_4$ and activated at 150 °C under dynamic vacuum.

Sample	**UiO66-propoxide_150C**
chemical formula	$C_{48.82}H_{24.77}O_{34.27}Zr_6$
formula mass	1706.93
crystal system	cubic
space group	*Fm*-3*m*
λ (Å)	0.71073
a (Å)	20.7604(12)
Z	4
V (Å^3)	8947.6(16)
temperature (K)	100(2)
density (g/cm^{-3})	1.267
measured reflections	6508
unique reflections	555
parameters	41
restraints	12
R_{int}	0.1161
θ range (deg)	2.78-27.10
R_1, wR_2	0.0359, 0.0847
S (GOF)	1.123
max/min res. dens. (e/Å^3)	0.56/-0.45

Table 2.13. SXRD data for UiO-66 synthesized from $Zr(OPr)_4$ and activated at 300 °C under dynamic vacuum.

Sample	**UiO66-propoxide_300C**
chemical formula	$C_{42.77}H_{25.34}O_{33.17}Zr_6$
formula mass	1617.25
crystal system	cubic
space group	*Fm*-3*m*
λ (Å)	0.71073
a (Å)	20.7475(9)
Z	4
V (Å^3)	8930.9(12)
temperature (K)	100(2)
density (g/cm^{-3})	1.203
measured reflections	7202
unique reflections	594
parameters	32
restraints	0
R_{int}	0.1046
θ range (deg)	2.78 – 27.85
R_1, wR_2	0.0292, 0.686
S (GOF)	1.094
max/min res. dens. (e/Å^3)	0.46/-0.48

Table 2.14. SXRD data for UiO-66 synthesized from $ZrBr_4$.

Sample	**UiO-66_ZrBr4**
chemical formula	$C_{41.76}H_{24.88}O_{34}Zr_6$
formula mass	1617.94
crystal system	cubic
space group	*Fm*-3*m*
λ (Å)	0.71073
a (Å)	20.7570(6)
Z	4
V (Å^3)	8943.2(8)
temperature (K)	100(2)
density (g/cm^{-3})	1.202
measured reflections	8796
unique reflections	745
parameters	32
restraints	0
R_{int}	0.0413
θ range (deg)	2.78-30.45
R_1, wR_2	0.0370, 0.1724
S (GOF)	1.354
max/min res. dens. (e/Å^3)	1.24/-0.59

Table 2.15. SXRD data for UiO-66 activated at 300 °C under dynamic vacuum and measured without exposure to air.

Sample	**dehydrox_UiO66**
chemical formula	$C_{45.12}H_{25.68}O_{30.48}Zr_6$
formula mass	1602.78
crystal system	cubic
space group	*Fm*-3*m*
λ (Å)	0.71073
a (Å)	20.6677(13)
Z	4
V (Å^3)	8828.3(17)
temperature (K)	130(2)
density (g/cm^{-3})	1.206
measured reflections	7202
unique reflections	594
parameters	32
restraints	0
R_{int}	0.0344
θ range (deg)	2.78-26.36
R_1, wR_2	0.0385, 0.1059
S (GOF)	1.194
max/min res. dens. (e/Å^3)	0.72/-0.44

Table 2.16. SXRD data for UiO-66 activated at 300 °C under dynamic vacuum and measured following exposure to air.

Sample	**UiO66_dehyd_rehyd**
chemical formula	$C_{43.15}H_{25.62}O_{33.54}Zr_6$
formula mass	1627.95
crystal system	cubic
space group	*Fm*-3*m*
λ (Å)	0.71073
a (Å)	20.7266(8)
Z	4
V (Å^3)	8904.0(10)
temperature (K)	100(2)
density (g/cm^{-3})	1.214
measured reflections	8254
unique reflections	912
parameters	41
restraints	12
R_{int}	0.0682
θ range (deg)	2.78-27.10
R_1, wR_2	0.0667, 0.2455
S (GOF)	1.250
max/min res. dens. (e/Å^3)	1.43/-1.09

Table 2.17. SXRD data for as-synthesized UiO-66 with BDC-Me_2 as the organic linker.

Sample	**DiMe-UiO66**
chemical formula	$C_{54.67}H_4O_{34.63}Zr_6$
formula mass	1762.02
crystal system	cubic
space group	*Fm*-3*m*
λ (Å)	0.77490(1)
a (Å)	20.804(3)
Z	4
V (Å^3)	9004(3)
temperature (K)	100(2)
density (g/cm^{-3})	1.300
measured reflections	21821
unique reflections	1159
parameters	46
restraints	0
R_{int}	0.1151
θ range (deg)	1.58-40.34
R_1, wR_2	0.0443, 0.1306
S (GOF)	1.165
max/min res. dens. (e/Å^3)	1.78/-0.95

Table 2.18. SXRD data for as-synthesized UiO-66 with BDC-NO_2 as the organic linker.

Sample	**NO_2-UiO66**
chemical formula	$C_{38.93}H_4N_{4.85}O_{40.82}Zr_6$
formula mass	1739.97
crystal system	cubic
space group	*Fm*-3*m*
λ (Å)	0.77490
a (Å)	20.7964(9)
Z	4
V (Å^3)	8994.2(12)
temperature (K)	100(2)
density (g/cm^{-3})	1.285
measured reflections	5113
unique reflections	1100
parameters	41
restraints	12
R_{int}	0.0284
θ range (deg)	3.02-40.19
R_1, wR_2	0.0379, 0.1446
S (GOF)	1.259
max/min res. dens. (e/Å^3)	1.09/-1.03

Table 2.19. SXRD data for as-synthesized UiO-66 with BDC-NH_2 as the organic linker.

Sample	**NH_2-UiO66**
chemical formula	$C_{39.89}H_{3.98}N_5O_{40.56}Zr_6$
formula mass	1749.42
crystal system	cubic
space group	*Fm*-3*m*
λ (Å)	0.77490
a (Å)	20.7988(12)
Z	4
V (Å^3)	8997.4(16)
temperature (K)	100(2)
density (g/cm^{-3})	1.291
measured reflections	20604
unique reflections	1406
parameters	48
restraints	0
R_{int}	0.1085
θ range (deg)	3.02–44.09
R_1, wR_2	0.799, 0.2226
S (GOF)	1.127
max/min res. dens. (e/Å^3)	2.15/-1.82

Table 2.20. SXRD data for as-synthesized UiO-66 with BDC-Br as the organic linker.

Sample	**Br-UiO66**
chemical formula	$C_{41.28}H_4Br_{5.18}O_{33.65}Zr_6$
formula mass	1999.46
crystal system	cubic
space group	*Fm*-3*m*
λ (Å)	0.77490
a (Å)	20.769(5)
Z	4
V (Å^3)	8959(6)
temperature (K)	100(2)
density (g/cm^{-3})	1.482
measured reflections	22975
unique reflections	999
parameters	50
restraints	0
R_{int}	0.0889
θ range (deg)	2.69-33.12
R_1, wR_2	0.0487, 0.1604
S (GOF)	1.158
max/min res. dens. (e/Å^3)	1.04/-0.77

The PXRD pattern of UiO-66 with the optimal ratio of 1:1 formic acid:DEF is shown to be highly crystalline and uniform when compared with the simulated crystal structure of UiO-66 (Figure 2.8).

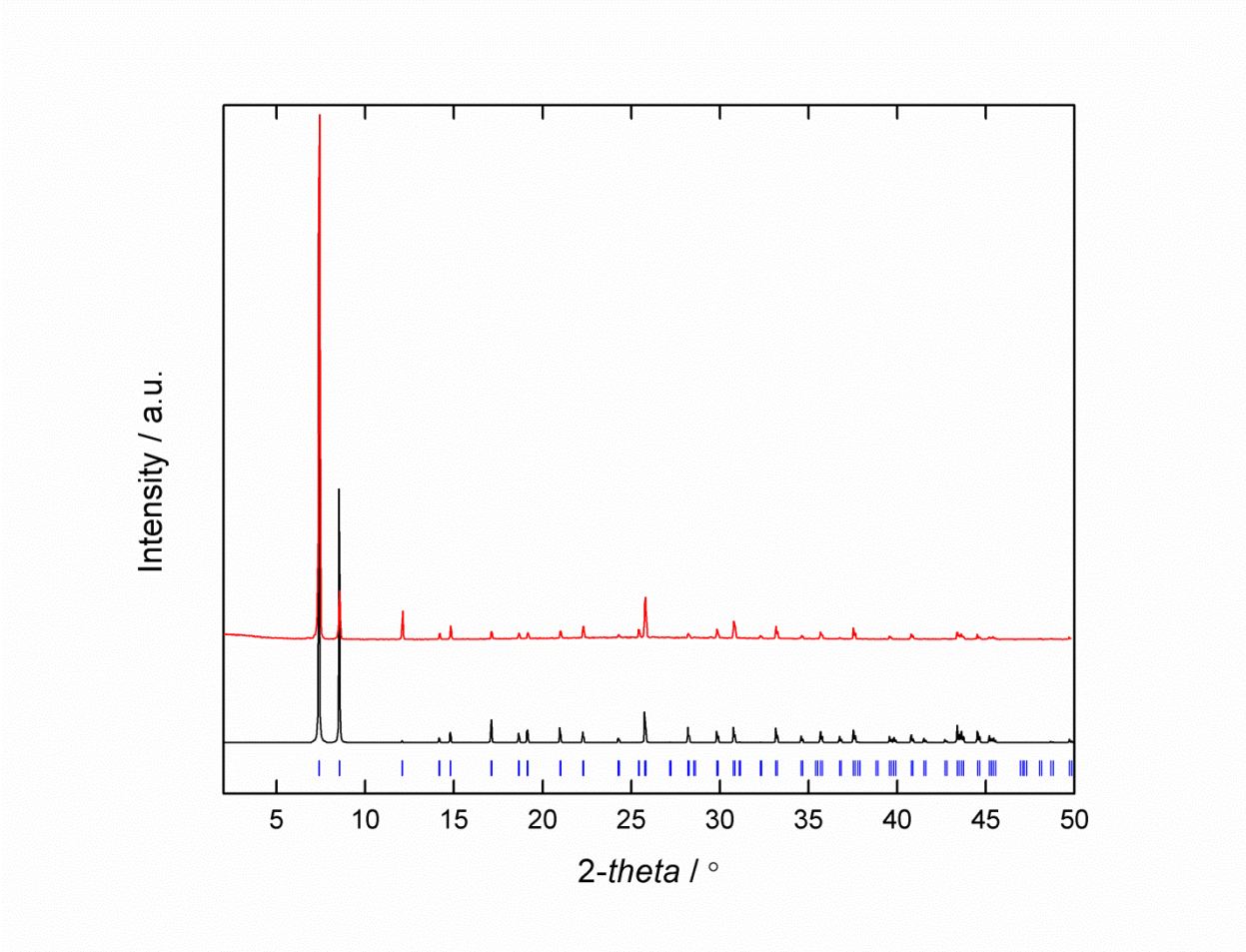

Figure 2.8. Comparison of the experimental PXRD pattern of UiO-66 (red) with the simulated pattern (black) from single crystal X-ray data.

Thermogravimetric Analysis

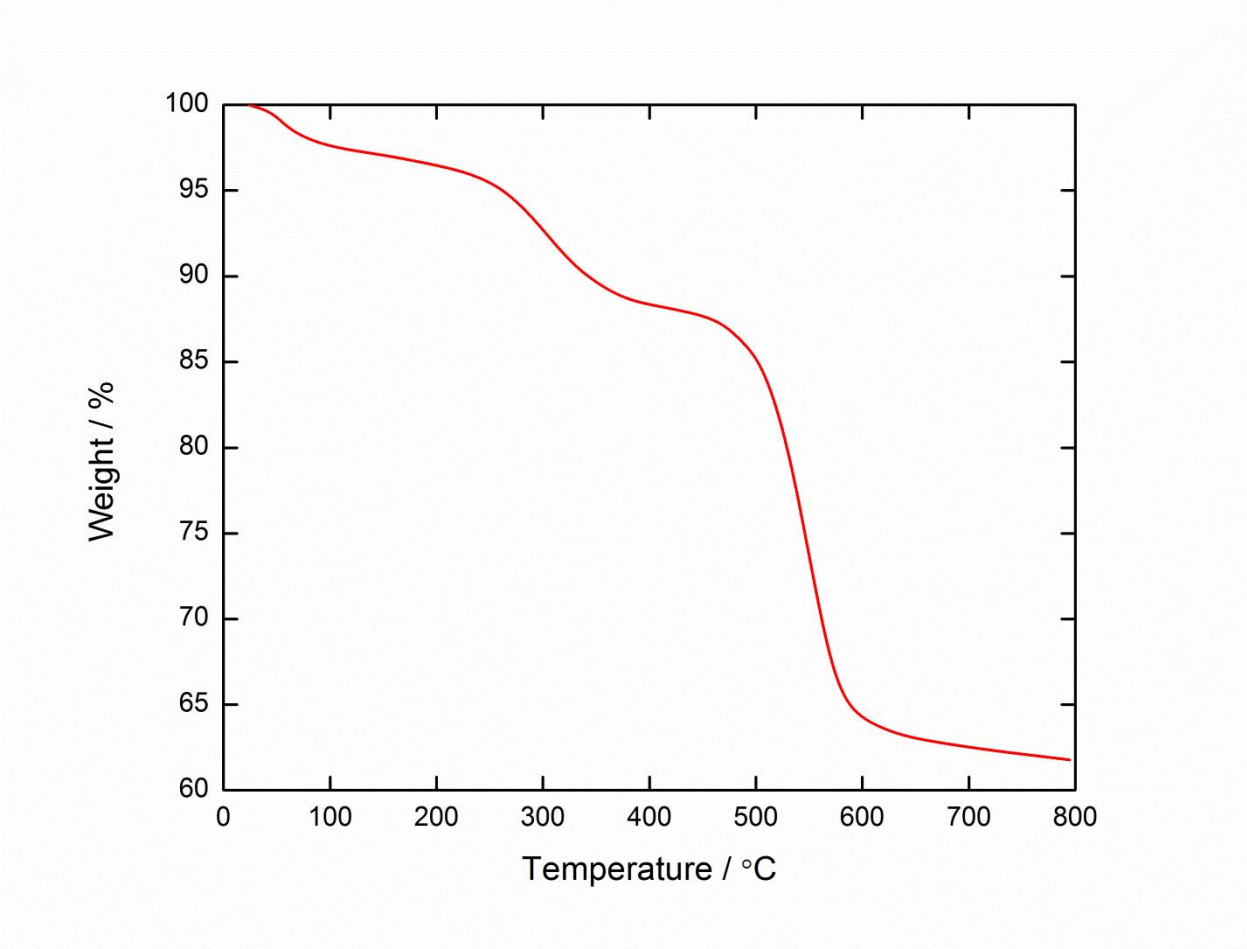

Figure 2.9. Thermogravimetric analysis (TGA) data of single crystal UiO-66 performed under argon atmosphere. Three steps are observed, first with loss of water, second also shows loss of water from the hydroxide counterion along with organic species, and finally the decomposition of the BDC linker.

N_2 Sorption Isotherms

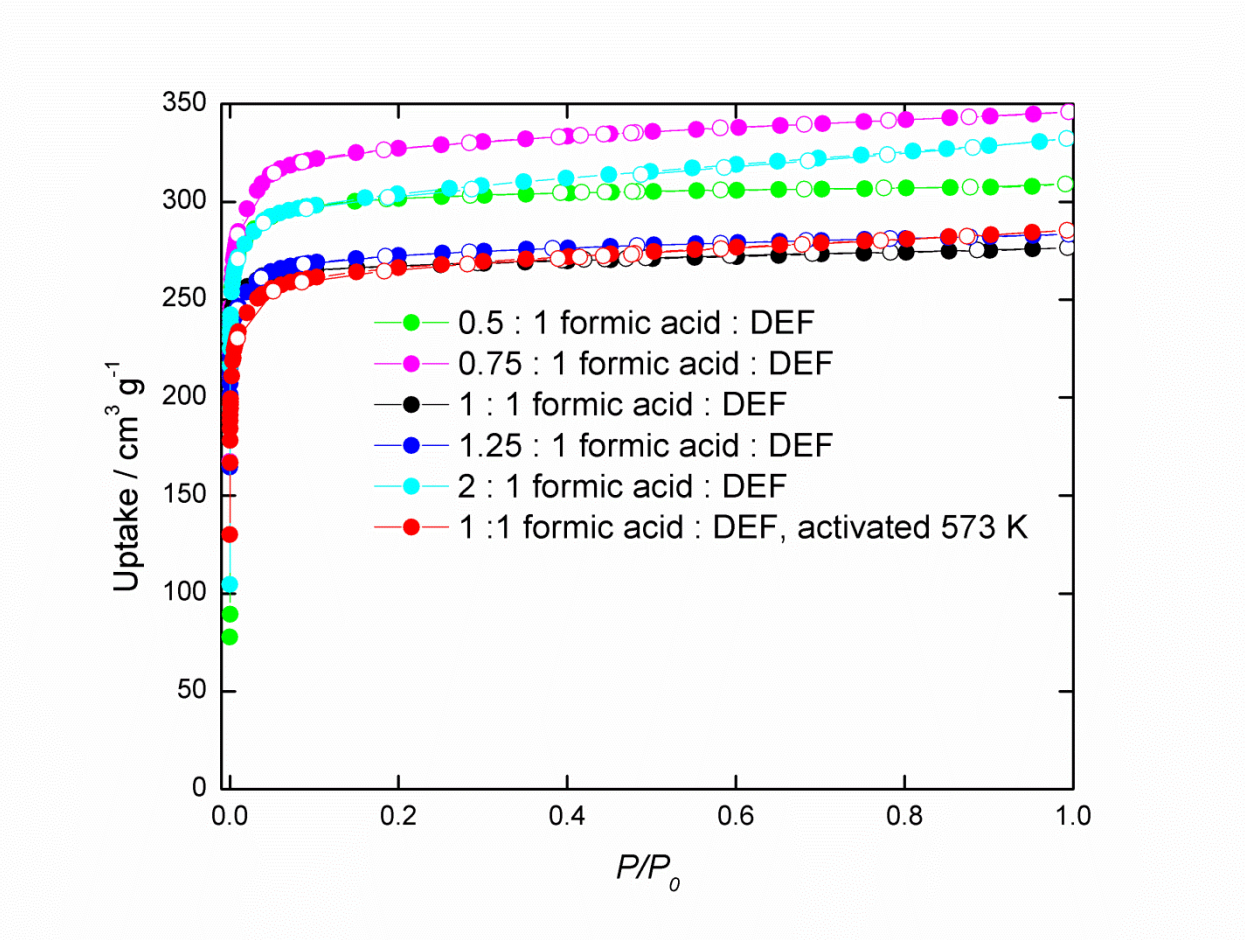

Figure 2.10. Synthesis using a variable amount of formic acid exhibits a large variation in surface area while still producing single crystals. This increase can be largely attributed to the number of defects, while activation at 573 K has only a minor effect on surface area. All samples are activated at 423 K unless otherwise noted.

Bibliography

(1) Jorgensen, J. D.; Hinks, D. G.; Radaelli, P. G.; Pei, S.; Lightfoot, P.; Dabrowski, B.; Segre, C. U.; Hunter, B. A. *Phys. C* **1991**, *185–189* (1), 184–189.

(2) West, A. R. *Basic Solid State Chemistry*, Second.; John Wiley & Sons Inc, **1999**.

(3) Long, R.; English, N. J.; Prezhdo, O. V. *J. Am. Chem. Soc.* **2013**, *135* (50), 18892–18900.

(4) Murugan, B.; Ramaswamy, A. V. *J. Am. Chem. Soc.* **2007**, *129* (11), 3062–3063.

(5) Nørskov, J. K.; Bligaard, T.; Hvolbaek, B.; Abild-Pedersen, F.; Chorkendorff, I.; Christensen, C. H. *Chem. Soc. Rev.* **2008**, *37* (10), 2163–2171.

(6) Aoki, T.; Chang, Y.; Badano, G.; Zhao, J.; Grein, C.; Sivananthan, S.; Smith, D. J. *J. Cryst. Growth* **2004**, *265* (1–2), 224–234.

(7) Ameloot, R.; Vermoortele, F.; Hofkens, J.; De Schryver, F. C.; De Vos, D. E.; Roeffaers, M. B. J. *Angew. Chem. Int. Ed.* **2013**, *52* (1), 401–405.

(8) Rickman, R. H.; Dunstan, P. R. *J. Raman Spectrosc.* **2014**, *45* (1), 15–21.

(9) Stammer, X.; Heißler, S. *Spectroscopy* **2013**, *28* (8), 22–27.

(10) Petkov, P. St.; Vayssilov, G. N.; Liu, J.; Shekhah, O.; Wang, Y.; Wöll, C.; Heine, T. *Chem. Phys. Chem.* **2012**, *13* (8), 2025–2029.

(11) Cliffe, M. J.; Wan, W.; Zou, X.; Chater, P. A.; Kleppe, A. K.; Tucker, M. G.; Wilhelm, H.; Funnell, N. P.; Coudert, F.-X.; Goodwin, A. L. *Nat. Commun.* **2014**, *5*, 4176–4183.

(12) Sturza, M.; Allred, J. M.; Malliakas, C. D.; Bugaris, D. E.; Han, F.; Chung, D. Y.; Kanatzidis, M. G. *Chem. Mater.* **2015**, *27* (9), 3280–3290.

(13) Janssen, Y.; Santhanagopalan, D.; Qian, D.; Chi, M.; Wang, X.; Hoffmann, C.; Meng, Y. S.; Khalifah, P. G. *Chem. Mater.* **2013**, *25* (22), 4574–4584.

(14) Fang, Z.; Bueken, B.; De Vos, D. E.; Fischer, R. A. *Angew. Chem. Int. Ed.* **2015**, *54* (25), 7234–7254.

(15) Fang, Z.; Du, J. P.; Kauer, M.; Zhang, W.; Lochenie, C.; Jee, B.; Albada, B.; Metzler-Nolte, N.; Po, A.; Weber, B.; Muhler, M.; Wang, Y.; Schmid, R.; Fischer, R. A. *J. Am. Chem. Soc.* **2014**, *136* (27), 9627–9636.

(16) Gagnon, K. J.; Perry, H. P.; Clearfield, A. *Chem. Rev.* **2012**, *112* (2), 1034–1054.

(17) Tu, B.; Pang, Q.; Wu, D.; Song, Y.; Weng, L.; Li, Q. *J. Am. Chem. Soc.* **2014**, *136* (41), 14465–14471.

(18) Shoaee, M.; Anderson, M. W.; Attfield, M. P. *Angew. Chem. Int. Ed.* **2008**, *47* (44), 8525–8528.

(19) Vermoortele, F.; Ameloot, R.; Alaerts, L.; Matthessen, R.; Carlier, B.; Fernandez, E. V. R.; Gascon, J.; Kapteijn, F.; De Vos, D. E. *J. Mat. Chem.* **2012**, *22* (20), 10313–10321.

(20) Cavka, J. H.; Jakobsen, S.; Olsbye, U.; Guillou, N.; Lamberti, C.; Bordiga, S.; Lillerud, K. P. *J. Am. Chem. Soc.* **2008**, *130* (42), 13850–13851.

(21) Wu, H.; Chua, Y. S.; Krungleviciute, V.; Tyagi, M.; Chen, P.; Yildirim, T.; Zhou, W. *J. Am. Chem. Soc.* **2013**, *135* (28), 10525–10532.

(22) Øien, S.; Wragg, D.; Reinsch, H.; Svelle, S.; Bordiga, S.; Lamberti, C.; Lillerud, K. P. *Cryst. Growth Des.* **2014**, *14* (11), 5370–5372.

(23) Wu, H.; Yildirim, T.; Zhou, W. *J. Phys. Chem. Lett.* **2013**, *4* (6), 925–930.

(24) Vermoortele, F.; Bueken, B.; Le Bars, G.; Van de Voorde, B.; Vandichel, M.; Houthoofd, K.; Vimont, A.; Daturi, M.; Waroquier, M.; Van Speybroeck, V.; Kirschhock, C.; De Vos, D. E. *J. Am. Chem. Soc.* **2013**, *135* (31), 11465–11468.

(25) Valenzano, L.; Civalleri, B.; Chavan, S.; Bordiga, S.; Nilsen, M. H.; Jakobsen, S.; Lillerud, K. P.; Lamberti, C. *Chem. Mater.* **2011**, *23* (7), 1700–1718.

(26) Katz, M. J.; Brown, Z. J.; Colón, Y. J.; Siu, P. W.; Scheidt, K. a; Snurr, R. Q.; Hupp, J. T.; Farha, O. K. *Chem. Comm.* **2013**, *49* (82), 9449–9451.

(27) Shearer, G. C.; Chavan, S.; Ethiraj, J.; Vitillo, J. G.; Svelle, S.; Olsbye, U.; Lamberti, C.; Bordiga, S.; Lillerud, K. P. *Chem. Mater.* **2014**, *26* (14), 4068–4071.

(28) Clearfield, A.; Vaughan, P. A. *Acta Cryst.* **1956**, *9*, 555–558.

Chapter 3: The Influence of Water on the Superacidity of Sulfated MOF-808

Introduction

The interface between a solid and its environment is the key for the resulting properties of a material. Indeed, knowledge of the chemical nature of this interface leads to an understanding of how materials interact with their environment. In non-porous solids, this interface is dominated by the external surface. Characterizing the molecular detail of interfaces is no mean feat since the chemistry of the bulk solid can obscure the surface chemistry that is responsible for many of the properties of the material. This is evidenced in the commercially available solid-state superacid catalyst, sulfated zirconia. Despite being studied extensively, an understanding of the nature of the Brønsted superacidic site remains controversial, in part due to the difficulty in characterizing the structure of an amorphous material with multiple models proposed,[1–6] but also because of wildly variable properties depending on preparation conditions.[7–10]

In porous crystalline materials such as metal-organic frameworks (MOFs), this interface is largely described by the chemical nature of the pore environment. This class of material offers not only unprecedented surface area and tunability upon which to perform chemistry, but the crystallinity also provides powerful means of characterizing the structure to a much greater level. The characterization of such heterogeneity does remain challenging since crystal structure analysis superimposes all of this information into one unit cell. While this approach yields a wealth of information including the pore size, shape and overall topology, crucial structural detail may still be lost or overlooked. This is especially applicable when considering the impact local structural elements may have on the resulting properties of the material.[11–13] Neglecting such detail can render a true understanding of the structure-property relationships intractable. In this report, a combination of crystallographic, spectroscopic and computational techniques have been employed to elucidate the pore environment of MOF-808 functionalized with sulfate and selenate species to determine the nature and position of the Brønsted superacidic sites, which are found to be water molecules with a strong hydrogen bond to chelating sulfate. Upon heating at elevated temperatures beyond those used for evacuating the pores of the MOF, these water molecules could be removed, and as a consequence the material loses its superacidic properties. With a strong understanding of the superacidic active site and how it is possible to manipulate it, a study into how low-value, short-chain hydrocarbons could be transformed into viable fuel additives catalyzed by Brønsted acids. Specifically, isobutene dimerization to isooctane was targeted, which following hydrogenation is employed as an octane booster.[14]

The superacid being studied, the zirconium-based material termed sulfated MOF-808 (S-MOF-808), can be prepared by first synthesizing pristine MOF-808 before exchanging the formate groups of this framework on the zirconium oxide cluster with sulfate species, simply by washing in dilute sulfuric acid.[15] The structure of as-synthesized pristine MOF-808, with the formula $Zr_6O_4(OH)_4(BTC)_2(HCOO)_5(OH_2)_2$, is made up of an octahedron of zirconium atoms that are triply bridged by μ^3-O and -OH groups. The formate groups bridge two zirconium atoms each to form a 'belt' around the cluster (Figure 3.1).[16] A cluster is connected to six other clusters by trimesate linkers, three above and three below the 'belt' of formates, into the diamond topology. Note that only five out of a possible six formates coordinate to the cluster, with water molecules replacing the last formate. As-synthesized sulfated MOF-808 (S-MOF-808) replaces

formate with sulfate groups and more terminal water molecules. Unfortunately, due to the apparent multiple binding modes of sulfate, a number of potential open metal site positions and uncertainty on charge-balancing limited early work on determining the source of the superacidic site in the first and, to date, only reported superacidic MOF.

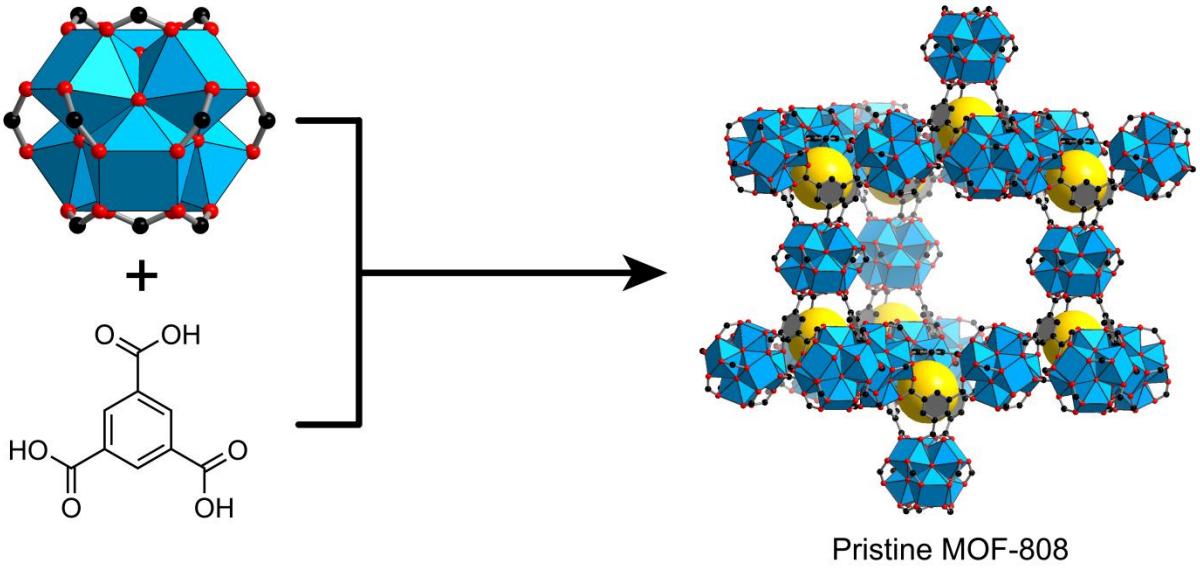

Figure 3.1. Synthesis of pristine MOF-808 constructed by 6-coordinate zirconium-based metal clusters containg formate groups and linked by benzenetricarboxylate into the diamond topology.

Experimental

Chemicals used in this work. *N,N*-dimethylformamide (DMF) was obtained from Fisher Scientific. Formic acid (purity > 98%) and anhydrous chloroform were obtained from EMD Millipore Chemicals. Anhydrous acetone was obtained from Acros Organics. Zirconium oxychloride octahydrate (>99.5%), hydrofluoric acid (aqueous, 48%), sulfuric acid (H_2SO_4, purity ≥ 95%), 1,3,5-benzenetricarboxylic acid (H_3BTC), selenic acid (aqueous, 40%) deuterated sulfuric acid (D_2SO_4, 96-98%, 99.5 atom % D), dimethylsulfoxide (DMSO-*d6*, >99.9%, 99.96% atom % D) and D_2O (99.9 atom % D) was obtained from Aldrich. Deuterated 1,3,5-benzenetricarboxylic acid (D_3DBTC, 97%, 98 atom % D) was obtained from CDN Isotopes. Trimethylphosphine oxide (TMPO, crystalline) was obtained from Alfa Aesar. All starting materials and solvents, unless otherwise specified, were used without further purification.

Analytical techniques. Single-crystal X-ray diffraction (SXRD) data were collected on beamline 11.3.1 at the Advanced Light Source, Lawrence Berkeley National Lab. Samples were mounted on MiTeGen® kapton loops and placed in a 100(2) K nitrogen cold stream provided by an Oxford Cryostream 700 Plus low temperature apparatus on the goniometer head of a Bruker D8 diffractometer equipped with a PHOTON100 CMOS detector operating in shutterless mode. Diffraction data were collected using synchrotron radiation monochromated using a silicon (111) reflection to a wavelength of 0.7749(1) Å. An approximate full-sphere of data was collected using a combination of phi and omega scans with scan speeds of 2 seconds per 4 degrees for the phi fast scans, and 5 and 15 seconds per degree for the omega scans at 2θ = 0 and -45 degrees, respectively. In all cases, the data were processed using the Bruker APEX2 software package.[17,18] Structures were solved by intrinsic phasing (SHELXT) and refined by full-matrix least squares on F^2 (SHELXL-2014) using the Olex2 software package.[19] All non-hydrogen atoms were refined anisotropically unless otherwise specified. Hydrogen atoms were geometrically calculated and refined as riding atoms. See Section S3 for more details.

Powder X-ray diffraction patterns (PXRD) were recorder using a Bruker D8 Advance diffractometer (Göbel-mirror monochromated Cu K_α radiation λ= 1.54056 Å). Elemental microanalyses (EA) for carbon, hydrogen, nitrogen and sulfur were performed in the Microanalytical Laboratory of the College of Chemistry at UC Berkeley, using a Perkin Elmer 2400 Series II CHNS elemental analyzer. Solution ^{1}H NMR spectra were acquired on a Bruker AVB-400 NMR spectrometer. N_2 sorption isotherms were measured on a Quantachrome Quadrasorb instrument, held at 77 K using a liquid nitrogen bath. Helium was used for the estimation of dead space for gas adsorption measurements. Ultra-high purity grade N_2 and He were used throughout the adsorption experiments.

Powder neutron diffraction data (PND) were collected at POWGEN at Oak Ridge National Laboratory, Tennessee. Two diffraction patterns were collected for each sample using center wavelengths 1.066 Å and 4.797 Å covering a d-spacing range of 0.5-15 Å.

Inductively coupled plasma-atomic emission spectroscopy (ICP-AES) was performed on a PerkinElmer Optima 7000 DV with 2% v/v aqueous nitric acid solution. Scanning electron microscope (SEM) images were obtained using a Zeiss Gemini Ultra-55 analytical scanning

electron microscope. FTIR spectra were collected in-house using a Bruker ALPHA Platinum ATR-FTIR Spectrometer equipped with a single reflection diamond ATR module.

General procedure for sample preparation. To reduce nucleation in the growth of MOF single-crystals, the inner surface of glass containers were rinsed with Sigmacote® siliconizing reagent, washed three times with acetone, and dried in oven before use. Following synthesis, the MOFs were washed with DMF. The molecular formulae of the MOFs were determined using a combination of elemental analysis (C, H, N and S), ^{1}H NMR (ratio of linker to formate) and ICP-OES (Zr, Se), and TGA-MS. A mixture of containing 20 μL of DMSO-*d6* and 580 μL of hydrofluoric acid (48 wt% in water) was used to digest 10 mg of each MOF for NMR measurements.

Native MOF-808 synthesis. Single crystals of MOF-808 was prepared following the reported procedure.[15] Briefly, $ZrOCl_2 \cdot 8H_2O$ (0.032 g, 0.10 mmol) and H_3BTC (0.022 g, 0.10 mmol) were dissolved separately in 2 ml DMF, then both solutions were combined in a 20 ml scintillation vial and 4 ml formic acid was added. This mixture was then placed in a pre-heated oven at 100 °C for three days. Colorless block crystals were collected in 81% yield based on Zr. As-synthesized MOF-808 single crystals were immersed in anhydrous DMF for three days followed by water for three days, during which time the solvent was exchanged three times per day. The same conditions were used for the preparation of deuterated MOF-808, except deuterated D_3BTC was used as the starting reagent, and washing was performed in D_2O instead of H_2O.

Preparation of Sulfated MOF-808. Approximately 50 mg of MOF-808 was immersed in 0.05 M sulfuric acid in H_2O for 24 hours and stirred at regular intervals. The treated solid was then washed with H_2O, then solvent exchanged by immersion in anhydrous acetone before exchanging into chloroform. For each step, the samples were washed for three days with the solvent being decanted and freshly replenished three times per day. The chloroform in the solvent-exchanged crystals was removed under dynamic vacuum (30 mTorr) for 24 h at room temperature, followed by 8 h at 80 °C and a further 16 h at 120 °C. The same conditions were used for the preparation of deuterated sulfated MOF-808, except deuterated sulfuric acid in D_2O was used, and all aqueous washings were carried out with D_2O.

^{1}H solution NMR spectra of the digested, activated and sulfated MOF-808 (400 MHz, DMSO-*d6*): 8.61 (s, BTC), 8.10 (s, HCOOH), 7.92 (s, DMF), peak area ratio (BTC:HCOOH:DMF) = 6.0:0.05:0.3. Anal.\calcd for $Zr_6O_4(OH)_4(C_9H_3O_6)_2(SO_4)_{2.3}(OH)_{1.4}(OH_2)_{3.1}(C_3H_7NO)_{0.4}$ = $Zr_6O_{34.1}C_{19.2}H_{20.4}S_{2.3}N_{0.4}$: C = 16.2%; H, 1.4%; N, 0.4%; S, 5.2%. Found: C = 17.2%; H, 1.3%; N, 0.6%; S, 5.4%.

Preparation of Selenated MOF-808. Approximately 50 mg of MOF-808 was immersed in 0.05 M selenic acid in H_2O for 24 hours and stirred at regular intervals. The treated solid was then washed with H_2O, then solvent exchanged by immersion in anhydrous acetone before exchanging into chloroform. For each step, the samples were washed for three days with the solvent being decanted and freshly replenished three times per day. The chloroform in the

solvent-exchanged crystals was removed under dynamic vacuum (30 mTorr) for 24 h at room temperature, followed by 8 h at 80 °C and a further 16 h at 120 °C.

^{1}H solution NMR spectra of the digested, activated and selenated MOF-808 (400 MHz, DMSO-*d6*): 8.64 (s, BTC), 7.85 (s, DMF), peak area ratio (BTC:HCOOH:DMF) = 6.00:0.00:0.5. Calculated formula $Zr_6O_4(OH)_4(C_9H_3O_6)_2(SeO_4)_{2.3}(OH)_{1.4}(C_3H_7NO)_{0.5}(H_2O)_{2.9}$ = $Zr_6O_{34}C_{19.5}H_{20.7}N_{0.5}Se_{2.3}$: C, 15.3%; H, 1.4%; N, 0.5%. Found: C, 15.4%; H, 0.9%; N, 0.7%.

Results and Discussion

Structural analysis of the superacidic framework began with the coordination mode of sulfate to the zirconium cluster. In aqueous solution, the sulfate groups are coordinated in both a bridging and chelating fashion (Figure 3.2), with the bridging mode dominating in a 4:1 ratio over chelating from SXRD analysis. In order to further characterize this system, selenated MOF-808 (Se-MOF-808) was also synthesized in a similar manner to sulfated MOF-808 (see Experimental section for details). This framework was found to contain only selenate that is bridging zirconium atoms in the as-synthesized state. However, upon activation under dynamic vacuum and heating at 120 ºC, both sulfate and selenate were found to have shifted into the chelating mode exclusively. This was confirmed using Rietveld refinement of the samples measured in an argon atmosphere. Since superacidity is only observed following sample activation, this chelating mode appears to be a key feature in the superacidic nature of sulfated MOF-808.

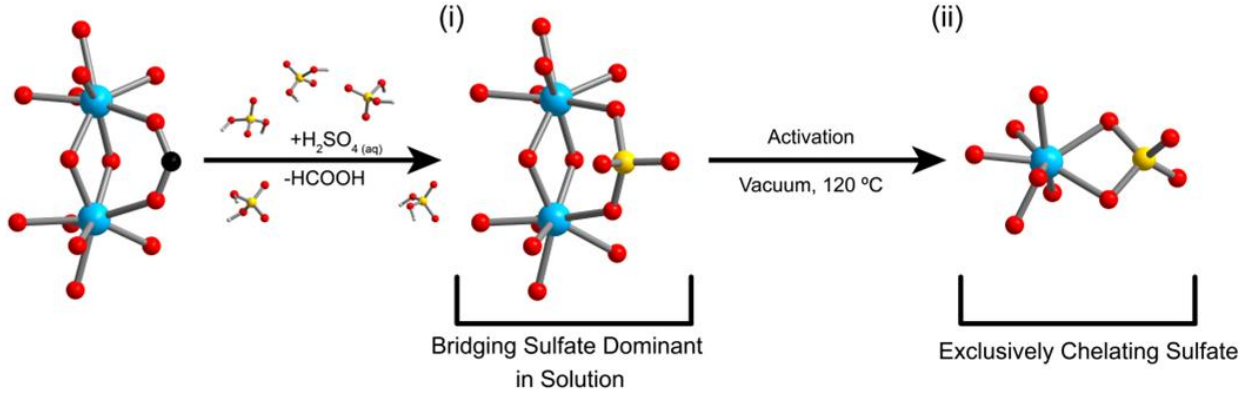

Figure 3.2. The formates that are bound to the zirconium oxide cluster can be substituted with sulfate anions by soaking the MOF in an aqueous solution of sulfuric acid. The sulfate groups which coordinate in a bidentate fashion to zirconium, predominantly by a bridging mode to two zirconium atoms when in solution, (i), and convert to exclusively the chelating mode to a single zirconium atom following activation by heating under dynamic vacuum (ii).

Following confirmation of the position of sulfate and selenate, the question of where charge-balancing is achieved was investigated. By elemental analysis, 2.3 sulfur atoms per 6 zirconium atoms were found, and thus an average of 2.3 sulfate per zirconium oxide cluster. Since each zirconium atom is in the +4 oxidation state, there is an excess of positive charge that is not properly accounted for with the model so far. To probe this, I turned to powder neutron diffraction in order to obtain better information on occupancies and thermal ellipsoids of light elements within the framework (Figure 3.3). A sample of S-MOF-808 with deuterated linker was measured at 10 K and 300 K and refined simultaneously against a structure model, revealing a 1:1 ratio of μ^3-O to μ^3-OH in both independent crystallographic positions within two standard deviations. An excess of μ^3-O is therefore not the source of charge-balancing. However, there is substantially more electron density located around the position of the oxygen, O6, connecting zirconium to sulfur, in the same location as coordinated water molecules are bound to the cluster in as-synthesized S-MOF-808. It is noteworthy to mention that the sulfate position could not be located by PND due to the low occupancy and extremely weak neutron scattering factor of

sulfur, so information from PXRD was used in combination with elemental analysis to confirm its presence in this sample.

Since the only electron density unaccounted for in this model is located at position O6, where water is present in the structure prior to activation, charge-balancing is thought to be achieved here by deprotonation of water molecules and resulting in terminal hydroxide. This assumption is quite plausible considering terminal water molecules bound to zirconium hydroxide clusters have been found to be strongly acidic.[20,21] The position O6 thus accounts for crystallographically superimposed oxygen from sulfate groups, hydroxide and water molecules that were not removed during the activation process. This overlap excludes the possibility of determining the precise coordinates of hydroxide, water and sulfate oxygen, but the total occupancy of these species was refined freely, converging to 78.4 ±1.1%. This corresponds to 9.4 oxygen atoms per cluster, out of a possible 12. Since there must be 4.6 oxygen atoms from 2.3 bidentate sulfate groups as found by elemental analysis, and 1.4 hydroxide groups for charge-balancing, this leaves 3.4 ±0.1 oxygen atoms unaccounted for, and are assigned to water. This observation was confirmed by thermogravimetric analysis coupled to a mass spectrometer (TGA-MS) on the evacuated sample, which demonstrated the loss of 3.1 water molecules per cluster and prior to structure decomposition (Figure 3.22). The first water signal observed from the mass spectrometer peaked at 143 ºC and indicates water is still present following evacuation and heating. After a plateau following the loss of water, the structure decomposes at around 350 ºC. This trend can be explained by considering that losing neutral, terminal water molecules would not collapse the structure, but once the framework is completely dehydrated, any further mass loss leads to structure decomposition since this involves the loss of charged species. Pooling evidence from elemental analysis, PND, ^{1}H-NMR of the digested MOF and TGA-MS, the overall formula for evacuated S-MOF-808 is $Zr_6O_4(OH)_4(BTC)_2(SO4)_{2.3}(OH)_{1.4}(OH_2)_{3.1}(DMF)_{0.5}$.

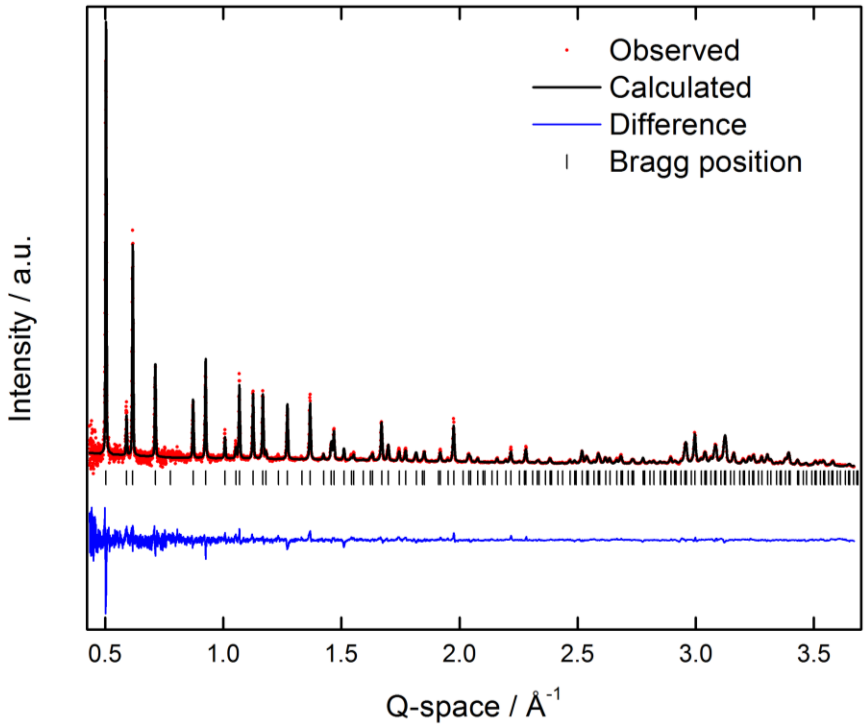

Figure 3.3. Rietveld refinement plot of S-MOF-808 from powder neutron diffraction data, with experimental data in red, calculated from the structure model in black, and the difference in blue.

With the overall chemical composition of S-MOF-808 now accurately known, the precise identity of the superacidic proton was investigated. The potential acidic sources are therefore discussed in turn. Firstly, terminal hydroxide may be eliminated simply because terminal water is present and bound to the cluster in the same manner as hydroxide. Protons on sulfate can also be ruled out since the pH of the solution when washed with water following incorporation of sulfate is 3.5, while the pK_{a2} value of sulfuric acid is 1.92.[22] Therefore, sulfate must be fully deprotonated at this stage. A direct comparison between μ^3-OH and terminal water is not as straightforward, however water molecules bound to the framework could be successfully removed by holding the temperature at 220 ºC overnight yet maintaining crystallinity and actually increasing in porosity. This sample will be hereafter referred to as dehydrated S-MOF-808. If the water molecules are indeed the most acidic species present, the superacidity should be lost. The sample unfortunately turns yellow-orange after this step, precluding Hammett indicator tests, but reproducing ^{31}P NMR with trimethylphosphine oxide as a probe reveals the loss of the resonance at 69 ppm, previously found to correspond with the strongly acidic site responsible for the catalytic activity in S-MOF-808 (Figure 3.4).[15,23] This experiment confirms the role of bound terminal water as the strongest Brønsted acid source. As found previously, exposure to atmospheric moisture also results in the loss of superacidity,[15] which is consistent with the proposition that sulfated zirconia requires a certain amount of moisture.[24]

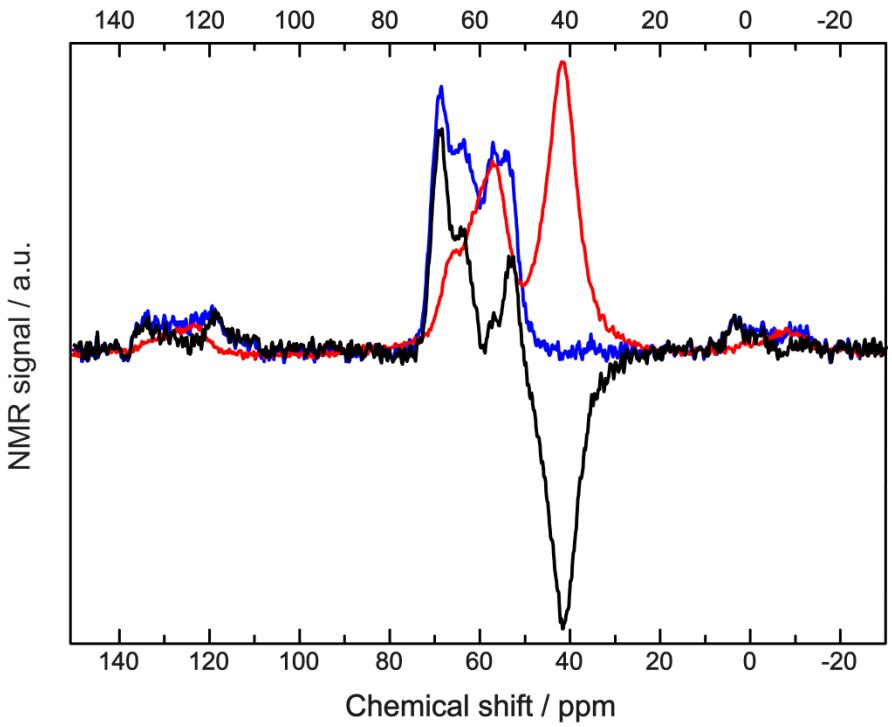

Figure 3.4. Plot of the ^{31}P NMR spectra of trimethylphosphine oxide (TMPO) mixed with (i) superacidic S-MOF-808 (blue), (ii) dehydrated S-MOF-808 (red), and the difference between the spectra (black). The peak at 69 ppm, assigned to the superacidic proton, is lost upon dehydration. The peak at 42 ppm is due to 'free' TMPO that is not interacting with the framework directly.

Having established the chemical origin of the superacidic proton source, the aim was to probe the local pore environment at the cluster in order to better understand the role of the structure as a whole which leads to the superacidic properties of S-MOF-808. Particularly of interest is the surrounding environment of the superacidic proton, since there are many possible cluster configurations. Conventional diffraction techniques only describe the average structure based on the unit cell, so the local environment of the superacidic proton was probed using *in situ* IR spectroscopy, focusing on the O-H stretches in S-MOF-808 (Figure 3.5). A minimum of six O-H stretches were observed in activated S-MOF-808. Two of these stretches, located at 3737 and 3767 cm^{-1}, are no longer present following dehydration of S-MOF-808, upon which superacidity is lost. Measuring the IR spectrum at intervals from room temperature up to 200 ºC shows no indication of any stretches merging, only peak broadening as a result of increased thermal motion, and thus up to this temperature the protons are not dynamically exchanging. The peak broadening is however reversible, as the O-H stretches sharpen again upon cooldown to room temperature.

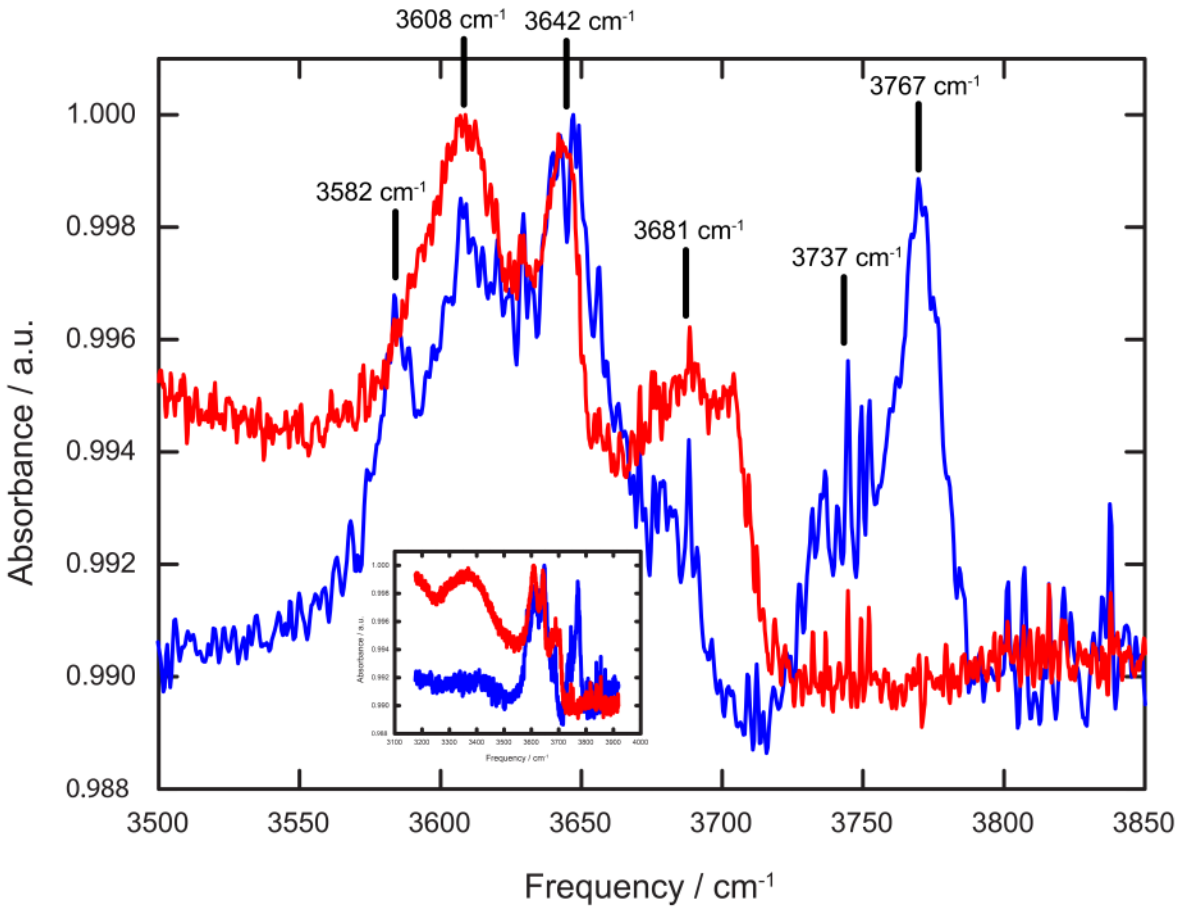

Figure 3.5. *In situ* IR spectra of superacidic S-MOF-808 (blue) compared to dehydrated S-MOF-808 (red). The most distinct differences are the loss of two peaks at 3737 cm^{-1} and 3767 cm^{-1}.

These experiments were also performed on Se-MOF-808, which was found to have 2.3 selenium atoms per 6 zirconium atoms by inductively-coupled plasma atomic emission spectroscopy (ICP-AES), similar superacidic character by ^{31}P NMR, loses 2.9 water molecules per cluster prior to structure decomposition, chelating groups only following activation despite exclusively bridging selenate in aqueous solution, and the same IR stretches present (see Appendices and Notes). The most noteworthy difference was in the TGA curve, where Se-MOF-808 decomposes at around 250 ºC compared with S-MOF-808 at 350 ºC. This is attributed to the much larger strain on the bigger chelating selenate group since the former is distorted to a much greater degree compared with chelating sulfate.

Local cluster configurations were modeled and geometrically optimized using density functional theory (DFT), with the experimental evidence from diffraction techniques, IR and elemental analysis discussed above used to define possible configurations. The formula $Zr_6O_4(OH)_4(C_2H_3O_2)_6(SO_4)_2(OH)_2(OH_2)_x$ was used as a representation of an average cluster, where x = 2 or 3. The restrictions on structural arrangement of the cluster included i) the core $[Zr_6O_4(OH)_4(C_2H_3O_2)_6]^{6+}$ is fixed, with μ^3-O and –OH groups arranged in the commonly reported alternating arrangement to minimize charge repulsion, (ii) modeling sulfate as chelating to zirconium as opposed to bridging, (iii) using terminal hydroxide to charge-balance the cluster,

(iv) including two to three water molecules per cluster. Additionally, individual clusters were modeled by truncating the linker with acetate groups, which assumes clusters are electronically decoupled. Early evaluation of cluster models by classical force field geometry optimization followed by energy calculation using DFT found that an uneven distribution of charge or chemical species resulted in much higher energy configurations, or even failed to converge. For instance, two hydroxides on one zirconium atom with two open metal sites on another was 300-400 kJ mol^{-1} higher in energy than both zirconium atoms assigned a hydroxide group each, depending on the exact configuration.

The most intriguing aspect of the clusters modeled was the interaction of water molecules when bound to a zirconium atom adjacent to that with a sulfate group bound to it. An O-H bond length of 0.98 Å was observed on the terminal water molecules in the clusters when the hydrogen atom on water is not involved in additional bonding besides to its parent oxygen atom. However, when the terminal water molecule is bound to zirconium that is adjacent to chelating sulfate, there is a very strong hydrogen bonding interaction with an O-H bond length ranging from 1.02 – 1.05 Å depending on the cluster configuration. This is significantly longer than the O-H bond with no hydrogen bonding. Further, the O-H---O angle of 163-166º and an extremely short H---O hydrogen bonding distance of 1.50 – 1.66 Å compounds the hydrogen bond strength. This indicates that the proton is very weakly bound. Indeed, the system can be viewed as a protonated conjugate of hydroxide and sulfate bound to zirconium, with the proton sitting between the two groups, but mostly located on the hydroxide. One example of the modeled clusters is represented in Figure 3.6, which contains two water molecules and two chelating sulfate groups located opposite each other. Knowing terminal water molecules on zirconium clusters are strongly acidic already, it is not surprising the combination of hydrogen bonding and the inductive effect of sulfate and open metal sites that exist on the cluster increase acidity into the superacidic range.

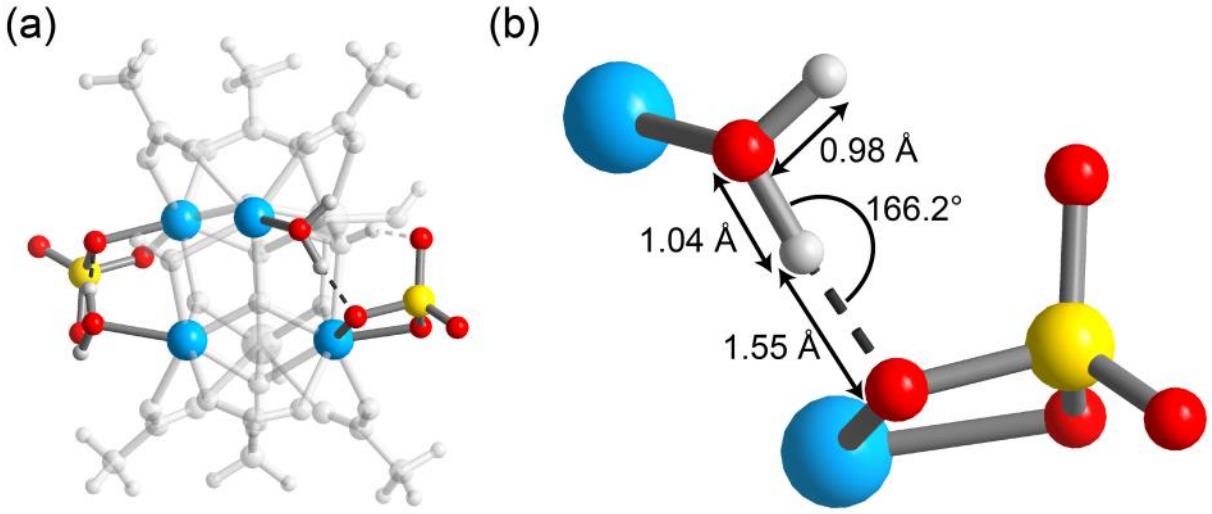

Figure 3.6. (a) Depiction of the zirconium cluster in S-MOF-808 as calculated by DFT geometry optimization, with (b) a close up view of the superacidic active site with relevant bond lengths and angles. Atoms not directly part of the active site are in gray, with zirconium otherwise in blue, oxygen in red, sulfur in yellow and hydrogen in white.

The discussed hydrogen bonding interaction is consistent with the IR data collected for the superacidic and dehydrated S-MOF-808 samples. Based on the stretches lost at 3737 and 3767 cm^{-1}, the water molecules cannot have two equivalent protons as the symmetric and asymmetric stretches are not coupled, being only 30 cm^{-1} apart. If coupling were to occur between two environmentally identical protons on water, a separation of 90 – 100 cm^{-1} is expected.[25,26] Another coupling scenario, whereby water is hydrogen bonding with hydroxide, can also be ruled out as this would result in red-shifted stretches in the region of 2600-2700 cm^{-1}.[27] Therefore, the IR data is consistent with the key active superacidic site involves the μ^1-water molecule on the adjacent zirconium atom to chelating sulfate.

This understanding of the structure-property relationship was applied to the dimerization of isobutene to form isooctene. Upon hydrogenation, the resulting commodity isooctane is highly valuable as a pure product, as it has an octane number of 100 and can be used as a fuel additive. For practical use, the oligomerization of isobutene into C12, C16 species and so on must be excluded as these would contaminate and eventually clog the fuel tank. Therefore, selectivity towards C8 isooctene is crucial.[28,29] The dimerization is typically performed under elevated pressures and in non-polar solvent. However, increasing the pressure tends to favor oligomerization, and a solvent system requires further purification steps. Instead, a continuous gas flow set-up was used, with isobutene diluted in helium, carried out at atmospheric pressure. The set-up offers the additional advantage of continuous, as opposed to batch production, and negates the need to purify isooctene from solvent mixtures.

S-MOF-808 was found to be active even at room temperature, with conversion peaking at 160 ºC at 21.5%, outperforming sulfated zirconia under the same conditions (Figure 3.7). The dimer selectivity obtained using S-MOF-808 is 100% at 80 ºC and lower, yet remains at 92.8% at 160 ºC. While both S-MOF-808 and sulfated zirconia both have similar selectively, under longer experiments of up to 15 days, S-MOF-808 does not lose activity or selectivity, maintaining a constant 15% conversion while sulfated zirconia drops by around 60%, from its starting conversion of 5.2%. S-MOF-808 does lose activity at 120 ºC and 160 ºC, and at a faster rate at the higher temperature. This is consistent with TGA data showing the loss of superacidic water occurring at these temperatures. Indeed, when dehydrated S-MOF-808 was tested, the activity was found to be much lower than that of S-MOF-808, with only 20% of the conversion rate at 80 ºC (Figure 3.7). Since the superacidic water is lost while the framework remains intact, the great majority of the catalytic activity of the material can be attributed to this species. The dehydrated MOF has a roughly linear dependence on the temperature, unlike S-MOF-808, since the material no longer suffers from water loss at elevated temperature. The selectivity for S-MOF-808 and dehydrated S-MOF-808 are almost identical, as with sulfated zirconia, indicating the superacidic active site is not what imparts the extremely high selectivity.

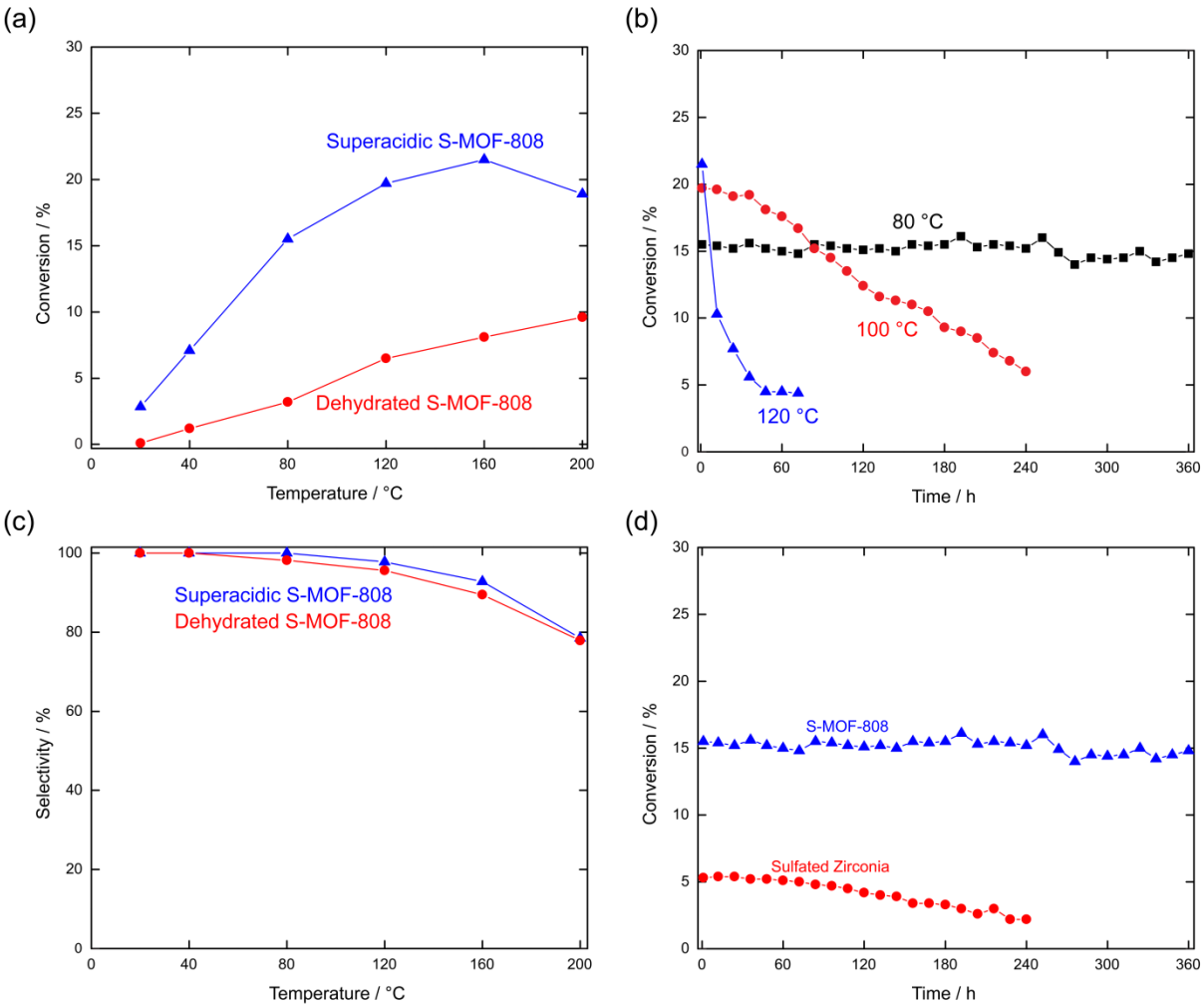

Figure 3.7. (a) Comparison of the rate of conversion for the superacidic, water-containing S-MOF-808 with the dehydrated form for the dimerization of isobutene. The superacidic water molecule is found to be responsible for the majority of the activity. The conversion percentage using superacidic S-MOF-808 as the catalyst can only be maintained over two weeks at 80 °C, with higher temperatures of 100 and 120 °C losing activity over time (b). This is likely due to the loss of water. The dehydrated form does display almost identical selectivity for the dimer over other oligomers however (c). The catalytic activity was compared with sulfated zirconia under the same conditions, which was found to have the same selectivity as the MOF, but about one third of the conversion rate at 80 °C (d). In addition, sulfated zirconia loses activity gradually over time unlike superacidic S-MOF-808.

Conclusion

In summary, the chemical features responsible for superacidity in S-MOF-808 have been identified as a terminal water molecule bound to zirconium and hydrogen bonding to an adjacent chelating sulfate group. The system can be viewed as a terminal hydroxide group adjacent to sulfate with a delocalized proton that mostly resides on the hydroxide group. If this proton is removed from the framework, superacidity is lost and the catalytic activity of S-MOF-808 is greatly reduced for the dimerization of isobutene, although the high selectivity remains. This has permitted the identification and manipulation of the active site of a solid-state material through a rational understanding as opposed to a trial and error approach, and could facilitate the design and synthesis of optimally-performing catalysts.

Appendices and Notes

Acknowledgements. This work could not have been completed without the valuable input of Tom Osborn-Popp, for discussions and solid-state NMR measurements, Ji Su, Jayeon Baek and Qingni Liu for isobutene dimerization measurements, Chang Yan for performing *in situ* IR measurements, Jon Weisberg for the DFT optimization calculations, Ashfia Huq for carrying out the powder neutron diffraction measurements, Philipp Urban for help with the PXRD Rietveld refinements, Markus Kalmutzki along with Juncong Jiang for discussions, and Bunyarat Rungtaweevoranit for SEM images. This work is funded by the U.S. Department of Defense, Defense Threat Reduction Agency (DTRA) and BASF SE (Ludwigshafen, Germany) for the synthesis component. I also thank Simon, J. Teat and Kevin J. Gagnon (Advance Light Source, Lawrence Berkeley National Laboratory, U.S.A.) for support during the single-crystal diffraction data collection at the beamline 11.3.1. Work at the Advanced Light Source is supported by the Director, Office of Science, Basic Energy Sciences, of the U.S. Department of Energy under Contract No. DE-AC02-05CH11231.

Powder Neutron Diffraction Experiments. Approximately 300 mg activated pristine deuterated MOF-808 was packed into a 6 mm vanadium can sealed with a titanium collar, copper gasket and aluminum lid in an argon glove box. After post-synthetic exchange with 0.05 M D_2SO_4 in D_2O followed by activation described in Section S1, sulfated deuterated MOF-808 was similarly loaded into the vanadium can. In both cases, data was collected at 10 K and 300 K for comparison.

Structure models were initially developed in Materials Studio 7.0 using the models from single crystal X-ray diffraction experiments as a starting point. These models were then refined against the powder neutron data, with atomic coordinates of the cluster and linker allowed to refine freely, with occupancies fixed based on the activated pristine MOF-808 model and knowledge of sulfate coordinates from the S-MOF-808 sample prior to activation from single crystal and powder X-ray data.

Pristine MOF-808 modeling. An initial structural model was developed based on MOF-808 single crystal data collected prior to activation (Figure 3.8). All hydrogen atoms in the structure were converted to deuterium atoms except for hydrogen on formate, which was not deuterated. To begin with, atomic coordinates were allowed to refine freely before being fixed at their converged values. With the linker and zirconium occupancies fixed at 100%, the thermal ellipsoids and occupancies of the remaining atoms were systematically refined. Note that the ellipsoids on the linker C1, C2, C3, and the ellipsoids of the μ^3-O and –OH pairs were constrained to be identical in order to aid refinement. The occupancies of the μ^3-O and –OH groups O2, O3, O4 and O5 refined to 47.9 ±1.0, 48.7 ±1.0, 50.7 ±3.2% and 49.5 ±3.2% respectively, meaning there has been no deprotonation of the μ^3-OH groups to account for charge-balancing. Note however that the data set collected at room temperature failed to converge O5, and allowing the position of O4 to refine freely moved it to intermediate coordinates between O4 and O5 in the data set collected at 10 K. This is not an indication that

O5 is not present as it is observed in the 10 K data set, but simply an averaging of the two positions due to thermal motion.

The ellipsoids of D3A and D5, corresponding to μ^3-OD, failed to converge indicating only partial exchange of hydrogen with deuterium. If hydrogen is partially present, this does not reflect the true occupancy of deuterium at this position as ^{1}H and ^{2}D signals cancel each other out. This could be additionally compounded from the terminal position of the deuterium atoms that increase disorder and thermal motion as is observed for H4 on formate. The formate carbon and hydrogen atoms, C4 and H4, refine to 84.1 ±1.1% and 85.5 ±2.3%, fixed to 83.3% as consistent with NMR data. Refinement of O6, which accommodated oxygen from formate and terminal water molecules coordinated zirconium, converged at 97.9 ±0.8%, which is consistent with terminal hydroxide groups completing the charge-balancing of the framework, and hence not being removed following activation as was found in S-MOF-808. The final refinement converged to wR_p = 3.20% and R_p = 11.20% (Figured 3.9 & 3.10).

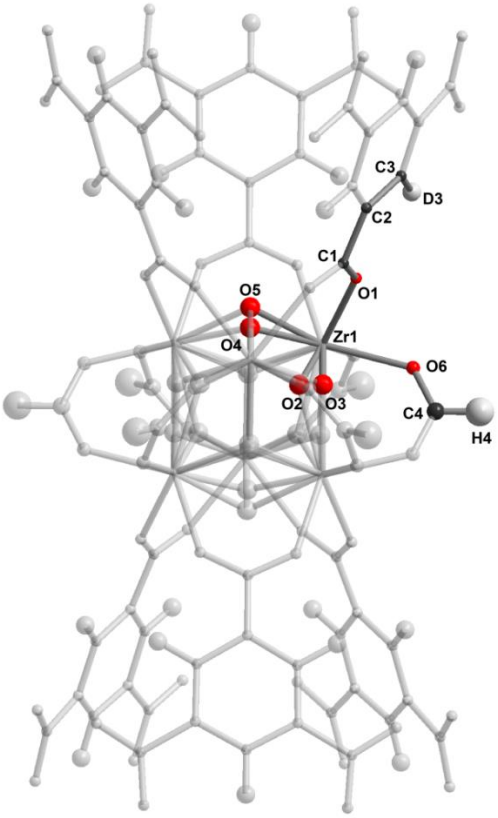

Figure 3.8. Representation of metal oxide cluster in pristine MOF-808 as found by powder neutron diffraction. The asymmetric unit is colored and labeled with zirconium in blue, oxygen in red, carbon in black and hydrogen/deuterium in white, while the remaining atoms are shaded in order to show how the framework extends. Thermal ellipsoids are represented at 50% probability, with all refined isotropically. wRp = 3.20%, Rp = 11.20%

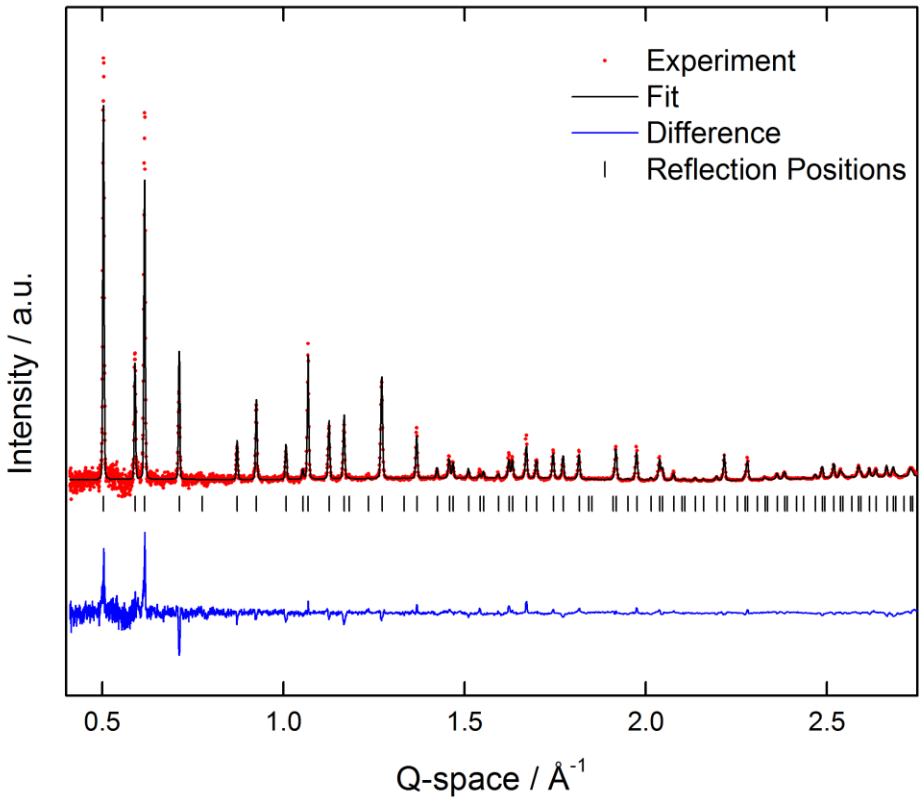

Figure 3.9. Powder neutron diffraction pattern of data for pristine MOF-808 activated at 120 °C, displaying the experimental pattern (red) and the fitted pattern obtained by Rietveld refinement of the structure (black). The difference plot (blue) as well as the Bragg positions (black) are provided.

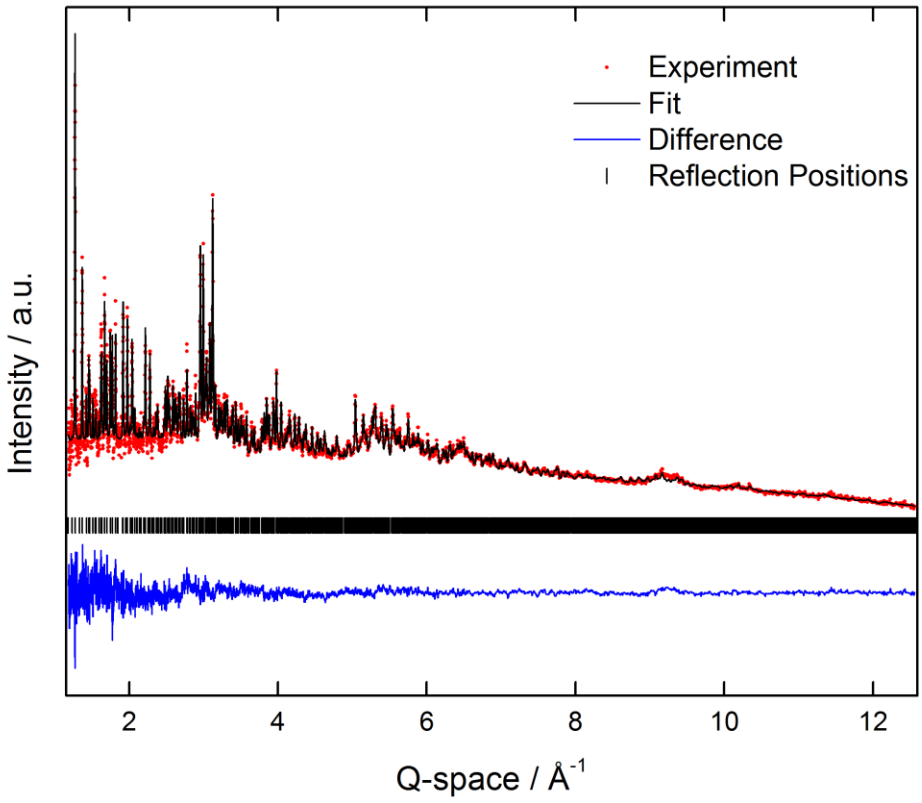

Figure 3.10. Powder neutron diffraction pattern of data collected at high Q-space values for pristine MOF-808 activated at 120 °C, displaying the experimental pattern (red) and the fitted pattern obtained by Rietveld refinement of the structure (black). The difference plot (blue) as well as the Bragg positions (black) are provided.

S-MOF-808 modeling. The coordinates and occupancies from the sulfated MOF-808 model prior to activation were imported and used as a starting point for Rietveld refinement. To begin with, atomic coordinates were allowed to refine freely before being fixed at their converged values. With the linker and zirconium occupancies fixed at 100%, the thermal ellipsoids and occupancies of the remaining atoms were systematically refined. Note that the ellipsoids on the linker C1, C2, C3, and the ellipsoids of the μ^3-O and –OH pairs were constrained to be identical in order to aid refinement. It was found that modeling S1, S2, O8A, O8B, O9A and O9B based on coordinates from single crystal data failed to converge with reasonable thermal ellipsoids. This is due to the very low occupancies of sulfate, found to be 12% and 6% for S1 and S2 in S-MOF-808 respectively, and prior to activation. It should be noted that the coherent neutron scattering length for sulfur is less than half that of oxygen, in contrast with X-ray diffraction where sulfur contains double the number of electrons as oxygen

and thus scatters X-rays much more readily. Since the refinement quality indicators, wR_p and R_p, displayed no significant difference between modeling and neglecting the sulfur atoms, and the inclusion of sulfur requires significant restraints to model whilst worsening the overall refinement quality, all sulfate atoms except for O6, which is oxygen bound to zirconium directly, were neglected in the final structure model. The presence of sulfate in the activated structure was however confirmed by elemental analysis and lack of formate by ^{1}H NMR, and evidence for the sulfate position in the framework was identified through PXRD as being exclusively in the chelating mode.

Additionally, it was found that the thermal ellipsoid of D3A and D5, corresponding to deuterium on μ^3-OD in the framework, failed to converge. This could be evidence for deprotonated μ^3-OD in the framework; however, free refinement of the occupancies of the corresponding oxygen atoms on the μ^3-O and -OD groups, O2 (53.5 ±1.1%) and O3 (48.5 ±1.1%) for D3 and O4 (49.8 ±2.1%), O5 (50.8 ±2.1) for D5 were found to be, within two standard deviations, in an equal ratio as in the sample prior to activation. It is therefore presumed not all deuterium was successfully exchanged into the framework, since any hydrogen present in the same position has a negative scattering length and would negate the signal from deuterium. Indeed, a roughly 1:2 ratio of D to H would contribute overall no scattering. This identification of such atoms present an additional challenge due to their terminal positions, increasing disorder and thermal motion.

At position O6, where sulfate and water coordinate to zirconium in the sample prior to activation, the occupancy refines to 78.7 ±1.1%, yet the contribution from sulfate only accounts for 38.3%, or 4.6 oxygen atoms out of 12 possible sites per cluster. Since the remaining density must be derived from water, and having established charge-balancing is not achieved elsewhere, I postulate some of this density must be deprotonated water to become terminal hydroxide. Based on the chemical formula, there is an average charge of -1.4 per cluster unaccounted for, and therefore 11.7% of this density is assigned to hydroxide, or 1.4 out of the 12 possible positions per cluster, (two per zirconium). In total, sulfate and hydroxide account for 50% of the observed density, leaving 28.7 ±1.1% as water molecules bound to the zirconium cluster, which translates to 3.4 ±0.1 water molecules per cluster, and the remaining 21.6 ±1.1% unoccupied positions corresponding to open metal sites. This result is consistent with previous experimental data indicating Lewis acid sites alongside Brønsted acid sites in S-MOF-808.[15] While the thermal ellipsoid for O6A is relatively large compared to other atoms in the structure, with at least three different species in different local environments and slightly different positions for each, this is reasonable. In the sample prior to activation with single crystal data, a larger anisotropic ellipsoid is also observed at position O6, reflecting the slightly strained conformation of the two binding modes of sulfate which are not perfectly overlapping with the oxygen atom from coordinated water, which illustrates this point (Figures 3.11 & 3.12).

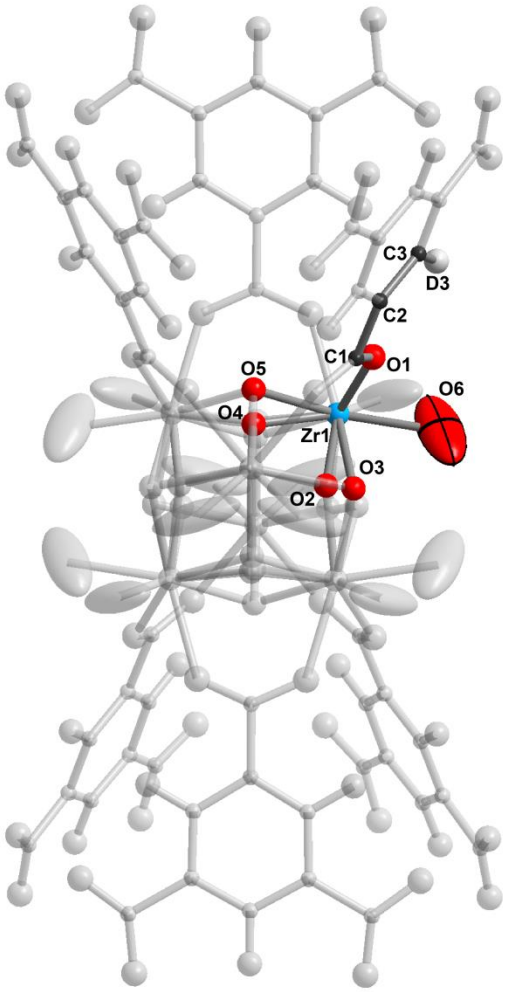

Figure 3.11. Representation of metal oxide cluster in S-MOF-808 as found by powder neutron diffraction. The asymmetric unit is colored and labeled with zirconium in blue, oxygen in red, carbon in black and deuterium in white, while the remaining atoms are shaded in order to show how the framework extends. Note the large ellipsoid for O6 relative to other atoms is expected as this position is representing at least four different sources of oxygen atoms including from water, hydroxide, bridging and chelating sulfate. Thermal ellipsoids are represented at 50% probability, with all except O6 refined isotropically. wRp = 2.91%, Rp = 9.59%

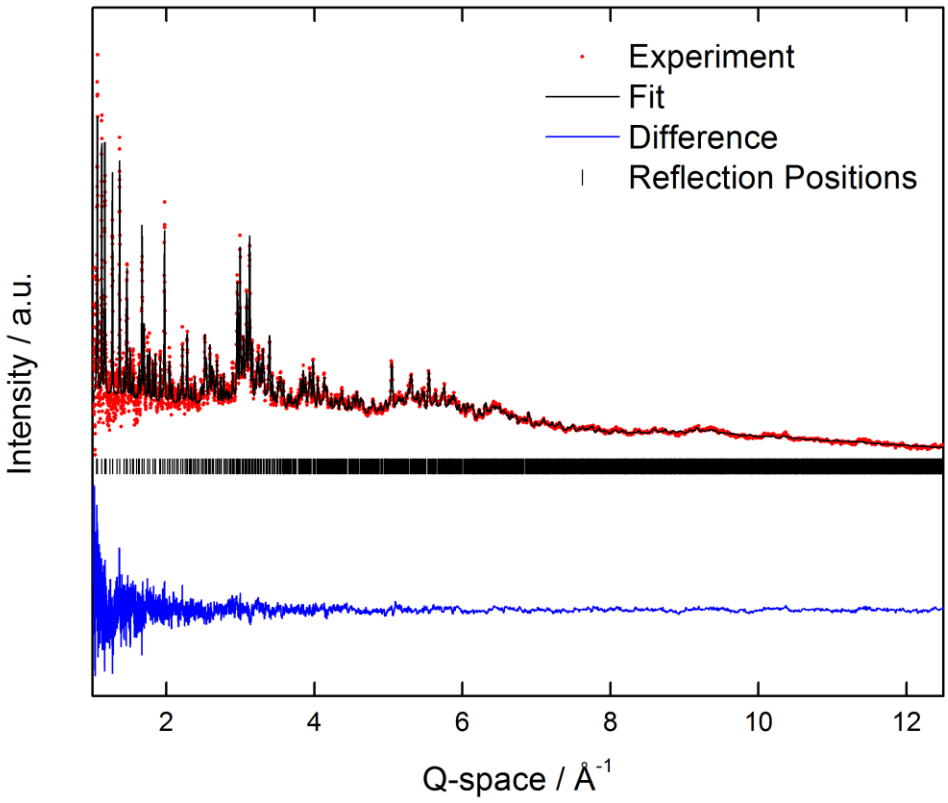

Figure 3.12. Powder neutron diffraction pattern of data collected at high Q-space values for S-MOF-808 activated at 120 °C, displaying the experimental pattern (red) and the fitted pattern obtained by Rietveld refinement of the structure (black). The difference plot (blue) as well as the Bragg positions (black) are provided.

Single Crystal X-ray Diffraction Analyses

Table 3.1. Crystal structure data for pristine MOF-808 prior to activation.

Sample	**Pristine MOF-808**
chemical formula	$Zr_6O_{37.12}C_{23}H_{15}$
formula mass	1432.67
crystal system	cubic
space group	*Fd*-3*m*
λ (Å)	0.77490
a (Å)	35.1364(13)
Z	16
V (Å^3)	43378(5)
temperature (K)	100
size /mm	0.015 × 0.015 × 0.010
density (g/cm^{-3})	0.877
measured reflections	60241
unique reflections	2487
parameters	78
restraints	0
R_{int}	0.0858
θ range (deg)	2.10-30.74
R_1, wR_2	0.0531, 0.1907
S (GOF)	1.110
max/min res. dens. (e/Å^3)	0.75/-0.89

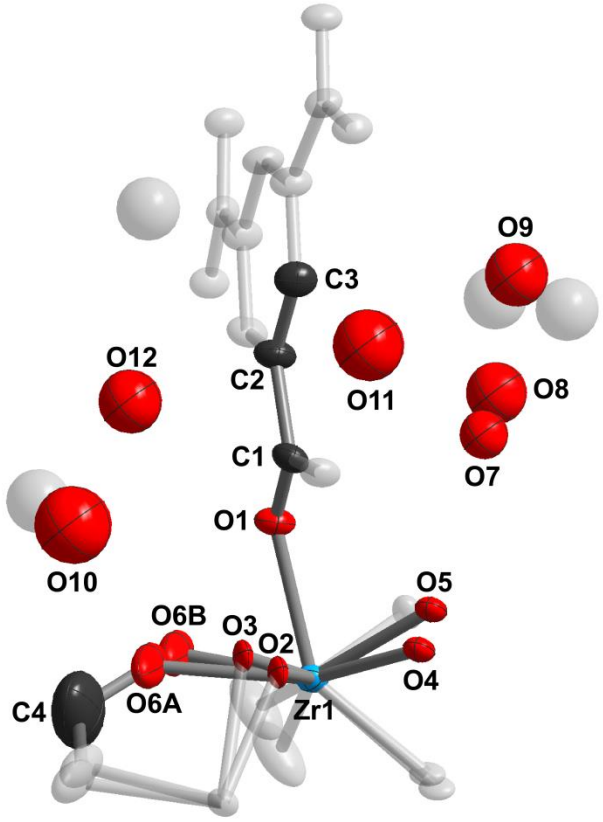

Figure 3.13. Representation of pristine MOF-808 prior to activation from SXRD data. The asymmetric unit is displayed in color, with additional atoms in gray to aid visualizing the structure. Thermal ellipsoids are displayed at 50% probability and atom colors are as follows: zirconium (blue), oxygen (red), carbon (black), sulfur (yellow). Hydrogen atoms are omitted for clarity.

The single crystal structure of S-MOF-808, while previously reported, was recollected with the aim of carefully investigating the sulfate positions and their relative ratios (Figure 3.14). Thus, the occupancy of sulfur was permitted to refine freely, with S1 (bridging mode) refining to 12.0 ±0.3%, and S2 (chelating mode) to 5.8 ±0.7%. S1 is split by a mirror plane and thus the total sulfate occupancy relative to zirconium is 29.8 ±1.3%, and corresponds to a 4:1 ratio of bridging to chelating sulfate in the pre-activated form. Note this configuration changes to exclusively chelating upon activation under dynamic vacuum at 120 °C. Ellipsoids of O2 and O3, O4 and O5, O6A and O6B were constrained in their pairs to be identical due to their close proximity. Oxygen atoms have been modeled within the cavity of the structure, representing highly disordered solvent molecules which are typically hydrogen bonding to the framework and are likely a combination of water and DMF molecules. Note that O11 and O12 have been modeled isotropically due to their low occupancy and proximity to other atoms in the model. The

geometry of sulfate was restrained to its known tetrahedral configuration using distance and angle restraints due to partial occupancy and positional overlap with solvent molecules.

Table 3.2. Crystal structure data for S-MOF-808 prior to activation.

Sample	**S-MOF-808**
chemical formula	$Zr_6O_{43.09}C_{18}H_{10}S_{1.79}$
formula mass	1520.35
crystal system	cubic
space group	*Fd*-3*m*
λ (Å)	0.77490
a (Å)	35.2075(13)
Z	16
V (Å^3)	43642(5)
temperature (K)	100
size /mm	0.015 × 0.015 × 0.010
density (g/cm^{-3})	0.926
measured reflections	70715
unique reflections	3175
parameters	101
restraints	7
R_{int}	0.0849
θ range (deg)	2.09-33.75
R_1, wR_2	0.0556, 0.1911
S (GOF)	1.117
max/min res. dens. (e/Å^3)	1.1/-0.6

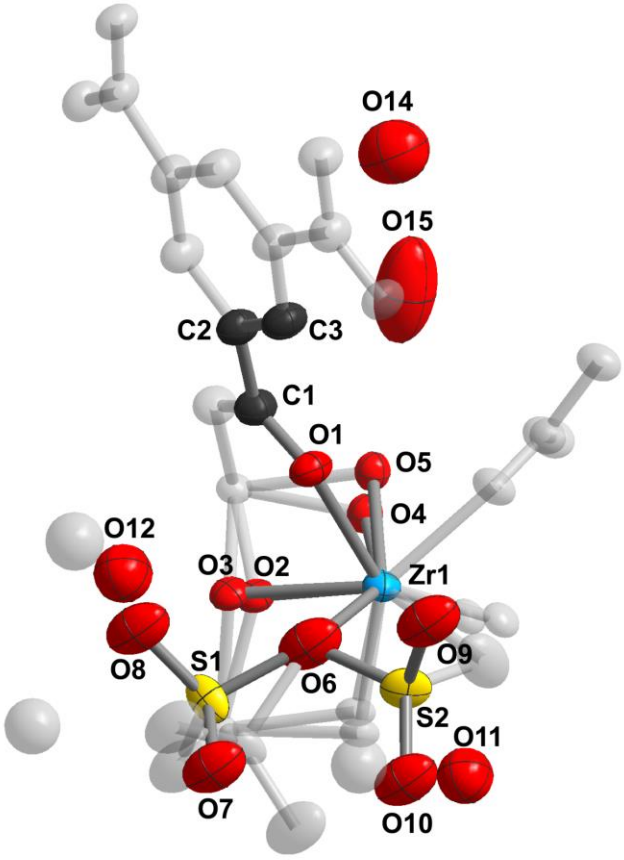

Figure 3.14. Representation of S-MOF-808 prior to activation from SXRD data. The asymmetric unit is displayed in color, with additional atoms in gray to aid visualizing the structure. Thermal ellipsoids are displayed at 50% probability and atom colors are as follows: zirconium (blue), oxygen (red), carbon (black), sulfur (yellow). Hydrogen atoms are omitted for clarity.

The single crystal structure of Se-MOF-808 was modeled the occupancy of sulfur was permitted to refine freely, with Se1 exclusively existing in the bridging mode in the pre-activated form (Figure 3.15). Note this configuration changes to exclusively chelating upon activation under dynamic vacuum at 120 °C. Ellipsoids of O2 and O3, O4 and O5, O6A and O6B were constrained in their pairs to be identical due to their close proximity. Oxygen atoms have been modeled within the cavity of the structure, representing highly disordered solvent molecules which are typically hydrogen bonding to the framework and are likely a combination of water and DMF molecules. Note that O7 through to O15 have been modeled isotropically due to their low occupancy and proximity to other atoms in the model. The geometry of selenate was restrained to its known tetrahedral configuration using distance and angle restraints due to partial occupancy and positional overlap with solvent molecules. Two low-angle reflections, (222) and (044), were omitted from the refinement due to their large discrepancy between calculated and experimental values. The reason for discrepancy is likely related to not fully accounting for the highly disordered solvent within the cavity.

Table 3.3. Crystal structure data for Se-MOF-808 prior to activation.

Sample	**Se-MOF-808**
chemical formula	$Zr_6O_{43.90}C_{18}H_{10}Se_{1.28}$
formula mass	1579.22
crystal system	cubic
space group	*Fd*-3*m*
λ (Å)	0.77490
a (Å)	35.2645(10)
Z	16
V (Å^3)	43854(4)
temperature (K)	100
size /mm	0.015 × 0.015 × 0.010
density (g/cm^{-3})	0.955
measured reflections	79733
unique reflections	2245
parameters	98
restraints	17
R_{int}	0.0858
θ range (deg)	1.8-29.5
R_1, wR_2	0.0510, 0.1672
S (GOF)	1.144
max/min res. dens. (e/Å^3)	0.8/-0.4

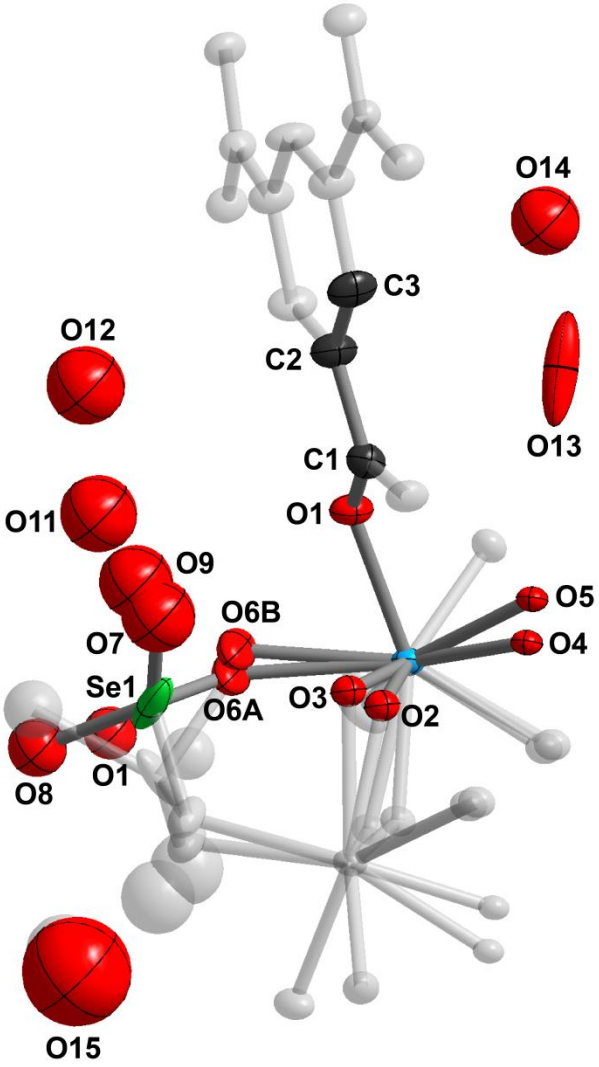

Figure 3.15. Representation of Se-MOF-808 prior to activation from SXRD data. The asymmetric unit is displayed in color, with additional atoms in gray to aid visualizing the structure. Thermal ellipsoids are displayed at 50% probability and atom colors are as follows: zirconium (blue), oxygen (red), carbon (black), selenium (green). Hydrogen atoms are omitted for clarity.

Powder X-ray Diffraction Patterns, Rietveld

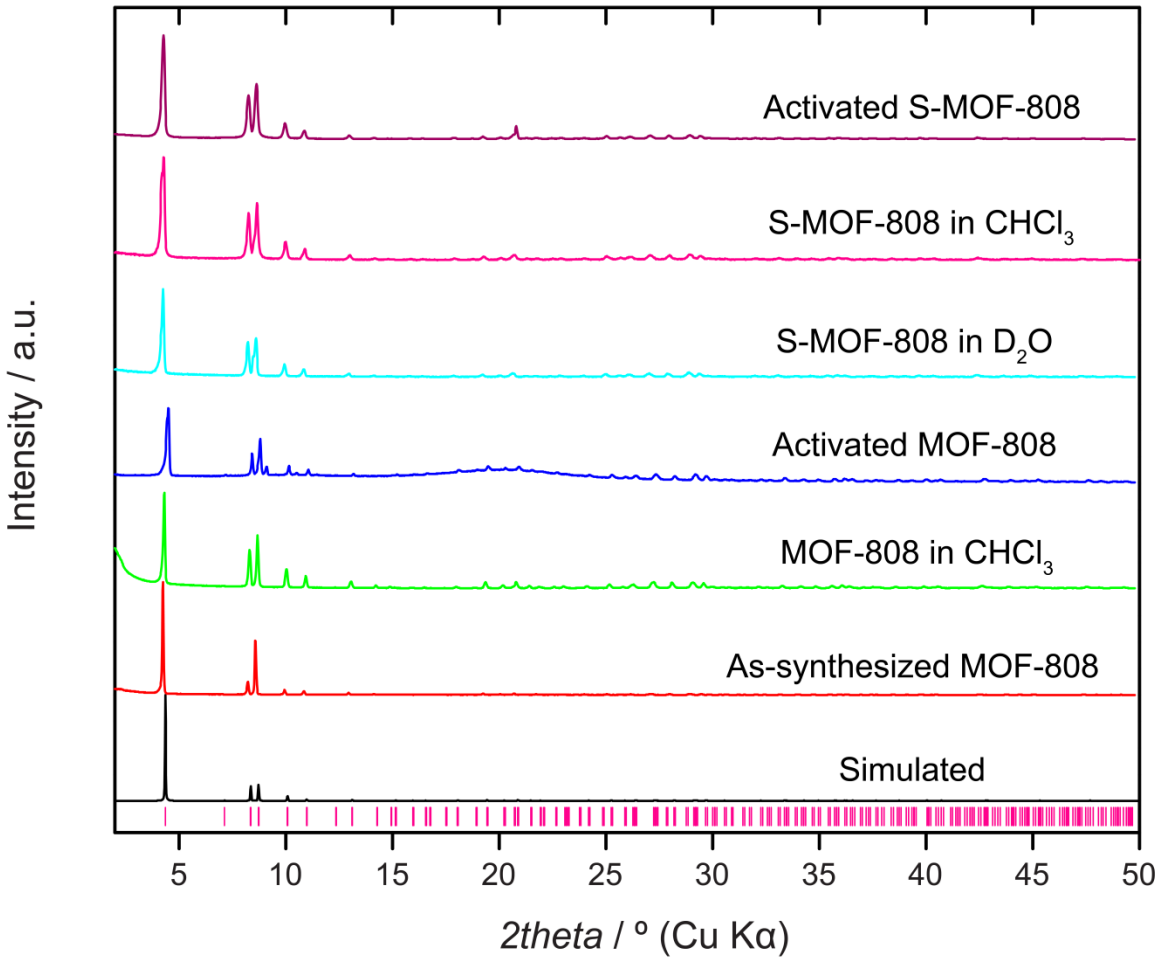

Figure3.16. PXRD patterns of deuterated MOF-808 after various stages of treatment. The pristine simulated pattern (black) is compared to the as-synthesized (red), after $CHCl_3$ (green), and after activation under dynamic vacuum (dark blue) of the pristine sample. The remaining patterns are immediately after treatment with D_2SO4 in D_2O (light blue), exchanging with $CHCl_3$ (pink) and activation of the sulfated sample (violet), showing crystallinity is retained.

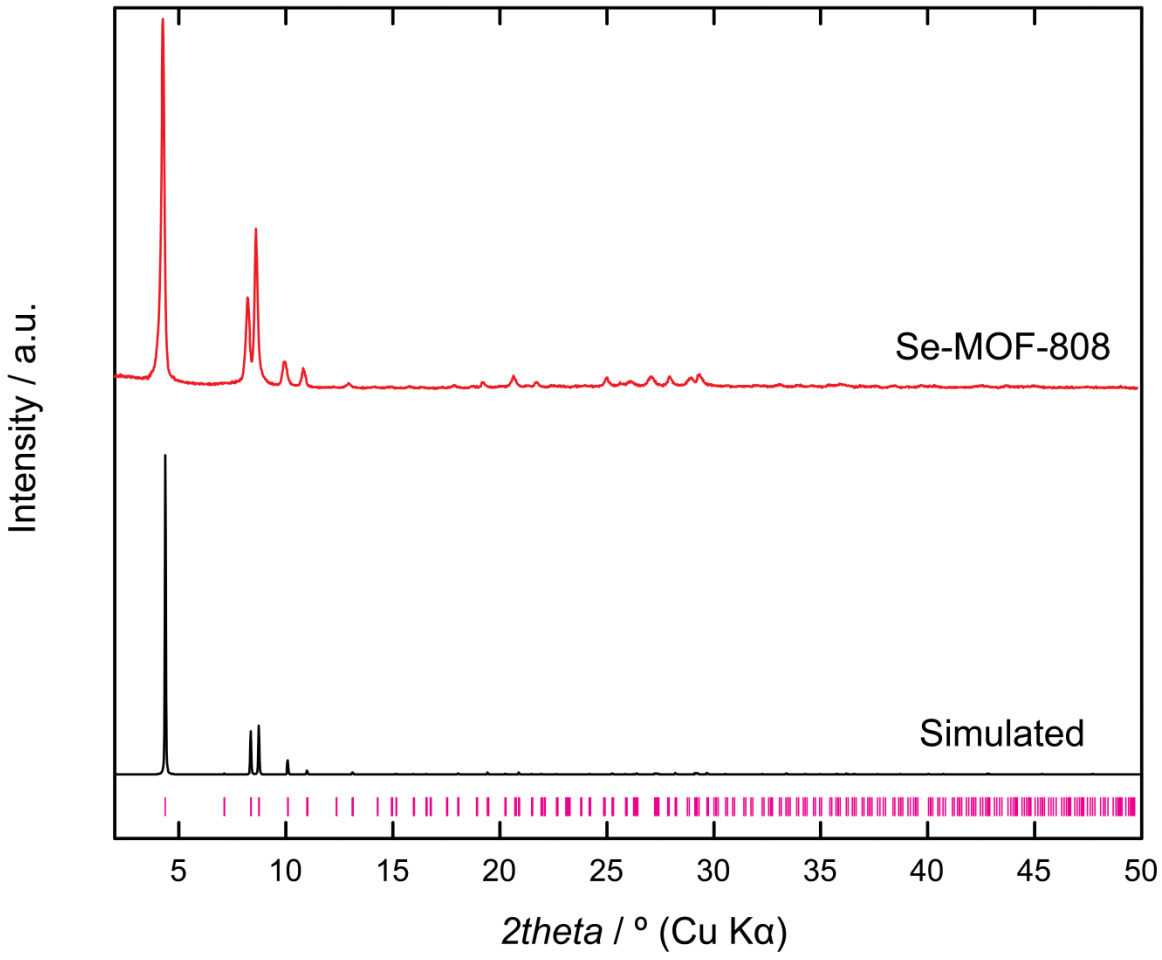

Figure 3.17. PXRD patterns of simulated MOF-808 (black) and after immersion with 0.05 M of selenic acid, solvent exchange and activation (red).

X-ray powder Rietveld refinements of the activated samples under argon (both Se-MOF-808 and S-MOF-808, Figures 3.18-21) were carried out using TOPAS 5.[30] Regarding the overall quality of the fits, it is noted that there is no solvent masking routine used, which could take the contribution of any residual density in the pores into account, such as the disordered argon atoms or any other remaining molecules. Thus, there are small systematic deviations visible in the difference plots, which might be due to anything what is left in the pores. Also, reflections 111 and 022 had to be excluded from the refinements, as the inclusion of those two reflections rendered the refinement unstable and yielded chemically unreasonable electron densities in the F_{obs}-F_{calc} plots. This data was used to determine the position of selenate and sulfate only, and the neutron data collected from the spallation source was used for occupancies and thermal ellipsoid parameters discussed in the main text due to the superior data quality and resolution obtained.

In the first steps of the refinement, a structure model was used without selenate/sulfate groups. In subsequent steps, those groups were located after inspection of the F_{obs}-F_{calc} plots. Geometrical constraints were applied during the refinement to retain symmetry $Fd\bar{3}m$: In particular, the Zr_6-octahedra were allowed to expand/contract isotropically. The phenyl ring of the BTC linker was allowed to move along the 3-fold axis. The angle between the center of the phenyl ring, the carbon atom the carboxylate group is binding to and the carboxylate carbon, however, were refined freely, as a slight distortion of the linker was observed in previous work.[15] Interatomic distances within the linker were constrained to their ideal values. Further constraints were applied to all oxygen atoms bound to the cluster and the selenate/sulfate as well as S/Se atoms themselves, to ensure they stayed on their ideal Wyckoff position. Anti-bump restraints were applied to the terminal oxygen atoms bound to S/Se. As of the low X-ray scattering contrast of hydrogen, no hydrogen atoms were refined other than the ones directly bound to the linker. In total, 3 isotropic displacement parameters were refined for the Se data. Specifically, one displacement parameter for the zirconium atom, one for all light elements besides the oxygens bridging zirconium and Se, and one for the selenate group. The results are as expected: $U_{iso}(Zr) < U_{iso}(\text{light atoms}) < U_{iso}(\text{selenate})$. The occupancy of the selenate/sulfate group was allowed to refine freely and is within the limits of the method and in reasonable agreement with the results from ICP and EA respectively. It has to be noted that the fit is worse for the S data than for Se. A reason for this could be the lower resolution. As a consequence, less parameters were refined. In particular the displacement parameters were fixed at reasonable values (0.03 for Zr, 0.05 for light atoms and 0.08 for the sulfate group). The chelating position of the sulfate group however was verified by inspecting the F_{obs}-F_{calc} plots. No significant electron density was found at a hypothetical bridging position.

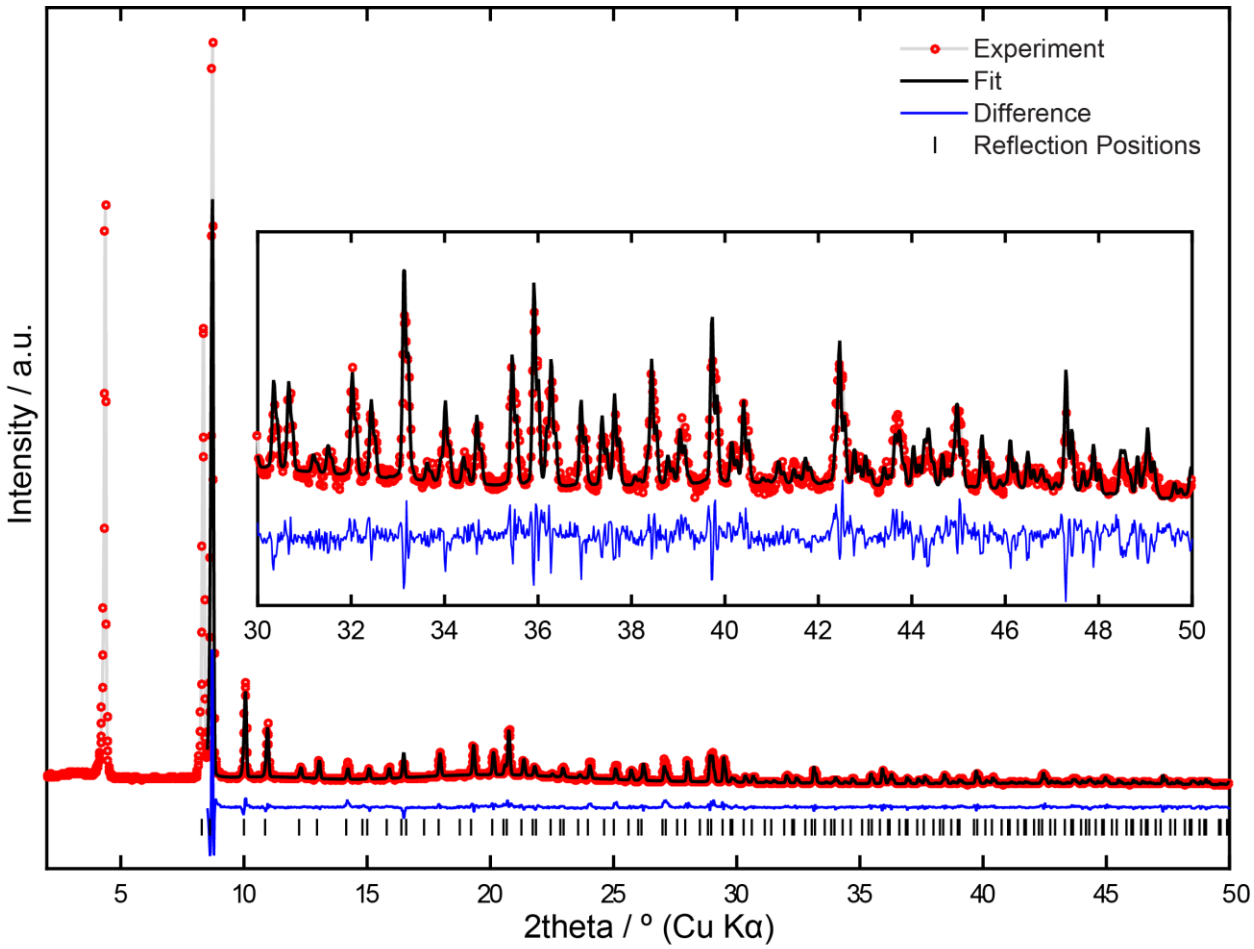

Figure 3.18. Powder X-ray diffraction pattern of S-MOF-808 activated at 120 °C, displaying the experimental pattern (red) and the fitted pattern obtained by Rietveld refinement of the structure (black). The difference plot (blue) as well as the Bragg positions (black) are provided. The data was collected under argon atmosphere at room temperature. R_p = 11.6%.

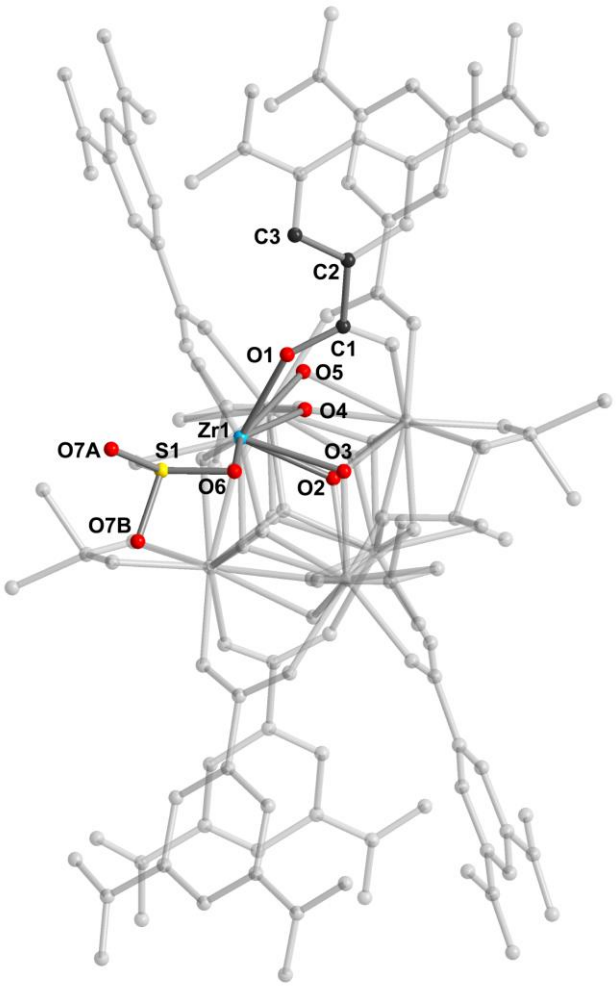

Figure 3.19. Representation of metal oxide cluster in S-MOF-808 as found by powder X-ray diffraction, revealing the exclusively chelating mode of sulfate. The asymmetric unit is colored and labeled with zirconium in blue, oxygen in red, carbon in black and sulfur in yellow, while the remaining atoms are shaded in order to show how the framework extends. Hydrogen atoms were omitted for clarity. Thermal ellipsoids are represented at 50% probability, with all refined isotropically.

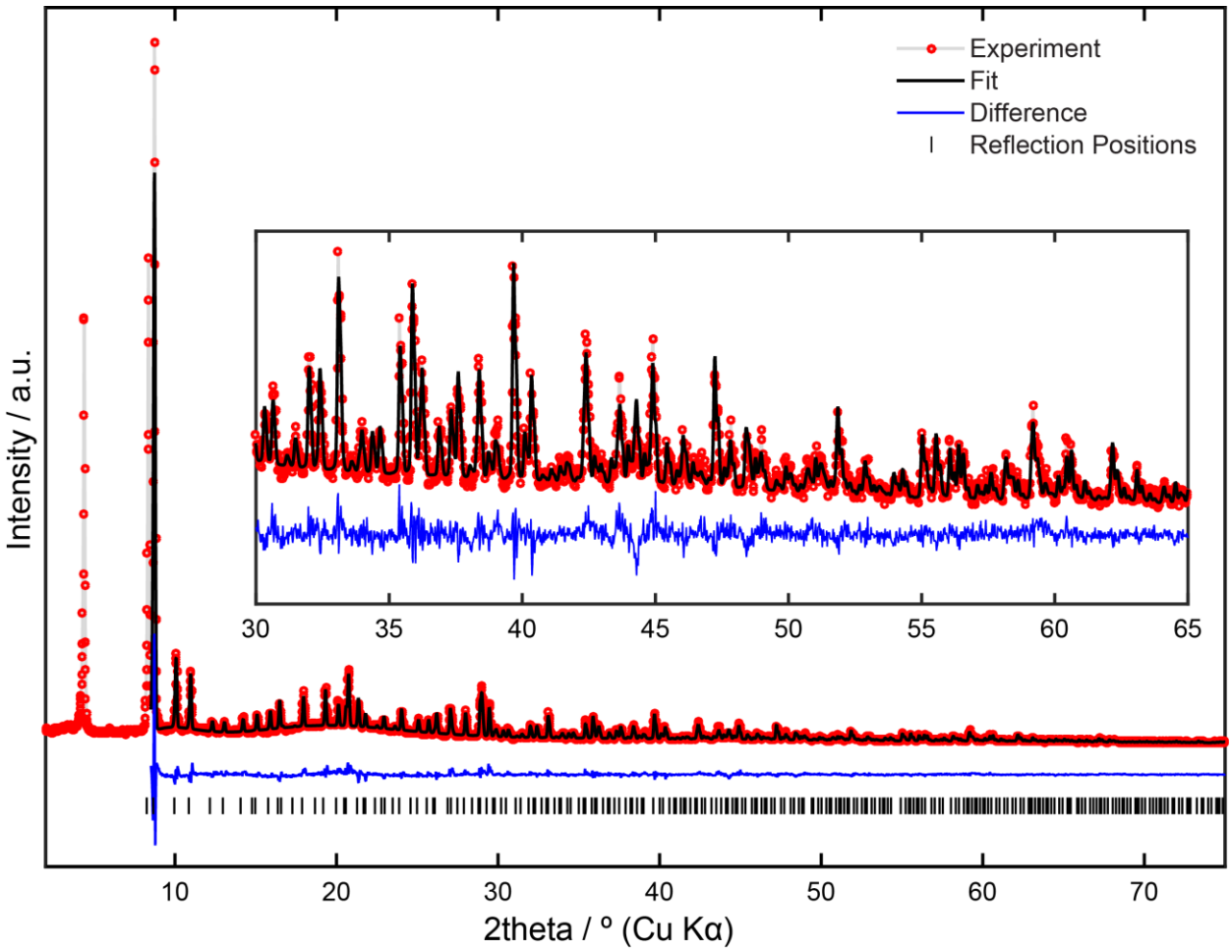

Figure 3.20. Powder X-ray diffraction pattern of Se-MOF-808 activated at 120 °C, displaying the experimental pattern (red) and the fitted pattern obtained by Rietveld refinement of the structure (black). The difference plot (blue) as well as the Bragg positions (black) are provided. The data was collected under argon atmosphere at room temperature. R_p = 10.5%.

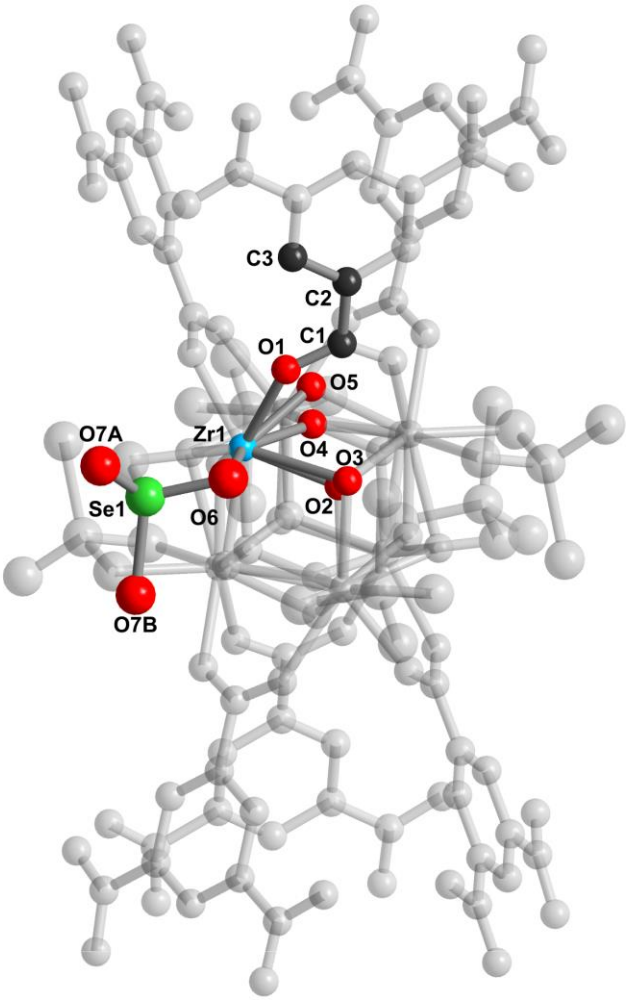

Figure 3.21. Representation of metal oxide cluster in Se-MOF-808 as found by powder X-ray diffraction, revealing the exclusively chelating mode of selenate. The asymmetric unit is colored and labeled with zirconium in blue, oxygen in red, carbon in black and sulfur in yellow, while the remaining atoms are shaded in order to show how the framework extends. Hydrogen atoms were omitted for clarity. Thermal ellipsoids are represented at 50% probability, with all refined isotropically.

Thermogravimetric Analysis. Thermogravimetric analysis coupled to a mass spectrometer (TGA-MS) was performed using a Netzsch STA 449 F5 Jupiter thermogravimetric analyzer coupled to a Netzsch QMS 403 D Aeolos mass spectrometer. A typical sample preparation method is as follows: the activated MOF sample was weighed in a glove box under argon atmosphere and transferred under argon to the TGA-MS. The sample chamber was then evacuated three times, refilling the chamber each time with argon. Next, the sample was heated at a rate of 2 °C min^{-1} to 800 °C with an argon flow rate of 20 ml min^{-1}. The water signal was quantified by repeating the experiment under identical conditions but with copper sulfate pentahydrate as a standard since this compound has well-characterized water loss steps. The area underneath the water signal plot was then used to quantify the amount of water being lost in the MOF by relating this to the known amount lost in the standard. The first water signal, peaking at 143 °C, corresponds to 0.96 mg H_2O in 24.5 mg S-MOF-808, which is 3.9% of the total mass. Taking the chemical formula of $Zr_6O_4(OH)_4(C_9H_3O_6)_2(SO_4)_{2.3}(OH)_{1.4}(OH_2)_x(DMF)_{0.4}$ = $Zr_6O_{31+x}C_{19.2}H_{14.2+2x}S_{2.3}N_{0.4}$, and assuming all terminal water molecules are lost after the first peak, then x = 3.1. This result is consistent with the PND data which indicates 3.4 ±0.1 water molecules per cluster. A similar calculation was performed on Se-MOF-808, containing 3.4% H_2O by weight. Considering the formula $Zr_6O_4(OH)_4(C_9H_3O_6)_2(SeO_4)_{2.3}(OH)_{1.4}(C_3H_7NO)_{0.5}(H_2O)_x$ = $Zr_6O_{31.1}C_{19.5}H_{14.9}N_{0.5}Se_{2.3}$ + xH2O, then x = 2.9.

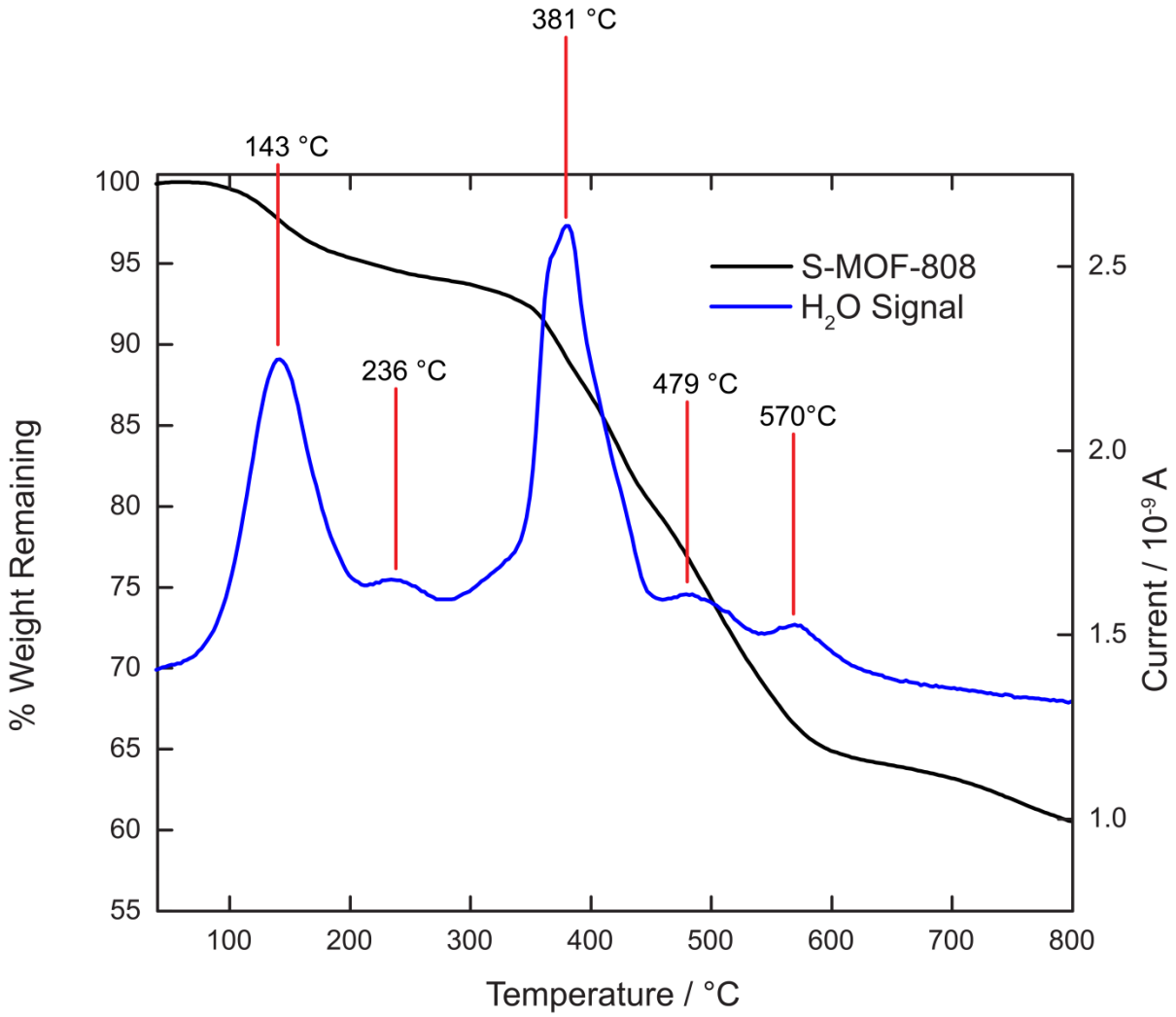

Figure 3.22. TGA-MS plot of activated S-MOF-808 under argon atmosphere with the thermogravimetric plot (black) and corresponding water loss signal (blue). The first mass loss, with the water signal peaking at 143 °C, corresponds of water coordinated to the framework that is lost prior to full structure decomposition beginning around 320 °C. Quantification of the water signals correspond to 3.1 water molecules per cluster for the first peak centered at 143 °C, 0.05 water molecules per cluster at 236 °C, and 4.5 water molecules at 381 °C.

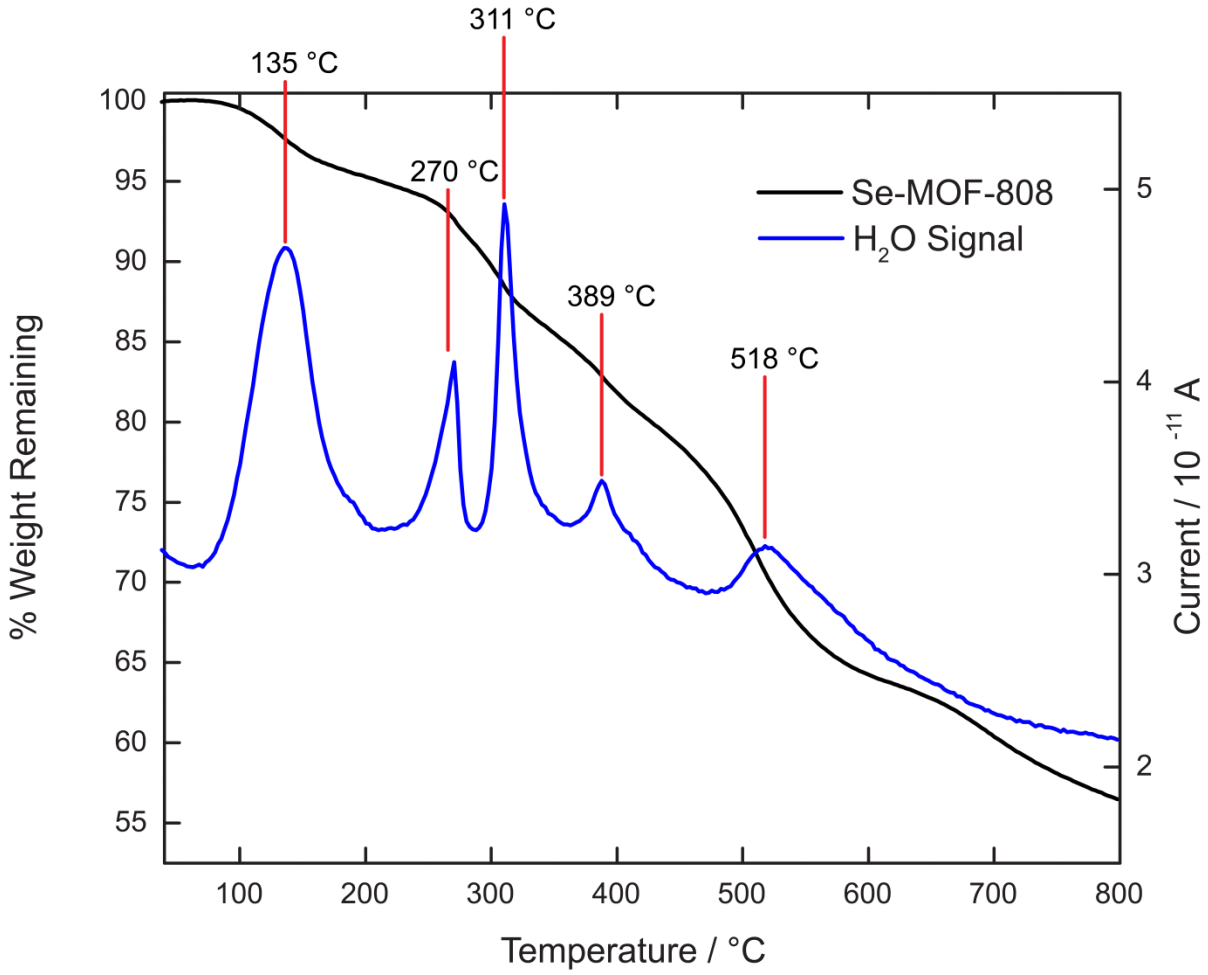

Figure 3.23. TGA-MS plot of activated Se-MOF-808 under argon atmosphere with the thermogravimetric plot (black) and corresponding water loss signal (blue). The first mass loss, with the water signal peaking at 135 °C, corresponds of water coordinated to the framework that is lost prior to full structure decomposition beginning around 270 °C. Quantification of the water signals correspond to 2.9 water molecules per cluster for the first peak centered at 135 °C.

N_2 Sorption Isotherms

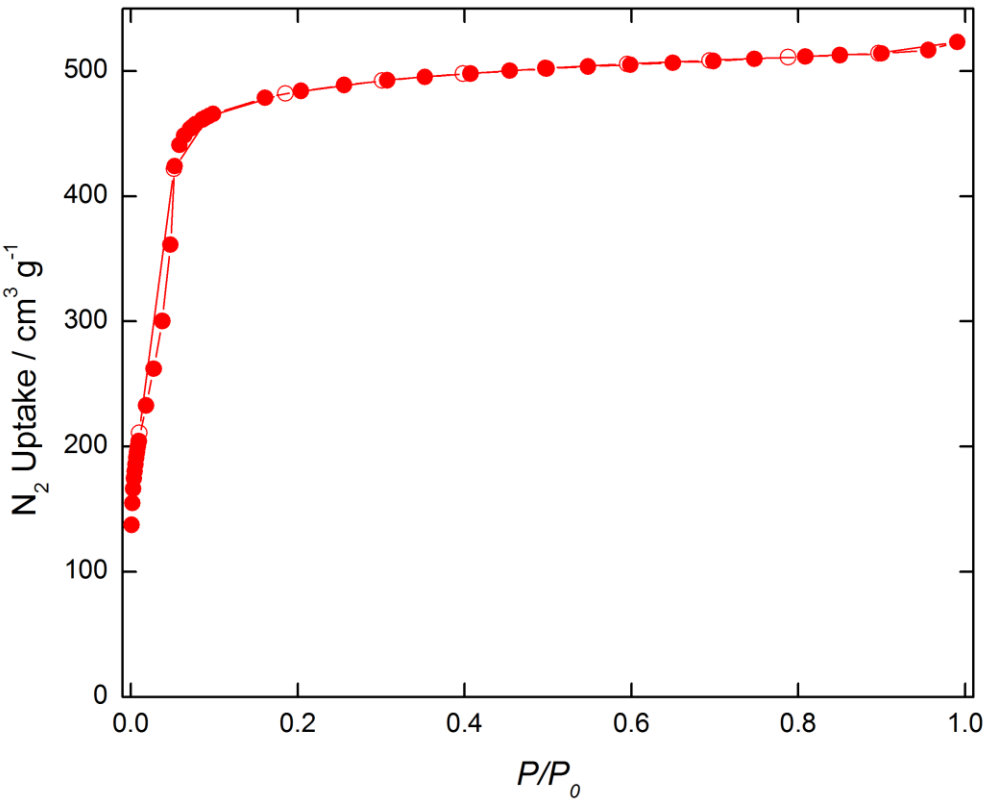

Figure 3.24. N_2 adsorption isotherm of pristine MOF-808 at 77K.

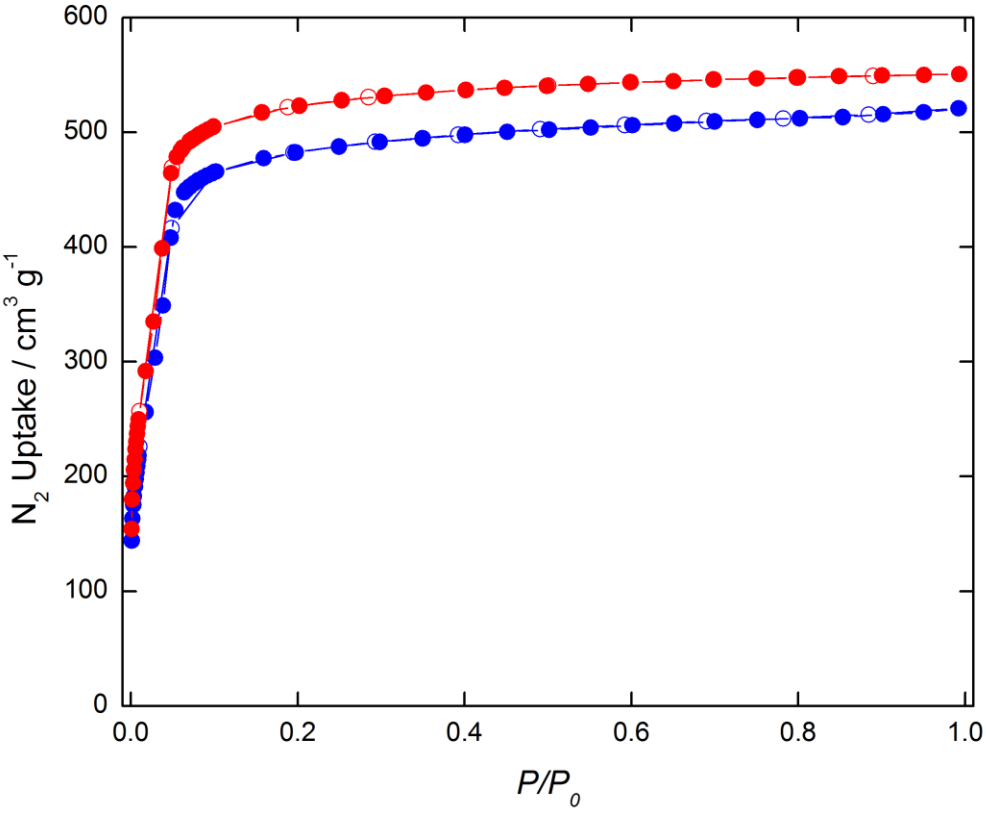

Figure 3.25. N_2 adsorption isotherms of S-MOF-808 (blue circles) and dehydrated S-MOF-808 (red circles) at 77K.

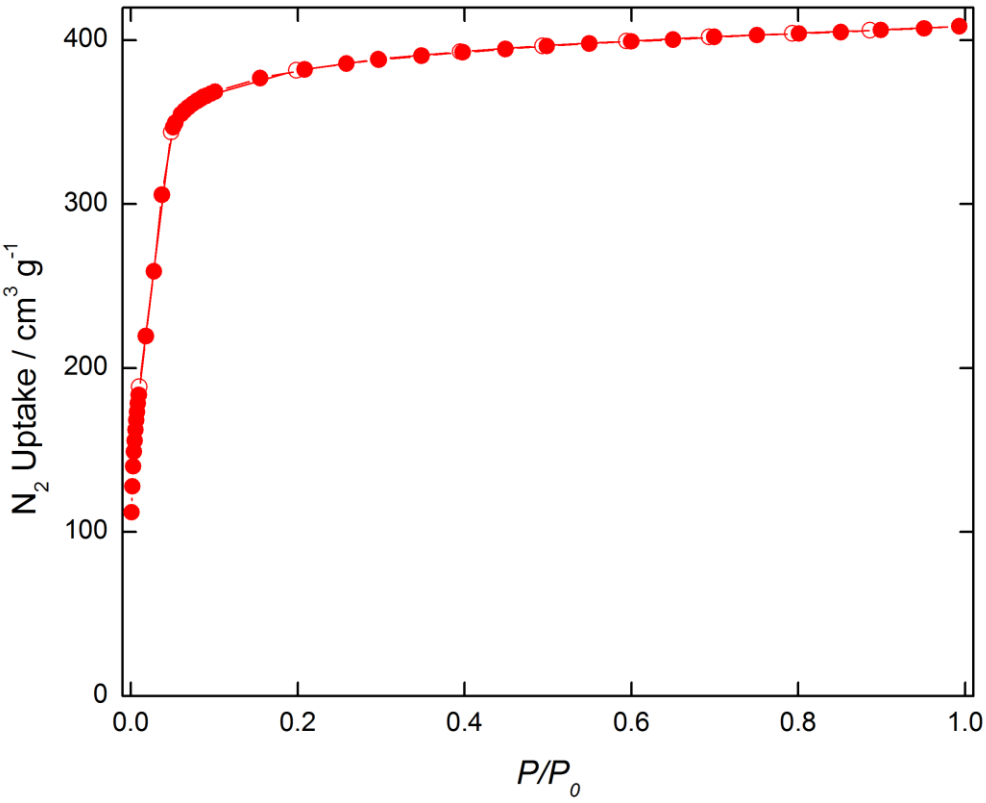

Figure 3.26. N_2 adsorption isotherm of Se-MOF-808 at 77K.

Solid State NMR Spectroscopy. Samples for ^{31}P solid state NMR were prepared following a slightly modified procedure based on the previously reported method.[15] Briefly, around 100 mg MOF sample was activated as described in Section S1, and 1.5 mL of 0.2 M TMPO in chloroform was added and mixed with the MOF sample. This suspension was then evacuated under dynamic vacuum at room temperature overnight, then at 50 °C for 8 hours. The resulting solid was then packed into 75 uL Doty XC5 Kel-F sealing cells under argon atmosphere, and inserted into a Doty 5 mm thin-wall zirconia rotor with Kel-F turbine caps. Solid state NMR spectra were collected using a 7.05 T magnet with a Tecmag Discovery spectrometer operating at 300.13 MHz for 1H and 121.5 MHz for ^{31}P. ^{31}P chemical shifts were externally referenced to aqueous H_3PO_4 (85%) at 0 ppm. Experiments were performed on a Doty 5-mm triple resonance MAS probe operating in $^{1}H/^{31}P/^{87}Sr$ mode. Magic angle spinning (MAS) was used to collect high resolution NMR spectra at a spinning rate of 8 kHz. ^{31}P NMR experiments were performed with a ^{31}P 90° pulse time of 6 μs and a continuous wave ^{1}H decoupling B_1 field of 60 kHz. Spectra were collected with 5120 scans and a recycle delay time of 11 s (Figure 3.27).

***In Situ* Infrared Spectroscopy**

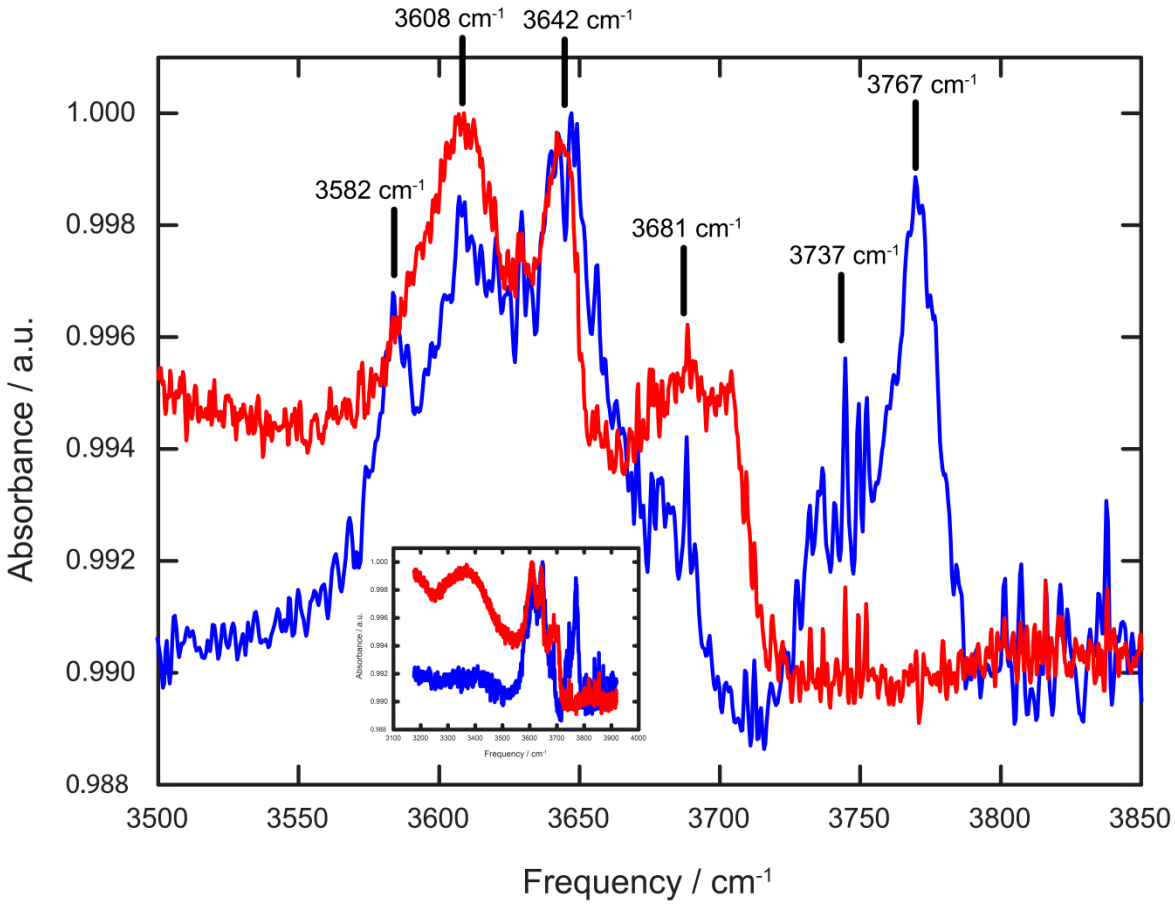

Figure 3.27. A comparison of the *in situ* IR spectra of activated (blue) and dehydrated (red) stages of S-MOF-808 in the energy region relevant to O-H stretches. The most notable feature is the loss of the two blue-shifted peaks at 3737 and 3767 cm^{-1}, and what appears to be the loss of the peak at 3582 cm^{-1}. The inset is included to show the broad feature centered around 3350 cm^{-1} in the dehydrated structure, which corresponds to a minute amount of water adsorbed onto the S-MOF-808 crystals.

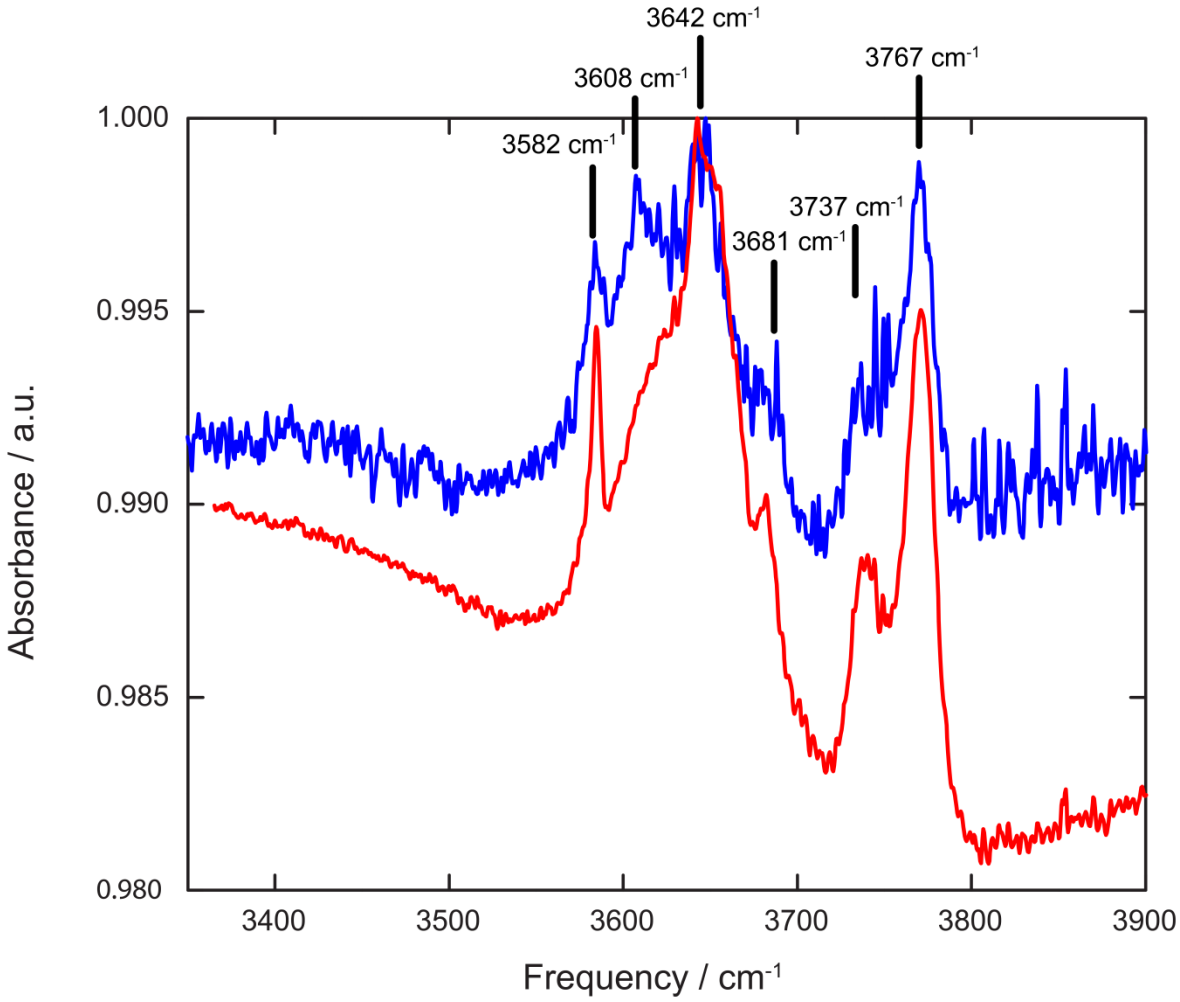

Figure 3.28. A comparison of the *in situ* IR spectra of activated S-MOF-808 (blue) and Se-MOF-808 (red) in the energy region relevant to O-H stretches. Both samples display the same O-H stretches, indicating the water and hydroxide environments in both samples are similar.

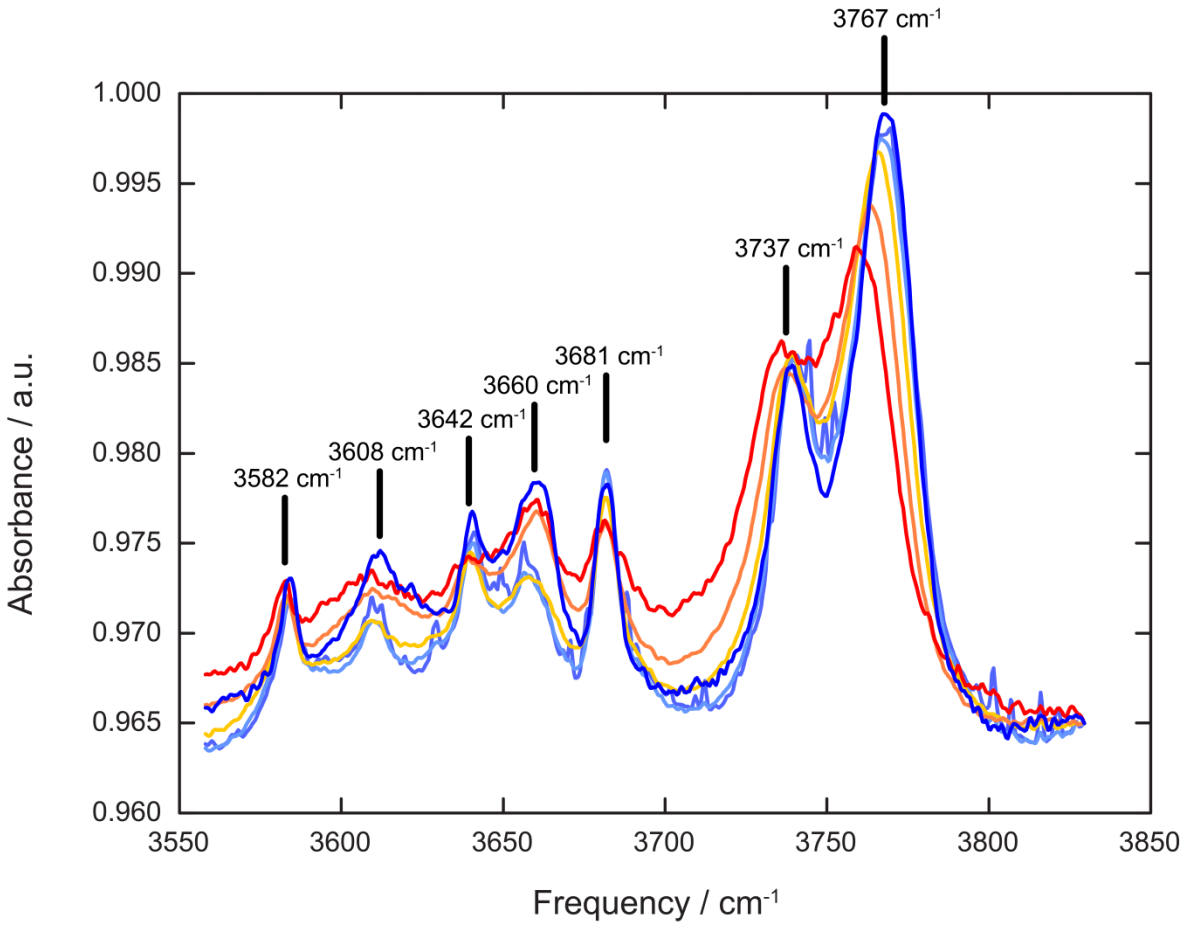

Figure 3.29. A comparison of the *in situ* IR spectra of activated S-MOF-808 at different temperatures in the energy region relevant to O-H stretches. Heating the sample broadens the peaks since the local environment becomes more disordered due to thermal motion, and the process is reversible between room temperature and 200 °C. The measurement was started at room temperature (baby blue) then heated gradually with data reported at 40 °C (light purple), 80 °C (yellow), 125 °C (orange), 200 °C (red), and cooled back down to room temperature (dark blue).

Scanning Electron Microscopy

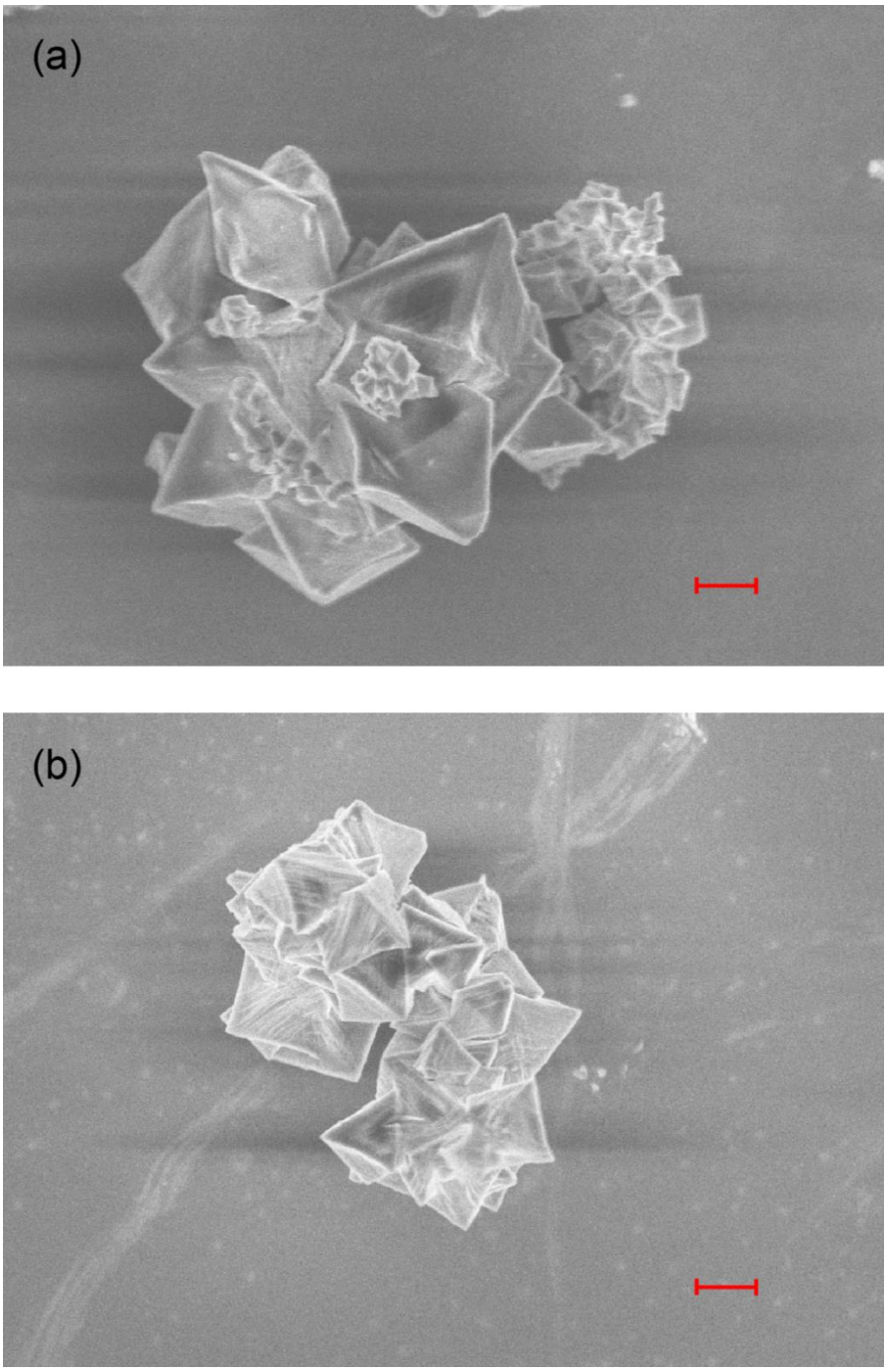

Figure 3.30. Scanning electron microscope (SEM) images of (a) S-MOF-808 and (b) Se-MOF-808 following activation under dynamic vacuum at 120 °C (scale bar 1 μm).

Cluster Geometry Optimization. Cluster optimizations were performed and geometrically optimized using density functional theory (DFT), based on the formula $Zr_6O_4(OH)_4(C_2H_3O_2)_6(SO_4)_2(OH)_2(OH_2)_x$, where x = 2 or 3. Acetate groups were used instead of BTC as a terminal ligand. The functional B97-D3 was chosen, which is the B97 functional with Grimme's dispersion term added on to account for dispersive effects that B97 misses. The chosen basis set was 6-31G* for all non-Zr atoms. For Zr, the CRENBL effective core potential was used for core electrons, with the matching CRENBL basis for valence electrons. A very fine grid consisting of 90 radial points and 590 angular points was selected for the numerical integration step to account for exchange-correlation.

Bibliography

(1) Arata, K. *Adv. Catal.* **1990**, *37*, 165.

(2) Ward, D. A.; Ko, E. I. *J. Catal.* **1994**, *150* (1), 18–33.

(3) Bensitel, M.; Saur, O.; Lavalley, J.-C.; Morrow, B. A. *Mater. Chem. Phys.* **1988**, *19* (1–2), 147–156.

(4) Clearfield, A.; Serrette, G. P. D.; Khazi-Syed, A. H. *Catal. Today* **1994**, *20* (2), 295–312.

(5) Kustov, L. M.; Kazansky, V. B.; Figueras, F.; Tichit, D. *J. Catal.* **1994**, *150* (1), 143–149.

(6) Adeeva, V; Dehaan, J. W.; Janchen, J; Lei, G. D.; Schunemann, V.; Vandeven, L. J. M.; Sachtler, W. M. H.; Vansanten, R. A. *J. Catal.* **1995**, *151* (2), 364–372.

(7) Bolis, V.; Magnacca, G.; Cerrato, G.; Morterra, C. *Langmuir* **1997**, *13* (5), 888–894.

(8) Hino, M.; Kurashige, M.; Matsuhashi, H.; Arata, K. *Thermochim. Acta* **2006**, *441* (1), 35–41.

(9) Arata, K. *Green Chem.* **2009**, *11* (11), 1719–1728.

(10) Yadav, G. D.; Nair, J. J. *Microporous Mesoporous Mater.* **1999**, *33* (1), 1–48.

(11) Cairns, A. B.; Goodwin, A. L. *Chem. Soc. Rev.* **2013**, *42* (12), 4881–4893.

(12) Furukawa, H.; Müller, U.; Yaghi, O. M. *Angew. Chem. Int. Ed.* **2015**, *54* (11), 3417–3430.

(13) Trickett, C. A.; Gagnon, K. J.; Lee, S.; Gándara, F.; Bürgi, H.-B.; Yaghi, O. M. *Angew. Chem. Int. Ed.* **2015**, *54* (38), 11162–11167.

(14) Mahdi, H. I.; Muraza, O. *Ind. Eng. Chem. Res.* **2016**, *55* (43), 11193–11210.

(15) Jiang, J.; Gándara, F.; Zhang, Y.-B.; Na, K.; Yaghi, O. M.; Klemperer, W. G. *J. Am. Chem. Soc.* **2014**, *136* (37), 12844–12847.

(16) Furukawa, H.; Gándara, F.; Zhang, Y.-B.; Jiang, J.; Queen, W. L.; Hudson, M. R.; Yaghi, O. M. *J. Am. Chem. Soc.* **2014**, *136* (11), 4369–4381.

(17) Bruker. In *APEX2 (Bruker AXS Inc., Madison, Wisconsin, U.S.A)*; 2010.

(18) Sheldrick, G. M. *Acta Crystallogr. Sect. A Found. Crystallogr.* **2007**, *64* (1), 112–122.

(19) Dolomanov, O. V.; Bourhis, L. J.; Gildea, R. J.; Howard, J. A. K.; Puschmann, H. *J. Appl. Crystallogr.* **2009**, *42* (2), 339–341.

(20) Åberg, M.; Glaser, J. *Inorg. Chim. Acta* **1993**, *206* (1), 53–61.

(21) Springborg, J. *Adv. Inorg. Chem.* **1988**, *32*, 55–169.

(22) Hall, J. In *Lab Manual for Zumdahl/Zumdahl's Chemistry*; 2002; p 656.

(23) Zheng, A.; Huang, S.-J.; Liu, S.-B.; Deng, F. *Phys. Chem. Chem. Phys.* **2011**, *13* (33), 14889.

(24) Fraenkel, D. *Chem. Lett.* **1999**, *9*, 917–918.

(25) Hare, D. E.; Sorensen, C. M. *J. Chem. Phys.* **1992**, *96* (1), 13–22.

(26) Vimont, A.; Goupil, J. M.; Lavalley, J. C.; Daturi, M.; Surblé, S.; Serre, C.; Millange, F.; Férey, G.; Audebrand, N. *J. Am. Chem. Soc.* **2006**, *128* (10), 3218–3227.

(27) Planas, N.; Mondloch, J. E.; Tussupbayev, S.; Borycz, J.; Gagliardi, L.; Hupp, J. T.; Farha, O. K.; Cramer, C. J. *J. Phys. Chem. Lett.* **2014**, *5* (21), 3716–3723.

(28) Izquierdo, J. F.; Vila, M.; Tejero, J.; Cunill, F.; Iborra, M. *Appl. Catal. A, Gen.* **1993**, *106* (1), 155–165.

(29) Kamath, R. S.; Qi, Z.; Sundmacher, K.; Aghalayam, P.; Mahajani, S. M. *Ind. Eng. Chem. Res.* **2006**, *45* (5), 1575–1582.

(30) *Bruker AXS, Madison, WI, USA.*

Chapter 4: Post-Synthetic Incorporation of Selenate, Chromate and Molybdate into MOF-808

Introduction

The post-synthetic modification of metal-organic frameworks (MOFs) has garnered significant attention in recent years for its potential to install functional groups that would not be possible to incorporate during the initial MOF synthesis.[1,2] These modifications can be performed in pre-selected sites on the framework, including both the linker and the metal clusters. For instance, the coordinatively unsaturated metal sites of Mg_2(dobpdc) have been functionalized with alkylamine moieties,[3] and separately the linker of its isoreticularly expanded form, IRMOF-74-III, has also been post-synthetically modified to contain dangling amine groups.[4] In both cases, these materials have been applied to the selective capture of CO_2 from wet flue gas without loss in performance over multiple cycles. This realization was a significant step forward for the practical use of MOFs in industrial CO_2 capture, since the unfunctionalized MOF-74-based frameworks offered high CO_2 uptake only after one cycle before succumbing to the competitive binding of water.[5] While the coordinatively unsaturated metal sites of MOF-74 are among the strongest-performing materials for pure CO_2 capture, the main limitation in their deployment for practical applications is the lack of selectivity for CO_2 over water.

The discovery of the potential for alkylamine-based functional groups for selective CO_2 capture from flue gas can be traced to their known application to this process combined with the highly porous and ordered nature of MOFs. This functionality has already been well-studied and used for this technology in the form of aqueous monoethanolamines (MEA), and its molecular chemistry is well-understood.[6,7] Specifically, a chemisorption process occurs where CO_2 is covalently bound to the amine group, forming a carbamate. This strong interaction is the driving force for selectivity towards CO_2. This chemical understanding allows for the possibility to rationally design porous materials with these functional groups using the tunability of MOFs, and combine the high internal surface area with a high density of these amine moieties to maximize CO_2 uptake.

While this rational design approach was successfully used for this application, an understanding of the binding site and mechanism within the frameworks are still of great value, especially since the MOFs are solid-state materials compared with the liquid phase of MEA. This has the potential to alter the structure-property functions as the different materials result in a very different environment for CO_2 uptake. A study of the binding sites in amine-appended Mg_2(dobpdc) brought this to the forefront, whereby an insertion mechanism between the metal-amine bond by the incoming CO_2 molecule.[8] Prior to this discovery, it was thought the CO_2 molecule would coordinate to the dangling amine group rather than that coordinating to the metal. Thus, the work was pivotal in the understanding the use of these materials as the chemical basis for the high and selective CO_2 capacity is derived from a different binding mechanism than originally thought, therefore altering the design principal of sorbent materials for carbon capture. Even though a carbamate forms through a chemisorptive process as with MEA, the pore environment, and more specifically the metal binding site plays a crucial role.

This structure-property relationship understanding was applied in the case of the superacidic zirconium-based framework sulfated MOF-808 (S-MOF-808) to develop an active catalyst for the selective isobutene dimerization in Chapter 3. The project was an extension of a previous study on the development of S-MOF-808 as a superacidic catalyst.[9] An understanding of the source of superacidity, being from terminal water molecule coordination to zirconium which forms a strong hydrogen bond to a chelating sulfate group, led to an understanding and subsequent optimization of the reaction conditions by controlling the temperature and the hydration level of the material. Without knowledge of the catalytically active site, a trial-and-error approach would have to be adopted to optimize the properties. This has the limitation of being an inefficient method of scientific investigation compared with rational design when trying to optimize a specific property. Additionally, the knowledge gained from the optimization process can be applied to other materials, but only with an understanding of the specific chemical requirements, in this case the presence of some moisture.

There are reports of studying the coordination geometry of posts-synthetically exchanged groups such as selenate, selenite and phosphate.[10,11] These studies were performed on the MOF known as NU-1000 which has the same zirconium-based cluster as MOF-808. Selenate, for instance, was found to coordinate in a bridging fashion by IR when immersed in water. In some cases such as with chromate, tungstate and other transition metal complexes, a large variety of coordination modes as well as cluster configurations can exist. This is reflected in the field of polyoxometallates which study and manipulate these configurations.[12,13] Gaining the knowledge of how these metal oxides persist in the solid state when bound to a MOF, as well as if or how the coordination environment can be manipulated, would be extremely valuable. This has the potential to rationally optimize materials for a given application without using trial and error methods.

The great promise of post-synthetically functionalized materials, and the power of deliberate design and property prediction based on the structure and chemical functionality present in an ordered array, this sub-field of MOFs is a prime area for further investigation. The focus of this Chapter is on extending the post-synthetic modification of pristine MOF-808, which contains exchangeable formate groups that were found to be exchangeable with sulfate moieties. Specifically, the installation of a range of metal and non-metal oxides was investigated, including selenic acid, chromic acid, sodium molybdate, sodium tungstate and phosphoric acid. The resulting modified frameworks were subsequently investigated to probe the chemical environment of the groups, with the goal of better understanding their chemistry.

Experimental

Chemicals used in this work. *N,N*-dimethylformamide (DMF) was obtained from Fisher Scientific. Formic acid (purity > 98%) and anhydrous chloroform were obtained from EMD Millipore Chemicals. Anhydrous acetone was obtained from Acros Organics. Zirconium oxychloride octahydrate (>99.5%), hydrofluoric acid (aqueous, 48%), sulfuric acid (H_2SO_4, purity ≥ 95%), 1,3,5-benzenetricarboxylic acid (H_3BTC), selenic acid (aqueous, 40%), chromium trioxide (purity ≥ 98%) sodium tungstate (purity > 99%) and sodium molybdate dehydrate (purity ≥ 99%) were obtained from Aldrich. Trimethylphosphine oxide (TMPO) was obtained from Alfa Aesar. All starting materials and solvents, unless otherwise specified, were used without further purification.

Analytical techniques. Single-crystal X-ray diffraction (SXRD) data were collected on beamline 11.3.1 at the Advanced Light Source, Lawrence Berkeley National Lab. Samples were mounted on MiTeGen® kapton loops and placed in a 100(2) K nitrogen cold stream provided by an Oxford Cryostream 700 Plus low temperature apparatus on the goniometer head of a Bruker D8 diffractometer equipped with a PHOTON100 CMOS detector operating in shutterless mode. Diffraction data were collected using synchrotron radiation monochromated using a silicon (111) reflection to a wavelength of 0.7749(1) Å. An approximate full-sphere of data was collected using a combination of phi and omega scans with scan speeds of 2 seconds per 4 degrees for the phi fast scans, and 5 and 15 seconds per degree for the omega scans at 2θ = 0 and -45, respectively. In all cases, the data were processed using the Bruker APEX2 software package,[14,15] structures were solved by intrinsic phasing (SHELXT) and refined by full-matrix least squares on F^2 (SHELXL-2014) using the Olex2 software package.[16] All non-hydrogen atoms were refined anisotropically unless otherwise specified. Hydrogen atoms were geometrically calculated and refined as riding atoms.

Powder X-ray diffraction patterns (PXRD) were recorder using a Bruker D8 Advance diffractometer (Göbel-mirror monochromated Cu K_α radiation λ= 1.54056 Å). Elemental microanalyses (EA) for carbon, hydrogen, nitrogen and sulfur were performed in the Microanalytical Laboratory of the College of Chemistry at UC Berkeley, using a Perkin Elmer 2400 Series II CHNS elemental analyzer. Solution ^{1}H NMR spectra were acquired on a Bruker AVB-400 NMR spectrometer. N_2 sorption isotherms were measured on a Quantachrome Quadrasorb instrument, held at 77 K using a liquid nitrogen bath. Helium was used for the estimation of dead space for gas adsorption measurements. Ultra-high purity grade N_2 and He were used throughout the adsorption experiments. X-ray photoelectron spectroscopy (XPS) was performed at the Molecular Foundry using the PHI 5400 XPS System.

Preparation of selenated MOF-808. Approximately 50 mg of MOF-808 was immersed in 0.05 M selenic acid in H_2O for 24 hours and stirred at regular intervals. The treated solid was then washed with H_2O, then solvent exchanged by immersion in anhydrous acetone before exchanging into chloroform. For each step, the samples were washed for three days with the solvent being decanted and freshly replenished three times per day. The chloroform in the solvent-exchanged crystals was removed under dynamic vacuum (30 mTorr) for 24 h at room temperature, followed by 8 h at 80 °C and a further 16 h at 120 °C.

^{1}H solution NMR spectrum of the digested, activated and selenated MOF-808 (400 MHz, DMSO-*d6*): 8.64 (s, BTC), 7.85 (s, DMF), peak area ratio (BTC:HCOOH:DMF) = 6.00:0.00:0.5. Calculated formula $Zr_6O_4(OH)_4(C_9H_3O_6)_2(SeO_4)_{2.3}(OH)_{1.4}(C_3H_7NO)_{0.5}(H_2O)_{2.9}$ = $Zr_6O_{34}C_{19.5}H_{20.7}N_{0.5}Se_{2.3}$: C, 15.3%; H, 1.4%; N, 0.5%. Found: C, 15.4%; H, 0.9%; N, 0.7%. Note ICP reveals 0.383:1 Se:Zr.

Preparation of chromated MOF-808. Approximately 50 mg of MOF-808 was immersed in 0.05 M chromium(VI) trioxide in H_2O for 24 hours and stirred at regular intervals. The treated solid was then washed with H_2O, then solvent exchanged by immersion in anhydrous acetone before exchanging into chloroform. For each step, the samples were washed for three days with the solvent being decanted and freshly replenished three times per day. The chloroform in the solvent-exchanged crystals was removed under dynamic vacuum (30 mTorr) for 24 h at room temperature, followed by 8 h at 80 °C and a further 16 h at 120 °C. Note ICP reveals 0.3027:1 Cr:Zr.

Preparation of molybdated MOF-808. Approximately 50 mg of MOF-808 was immersed in 0.05 M sodium molybdate in H_2O for 24 hours and stirred at regular intervals. The treated solid was then washed with H_2O, then solvent exchanged by immersion in anhydrous acetone before exchanging into chloroform. For each step, the samples were washed for three days with the solvent being decanted and freshly replenished three times per day. The chloroform in the solvent-exchanged crystals was removed under dynamic vacuum (30 mTorr) for 24 h at room temperature, followed by 8 h at 80 °C and a further 16 h at 120 °C.
$Zr_6O_{32.52}H_{14.76}C_{18}Mo_{2.38}$ = $Zr_6O_{5.24}(OH)_{2.76}(C_9H_3O_6)_2(MoO_4)_{2.38}(H_2O)_3$: C, 14.2%; H, 1.0%; N, 0.0%. Found: C, 14.1%; H, 1.2%; N, >0.3%. Note ICP reveals 0.3961:1 Mo:Zr.

Results and Discussion

The post-synthetic modification (PSM) of pristine MOF-808 was carried out by immersing the MOF sample in 0.05 M of the desired metal oxide (Figure 4.1). In the case of exchanging molybdate, the fully deprotonated sodium salt was used, while selenic acid and chromic acid, in the form of chromium(VI) oxide dissolved in water, were the starting materials. Sodium tungstate was also investigated, though even at an order of magnitude of further dilution to 0.005 M Na_2WO_4 in water, the framework was found to be destroyed as the powder X-ray diffraction (PXRD) pattern displayed no reflections. The same case was found when using phosphoric acid and trisodium phosphate, both of which destroy the framework upon soaking with concentrations of 0.01 M or greater of these compounds in aqueous solutions. Following exchange, the MOFs were washed in water for three days and the crystal structures studied. Selenated MOF-808 (Se-MOF-808) shows that selenate replaces formate in an exclusively bridging manager when in DMF, and none found in the chelating mode as is the case in sulfated MOF-808 under these conditions (see Chapter 3 for details).

Chromium-containing MOF-808 (Cr-MOF-808) has chromate adopting the same bridging coordination mode, but also with a smaller percentage coordinating to zirconium in a chelating fashion, meaning coordination is bidentate but only to a single zirconium atom. The partially occupied oxygen atoms on both chromium positions were for the most part not possible to resolve due to low occupancy, disorder and the overlapping of their positions with electron density from solvent molecules. For similar reasons, the protons, if any, on chromate could not be located, so the protonation state could not be confirmed. The pK_a values for H_2CrO_3 are 0.74 and 6.49 respectively, which suggests it is possible for both CrO_3^{2-} and $HCrO_3^-$ to exist.[17] More detailed experiments, such as measuring the acidity of the solution, are required to inform further on this. The bond lengths for Cr-O in sodium chromate are around 1.63 Å,[18] so distance restraints were applied since the oxygen and chromium positions are relatively poorly defined due to the disorder. The bridging and chelating coordination modes exist in a roughly 3:5 ratio based on freely refining the occupancies of these sites from SXRD data. Inductively-coupled plasma-mass spectrometry (ICP-MS) confirmed the presence of chromium, with a Zr:Cr ratio of 1:0.303. The occupancy of chromium was found to be lower by single crystal diffraction when compared with analysis of the bulk sample. There are a few possible reasons why this is the case, the most likely of which is that the selection of a large single crystal compared with the bulk contains less chromate because the exchange is limited by diffusion into the large crystals. Another possibility is that not all chromate is coordinating to the metal cluster, and hence is not detected crystallographically. However, the sample was washed multiple times with water, acetone and chloroform prior to activation, with elemental analysis, ^{1}H NMR and the PXRD pattern indicating the MOF is pure phase and additional, non-coordinating chromate is expected to have been removed.

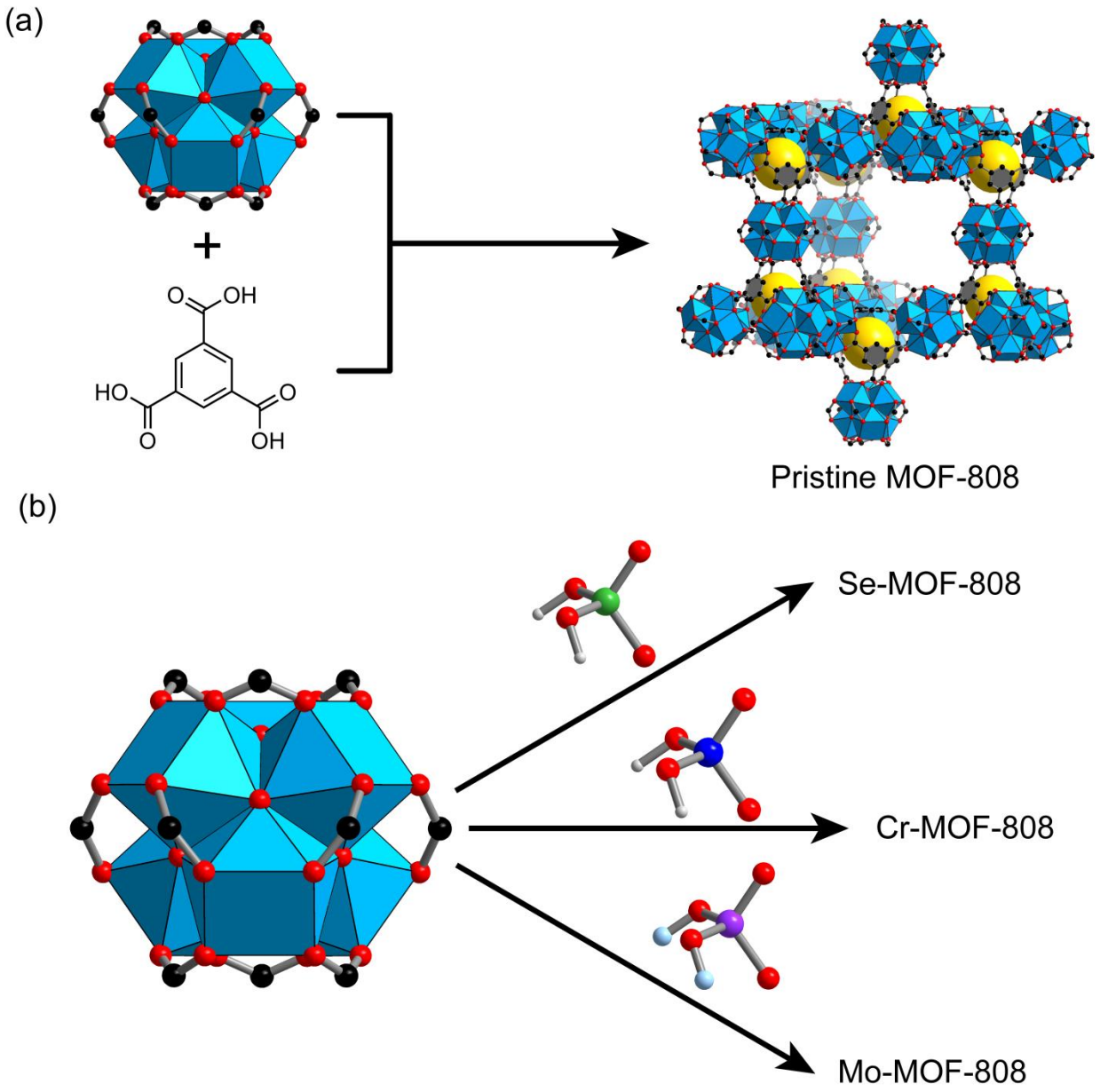

Figure 4.1. (a) Synthesis of pristine MOF-808 constructed by 6-coordinate zirconium-based metal clusters containing formate groups and linked by benzenetricarboxylate into the diamond topology. These formates may be substituted with selenate, chromate and molybdate anions as in (b). Selenic acid, chromium trioxide and sodium molybdate were used as starting materials. Color scheme is as follows: Zr, light blue; C, black; O, red; Se, green; Cr, dark blue; Mo, purple; Na, ice blue; H, white. Hydrogen atoms on all except the anions were omitted for clarity.

The final successful exchange was the incorporation of molybdate into MOF-808 (Mo-MOF-808). As with Cr-MOF-808, a dominant bridging mode is apparent along with a smaller monodentate component (17.4 ±0.4 and 3.5 ±0.2% respectively). The pK_a of $HMoO_4^-$ is 6.0,[19] and the presence of two coordinating modes is attributed to this intermediate pK_a value that permits the oxide to exist in two different protonation states in the MOF and an aqueous

environment. This may be the reason for the monodentate binding mode, although similarly to Cr-MOF-808, hydrogen atoms could not be located due to low occupancy and disorder. ICP-MS confirms the presence of Mo, and just as is the case with Cr-MOF-808, less molybdenum is detected by SXRD on the single crystal compared with the bulk. The presence of Mo in the +6 oxidation state was confirmed by X-ray photoelectron spectroscopy, revealing peaks at 234.4 and 237.6 eV, corresponding to the $3d_{5/2}$ and $3d_{3/2}$ for Mo(VI) respectively.[20] Figure 4.2 displays the experimentally determined oxide binding modes.

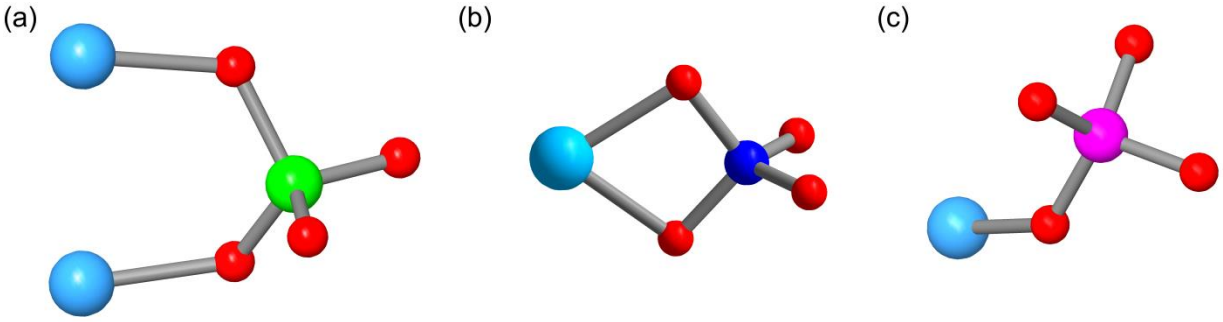

Figure 4.2. The three binding modes observed following incorporation of the oxides exhibited in an aqueous environment. (a) All frameworks display the bridging mode, with Se-MOF-808 having this coordination geometry exclusively. (b) Cr-MOF-808 also has a minor chelating component, and (c) molybdate in Mo-MOF-808 can bind in a monodentate fashion. Color scheme is as follows: light blue, Zr; red, O; green, Se; dark blue, Cr; purple, Mo.

In Cr- and Mo-MOF-808, the source of charge-balancing is not clear. While Se-MOF-808, which has an analogous structure to S-MOF-808 and therefore is likely charge-balanced by hydroxide ions terminally bound to Zr (see Chapter III for further details), the frameworks would require three fully deprotonated chromate or molybdate moieties per cluster for charge neutrality. The sources of charge-balancing are likely to be terminal hydroxide ions as in S- and Se-MOF-808, or could be from the deprotonation of the μ^3-bridging OH groups. However, the proton topology is not so straightforward since the protonation states of chromate and molybdate require further investigation too.

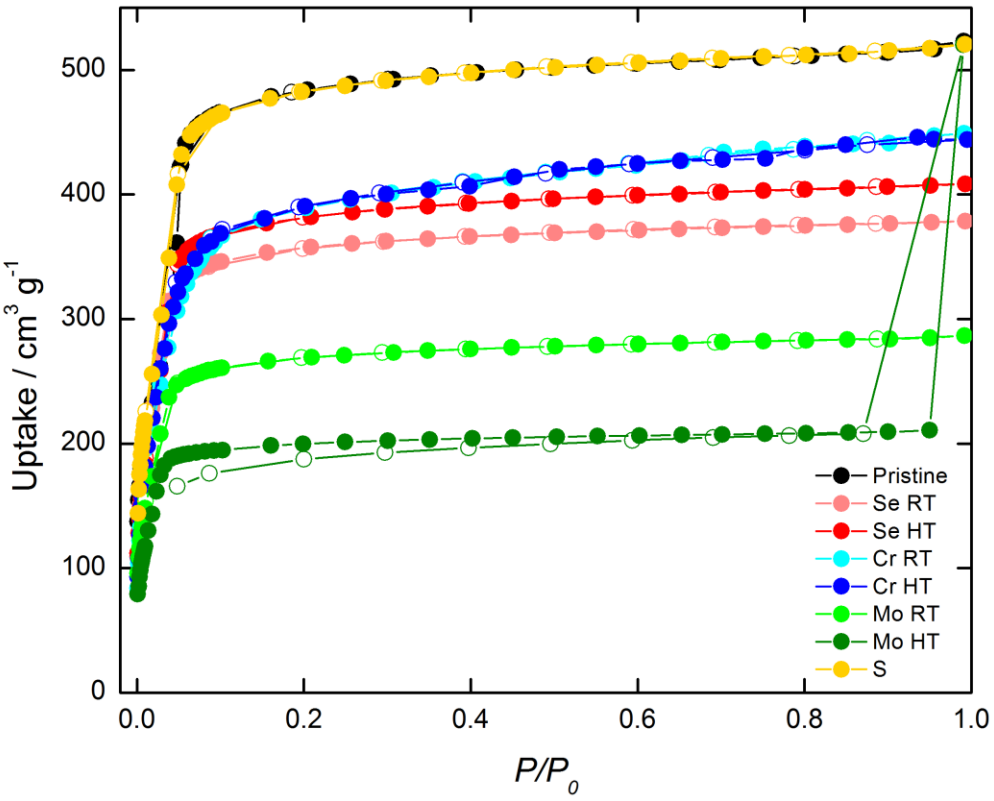

Figure 4.3. N_2 uptake at 77 K for Se-, Cr- and Mo-MOF-808 compared to sulfated and pristine versions of the framework, for which the solvent evacuation was performed at 120 °C. HT = high activation temperature (120 °C), RT = room temperature activation. The temperature has no effect on the N_2 uptake of Cr-MOF-808, but higher temperature substantially reduces the uptake for Mo-MOF-808. Se-MOF-808 shows a slight increase after evacuation at elevated temperature.

Surface area analysis was performed using N_2 sorption at 77 K (Figure 4.3). Each sample, Se-, Cr- and Mo-MOF-808 was evacuated under dynamic vacuum at room temperature and at 120 °C. The N_2 uptake was found to be greater for Se-MOF-808 only when evacuating while heating. That of Cr-MOF-808 is unaffected by evacuation temperature while Mo-MOF-808's comparatively low surface area drops even further when heat is applied. The PXRD pattern of Mo-MOF-808 displays evidence of some structural degradation as the reflections are weaker and broader than prior to activation. However, there is no obvious loss in crystallinity for Se- or Cr-MOF-808 following evacuation (Figure 4.4). It is not clear what is responsible for this difference between frameworks, although there was some evidence of crystal damage following exchange in chloroform based on the PXRD pattern.

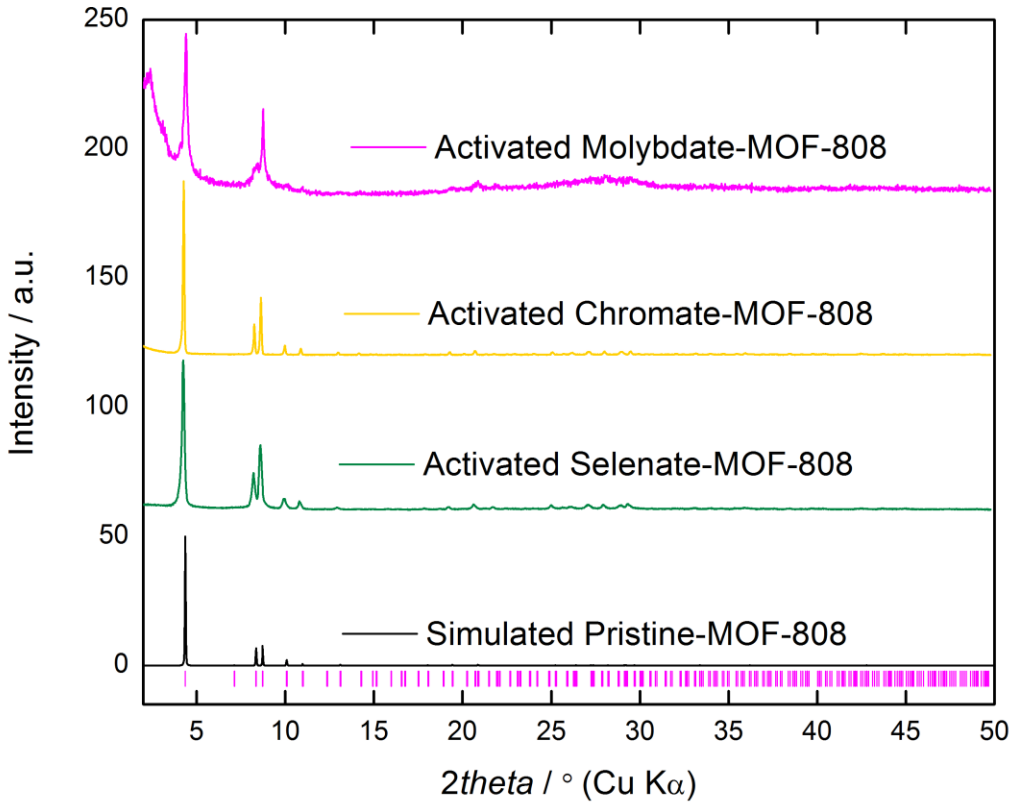

Figure 4.4. Powder X-ray diffraction patterns of Se- (green), Cr- (yellow) and Mo-MOF-808 (purple) measured following activation under dynamic vacuum at 120 °C. Mo-MOF-808 in particular appears to have suffered some degradation in crystallinity, but overall the frameworks remain structurally intact.

Thermogravimetric analysis (TGA) was performed on the activated MOFs under nitrogen atmosphere (Figure 4.5) and compared with that of the original sulfated MOF-808. In all cases, some mass is lost immediately, which is most likely water or other remaining solvent molecules that are adsorbed onto the framework, or perhaps bound to zirconium in a terminal fashion as observed in S-MOF-808. Note that these samples were exposed to the atmosphere following evacuation of the pores, but prior to the TGA measurement. Following this initial mass loss, all frameworks exhibit a plateau prior to complete structure degradation. S- and Mo-MOF-808 exhibit the highest thermal stability based on these TGA measurements, with both frameworks fully breaking down at above 500 °C. Se-MOF-808 decomposes little above 400 °C while Cr-MOF-808 degrades beyond 200 °C.

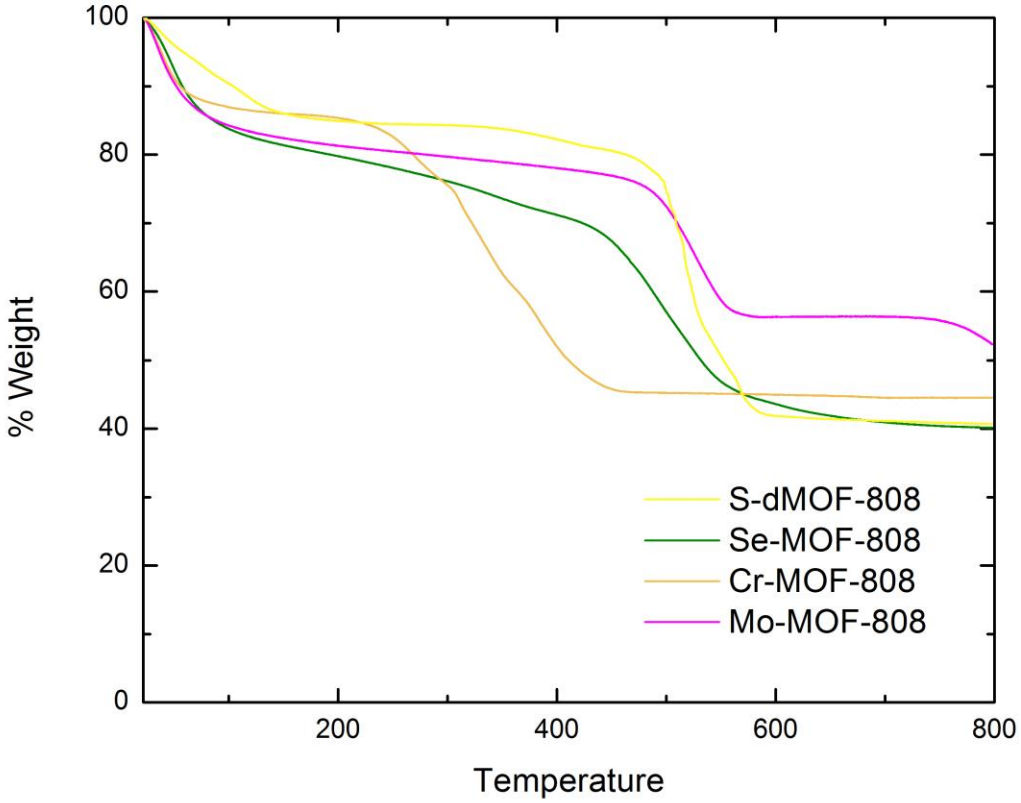

Figure 4.5. Thermogravimetric analysis of Se- (green), Cr- (orange) and Mo-MOF-808 (purple) compared with sulfated MOF-808 (yellow), performed under nitrogen atmosphere. All frameworks lose some mass immediately, attributed to adsorbed and bound water and solvent molecules before reaching a plateau. The overall thermal stability varies greatly, with Mo-MOF-808 exhibiting a similar framework degradation temperature to S-MOF-808, with Se-MOF-808 degrading at an intermediate temperature of around 450 °. Cr-MOF-808 degrades at the lowest temperature, with the second mass loss occurring around 250 °C.

Conclusion

The structural characterization of the post-synthetically modified MOF-808 frameworks with selenate, chromate and molybdate reveals these frameworks can adopt three different coordination modes between them. The most common mode, appearing in all solution-phase structures, is bridging two zirconium atoms and is how selenate binds exclusively. Chromate can also take on a chelating mode to a single zirconium atom, as is found in S-MOF-808 and was the mode found to be essential for the superacidic properties of the sulfated version. Mo-MOF-808 displays the final possibility, with a small component of molybdate binding in a monodentate fashion. The protonation states of all of these binding modes could not be confirmed, but would be very insightful to study as this could provide insight into how the binding mode and protonation state can affect the resulting framework acidity among other properties.

The MOFs were further characterized by TGA, ^{1}H solution NMR, ICP-MS, EA, PXRD and N_2 uptake to investigate whether these materials remain structurally intact and maintain permanent porosity upon solvent removal. The temperature used to activate these frameworks was found to have a substantial influence on the surface area, and the frameworks have remarkably different thermal stabilities. This is perhaps unexpected since the structural connectivity is similar, at least in solution, in all cases. There is a possibility that the binding mode changes upon solvent removal, though this requires further investigation to determine if this would be a factor. It is clear from this however, that the chemical nature of the moiety exchanged onto the framework has a dramatic effect on the subsequent physical as well as chemical properties of the materials.

Appendices and Notes

Acknowledgements. I would like to thank Juncong Jiang for discussions and advice, as well as Simon J. Teat and Kevin J. Gagnon (Advance Light Source, Lawrence Berkeley National Laboratory, U.S.A.) for support during the single-crystal diffraction data collection at the beamline 11.3.1. Work at the Advanced Light Source is supported by the Director, Office of Science, Basic Energy Sciences, of the U.S. Department of Energy under Contract No. DE-AC02-05CH11231. This work is funded by the U.S. Department of Defense, Defense Threat Reduction Agency (DTRA) and BASF SE (Ludwigshafen, Germany) for the synthesis component.

Single crystal X-ray diffraction data for Se-, Cr- and Mo-MOF-808.

Table 4.1. Crystallographic data of Se-MOF-808 after soaking in selenic acid and washing with water for three days.

Sample	**Se-MOF-808**
chemical formula	$Zr_6O_{43.90}C_{18}H_{10}Se_{1.28}$
formula mass	1579.22
crystal system	cubic
space group	*Fd*-3*m*
λ (Å)	0.77490
a (Å)	35.2645(10)
Z	16
V (Å^3)	43854(4)
temperature (K)	100
size /mm	0.015 × 0.015 × 0.010
density (g/cm^{-3})	0.955
measured reflections	79733
unique reflections	2245
parameters	98
restraints	17
R_{int}	0.0858
θ range (deg)	1.8-29.5
R_1, wR_2	0.0510, 0.1672
S (GOF)	1.144
max/min res. dens. (e/Å^3)	0.8/-0.4

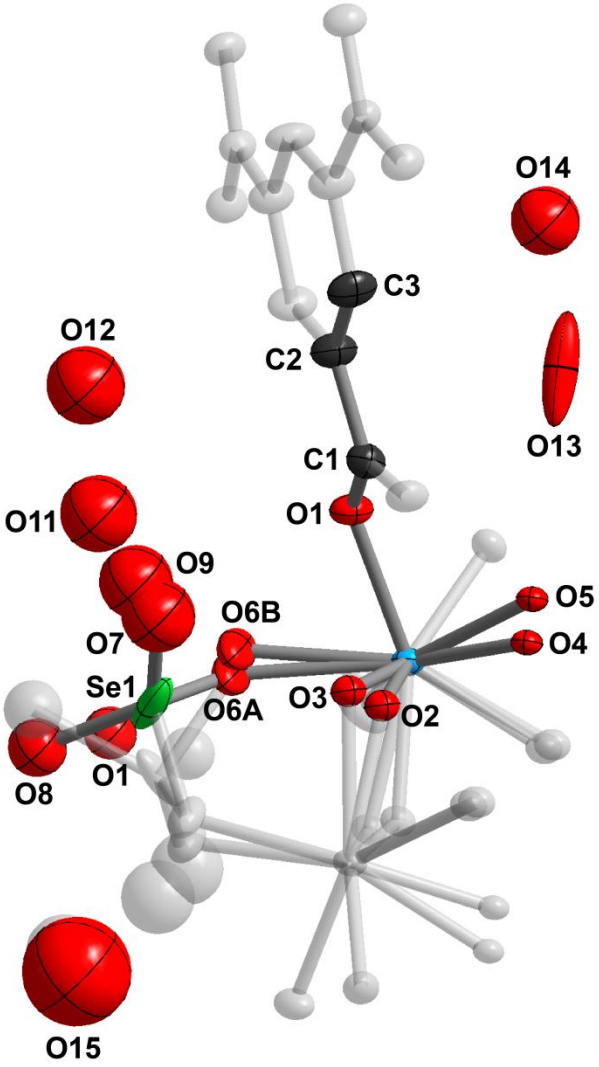

Figure 4.6. Representation of Se-MOF-808 in aqueous solution from SXRD data. The asymmetric unit is displayed in color, with additional atoms in gray to aid visualizing the structure. Thermal ellipsoids are displayed at 50% probability and atom colors are as follows: Zr, blue; O, red; C, black; Se, green. Hydrogen atoms are omitted for clarity.

Table 4.2. Crystallographic data of Se-, Cr- and Mo-MOF-808 after soaking in chromic acid and washing with water for three days.

Sample	**Cr-MOF-808**
chemical formula	$Zr_{96}O_{613.60}C_{288}H_{160}Cr_{7.87}$
formula mass	22604.11
crystal system	cubic
space group	*Fd*-3*m*
λ (Å)	0.77490
a (Å)	35.2528(10)
Z	1
V (Å^3)	43811(4)
temperature (K)	100
size /mm	0.015 × 0.015 × 0.010
density (g/cm^{-3})	0.857
measured reflections	75114
unique reflections	1951
parameters	82
restraints	6
R_{int}	0.1355
θ range (deg)	2.09 – 27.9
R_1, wR_2	0.0605, 0.2025
S (GOF)	1.129
max/min res. dens. (e/Å^3)	0.76 / -0.75

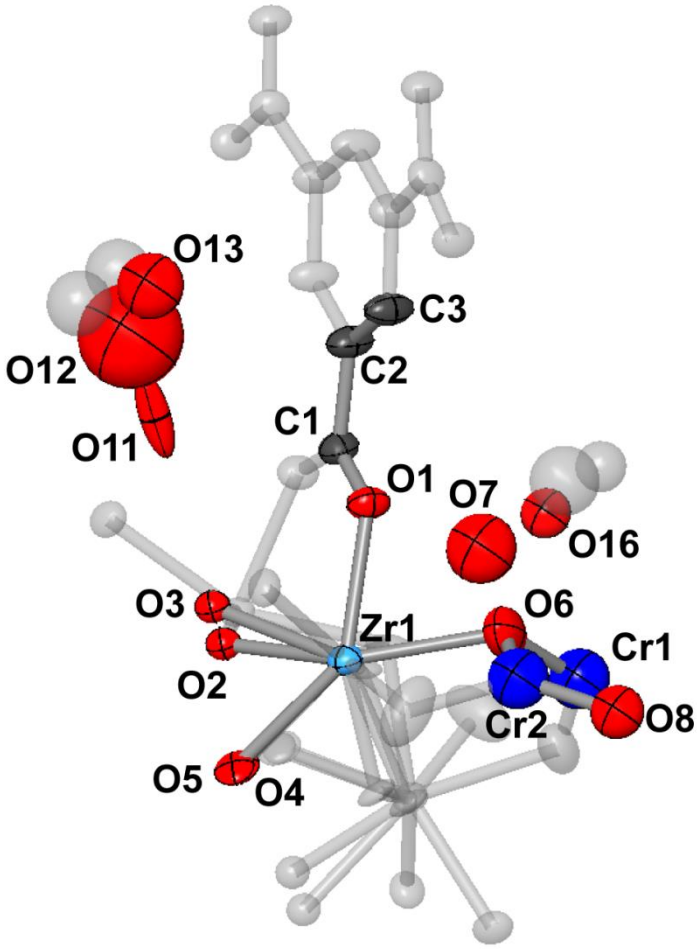

Figure 4.7. Representation of Cr-MOF-808 in aqueous solution from SXRD data. The asymmetric unit is displayed in color, with additional atoms in gray to aid visualizing the structure. Thermal ellipsoids are displayed at 50% probability and atom colors are as follows: Zr, blue; O, red; C, black; Cr, dark blue. Hydrogen atoms are omitted for clarity.

Table 4.3. Crystallographic data of Mo-MOF-808 after soaking in sodium molybdate and washing with water for three days.

Sample	**Mo-MOF-808**
chemical formula	$Zr_{24}O_{167.40}C_{72}H_{34.09}Mo_{6.51}$
formula mass	6391.33
crystal system	cubic
space group	*Fd*-3*m*
λ (Å)	0.77490
a (Å)	35.2996(9)
Z	4
V (Å^3)	43985(3)
temperature (K)	100
size /mm	0.015 × 0.015 × 0.010
density (g/cm^{-3})	0.965
measured reflections	118730
unique reflections	2102
parameters	96
restraints	73
R_{int}	0.1013
θ range (deg)	2.09 – 28.65
R_1, wR_2	0.603, 0.2097
S (GOF)	1.223
max/min res. dens. (e/Å^3)	1.10 / -0.76

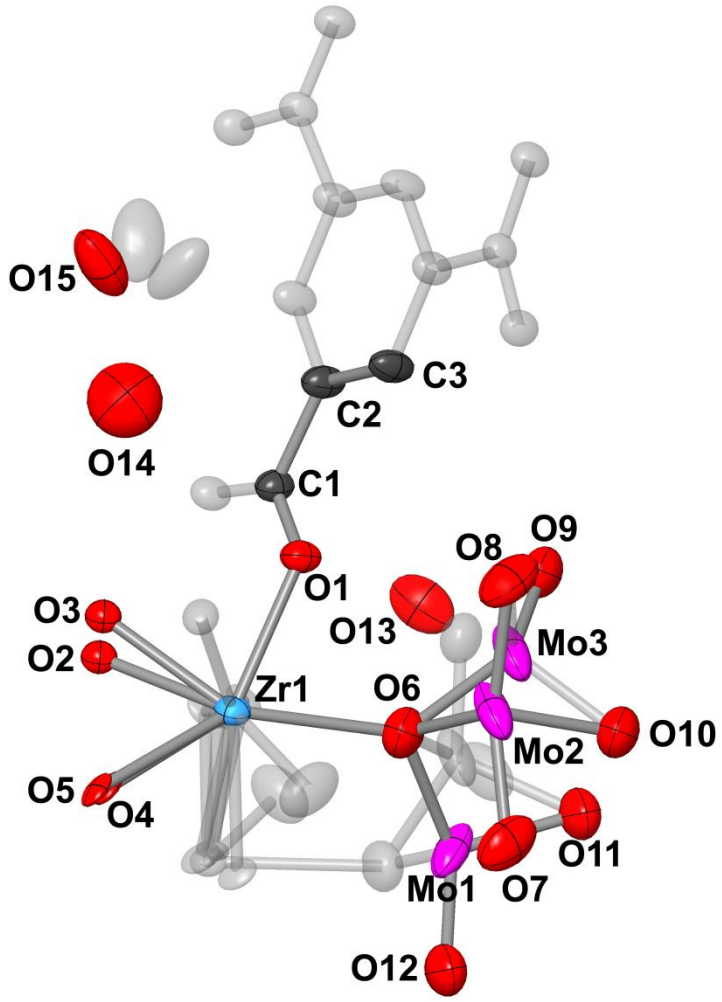

Figure 4.8. Representation of Mo-MOF-808 in aqueous solution from SXRD data. The asymmetric unit is displayed in color, with additional atoms in gray to aid visualizing the structure. Thermal ellipsoids are displayed at 50% probability and atom colors are as follows: Zr, blue; O, red; C, black; Mo, purple. Hydrogen atoms are omitted for clarity.

Bibliography

(1) Song, Y. F.; Cronin, L. *Angew. Chem. Int. Ed.* **2008**, *47* (25), 4635–4637.

(2) Cohen, S. M. *J. Am. Chem. Soc.* **2017**, *139* (8), 2285–2863.

(3) McDonald, T. M.; Lee, W. R.; Mason, J. A.; Wiers, B. M.; Hong, C. S.; Long, J. R. *J. Am. Chem. Soc.* **2012**, *134* (16), 7056–7065.

(4) Fracaroli, A. M.; Furukawa, H.; Suzuki, M.; Dodd, M.; Okajima, S.; Gándara, F.; Reimer, J. A.; Yaghi, O. M. *J. Am. Chem. Soc.* **2014**, *136* (25), 8863–8866.

(5) Kizzie, A. C.; Wong-Foy, A. G.; Matzger, A. J. *Langmuir* **2011**, *27* (10), 6368–6373.

(6) Xie, H.-B.; Zhou, Y.; Zhang, Y.; Johnson, J. K. *J. Phys. Chem. A* **2010**, *114* (43), 11844–11852.

(7) Danckwerts, P. V. *Chem. Eng. Sci*. **1979**, *34* (4), 443–446.

(8) McDonald, T. M.; Mason, J. A.; Kong, X.; Bloch, E. D.; Gygi, D.; Dani, A.; Crocellà, V.; Giordanino, F.; Odoh, S. O.; Drisdell, W. S.; Vlaisavljevich, B.; Dzubak, A. L.; Poloni, R.; Schnell, S. K.; Planas, N.; Lee, K.; Pascal, T.; Wan, L. F.; Prendergast, D.; Neaton, J. B.; Smit, B.; Kortright, J. B.; Gagliardi, L.; Bordiga, S.; Reimer, J. A.; Long, J. R. *Nature* **2015**, *519* (7543), 303–308.

(9) Jiang, J.; Gándara, F.; Zhang, Y.-B.; Na, K.; Yaghi, O. M.; Klemperer, W. G. *J. Am. Chem. Soc.* **2014**, *136* (37), 12844–12847.

(10) Howarth, A. J.; Katz, M. J.; Wang, T. C.; Platero-Prats, A. E.; Chapman, K. W.; Hupp, J. T.; Farha, O. K. *J. Am. Chem. Soc.* **2015**, *137* (23), 7488–7494.

(11) Deria, P.; Bury, W.; Hod, I.; Kung, C. W.; Karagiaridi, O.; Hupp, J. T.; Farha, O. K. *Inorg. Chem.* **2015**, *54* (5), 2185–2192.

(12) Müller, A.; Peters, F.; Pope, M. T.; Gatteschi, D. *Chem. Rev.* **1998**, *98* (1), 239–272.

(13) Borrás-Almenar, J. J.; Coronado, E.; Müller, A.; Pope, M. *Polyoxometalate Molecular Science*; **2003**.

(14) Bruker. In *APEX2 (Bruker AXS Inc., Madison, Wisconsin, U.S.A)*; **2010**.

(15) Sheldrick, G. M. *Acta Crystallogr. Sect. A Found. Crystallogr.* **2007**, *64* (1), 112–122.

(16) Dolomanov, O. V.; Bourhis, L. J.; Gildea, R. J.; Howard, J. A. K.; Puschmann, H. *J. Appl. Crystallogr.* **2009**, *42* (2), 339–341.

(17) Inoue, Y.; Sakai, T.; Kumagai, H. *J. Chromatogr. A* **1995**, *706* (1–2), 127–136.

(18) Sim, G. A.; Sutton, L. E. *Molecular Structure by Diffraction Methods, Volume 4*; **1973**.

(19) Li, M.; Twardowski, Z.; Mok, F.; Tam, N. *J. Appl. Electrochem.* **2007**, *37* (4), 499–504.

(20) Swartz, W. E.; Hercules, D. M. *Anal. Chem.* **1971**, *43* (13), 1774–1779.

Chapter 5: Synthesis and Characterization of MOFs with Potential for Structural Heterogeneity

Introduction

The concept of 'heterogeneity within order', whereby structurally and chemically different components are brought together to function synergistically within a framework, has arguably been a landmark development in the field of MOFs as a means to construct synthetic materials with unprecedented complexity yet in a controlled manner.[1–7] This combination of complexity and control is something that Nature has successfully harnessed. The archetypal example of enzymes illustrates the concept well, as the active sites have a very well-defined size, shape and arrangement of chemical functional groups. As yet, we as chemists have not approached the capabilities of Nature, though MOFs offer a huge amount of potential to harness some of it. Indeed, MOFs already offer outstanding tunability of the pore metrics, and by extension steric environment. Additionally, a large variety of functional groups may be incorporated and utilized in these materials. The next stage of development, which has only very recently begun, is to introduce structural complexity that cooperates synergistically to achieve a desired property. For instance, a series of MTV-IRMOF-74-III materials were prepared, containing an organic linker with only hydrophobic groups, and another with an aromatic amine.[8] Such a mixed linker system was used to prevent pore blockage during the post-synthetic functionalization of the aromatic amine, which was performed sequentially with amino acid groups to incorporate up to three peptides per linker. This heterogeneous system was found to selectively cleave the serine peptide bond in a pentapeptide. The reaction is known to occur using the enzyme TEV protease, and the proposed mechanism indicates a cooperative effect between aspartate, histidine and cysteine is needed for the reaction to occur. A very specific and selective reaction like this was not possible without the combined influence of the MOF structure and the tripeptide, demonstrating the need for molecular level control of the arrangement of multiple functional groups, and hence heterogeneity within order.

With the goal of developing this area in mind, a series of MOFs containing an array of little-explored functional groups, with a focus on the chemistry of the organic linker rather than the metal cluster, were synthesized and characterized crystallographically. These materials offer the potential for post-synthetic modification to design new materials with molecular level precision of the arrangement of functional groups. This was investigated by the use of (i) phosphonate-based organic linkers which contain three terminal oxygen atoms, per phosphorus atom, each with many orders of magnitude difference in pK_a, (ii) L-aspartate-based linkers with two flexible carboxylate groups and an amide linkage, and (iii) the use of a disulfide group as part of the linker backbone. In particular, the interactions between functional groups and the pore environment were particularly of interest due to the complex nature of the resulting frameworks.

Experimental

Chemicals used in this work. *N,N*-dimethylformamide (DMF) was obtained from Fisher Scientific. (2*S*,2'*S*)-2,2'-(terephthaloylbis(azanediyl))disuccinic acid (H_4BDA) and (2*S*,2'*S*)-2,2'-(([1,1'-biphenyl]-4,4'-dicarbonyl)bis(azanediyl))disuccinic acid (H_4BPDA) were synthesized as described in the literature.[9] All starting materials and solvents, unless otherwise specified, were used without further purification.
Methanol and ethanol (reagent grade) were obtained from EMD Millipore Chemicals. 1-Butyl-3-methylimidazolium tetrafluoroborate (BMIM BF_4, ≥98%), bromine (≥99.99%) , triisopropyl phosphite (95%), tetraphenylmethane (97%), $Pd(PPh_3)_4$ (99%), HCl (37%, aqueous), iodine (>99.8%), *tert*-butyl bromide (98%), benzene (reagent grade), aluminum chloride (99.99%), 4-mercaptobenzoic acid (99%), $Zn(OAc)_2{\cdot}2H_2O$ (>99.999%), sodium hydroxide and sodium bisulfate were purchased from Sigma-Aldrich. N,N-diethylformamide (DEF) was obtained from BASF SE and purified using activated charcoal. 1-bromoadamantange was obtained from VWR International Ltd. Other solvents and reagents were obtained from commercial sources and used without further purification.

Analytical techniques. Single-crystal X-ray diffraction (SXRD) data were collected on beamline 11.3.1 at the Advanced Light Source, Lawrence Berkeley National Lab. Samples were mounted on MiTeGen® kapton loops and placed in a 100(2) K nitrogen cold stream provided by an Oxford Cryostream 700 Plus low temperature apparatus on the goniometer head of a Bruker D8 diffractometer equipped with a PHOTON100 CMOS detector operating in shutterless mode. Diffraction data were collected using synchrotron radiation monochromated using a silicon (111) reflection to a wavelength of 0.7749(1) Å. An approximate full-sphere of data was collected using a combination of phi and omega scans with scan speeds of 2 seconds per 4 degrees for the phi fast scans, and 5 and 15 seconds per degree for the omega scans at 2θ = 0 and -45, respectively. In all cases, the data were processed using the Bruker APEX2 software package,[10,11] structures were solved by intrinsic phasing (SHELXT) and refined by full-matrix least squares on F^2 (SHELXL-2014) using the Olex2 software package.[12] All non-hydrogen atoms were refined anisotropically unless otherwise specified. Hydrogen atoms were geometrically calculated and refined as riding atoms.

Powder X-ray diffraction patterns (PXRD) were recorder using a Bruker D8 Advance diffractometer (Göbel-mirror monochromated Cu K_α radiation λ= 1.54056 Å). Elemental microanalyses (EA) for carbon, hydrogen, nitrogen and sulfur were performed in the Microanalytical Laboratory of the College of Chemistry at UC Berkeley, using a Perkin Elmer 2400 Series II CHNS elemental analyzer. Solution ^{1}H NMR spectra were acquired on a Bruker AVB-400 NMR spectrometer. N_2 sorption isotherms were measured on a Quantachrome Quadrasorb instrument, held at 77 K using a liquid nitrogen bath. Helium was used for the estimation of dead space for gas adsorption measurements. Ultra-high purity grade N_2 and He were used throughout the adsorption experiments.

Synthesis of tetrakis[4-(dihydroxyphosphoryl)phenyl]methane (1). The synthesis route was reproduced from the literature from multiple sources, with minor modifications.[13,14] Briefly, bromine (10 mL, 195 mmol) was added to tetraphenylmethane (9.0 g, 28 mmol) whilst stirring. The reaction was left for 2 h before pouring into ethanol at -78 °C with stirring. This

mixture was then filtered and the resulting solid washed with saturated aqueous $NaHSO_3$, then dried overnight, yielding a white solid, tetra(4-bromophenyl)methane (81.2% yield).

Next, (tetra(4-bromophenyl)methane (2.0 g, 3.1 mmol) was then added to a dried round-bottom flask under N_2 with $Pd(PPh_3)_4$ (90 mg, 0.078 mmol) and triisopropyl phosphite (24 mL, 97.2 mmol). The solution was then heated to reflux for four hours. At this point, additional $Pd(PPh_3)_4$ (90 mg, 0.078 mmol) and triisopropyl phosphite (8 mL, 32.4 mmol) was added, and refluxed for a further 20 hours. Upon cooling, the white crystalline product was filtered and washed with hexane to give the octaethyl ester, tetrakis[4-(diisopropoxyphosphoryl)phenyl]methane (74.3% yield).

^{1}H-NMR ($CDCl_3$) δ = 7.70 (8H, dd, J = 12.9, 8.4 Hz, arom.-H), 7.24 (8H, d, 3.7 Hz, arom.-H), 4.72 (m, arom.-H), 1.37 (24H, d, 6.2 Hz, -CH_3), 1.25 (24H, d, 6.2 Hz, -CH_3) ppm. ^{31}P-{^{1}H}-NMR ($CDCl_3$): δ = 17.4 ppm.

The ester (1.11 g, 1.14 mmol) was then hydrolyzed in aqueous 37% HCl (20 mL) under reflux overnight. The white precipitate was filtered, washed with water and dried, giving tetrakis(4-phosphonophenyl)methane in quantitative yield.
^{1}H NMR ($CDCl_3$) δ = 7.75 (8H, d), 7.29 (8H, d), 4.96 (8H, m).

Synthesis of tetrakis[4-(dihydroxyphosphoryl)phenyl]adamantane (2). The synthesis route was reproduced from the literature from multiple sources, with minor modifications.[13–15] Briefly, 1-bromoadamantane (9 g, 42 mmol) was added to a round-bottom flask with *tert*-butyl bromide (14.3 mL, 127 mmol) and anhydrous $AlCl_3$ (560 mg, 4.2 mmol) in benzene (80 mL) and heated under reflux at 80 °C for 4 h. The precipitate was washed with benzene (50 mL), water (50 mL) and $CHCl_3$ (75 mL) before being dried under vacuum to give tetraphenyladamantane. Next, bromine (10 mL, 195 mmol) was added to tetraphenyladamantane (10 g, 23 mmol) whilst stirring. The reaction was left for 2 h before pouring into ethanol at -78 °C with stirring. This mixture was then filtered and the resulting solid washed with saturated aqueous $NaHSO_3$ (50 mL) and water (100 mL), then dried overnight, yielding a white solid (tetra(4-bromophenyl)adamantane (76.3% yield).

Next, (tetra(4-bromophenyl)adamantane (1.19 g, 1.57 mmol) was then added to a dried round-bottom flask with $Pd(PPh_3)_4$ (45 mg, 0.039 mmol) and triisopropyl phosphite (12 mL, 48.6 mmol). The solution was then heated to reflux for four hours. At this point, additional $Pd(PPh_3)_4$ (45 mg, 0.039 mmol) and triisopropyl phosphite (4 mL, 16.2 mmol) was added, and refluxed for a further 20 hours. Upon cooling, the white crystalline product was filtered and washed with hexane to give the octaethyl ester, tetrakis[4-(diisopropoxyphosphoryl)phenyl]adamantane (63.2% yield).
^{1}H-NMR ($CDCl_3$) δ = 7.78 (8H, dd, J = 12.9, 8.1 Hz, arom.-H), 7.51 (8H, m, arom.-H), 4.66 (dd, 13.5, 6.6 Hz, CH), 2.17 (12H, s, CH_2), 1.35 (24H, d, 6.1 Hz, -CH_3), 1.20 (24H, d, 6.2 Hz, -CH_3) ppm. ^{31}P-{^{1}H}-NMR ($CDCl_3$): δ = 17.4 ppm.

The ester (1.25 g, 1.14 mmol) was then hydrolyzed in aqueous 37% HCl (20 mL) under reflux overnight. The precipitate was filtered, washed with methanol and dried, giving tetrakis(4-phosphonophenyl)adamantane in quantitative yield.

^{1}H NMR ($CDCl_3$): δ = 7.78 (8H, dd, J = 12.9, 8.1 Hz, arom.-H), 7.51 (8H, m, arom.-H), 2.17 (12H, s, CH_2). ^{31}P-{^{1}H}-NMR ($CDCl_3$): δ = 17.4 ppm.

Synthesis of PMOF-1. Stock solutions of 0.2 M $Zn(OAc)_2 \cdot 2H_2O$ and 0.2 M of **3** were prepared in deionized water. Then, the $Zn(OAc)_2 \cdot 2H_2O$ solution (0.5 mL, 0.1 mmol) was mixed with the stock solution of **3** (0.5 mL, 0.1 mmol) with BMIM BF_4 (0.25 mL, 1.3 mmol, heated slightly for easier distribution, into a 20 mL autoclave. The mixture was stirred and placed in the oven at 150 °C for 3 d, giving needle crystals (yield of 37% based on **3**).

Synthesis of PMOF-2. Stock solutions of 0.2 M $Zn(OAc)_2 \cdot 2H_2O$ and 0.2 M of **3** were prepared in deionized water. Then, the $Zn(OAc)_2 \cdot 2H_2O$ solution (0.5 mL, 0.1 mmol) was mixed with the stock solution of **3** (0.5 mL, 0.1 mmol) with BMIM BF_4 (0.25 mL, 1.3 mmol, heated slightly for easier distribution, into a 20 mL autoclave. The mixture was stirred and placed in the oven at 120 °C for 3 d, giving needle crystals (yield of 37% based on **3**).

Synthesis of PMOF-3. Stock solutions of 0.3 M $Zn(OAc)_2 \cdot 2H_2O$ and 0.3 M of phenyl-4,4'-diylbis(phosphonic acid) were prepared in deionized water. Then, the $Zn(OAc)_2 \cdot 2H_2O$ solution (0.25 mL, 0.075 mmol) was mixed with the stock solution of **3** (0.65 mL, 0.20 mmol) and diluted with deionized water (0.1 mL) in a 4 mL scintillation vial. The mixture was stirred and placed in the oven at 100 °C for 3 d, giving large prismatic crystals (yield of 61% based on $Zn(OAc)_2 \cdot 2H_2O$).

Synthesis of 4,4'-dithiobenzoic acid (3). The synthesis route was adapted from the literature.[16] Briefly, to a solution of 4-mercaptobenzoic acid (1.5 g, 9.74 mmol) in ethanol (100 mL), a saturated solution of I_2 in ethanol was added slowly. Iodine was added until a pale yellow color persists in the mixture. The off-white precipitate was filtered and washed with ethanol, then dried at room temperature under vacuum with a yield of 95%.

^{1}H-NMR (DMSO-*d6*): δ = 7.63 (d, 4H, J = 8.2 Hz, arom. -H); 7.93 (d, 4H, J = 8.5 Hz, arom. -H). ^{13}C NMR (DMSO-*d6*): δ = 126.12, 129.70, 130.23, 140.74 (arom. C); 166.58 (CO_2H).

Synthesis of MOF-90. Stock solutions of 0.3 M $Zn(NO_3)_2 \cdot 6H_2O$ and 0.1 M of **3** were prepared in *N,N'*-diethylformamide (DEF). Then, the $Zn(NO_3)_2 \cdot 6H_2O$ solution (65 μL, 0.020 mmol) was mixed with the stock solution of **3** (150 μL, 0.015 mmol) and diluted with 1.45 mL DEF in a 4 mL scintillation vial. The solution was shaken and placed in the oven at 65 °C for 4 d, giving needle crystals (yield of 55% based on **3**).

Synthesis of MOF-91. Stock solutions of 0.1 M $Zn(NO_3)_2 \cdot 6H_2O$ and 0.1 M of **3** were prepared in *N,N'*-diethylformamide (DEF). Then, the $Zn(NO_3)_2 \cdot 6H_2O$ solution (0.6 mL, 0.06 mmol) was mixed with the stock solution of **3** (0.6 mL, 0.06 mmol) and diluted with 0.3 mL

DMF in a 4 mL scintillation vial. The solution was shaken and placed in the oven at 65 °C for 3 d, giving block-shaped crystals (yield of 64% based on **3**).

Synthesis of MOF-705. The synthesis of single crystal MOF was achieved by dissolving the (2*S*,2'*S*)-2,2'-(terephthaloylbis(azanediyl))disuccinic acid (H_4BDA, **4**) in DEF at 0.1 M. To a 4 mL scintillated vial, 2.5 mL of a freshly prepared solution of 10% (v/v) 1.0 M $NaOH_{(aq)}$ in methanol was added. To the methanolic solution, 50 µL of the linker solution was added followed by swirling to homogenize the solution. This was followed by the addition of 50 µL of 1.0 M $Mg(NO_3)_2 \cdot 6H_2O$ solution in DEF. The mixture was shaken briefly and placed in a 50 °C oven until needle shaped crystals precipitated at the bottom and on the walls (as-synthesized) with the dimensions of 0.01 × 0.01 × 0.05 mm^3. The resulting crystals were washed in methanol for four days, three times per day. The solvent was removed by treating with supercritical CO_2 (SC-CO_2). The sample was then activated using dynamic vacuum, first at room temperature for 6 h followed by heating to 70 °C for 6 h. Elemental analysis of the sample activated following SC-CO_2: Calcd. for $Na_8C_{34}H_{34}N_4O_{24}$ = Na_8(**4**)$_2$(methanol)$_2$(H_2O)$_2$: C, 38.27; H, 3.19; N, 5.25. Found: C, 38.12; H, 2.66; N, 5.45%.

Synthesis of MOF-706. The same procedure described above was used, but instead with (2*S*,2'*S*)-2,2'-(([1,1'-biphenyl]-4,4'-dicarbonyl)bis(azanediyl))disuccinic acid (H_4BPDA, **5**) and with heating at 70 °C. The crystals dimensions were 0.05 × 0.05 × 0.03 mm^3. The resulting crystals were washed with methanol three times a day for two days, then with acetone four times a day for two days. To remove the solvent from the MOF, it was treated using SC-CO_2 followed by vacuum at room temperature for 6 h. EA of the SC-CO_2 activated sample: Calcd. for $Na_8C_{34}H_{34}N_4O_{24}$ = Na_8(**5**)$_2$(H_2O)$_4$: C, 36.68; H, 3.53; N, 5.52. Found: C, 36.78; H, 3.59; N, 3.82%.

Results and Discussion

PMOF-1, -2 and -3. Despite tens of thousands of MOFs in existence today, only a handful exists that are built up using only phosphonate-based linkers.[17–22] This likely in part due to the popularity of carboxylate-based MOFs, but there are significant challenges in synthesizing porous and crystalline frameworks due to linker solubility and the tendency to form dense structures.[23] Despite this, phosphonate-based MOFs offer a lot of potential for structural heterogeneity as the three oxygen atoms on phosphonate can coordinate with metals in any protonation state, or may not even coordinate at all. The frameworks are also generally water-stable, with the prominent application of proton conductivity.[18,24] This generally takes advantage of acidic protons that remain as part of the phosphonate linker. Proton conductivity can also be influenced by the presence of counterions within the pores such as imidazolium.[25] Imidazolium is highly acidic due to the presence of heteroatoms adjacent to the neutral carbene, afforded following deprotonation (Scheme 1). It has been found that ionic liquids as a co-solvent with water are beneficial for the synthesis of phosphonate-based frameworks,[26] as has been previously shown in zeolites and related materials.[27]

Scheme 5.1. Depiction of the deprotonation of BMIM, forming a carbene stabilized by heteroatoms.

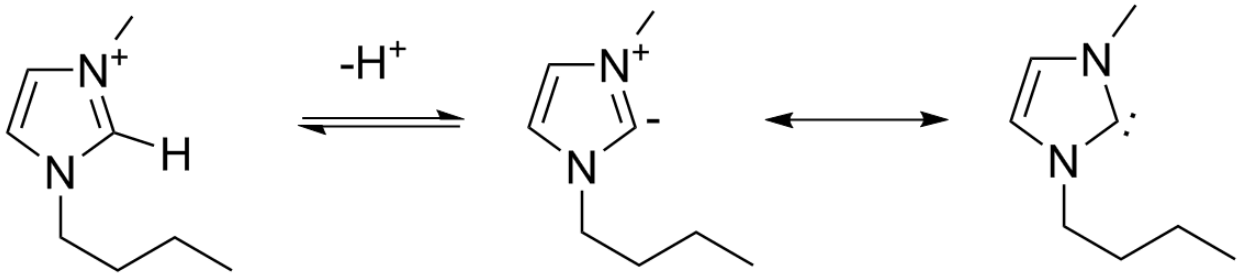

To overcome the typically dense, 2D frameworks that are more commonly observed in phosphonate-based frameworks, two tetratopic linkers, tetrakis(4-phosphonophenyl)methane (**1**) and its isoreticular expansion with an adamantane core, tetrakis(4-phosphonophenyl)adamantane (**2**), were synthesized (Scheme 2). These linkers are designed to provide a rigid unit that, along with a roughly tetrahedral geometry, would lead to a 3D framework with cavities.

Scheme 5.2. Synthesis route for tetrakis(4-phosphonophenyl)methane (**1**). Note that the same synthesis route was employed for tetrakis(4-phosphonophenyl)adamantane (**2**).

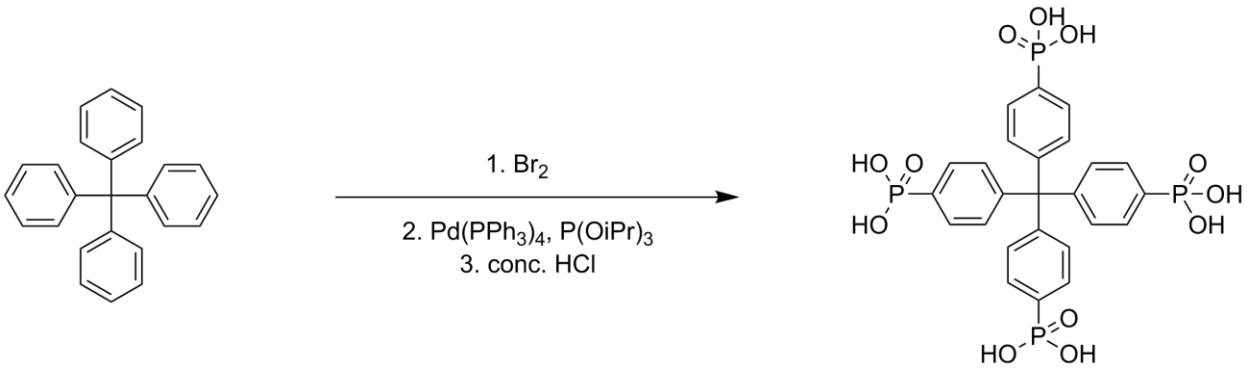

A total of three new MOFs based on phosphonate linkages have been synthesized, two of which (PMOF-1 and -2) are 3D while the last (PMOF-3) is a 2D extended framework. PMOF-2 crystallizes in the space group *P*-1, with two independent linkers, four zinc atoms and two BMIM cations in the asymmetric unit (Figure 5.1). All phosphonate groups coordinate to zinc through two oxygen atoms. Three of the four phosphonate groups on both linkers possess a charge state of -1 with only one deprotonated hydroxyl group, while the final phosphonate moiety is fully deprotonated. The secondary building unit (SBU) is a 1D rod of tetrahedral zinc atoms joined by O-P-O units. The structure contains perpendicular channels of around 6.5 Å diameter atom-to-atom. Within these channels, both BMIM and water molecules are present. Since not all phosphonate hydroxyl groups are deprotonated, the 1D SBU also has a hydrogen bonding network that links the phosphonate groups to each other, and to the water molecules in the channels. In combination with the imidazolium cation in the pore, these acidic protons provide a potentially effective way of carrying charge by proton conductivity. Their protonation states are determined by the P-O bond length, with a single bond being around 1.56 Å compared to 1.51 Å for a double bond, with confirmation of the presence of hydrogen atoms from the Fourier difference map where possible.

PMOF-1 crystallizes in the space group *C*2/*c*, with two zinc atoms but only one linker and one BMIM cation in the asymmetric unit (Figure 5.1). Similarly however, three of the phosphonate groups on the linkers have one deprotonated hydroxyl, while the last moiety has both deprotonated and all three oxygen atoms in the phosphonate group coordinating to zinc atoms. The main structural difference is that the channels, which are around 6.1 Å atom-to-atom do not intersect perpendicular to one another, but are only present parallel with the 1D SBU. However, the water and phosphonate hydroxyl group hydrogen bonding network is still present, and a comparison of the proton conductivity properties of both could shed light on the effect that the channel orientation has on such properties.

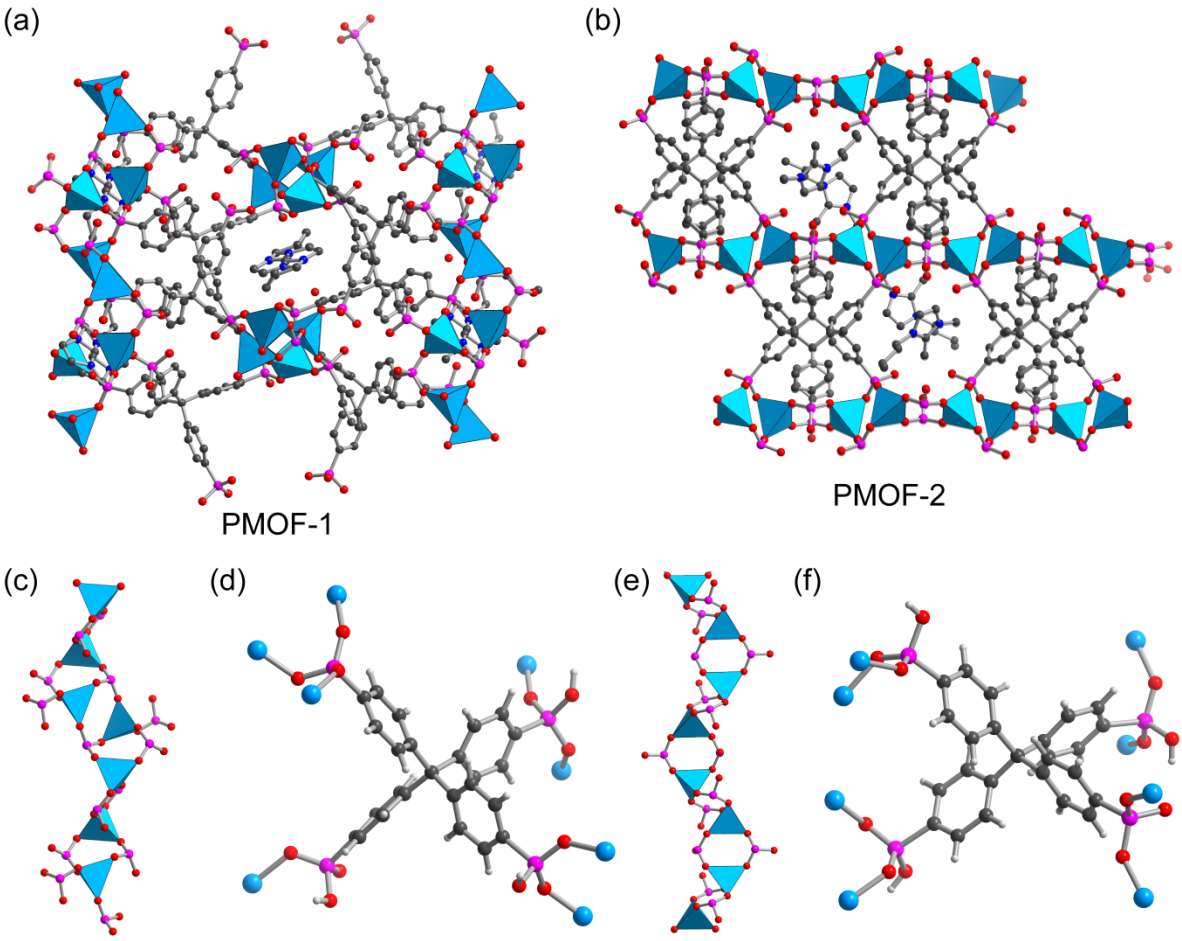

Figure 5.1. (a) and (b) show the overall 3D structure of PMOF-1 and PMOF-2 respectively. The main difference in how the structures extend are the alternating 1D SBUs which are perpendicular to each other in PMOF-1, but are parallel in PMOF-2. BMIM lines the channels of both frameworks. (c) and (e) depict the 1D SBUs of PMOF-1 and PMOF-2 respectively, while (d) and (f) display how the linkers are coordinated to zinc. In the case of PMOF-1 (d), there are three types of coordination mode: monodentate, bidentate and tridentate, with the first two modes leaving a dangling hydroxyl group. For PMOF-2 (f), All modes are bidentate, with three of the four phosphonate groups leaving room for a dangling hydroxyl group. Hydrogen atoms were omitted for clarity, except in (d) and (f). Color scheme is as follows: Zn, blue or blue polyhedral; C, black; O, red; N, green; H, white.

PMOF-3, with its ditopic linker, forms 2D sheets of tetrahedral zinc atoms bridged by phosphonate groups (Figure 5.2). These sheets are interacting through hydrogen bonds of the phosphonate hydroxyl groups that remain protonated, thus acting as the donor groups. The dense nature of this structure may well be a result of the large number of interactions between adjacent phosphonate groups as well as the T-shape pi stacking that occurs between phenyl rings. The larger tetrahedral linkers used in the synthesis of PMOF-1 and -2 force such groups apart and perhaps makes linker packing less efficient compared with phenyl-4,4'-diylbis(phosphonate), thus allowing the formation of cavities filled with solvent. This dense packing issue may be less significant with carboxylate-based MOFs since the carboxylate groups are almost always fully

deprotonated and coordinating to metals, precluding additional interactions observed with phosphonate-based linkers. Indeed, PMOF-3 does not contain cavities, although water molecules are involved in the hydrogen bonding network between sheets.

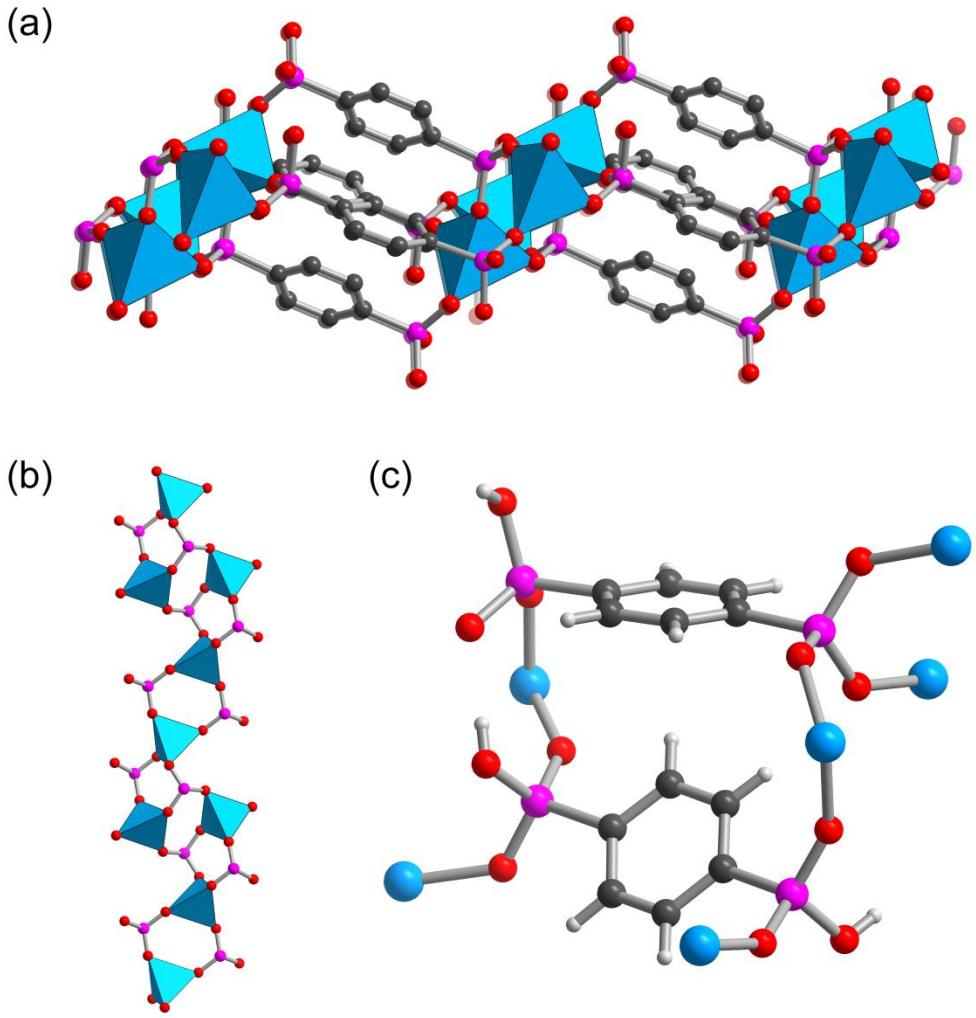

Figure 5.2. (a) Representation of the 2D sheet formed in PMOF-3, with the linker bridging 1D SBUs. (b) Shows the connectivity of the 1D SBU, with phosphonate groups bridging zinc atoms. The coordination environment of the two types of linkers in PMOF-3 is shown in (c), with one linker containing a triply bridging phosphonate group that is fully deprotonated, with the opposite side monodentate, with a dangling oxygen and hydroxyl group. Both phosphonate groups in the second linker are doubly bridging, with each encompassing a dangling hydroxyl unit. As with PMOF-1 and PMOF-2, BMIM lines the channels, in this case between the 2D sheets to complete charge-balancing.

The bulk purity of the structures was confirmed by PXRD (Figure 5.3). However, in the case of PMOF-2, the experimental powder pattern is a poor match for the simulated one, even though the crystals in the sample appear as uniform needles in what appears to be pure phase from visualization under the optical microscope. The differences could potentially be from a phase change since the PXRD pattern was collected at room temperature and the single crystal

structure at 100 K, but more investigation is needed. Additionally, the reflections for PMOF-3 have some discrepancy in intensity between the simulated and experimental structures despite reflection positions matching. This is most likely due to preferred orientation of the needle-shaped crystals. For instance, the third reflection, (100), is particularly intense compared to the simulated pattern. This could be because the crystals are mostly lying on the long edge of the needle, and thus the (100) reflection is overrepresented in diffraction conditions compared to the others. In light of the similarity of the structures of PMOF-1 and -2 but the uncertainty on bulk purity for the latter, the properties of PMOF-1 were investigated.

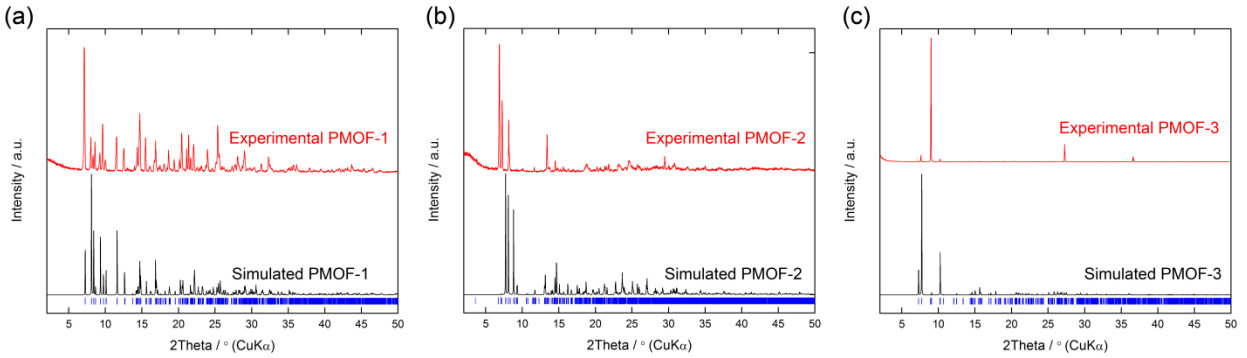

Figure 5.3. Powder X-ray diffraction (PXRD) patterns of PMOF-1 (a), -2 (b) and -3 (c) with the simulated pattern in black and the experimental pattern in red. The differences in reflection intensity are attributed to preferred orientation of the needle and plate-shaped crystals.

Following evacuation of the pores at 150 °C under dynamic vacuum, no measurable surface area was observed from N_2 sorption at 77 K despite retention of crystallinity. This is not surprising due to the relatively small pores and the presence of the BMIM counterions within them. However, PMOF-1 does take a moderate amount of water, with up 27 cm^3 g^{-1} measured at 25 °C and saturated humidity (Figure 5.4). Considering the stability of this MOF in water, in which it is synthesized, the hydrogen bonding network and imidazolium cations, this material has promising potential for proton conductivity.

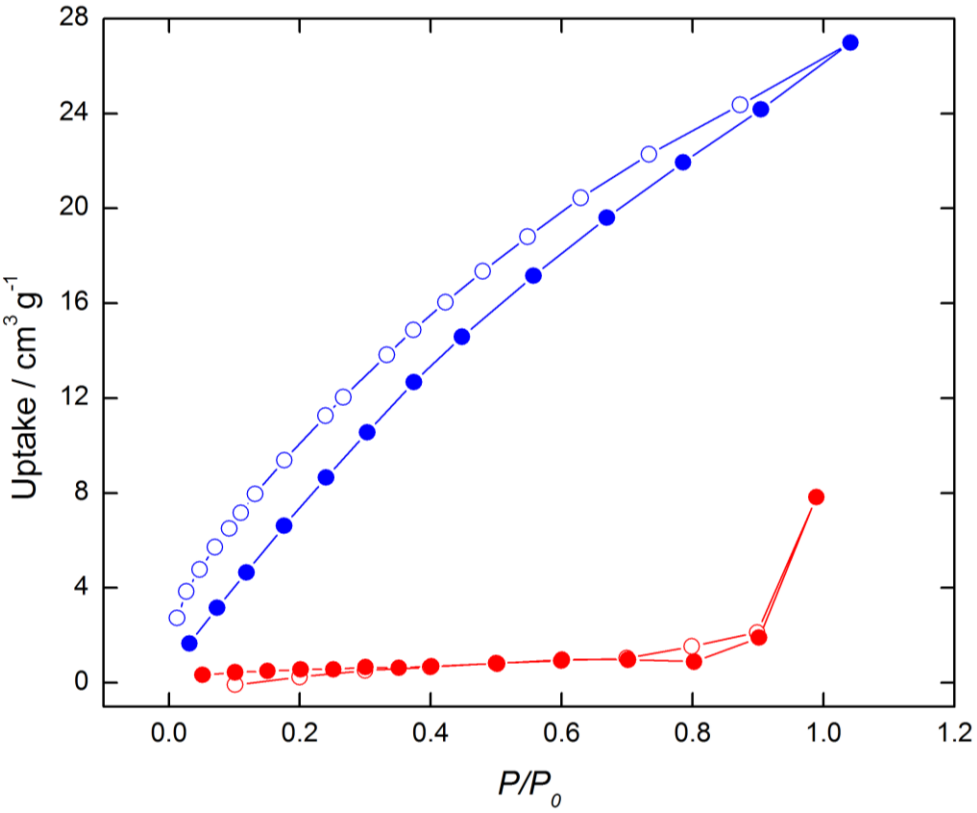

Figure 5.4. Comparison of the H_2O uptake at 298 K (blue) with the N_2 uptake at 77 K (red) for PMOF-1. Despite having no significant N_2 uptake, and so no significant internal surface area based on N_2 adsorption, PMOF-1 displays moderate H_2O uptake.

MOF-705 and -706. Two isoreticular sodium-based MOFs, termed MOF-705 and -706 and with the formulae $[Na_4(BDA)(CH_3OH)(H_2O)]$ and $[Na_4(BPDA)(CH_3OH)(H_2O)_2]$ respectively (BDA = 1,4-benzenedicarboxylate, BPDA = (1,1'-biphenyl)-4,4'-dicarboxylate), which contain a unique 2D secondary building unit were characterized by single crystal X-ray diffraction. Their syntheses afforded needle-shaped colorless single crystals with the dimensions of 0.01 × 0.01 × 0.05 mm^3 for MOF-705 and 0.005 × 0.005 × 0.03 mm^3 for MOF-706. MOF-705 crystallizes in the chiral monoclinic $P2_1$ space group bearing the infinite 2D sodium oxide sheets extended in the [100] and [010] directions (Figure 5.5a), with a repeat unit of four edge-sharing sodium atoms (Figure 5.5b). The first of these has square pyramidal geometry (Na(1)), while the two in the middle are distorted trigonal bipyramids (Na(2) and Na(3)), and the last is a distorted octahedron (Na(4)). All the coordinating moieties are structural (an integral part of the MOF backbone) except for the octahedral Na(4), which is completed by the coordination of one methanol molecule. The Na(1) centers are bridged by two μ^2 water molecules in the [100] direction (Figure 5.5b), while μ^3 carboxylates connect all sodium atoms in the [010] direction. Completing the 3D structure, the linker joins these sodium oxide sheets in the [001] direction. The same applies for MOF-706, except that water molecules replace methanol coordinated to Na(4). MOF-706 is the isoreticularly expanded form, whereby the structure remains identical,

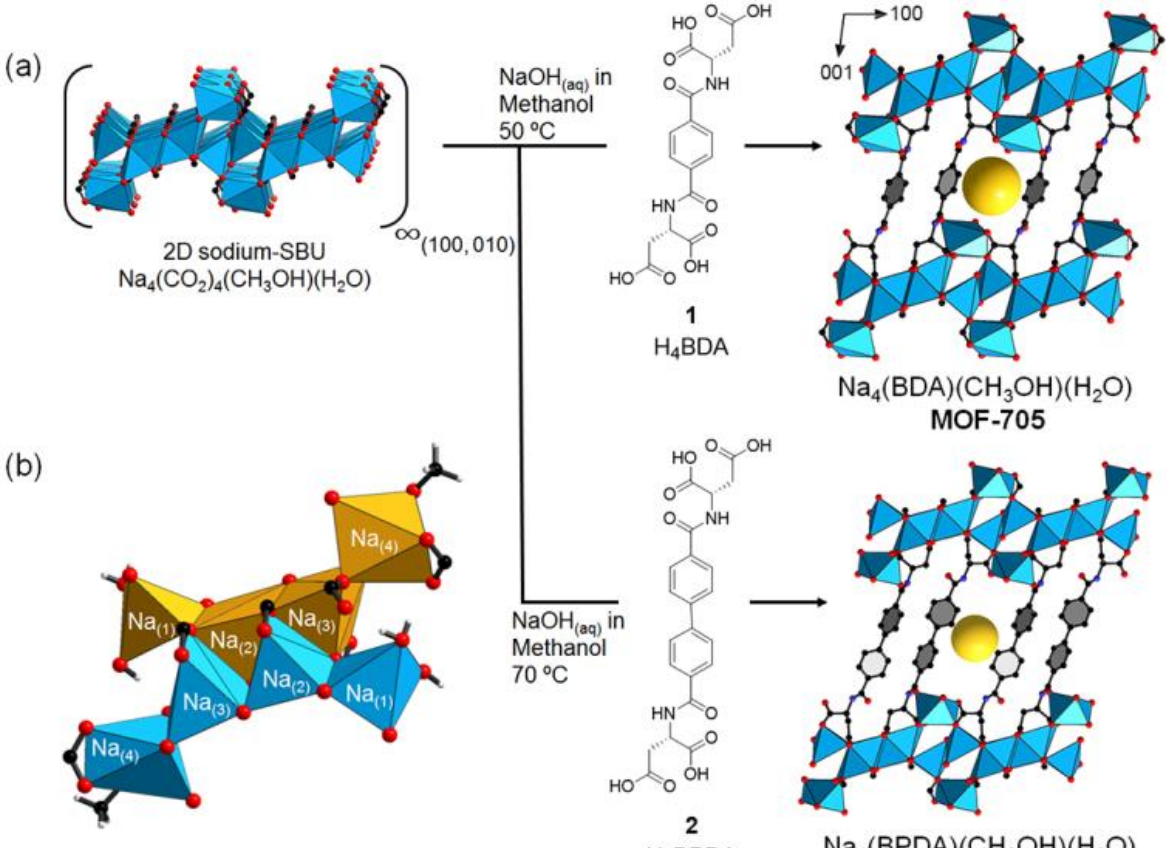

Figure 5.5. (a) Description of synthesis conditions and structures of MOF-705 and its isoreticular expansion, MOF-706. The frameworks are made up of 2D sodium oxide sheets joined together by organic linkers, H_4BDA and H_4BPDA respectively. (b) Two sets of the repeat unit ($Na_{(1)}$ – $Na_{(4)}$) forming the sodium oxide sheets.

save in this case for the terminal ligands completing the coordination sphere of sodium.

MOF-705 was immersed in a variety of organic solvents to explore the most suitable activation conditions. However, conventional methods to remove solvent from the pores were not successful, so supercritical CO_2 (SC-CO_2) activation from methanol was used.This yielded a crystalline material that was air stable for over a month in ambient conditions, as proven by PXRD and scanning electron microscopy (SEM). SXRD experiments showed that methanol is still coordinated after this treatment, but can be removed to widen the pores by simply heating the SC-CO_2 activated sample at 70 °C under vacuum for 6 h. Note that further characterization work was performed, in particular related to CO_2 separation from N_2, which are included in the published manuscript.[9]

MOF-90 and -91. Using the disulfide-based carboxylate linker 4,4'-dithiobenzoic acid (H_2DTB), two new zinc-based MOFs were synthesized and termed MOF-90 and -91. MOF-90 is built with an SBU that is similar to that of MOF-5, with a Zn_4O unit.[28] However MOF-90 has one octahedral zinc atom, with two terminal DEF molecules, and three tetrahedral zinc atoms in contrast with MOF-5 that has all four zinc atoms as tetrahedral. Besides the aforementioned terminal DEF molecules, each zinc atom is coordinated to oxygen atoms from μ^2-bridging carboxylate groups on the linker (Figure 5.6). The octahedral zinc atom causes some distortion of the linker extension, breaking the otherwise 3-fold symmetry. These units form 1D chains due to the 81.56(19)° C-S-S-C torsion angle observed as part of the linkage, causing the linker to turn in on itself. These chains pack together through van der Waals interactions between the disulfide unit and a phenyl ring from an adjacent chain, as well as between the coordinated DEF molecules and the linker. More DEF molecules fill the cavities between chains.

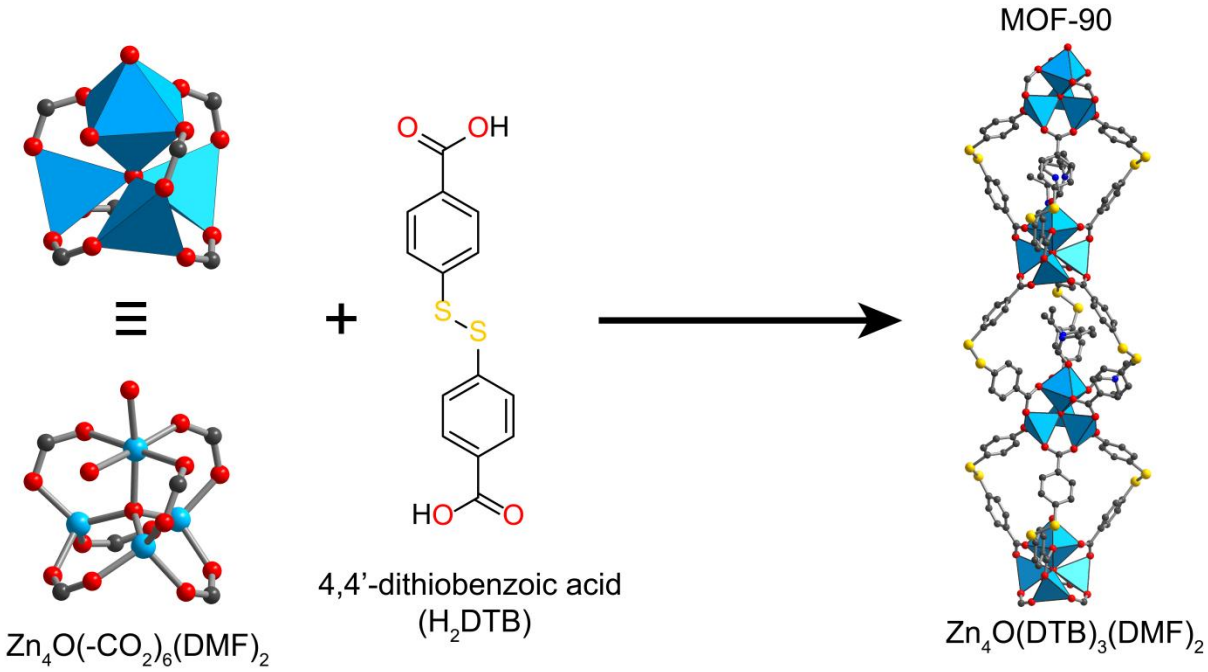

Figure 5.6. Synthesis of MOF-90, displaying the SBU and linker of the MOF. The framework extends as 1D chains, with the linker bending in on itself to link up adjacent zinc-based clusters.

MOF-91 has a 1D SBU, this time with the linker maintaining a C-S-S-C torsion angle of 81.11(6)°, but the linker instead bridges two 1D SBUs (Figure 5.7). The framework also has tetrahedral and octahedral zinc atoms in the SBU, but here they alternate, with two tetrahedral zinc atoms parallel with one another, and one octahedral zinc atom linked to them through two μ^3-OH groups and four μ^2-carboxylate units from the linker. The hydroxyl groups alternate above and below the plane of the SBU, and are hydrogen bonded to DMF in the square-shaped cavity of around 10 Å in diameter atom-to-atom. This forms a 2D sheet, stacking on top of one another through a parallel π stacking configuration. There are also van der Waals interactions between the disulfide units and the SBUs and linkers from adjacent sheets.

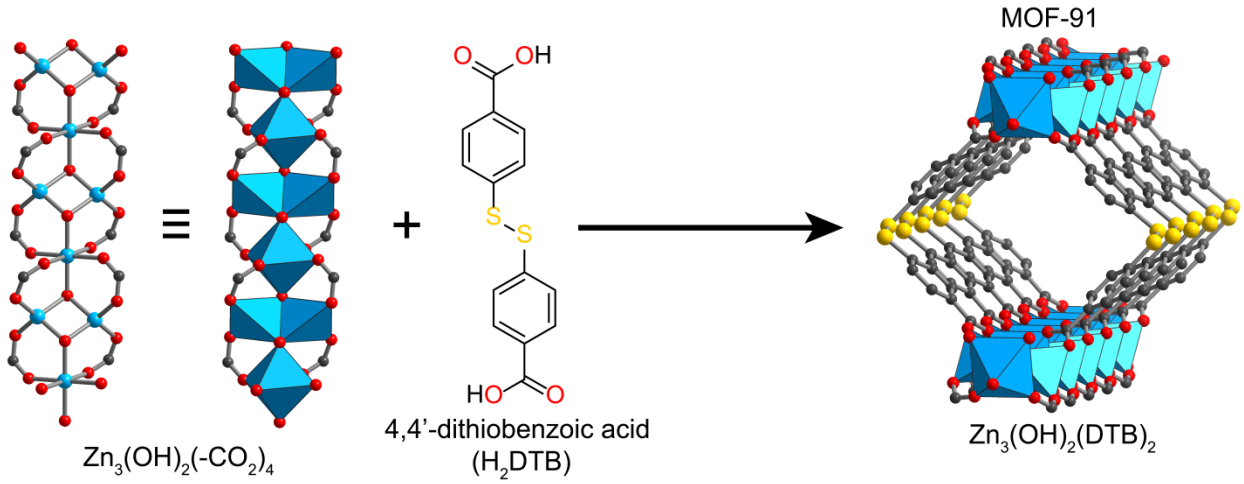

Figure 5.7. Synthesis of MOF-91, displaying the 1D SBU and linker of the MOF. The framework extends as 2D sheets, with the linker bending in on itself to link up adjacent zinc-based clusters.

These frameworks are intriguing as they offer functionalities with quite different chemical stabilities. Many MOFs can be broken down through hydrolysis of the metal-carboxylate position, either in water or under acid or basic conditions. This destroys the entire framework, including the SBU. To determine framework stability, MOF-91 was immersed in DMF, methanol, acetone, chloroform and water. In all but water, the framework remains intact as determined by PXRD. In the latter, a phase change occurs that remains undetermined. However, the disulfide unit offers an alternative method of cleaving the framework without also breaking down the SBU by reduction to thiol. Reducing conditions can be such that the metal-carboxylate bond remains intact. The bond dissociation energy of 1,1'-disulfanediyldibenzene, essentially the linker used here without the carboxylate groups, has a bond dissociation energy of 55 kcal mol^{-1}, or 520 nm, and so could alternatively be cleaved by light irradiation.[29,30] Preliminary attempts at bond cleavage have been attempted, including by addition of $NaBH_4$ in a 1:1 ratio with the linker in DMF. The former, after leaving MOF-91 for 3 days in the solution, appears stable with no change to the PXRD pattern. An excess of $NaBH_4$ was also investigated with the same result. The alternative of bond cleavage through exposure to UV light (365 nm) was attempted, and this also maintained structural integrity following overnight exposure (Figure 5.8). This may be because, following cleavage, the thiolate groups remain aligned adjacent to each other due to the large number of other disulfide groups nearby, holding the framework in place. This would allow for easy oxidation back to a disulfide unit, which occurs slowly under oxidizing atmospheric conditions. To counteract this, benzenethiol was added to the mixture, however this disintegrated the framework.

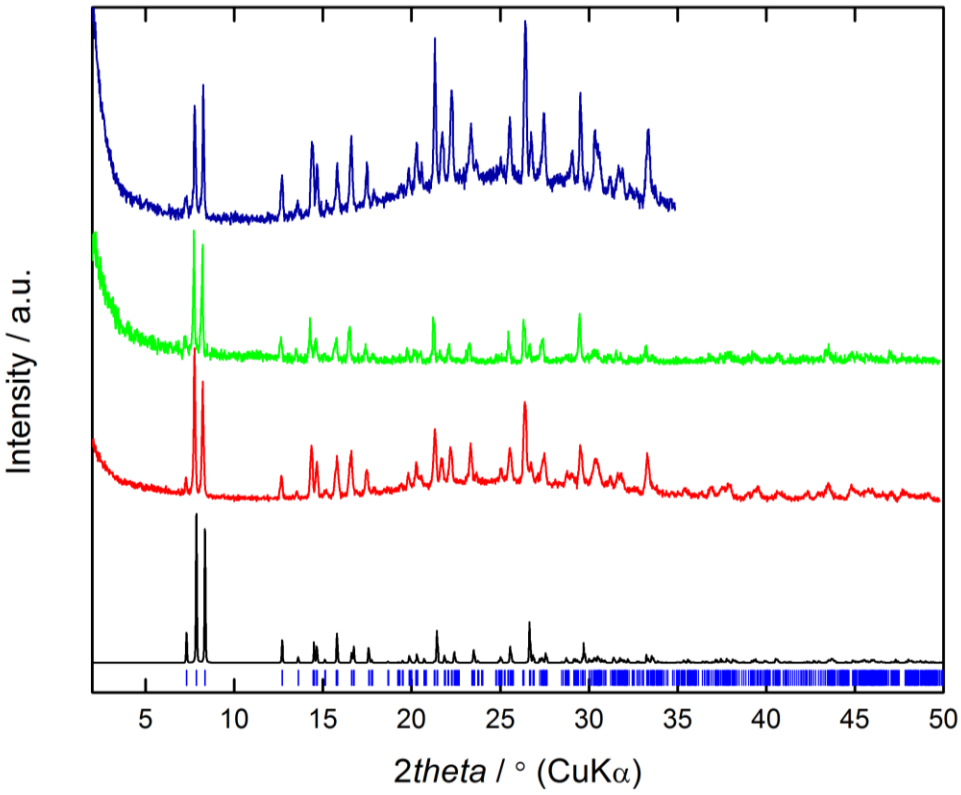

Figure 5.8. Powder X-ray diffraction (PXRD) patterns of MOF-91 simulated from single crystal data (black), experimental as-synthesized (red), after treatment with excess $NaBH_4$ in DMF overnight (green), and after UV irradiation at 365 nm overnight in DMF (dark blue). Neither treatment broke down the MOF structure.

Conclusion

The work shown herein demonstrates the diversity that can be obtained from using unconventional linkers, including amide-based and disulfide-containing carboxylate linkers, and even phosphonate-based linkers which offer water stability and multiple binding modes with each approach discussed offers the potential for unique properties. For instance, the phosphonate-based MOFs, PMOF-1 through 3, are water-stable and have dangling hydroxyl groups that are non-coordinating. The acidity and hydrogen bonding network of these groups are potentially crucial for proton conduction, and offer Brønsted acidity that could be used for catalytic conversions. The use of a tetrahedral building unit is an approach that can overcome the problem with other known phosphonate MOFs of a dense, non-porous structure that precludes diffusion of species through the pores.

MOF-90 and -91, with the disulfide link, have shown to be successful in the synthesis of MOFs with non-linear linkers. However, what is perhaps the most exciting possibility for these frameworks is to take advantage of the radically different chemistry of the functional groups in the system to selectively cleave the disulfide bond, leaving the Zn-O bond, and therefore the metal cluster, intact. Such a transformation could then be utilized to construct new MOFs by linking up different metal clusters, or clusters comprised of different metals, to create new materials that could not be synthesized under solvothermal conditions. A further exciting possibility is to cleave the disulfide bond and recrystallize the metal clusters. This would be particularly interesting in the case of MOF-91 since the SBU is a 1D rod. Thus, cleaving the disulfide unit would result in a chemically well-defined nanorod based on zinc oxide, a known semiconductor. This approach could potentially be expanded to other metals such as indium, which are also appealing as semiconductors or entirely different uses.

MOF-705 and -706, which are made up of linkers containing four carboxylate groups joined to a flexible alkyl chain, along with an amide unit, demonstrate how the use of multiple coordinating groups can stabilize sodium-based frameworks which otherwise typically collapse. These units can be readily synthesized using L-aspartate groups that could in principal be replaced by other amino acids for further modifications to the incorporated functional groups.

Each series of MOFs has its own unique characteristics, yet all are united by the same principle: the introduction of heterogeneity into frameworks exponentially increases the richness of the chemistry in the material. To take full advantage of this, a careful structural study is necessary to relate the framework and chemical features to the resulting properties of the material. It is hoped this study will facilitate a greater understanding of the chemistry of extended frameworks at a molecular level as well as being a springboard to the development of the next generation of materials.

Appendices and Notes

Acknowledgements. I would like to thank Dr. Peter Siman for synthesizing MOFs-705 and -706, as well as preparing the L-aspartate linkers and helpful discussions. I also thank Dr. S. Teat, Dr. Kevin J. Gagnon and Dr. Laura McCormick for support during the synchrotron X-ray diffraction data acquisition support at the beamline 11.3.1 (Advanced Light Source, Lawrence Berkeley National Laboratory). I further thank Kevin for initiating the phosphonate project and for conceiving and discussing this idea, Bing Zhang for help with organic synthesis, Hoe Wan for synthesis optimization and assisting with MOF-90 and -91 synthesis. Work performed at the Advanced Light Source is supported by the Director, Office of Science, Office of Basic Energy Sciences, of the U.S. Department of Energy under Contract No. DE-AC02-05CH11231.

Single crystal X-ray diffraction data for PMOF-1, -2, -3

Table 5.1. Crystallographic data of PMOF-1, PMOF-2 and PMOF-3.

Sample	**PMOF-1**	**PMOF-2**	**PMOF-3**
chemical formula	$Zn_4\,C_{57}\,H_{38}\,N_2\,O_{25.67}\,P_8$	$Zn_4\,C_{68}\,H_{72}\,N_4\,O_{32}\,P_8$	$Zn_4\,C_{41}\,H_{31}\,N_4\,O_{30}\,P_8$
formula mass	1670.85	1966.53	1568.94
crystal system	monoclinic	triclinic	triclinic
space group	*C*2/*c*	*P*-1	*P*-1
λ [Å]	0.77490	0.77490	0.77490
***a* [Å]**	21.1539(12)	12.3855(6)	10.4577(6)
***b* [Å]**	12.8789(7)	14.0745(6)	12.6906(7)
***c* [Å]**	25.2924(14)	25.4514(12)	13.1577(7)
α (degrees)	90	95.282(2)	69.191(2)
β (degrees)	105.008(3)	100.630(2)	75.256(2)
γ (degrees)	90	108.328(2)	70.937(2)
Z	4	2	1
***V* [Å^3]**	6655.6(6)	4085.4(3)	1523.73(15)
T [K]	100	100	100
density [g cm^{-3}]	1.667	1.599	1.710
measured reflections	43985	89526	52896
unique reflections	6827	25026	11074
parameters	454	1072	513
restraints	6	1	7
R_{int}	0.0680	0.0382	0.0265
θ range (degrees)	2.04 – 29.02	2.09 – 33.69	2.23 – 35.95
R_1, wR_2	0.0582, 0.1661	0.0575, 0.1668	0.0292, 0.0828
S (GOF)	1.096	1.026	1.040
max / min res. dens. [e Å^{-3}]	1.10 / -0.68	1.10 / -0.93	1.14 / -0.87

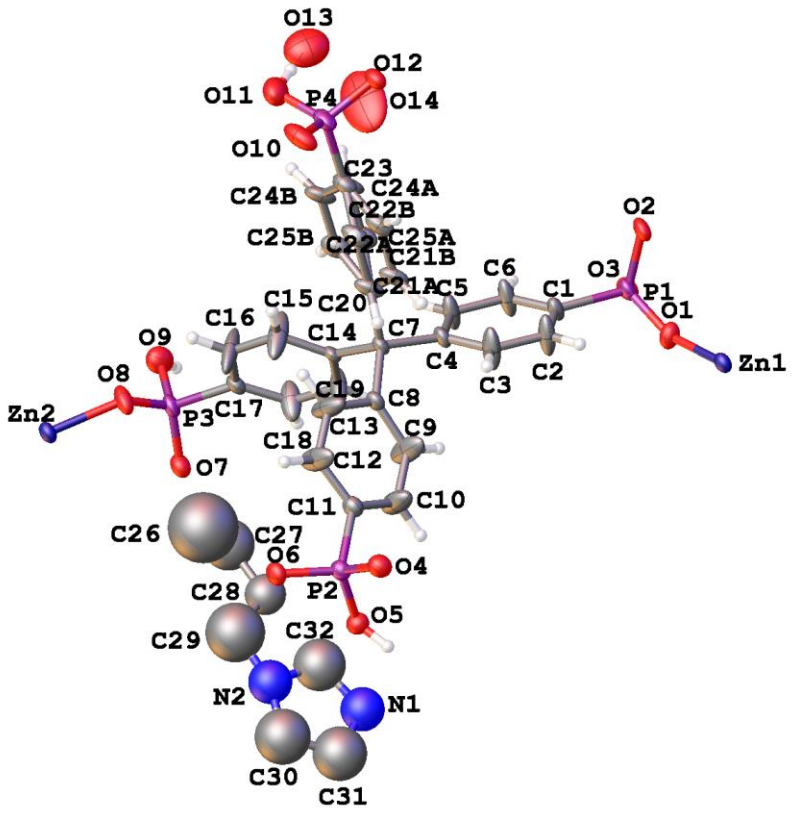

Figure 5.9. Asymmetric unit of PMOF-1.

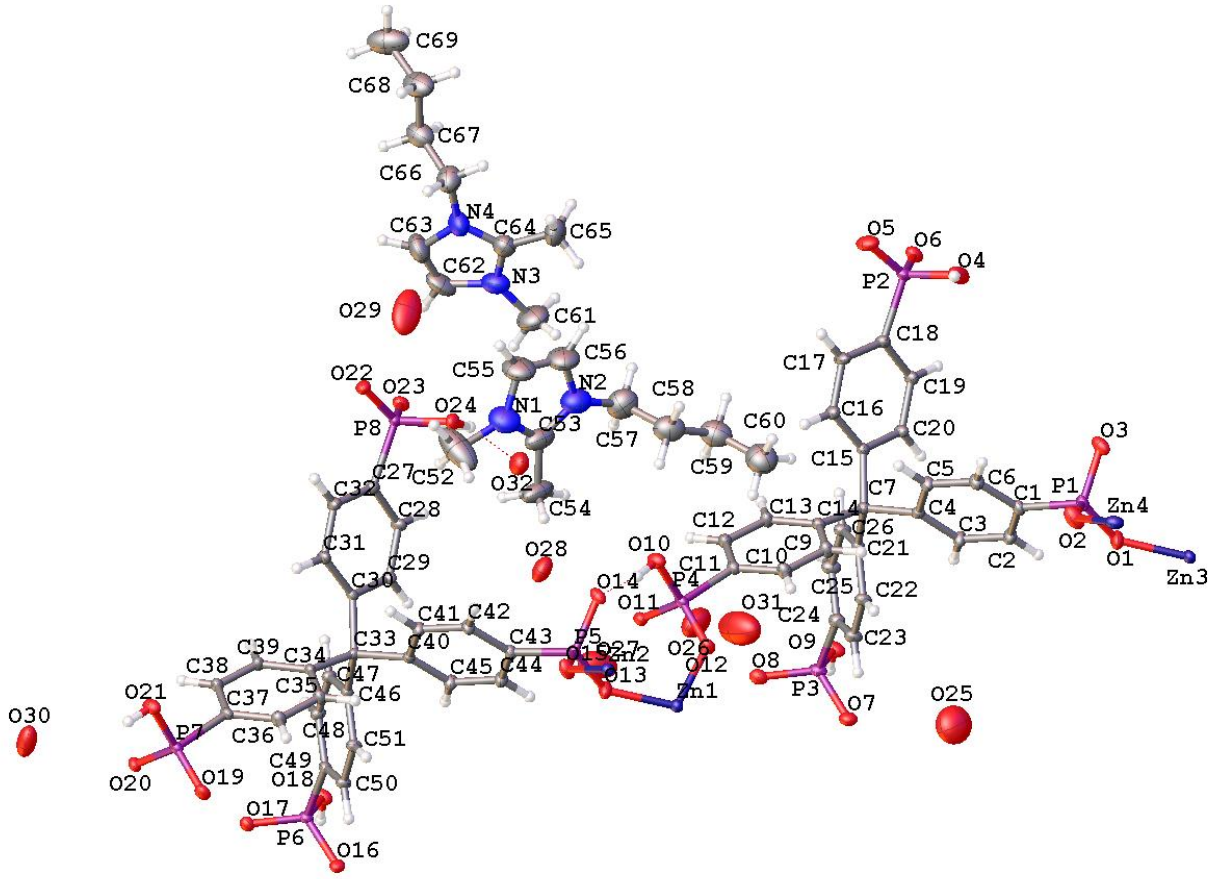

Figure 5.10. Asymmetric unit of PMOF-2.

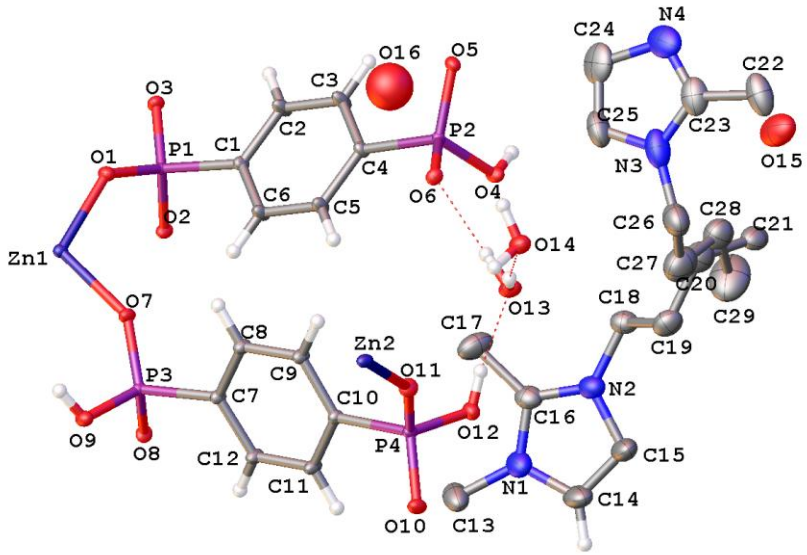

Figure .5.11. Asymmetric unit of PMOF-3

Single crystal X-ray diffraction data for MOF-90 and -91

Table 5.2. Crystallographic data of as-synthesized MOF-90 and MOF-91.

Sample	**MOF-90**	**MOF-91**
chemical Formula	$Zn_{16}\ C_{248}\ H_{265}\ N_{16}\ O_{68}\ S_{24}$	$Zn_3\ C_{34}\ H_{32}\ N_2\ O_{12}\ S_4$
formula mass	6373.10	984.96
crystal system	monoclinic	triclinic
space group	*C2/c*	*P*-1
λ [Å]	0.77490	0.77490
***a* [Å]**	33.5511(16)	6.2337(3)
***b* [Å]**	23.8501(12)	12.4396(5)
***c* [Å]**	21.5671(11)	13.1628(6)
α (degrees)	90	66.888(2)
β (degrees)	127.822(2)	89.256(2)
γ (degrees)	90	79.774(2)
Z	2	1
***V* [Å^3]**	13632.4(12)	922.06(7)
T [K]	100	100
density [g cm^{-3}]	1.553	1.774
measured reflections	90546	22006
unique reflections	14032	6691
parameters	924	255
restraints	210	1
R_{int}	0.0840	0.0309
θ range (degrees)	2.15 – 29.08	3.19 – 35.94
R_1, wR_2	0.432, 0.1088	0.0240, 0.0644
S (GOF)	1.007	1.021
max / min res. dens. [e Å^{-3}]	0.85 / -0.61	0.77 / -0.55

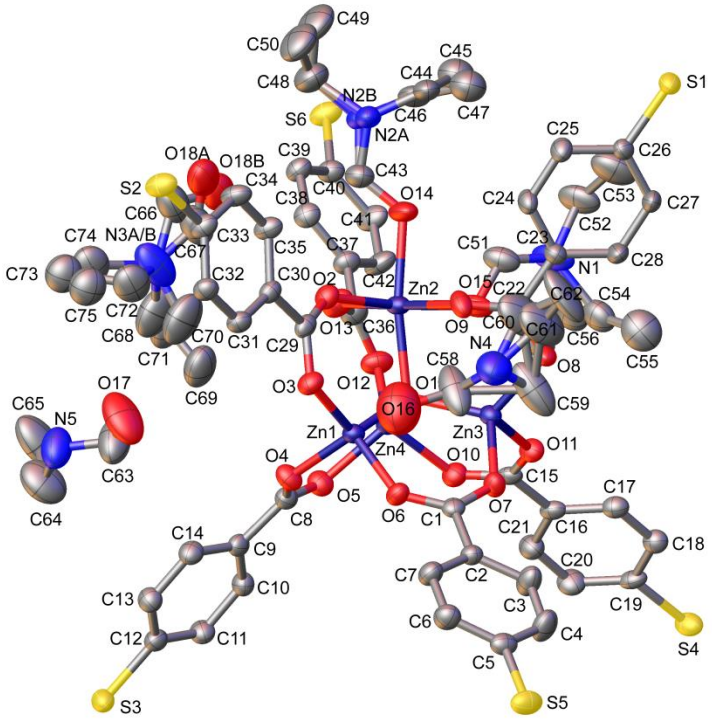

Figure 5.12. Asymmetric unit of MOF-90.

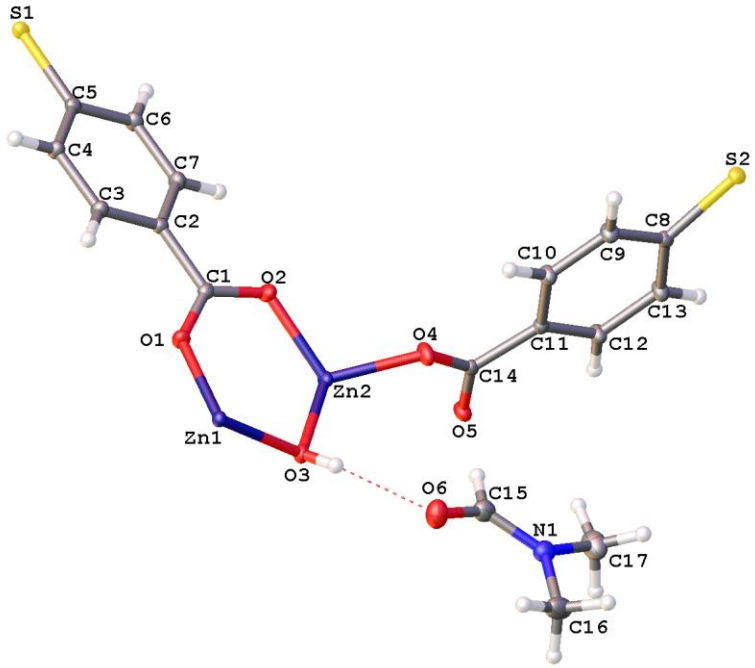

Figure 5.13. Asymmetric unit of MOF-91.

Single crystal X-ray diffraction data for MOF-705 and 706

Table 5.3. Crystallographic data of MOF-705 and MOF-706, both as-synthesized and after supercritical CO_2 exchange.

Sample	MOF-705_as	MOF-705_sc	MOF-706_as	MOF-706_sc
chemical formula	C_{17} H_{18} N_2 Na_4 O_{12}	C33.08 H33.70 N4 Na8 O25.71	$C_{22.5}$ H_{18} N_2 Na_4 O_{12}	C22.25 H19.25 N2 Na4 O11.5
formula mass	534.29	1082.58	618.87	590.61
crystal system	monoclinic	monoclinic	monoclinic	monoclinic
space group	$P2_1$	$P2_1$	$P2_1$	$P2_1$
λ [Å]	1.54178	0.77490	0.88560	1.03330
***a* [Å]**	11.8894(4)	24.0448(19)[a]	12.0790(15)	11.9807(16)
***b* [Å]**	5.2299(2)	5.2432(5)	5.2419(6)	5.2345(6)
***c* [Å]**	17.4663(5)	16.9833(14)	21.254(3)	21.796(3)
β (degrees)	97.279(2)	103.366(6)	103.886(6)	99.274(10)
Z	2	2	2	2
***V* [Å^3]**	1077.3(1)	2083.1(3)	1306.4(3)	1349.1(3)
T [K]	100(2)	100(2)	100(2)	100(2)
density [g cm^{-3}]	1.647	1.726	1.573	1.454
measured reflections	23262	18857	7646	6359
unique reflections	4415	4815	1594	1980
parameters	334	623	327	345
restraints	34	19	106	130
R_{int}	0.0889	0.1078	0.1134	0.1002
θ range (degrees)	2.55 - 74.52	2.568 – 23.539	2.164 - 21.724	2.504 – 28.238
R_1, wR_2	0.0415, 0.0965	0.0684, 0.1878	0.0721, 0.2093	0.1176, 0.3174
S (GOF)	1.037	1.009	1.007	1.273
max / min res. dens. [e Å^{-3}]	0.366 / -0.241	0.692 / -0.346	0.535 / -0.457	0.732 / -0.673

[a]the unit cell is doubled due to superstructure in which water and methanol coordinate to Na(4) alternatively.

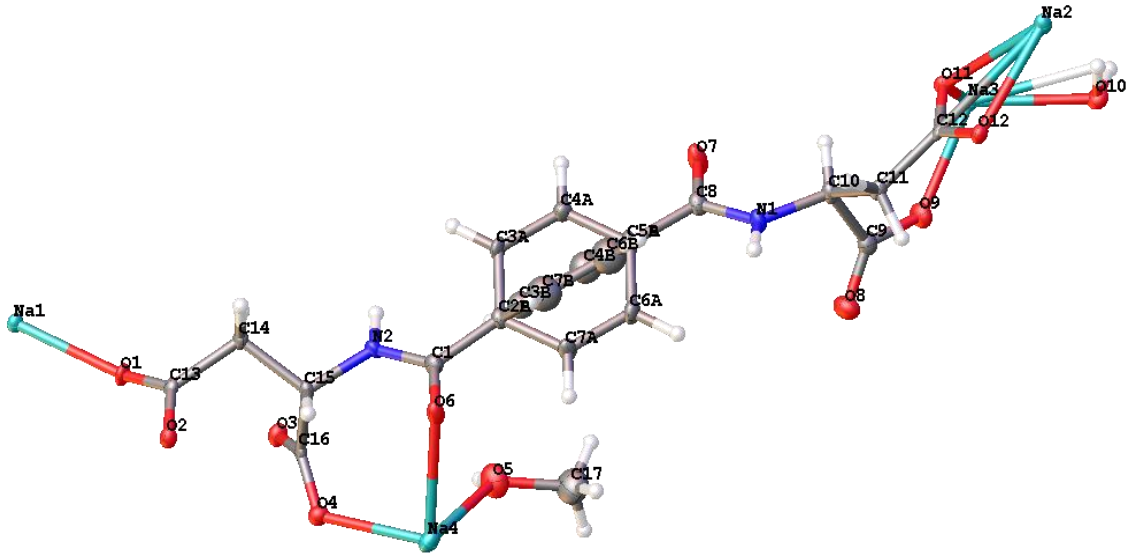

Figure 5.14. Asymmetric unit of MOF-705_as.

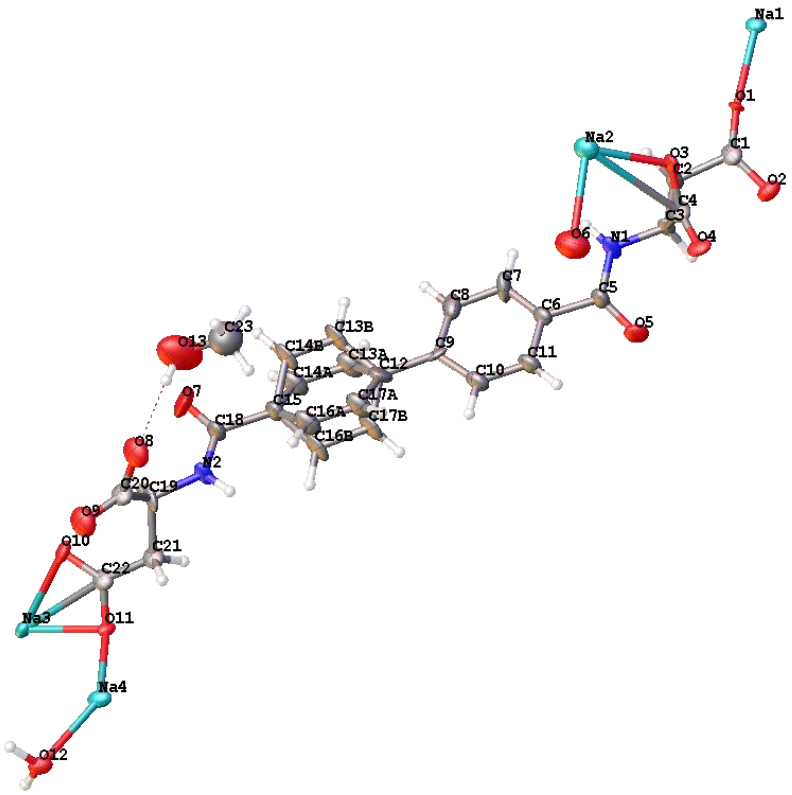

Figure 5.15. Asymmetric unit of MOF-706_as.

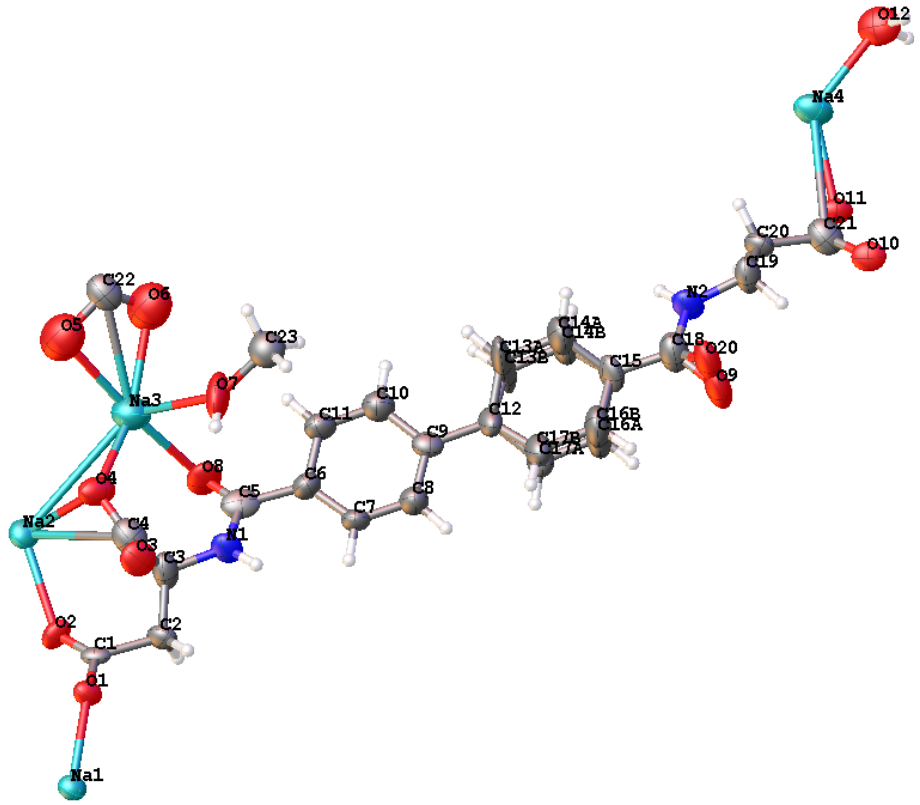

Figure 5.16. Asymmetric unit of MOF-706_sc.

Bibliography

(1) Furukawa, H.; Müller, U.; Yaghi, O. M. *Angew. Chem. Int. Ed.* **2015**, *54* (11), 3417–3430.

(2) Sue, A. C.-H.; Mannige, R. V; Deng, H.; Cao, D.; Wang, C.; Gándara, F.; Stoddart, J. F.; Whitelam, S.; Yaghi, O. M. *Proc. Natl. Acad. Sci. U.S.A.* **2015**, *112* (18), 5591–5596.

(3) Choi, K. M.; Jeon, H. J.; Kang, J. K.; Yaghi, O. M. *J. Am. Chem. Soc.* **2011**, *133* (31), 11920–11923.

(4) Catarineu, N. R.; Schoedel, A.; Urban, P.; Morla, M. B.; Trickett, C. A.; Yaghi, O. M. *J. Am. Chem. Soc.* **2016**, *138* (34), 10826–10829.

(5) Yuan, S.; Qin, J. S.; Zou, L.; Chen, Y. P.; Wang, X.; Zhang, Q.; Zhou, H. C. *J. Am. Chem. Soc.* **2016**, *138* (20), 6636–6642.

(6) Tu, B.; Pang, Q.; Ning, E.; Yan, W.; Qi, Y.; Wu, D.; Li, Q. *J. Am. Chem. Soc.* **2015**, *137* (42), 13456–13459.

(7) Rijnaarts, T.; Mejia-Ariza, R.; Egberink, R. J. M.; van Roosmalen, W.; Huskens, J. *Chem. Eur. J.* **2015**, *21* (29), 10296–10301.

(8) Fracaroli, A. M.; Siman, P.; Nagib, D. A.; Suzuki, M.; Furukawa, H.; Toste, F. D.; Yaghi, O. M. *J. Am. Chem. Soc.* **2016**, *138* (27), 8352–8355.

(9) Siman, P.; Trickett, C. A.; Furukawa, H.; Yaghi, O. M. *Chem. Commun.* **2015**, *51* (98), 17463–17466.

(10) Bruker. In *APEX2 (Bruker AXS Inc., Madison, Wisconsin, U.S.A)*; **2010**.

(11) Sheldrick, G. M. *Acta Crystallogr. Sect. A Found. Crystallogr.* **2007**, *64* (1), 112–122.

(12) Dolomanov, O. V.; Bourhis, L. J.; Gildea, R. J.; Howard, J. A. K.; Puschmann, H. *J. Appl. Crystallogr.* **2009**, *42* (2), 339–341.

(13) Schütrumpf, A.; Kirpi, E.; Bulut, A.; Morel, F. L.; Ranocchiari, M.; Lork, E.; Zorlu, Y.; Grabowsky, S.; Yücesan, G.; Beckmann, J. *Cryst. Growth Des.* **2015**, *15* (10), 4925–4931.

(14) Yang, Z.-Z.; Zhao, Y.; Zhang, H.; Yu, B.; Ma, Z.; Ji, G.; Liu, Z. *Chem. Commun.* **2014**, *50* (90), 13910–13913.

(15) Valera, S.; Taylor, J. E.; Daniels, D. S. B.; Dawson, D. M.; Athukorala Arachchige, K. S.; Ashbrook, S. E.; Slawin, A. M. Z.; Bode, B. E. *J. Org. Chem.* **2014**, *79* (17), 8313–8323.

(16) Basu, P.; Nemykin, V. N.; Sengar, R. S. *Inorg. Chem.* **2003**, *42* (23), 7489–7501.

(17) Plabst, M.; Bein, T. *Inorg. Chem.* **2008**, *47* (10), 4481–4489.

(18) Taylor, J. M.; Mah, R. K.; Moudrakovski, I. L.; Ratcliffe, C. I. *J. Am. Chem. Soc.* **2010**, *132* (2), 14055–14057.

(19) Iremonger, S. S.; Liang, J.; Vaidhyanathan, R.; Martens, I.; Shimizu, G. K. H.; Daff, T. D.; Aghaji, M. Z.; Yeganegi, S.; Woo, T. K. *J. Am. Chem. Soc.* **2011**, *133* (50), 20048–20051.

(20) Taylor, J. M.; Vaidhyanathan, R.; Iremonger, S. S.; Shimizu, G. K. H. *J. Am. Chem. Soc.* **2012**, *134* (35), 14338–14340.

(21) Kinnibrugh, T. L.; Ayi, A. A.; Bakhmutov, V. I.; Zoń, J.; Clearfield, A. *Cryst. Growth Des.* **2013**, *13* (7), 2973–2981.

(22) Zheng, T.; Gao, Y.; Chen, L.; Liu, Z.; Diwu, J.; Chai, Z.; Albrecht-Schmitt, T. E.; Wang, S. *Dalt. Trans.* **2015**, *44* (41), 18158–18166.

(23) Gagnon, K. J.; Perry, H. P.; Clearfield, A. *Chem. Rev.* **2012**, *112* (2), 1034–1054.

(24) Sadakiyo, M.; Yamada, T.; Kitagawa, H. *J. Am. Chem. Soc.* **2009**, *131* (29), 9906–9907.

(25) Sen, S.; Nair, N. N.; Yamada, T.; Kitagawa, H.; Bharadwaj, P. K. *J. Am. Chem. Soc.* **2012**, *134* (47), 19432–19437.

(26) Gagnon, K. J.; Prosvirin, A. V; Dunbar, K. R.; Teat, S. J.; Clearfield, A. *Dalt. Trans.* **2012**, *41* (14), 3995–4006.

(27) Morris, R. E. In *Zeolites and Catalysis: Synthesis, Reactions and Applications*; Wiley-VCH, **2010**; pp 87–105.

(28) Li, H.; Eddaoudi, M.; O'Keeffe, M.; Yaghi, O. M. *Nature* **1999**, *402* (11), 276–279.

(29) Dénès, F.; Pichowicz, M.; Povie, G.; Renaud, P. *Chem. Rev.* **2014**, *114*, 2587–2693.

(30) Fritze, U. F.; von Delius, M. *Chem. Commun.* **2016**, *52* (38), 6363–6366.

Chapter 6: Crystallographic Disorder in Zeolitic Imidazolate Frameworks

Introduction

The quality of MOF crystals in terms of their size and crystallinity can vary drastically, ranging from the possibility of high enough resolution data and structure model quality for charge density studies through to extracting only unit cell information. Thus, while the International Union for Crystallography (IUCr) requires a resolution of 0.84 Å for publishing small molecule crystal structures,[1] this does not imply that data with lower resolution than this are not worth publishing. Far from it, as even the most basic knowledge of the structure can be vital, depending on what kind of information is needed.

The process of solving and refining the crystal structures of MOFs can be viewed as a hybrid between small molecule crystallography, where atomic level resolution is expected, and protein crystallography, which makes use of the known shapes of amino acid residues that make up the protein as rigid bodies to model the structure. In protein crystallography, the techniques used allow structural information to be extracted at a resolution as low as 6 Å.[2] Of course, such information will not be as detailed or as precise as the same structure resolved at higher resolution due to limitations in the number of observed reflections as well as the ability to resolve the location of electron density.

To demonstrate this concept, the structure of triclinic lysozyme is displayed in Figure 6.1, cut to the labeled resolution. At a limit of 5 Å, not much of the structure can really be identified, with perhaps the most rigid features of the phenyl ring and amide functional groups visible. At 3 Å, the overall contour of the structure can be seen, but chemical features such as the phenyl ring cannot be readily identified. Reaching 2 Å allows for features such as the phenyl ring can now be resolved into a ‘donut’ shape rather than simply a region of electron density, although atomic positions are still elusive as the resolution is lower than the bond lengths in the structure. At 1.5 Å resolution and higher is the beginning of separating out atomic features in organic chemistry, as the C-C single bond length is 1.54 Å, thus the resolution is similar to that of covalent bonds. The distinction of atomic features further improves with resolution since the vast majority of electron density is centered on the nucleus, and what is actually resolved depends on the achieved resolution. For instance, carbon and oxygen as part of carbonyl groups are distinguishable at a resolution of 1.2 Å or so, since the bond length is around that value. At extremely high resolution, the deformation of electron density, for instance due to bonding, can be studied.

This example illustrates that the information that can be extracted from crystal structures varies dramatically depending on the data quality, and its usefulness largely depends on the intent of the scientist analyzing the data. If knowledge of the topology or pore size of a framework is desired, a resolution of 2 Å may be sufficient. On the other hand, if a distinction between a single and a double C-C bond is needed, such resolution has no value as these cannot be differentiated.

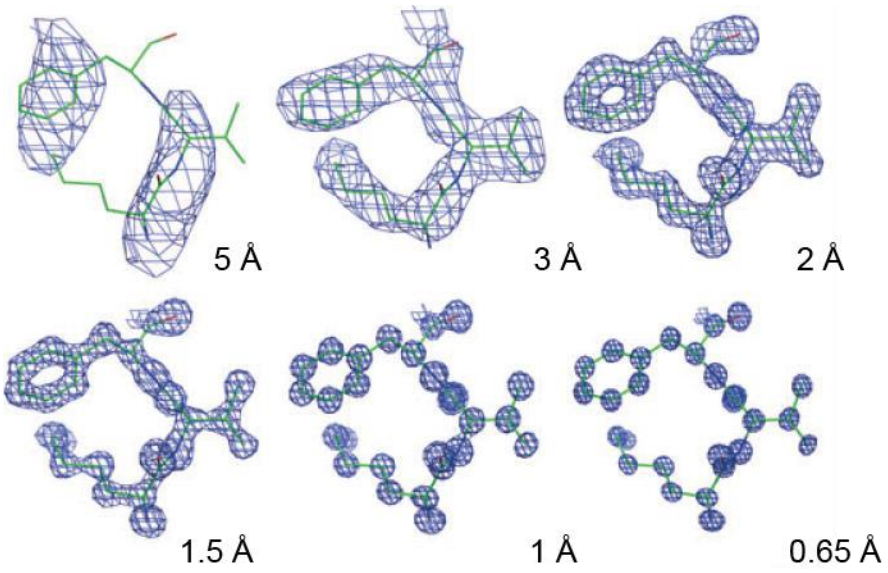

Figure 6.1. The appearance of electron density as a function of the resolution of the experimental data. The N-terminal fragment (Lys1–Val2–Phe3) of triclinic lysozyme (PDB code 2vb1)[3] with the (F_{obs}, φ_{calc}) maps calculated with different resolution cut-off. Whereas at the highest resolution of 0.65 Å there were 184,676 reflections used for map calculation, at 5 Å resolution only 415 reflections were included. This figure is reproduced with permission from Wiley.

An appreciation of the capabilities and limitations of crystallographic data is essential not only for interpreting the data itself, but also for knowing what is acceptable in terms of structure refinement and modeling for a given data set. For MOFs, knowledge of topology is invaluable even if atomic resolution cannot be achieved, and the use of techniques from structural biology can be crucial in solving and refining the framework. These include the use of rigid bodies for the organic linker, which quite often have a well-defined geometry just as amino acid residues do.

In this work, a series of 15 mixed linker zeolitic imidazolate frameworks (ZIFs), which are composed of metal atoms linked by imidazolate groups.[4] Together, they function as a mimic for the geometric features obtained in the structures of zeolites, were structurally characterized by single crystal X-ray diffraction (SXRD). The use of mixed linkers was found to be an invaluable tool for accessing topologies that were previously only predicted, including the largest ever reported unit cell of a synthetic extended framework. In all cases, the resolution was limited to between 1 and 1.7 Å, thus not reaching the target 0.84 Å. Despite this, it was possible to solve and refine structural models for all of these frameworks using a variety of different approaches depending on the data quality, including making use of the charge flipping algorithm,[5] computationally modeling the framework and linker geometries, and rigid body refinement which will be discussed herein.

Experimental

Single-Crystal X-ray Diffraction Analyses. SXRD data was used to determine the connectivity and topology of the ZIFs. The data were collected using a combination of synchrotron radiation on beamlines 11.3.1 and 5.0.2 at the Advanced Light Source (ALS) at Lawrence Berkeley National Lab (LBNL), beamline 17U1 at Synchrotron Radiation Facility (SSRF) in Shanghai, China, a Bruker D8-Venture diffractometer and a Bruker MicroSTAR-H APEX II diffractometer in College of Chemistry, UC Berkeley (CheXray). For all ZIFs, as-synthesized crystals were measured. Specifically, data for ZIF-303, 360, 365, 486, 412, 413, 414, 516, and 725 were collected at beamline 11.3.1 of the ALS at LBNL, equipped with a Bruker Photon 100 CMOS area detector using synchrotron radiation (10-17 KeV); data for ZIF-615 was collected at beamline 5.0.2 of the ALS at LBNL with a PILATUS3 S 6M detector at 0.89990 Å; data for ZIF-408 and 586 were collected at beamline BL17U1 at SSRF, data for ZIF-386 and 410 were collected on a Bruker MicroStart diffractometer equipped with a CCD area detector using rotating-anode Cu Kα radiation (λ = 1.54184 Å); data for ZIF-376 was collected on a Bruker D8 Venture diffractometer equipped with a CMOS area detector using micro-focus Cu Kα radiation (λ = 1.54184 Å). The resolution obtained for all samples was limited due to inherent disorder in the crystals. This resulted in poorly resolved reflections at higher resolution, so the global data were cut to lower resolution in order to improve refinement of the models. However, the resolution was still sufficient to locate electron density peaks in the difference map to establish the connectivity of the structures. Data from NMR and elemental analysis were used as a starting point for the occupancies of functionalized imidazolates except for ZIF-376, which could not be purified. Unless otherwise noted, all non-hydrogen atoms, in particular the positions of functional groups on the imidazole rings, were located using the difference map during refinement. Typically, the restraints and constraints used on the refined model include rigid group restraints such as restraining phenyl and imidazolate rings to be planar with the appropriate distances applied from other known structure models, and rigid-bond restraints which are derived from a sound chemical basis.[6] Samples were mounted on MiTeGen® kapton loops and placed in a 100(2) K nitrogen cold stream unless otherwise specified. See the individual description for each ZIF for further details.

In all cases except for ZIF-615, the data were processed with the Bruker APEX2 software package[7,8] which were integrated using SAINT and corrected for the absorption by SADABS routines (no correction was made for extinction or decay). ZIF-615 was processed using CrysalisPRO.[9] ZIF-303 was processed as a two-domain twin using TWINABS as part of the Apex2 software package. All structures were solved by intrinsic phasing (SHELXT) and were refined by full-matrix least squares on F^2 (SHELXL-2014), except for except for ZIF-408 and -586, which were solved by direct methods. Attempts to solve the structure of ZIF-408 from early samples were performed using Superflip[5] as other methods were unsuccessful initially. Hydrogen atoms were geometrically calculated and refined as riding atoms. In all structures, highly disordered guest molecules occupying the cavities of the structure, which could not be modeled and so were accounted for using solvent masking using the Olex2 software package,[10,11] except for ZIF-585 where SQUEEZE in PLATON's software package was used.[12] For some ZIFs, as will be discussed, a rigid body model was used for imidazolate linker due to the extremely low resolution precluding traditional small-molecule refinement. In general, specific details can be found in the CIF and in the individual ZIF's details listed in the Appendices and Notes.

Results and Discussion

Due to the less than ideal sample quality, which was most often limited by the inherent disorder within the crystals studied, the Advanced Light Source was heavily utilized to collect data for structure modeling. In total, fifteen new ZIFs were modeled and classified according to topology. All data for these ZIFs is provided in the Appendices and Notes, and this section will focus on a few case studies which required non-standard techniques for solution and refinement. All ZIFs were modeled from the single crystal X-ray data, but with the prior knowledge of the linker and elemental composition, obtained from ^{1}H solution NMR of the digested MOF and elemental microanalysis respectively. This information that is external to the structural data collected from SXRD was used as an aid to structure modeling by ensuring the linker composition is consistent with this data. In the ideal case, the structural data would be used to confirm the ^{1}H NMR and elemental microanalysis data. This was possible in most instances but not all. In the cases that match relatively poorly, differences are attributed to some small variations from single crystal to single crystal. The exception to this is ZIF-813, which could not be purified and as a result the composition was estimated from SXRD data. Fortunately, in many cases different imidazolates were not disordered in the same crystallographic position, but were present in an ordered manner, giving rise to previously unreported topologies. This linker influence will be discussed in the case studies.

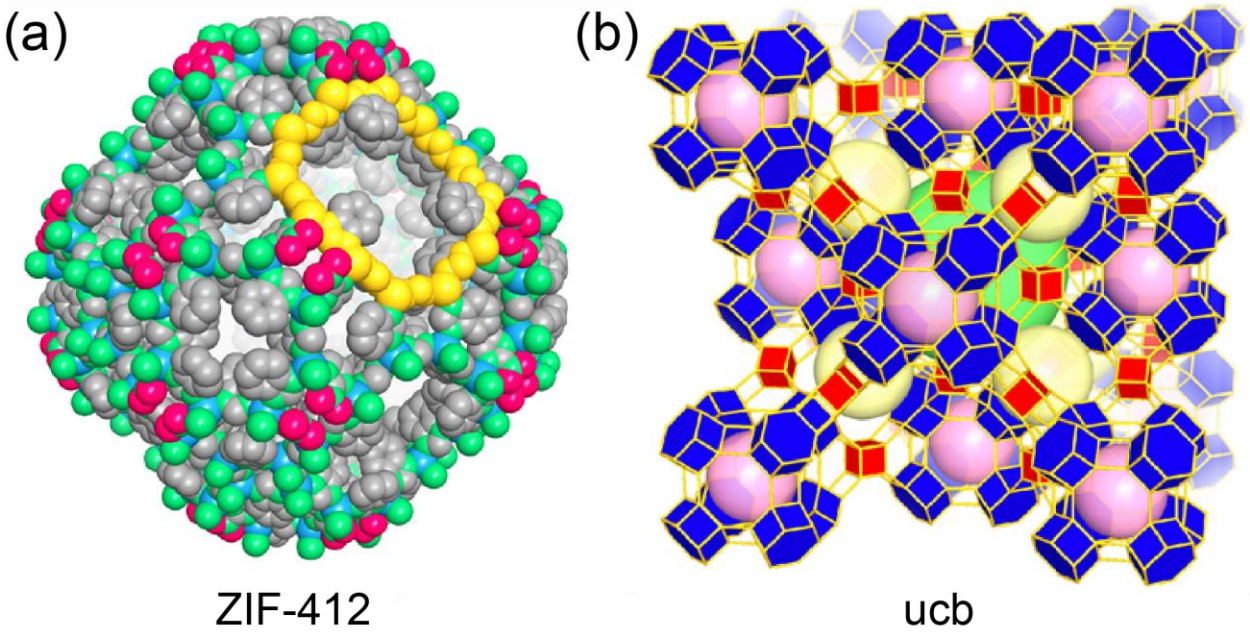

Figure 6.2. Depiction of the structure of ZIF-412, $Zn(bIM)_{1.13}(nIM)_{0.62}(Im)_{0.25}$, with the largest cavity shown in (a) in space-filling view, and the overall topology, **ucb**, displayed in (b). The color scheme is as follows: blue, zinc; N, green; C, gray; O, pink. Hydrogen atoms have been omitted for clarity. The topology is represented as a combination of hexagonal prisms (dark blue) and cubes (red).

The first example to be discussed is ZIF-412. This ZIF has the formula $Zn(bIM)_{1.13}(nIM)_{0.62}(Im)_{0.25}$ (bIM = benzimidazolate, nIm = 2-nitroimidazolate, Im= imidazolate) and thus contains three types of imidazole linkers. It, along with its topological analogs also reported in this work known as ZIF-413 and ZIF-414, has one of the largest unit cells of any synthetic crystal to date, with a volume exceeding 376,000 $Å^3$. This ZIF crystallizes in the space group *Fm*-3*m*, and in a new topology, termed **ucb**. The framework can be described as built up of hexagonal prisms connected to squares in a 3:4 ratio, with each hexagonal prism connected to three cubes and three other hexagonal prisms. Each cube is linked to four hexagonal prisms (Figure 6.2). The vertices of these shapes are the positions of the zinc atoms. Data for this crystal were collected to 1.25 Å resolution. The structure quality and resolution were sufficient to model atom positions anisotropically and without restraining bond distances and angles. However, some restraints on thermal ellipsoids were used, namely RIGU as the SHELX instruction. This restricts the anisotropic displacement parameters along the bond between two atoms.[6] The restraint is based on the assumption that the chemical bond in question is rigid, and therefore the relative motion of the atoms only occurs perpendicular to the bond. This assumption is particularly applicable for strong directional bonds such as a covalent bond. It is perhaps more suitable in this case than a SIMU restraint, whereby all 6 anisotropic displacement parameters are restrained to be similar to one another, because the atoms may have a different range of motion, or greater static disorder, the further away from the zinc atom they are. This is because the zinc atoms serve as anchor points for four different imidazolate linkers, making this position quite rigid. However, the imidazolates are free to rotate above and below the plane of the connecting zinc atoms. This is indeed observed in this structure, most clearly in the benzimidazolate linkers, with the nitrogen atoms bonded to zinc displaying the smallest and closest to sphere-like ellipsoids while the carbon atoms in the phenyl ring are increasingly elliptical perpendicular to the bonds (Figure 6.3).

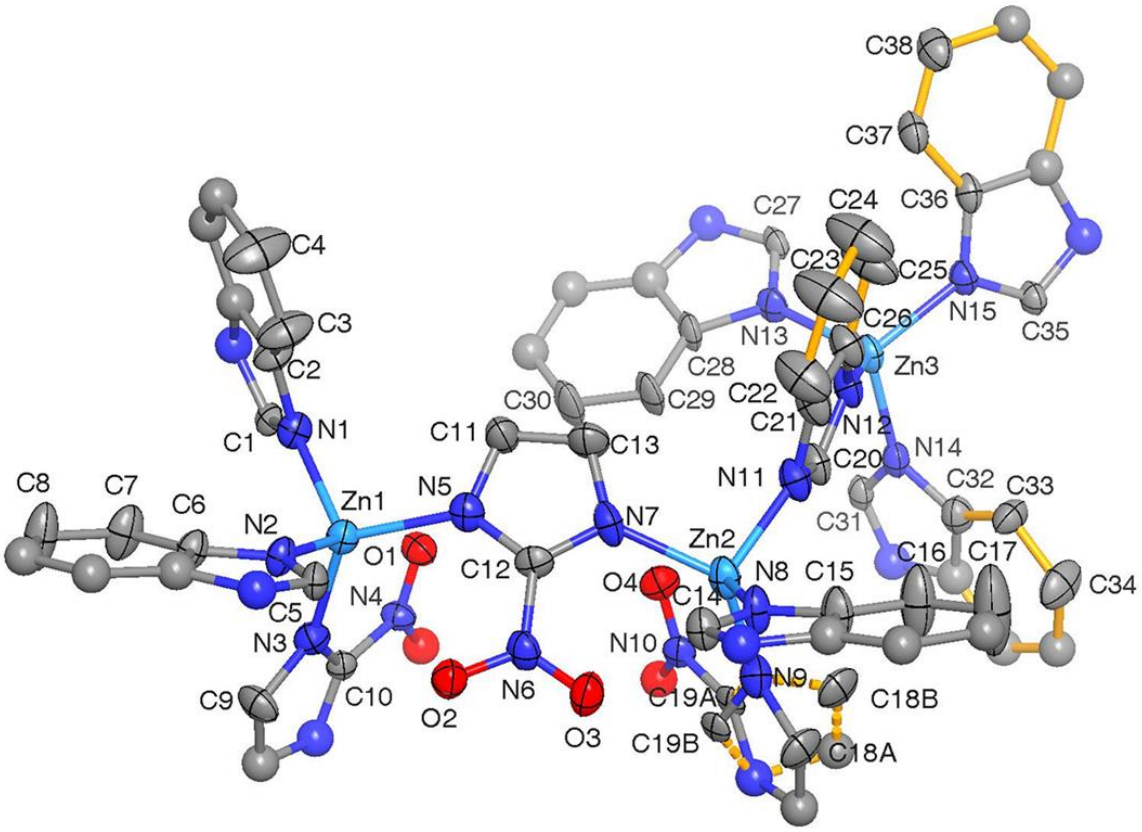

Figure 6.3. Asymmetric unit in the single crystal structure of ZIF-412 (thermal ellipsoids with 15% probability). Hydrogen atoms are omitted for clarity. Orange bonds represent the disordering of bIm and Im. Symmetry-related atoms are not labeled and represented as spheres. The further away the atoms are from the zinc nodes, the greater the anisotropic displacement is perpendicular to the bonds.

During the refinement, the imidazolate ring was first established before assigning the functional group positions in the framework. The three types of imidazolates present were benzimidazolate (bIm), 2-nitroimidazolate (nIm) and imidazolate (Im). The first two are most straightforward to identify, with the presence of a phenyl ring on the 4,5-position and a nitro group on the 2-position respectively, both with characteristic shapes. On the other hand, plain Im is characterized by the lack of functional groups, with hydrogen atom positions being intractable using this data set. This is a result of the limited resolution, which is lower than a typical C-H bond of approximately 1 Å as well as structural disorder. Additionally, hydrogen atoms are particularly challenging or impossible to locate because of their small contribution to the electron density map.

Interestingly, it was found that the steric hindrance imparted by these functional groups have a dramatic influence on the resulting structure: in contrast to the isoreticular principle in MOFs, whereby functional groups on a given linker may be substituted for each other without modifying the structure,[13] these functional groups dictate the topology. The functional groups on the 2-position point towards the inner, smaller ring while groups on the 4,5-positions are directed

towards the larger, outer rings. As a result, imidazolates with both large and small functional groups are needed to form this structure since the large groups create steric hindrance, forcing the framework to expand to accommodate them. On the other hand, smaller functional groups, in this case the hydrogen atoms on the 4,5-position of nIm, are necessary to prevent the large functional groups from clashing with each other. Indeed, C2 on the phenyl ring of bIm is located 3.8 Å away from C11 on 2-nIm. If nIm was replaced with bIm, the two phenyl rings would be too close and clash with one another (Figure 6.3). Equally, O2 on nIm is located 3.2 Å away from C5 on the adjacent bIm. If bIm was replaced by nIm, this would bring the nIm groups in very close proximity that would be chemically impossible. In this manner, ordering between nIm and bIm is formed, and explains why this topology is formed over more commonly observed ZIF topologies such as **gme** or **sod**.

Beyond the ordering of the functionalized imidazolates, it was found that this topology could not be formed without the presence of simple, unfunctionalized imidazolate. Crystallographically, the reasons for this are less clear as imidazolate was found to be disordered over the same position as both bIm and 2-nIm, albeit only in select crystallographically independent sites and not across the whole structure. The steric hindrance may well still be playing a role, and the effect of linker functionality and steric hindrance on the final structure is discussed in more detail in the full manuscript of this multivariate ZIF project.[4] The exact ratio in each site was modeled based on comparing unrestrained ellipsoid sizes and by making use of ^{1}H digestion NMR data. In the instances of these disordered linkers, additional restraints were applied, including FLAT and SADI, as a means of treating the overlap of electron density due to the disorder. FLAT is used as a restraint on linker planarity as the imidazolates are aromatic while SADI restrains the bond distances to be similar to each other. SADI is desirable over a hard restraint such as DFIX for restricting bond distances as SADI imposes restrictions based on the single crystal data for this particular sample. This is unlike DFIX which makes use of external information from other crystal structures which have reported bond lengths in imidazoles.

Once all of the elements heavier than carbon were assigned, with the disorder accounted for in a reasonable manner and the ellipsoids were refined anisotropically with reasonable parameters, the hydrogen atoms were placed geometrically. With all materials being porous, highly disordered guest molecules occupying the cavities could not be modeled. Instead, the electron density contribution was accounted for using solvent masking as part of the Olex2 software package, except for ZIF-303 and ZIF-615 where SQUEEZE in PLATON's software package was used.

This refinement approach was utilized in a similar manner with ZIF-413, -414, -410, -386, -486, -360, -365 and -376. For ZIF-303, a twin component had to be additionally accounted for, and data for ZIF-725 could only be obtained to 1.38 Å. This drop in resolution led to the need for additional, harder restraints for an anisotropic refinement, including EADP to constrain the ellipsoids to have exactly the same parameters. Compared to the other ZIFs mentioned, the resolution drop calls into question the need for an anisotropic refinement. After all, at this resolution, C-C single bonds can be distinguished while aromatic C-C and C-N bonds are at the

limit. In this case, an anisotropic refinement was performed, though this does require a large number of restraints and in reality does not provide much additional, reliable information about the structure. However, it can be noted that a rough trend of the ellipsoids becoming more elliptical as their distance from zinc increased, particularly in 5-bromobenzimidazole. This effect is similar to that observed in the other ZIFs for which data was collected at higher resolution, whereby atoms further from zinc have more freedom to rotate.

With these ZIFs, the data quality and resolution is sufficient to (i) solve the structure using conventional intrinsic phasing or direct methods, and (ii) refine individual atom positions independently, or with mostly gentle restraints. However, standard solution methods were not possible for all ZIFs studied, most notably early attempts at solving ZIF-408, which was eventually found to be an isoreticular version of the 5-chlorobenzimidazole-based ZIF-100. The initial data set obtained for this ZIF was limited to 1.7 Å resolution. Instead of the more common solution methods, the charge flipping algorithm was used through the program Superflip.[5] The basic premise of the program is to assign random phases to reflections and an electron density map calculated as a result. The unit cell is divided into a grid, and grid points below a certain positive threshold are multiplied by -1. New phases are calculated based on this new electron density map, and the process is repeated. Charge flipping makes no assumptions about symmetry, treating the electron density as *P*1 and later estimating the symmetry from the electron density map. This method of obtaining an initial structure solution can be very effective for solving structures with significant differences in electron density within a unit cell. Therefore large pore ZIFs, which contain zinc atoms but also highly disordered solvent in the cavities, are well-suited to this method.

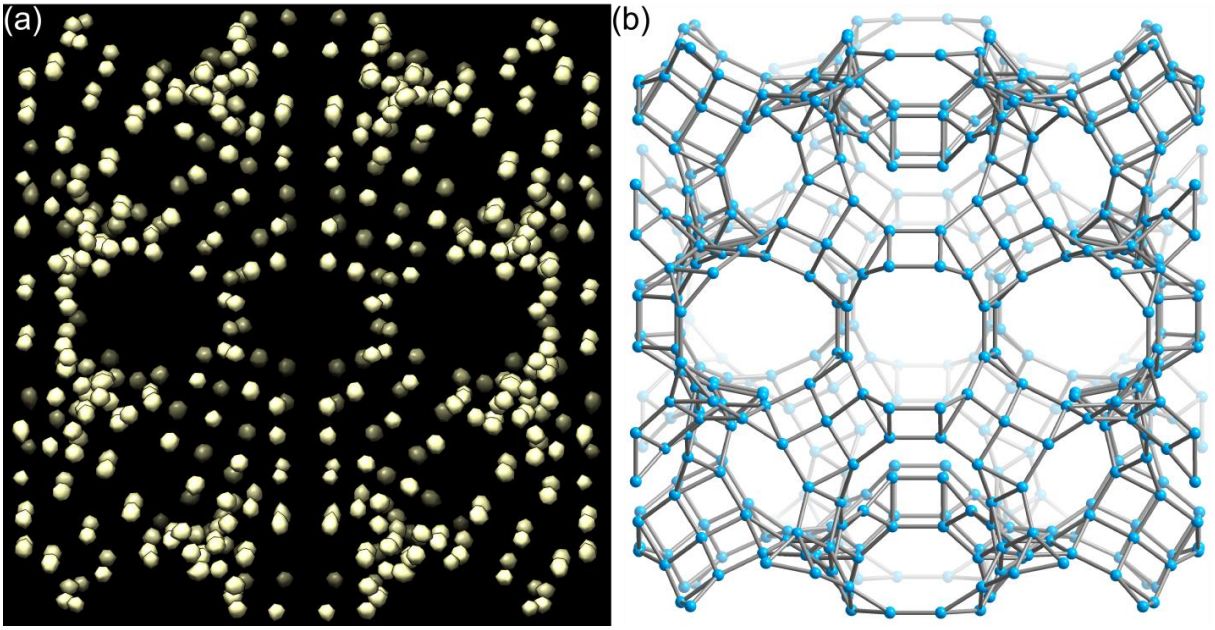

Figure 6.4. (a) Comparison of the electron density map determined generated in Chimera[14] and using the Superflip algorithm[5] with (b) the topology of ZIF-408, as found from the refinement of the single crystal structure.

An initial solution for ZIF-408 found from charge flipping confirmed the space group of *Im*-3 based on the symmetry of the electron density. This space group was also found during processing the data using Apex2 software.[7] The electron density map, illustrated in Figure 6.4, clearly shows the positions of zinc atoms as well-defined spheres of electron density. The electron density was confirmed to be the positions of zinc atoms as all spheres were separated by approximately 6 Å. This is a common feature of all ZIFs since this class of materials all contain the same linkage of Zn-N-C-N-Zn, regardless of the imidazolate used.[15] Further atom positions at this stage were not readily visible, though the initial zinc atom positions were sufficient to determine initial phases for a stable and meaningful refinement to study the rest of the structure. Since the resolution was so low, reducing both the number of data points available as well as making the distinction between atoms on the imidazolate groups intractable, a rigid body refinement method was used. In this technique, a model of the imidazolate linker was first geometrically optimized in Materials Studio 7.0 using the Forcite module. A universal force field was employed, with the Smart algorithm for the energy mimization procedure. Using this geometry optimization procedure, a model of the framework was built with Materials Studio by taking the solved zinc positions and placing a basic, unfunctionalized imidazolate group and placed between zinc atoms located 6 Å apart. The unfunctionalized imidazolate was used as a starting point since all imidazolates, regardless of their functionality, will contain this basic building block. A geometry optimization routine was performed on the structure, checked for consistency, and the model was refined against the reflection data with a rigid body refinement restraint used for the imidazolate ring. Such a restraint allows for the rotation of the imidazolate group as a whole while keeping the individual atom positions in the same relative position to one another. This is a chemically reasonable restraint as the geometry of imidazolate is well-known, with little flexibility between atoms in the aromatic ring, despite allowing free movement of the body as a whole.

The difference map was then used to locate functional groups. While individual atoms were not necessarily obvious to locate in the refinement program as electron density peaks, the difference map shows the characteristic shape of the functional group, such as a planar donut for the phenyl ring in 5-chlorobenzimidazolate. Once a functional group was located, it was added to the structure model in Materials Studio, and the new model was refined against the reflection data in an iterative process (Figure 6.5). Since all atoms in the unit cell contribute to the structure factors, this method of progressively refining more of the structure allows for more and more atomic features to be observed in the difference map until the structure model is taken as far as the data allows. Note that ZIF-516, -586 and -615 were all modeled using this approach.

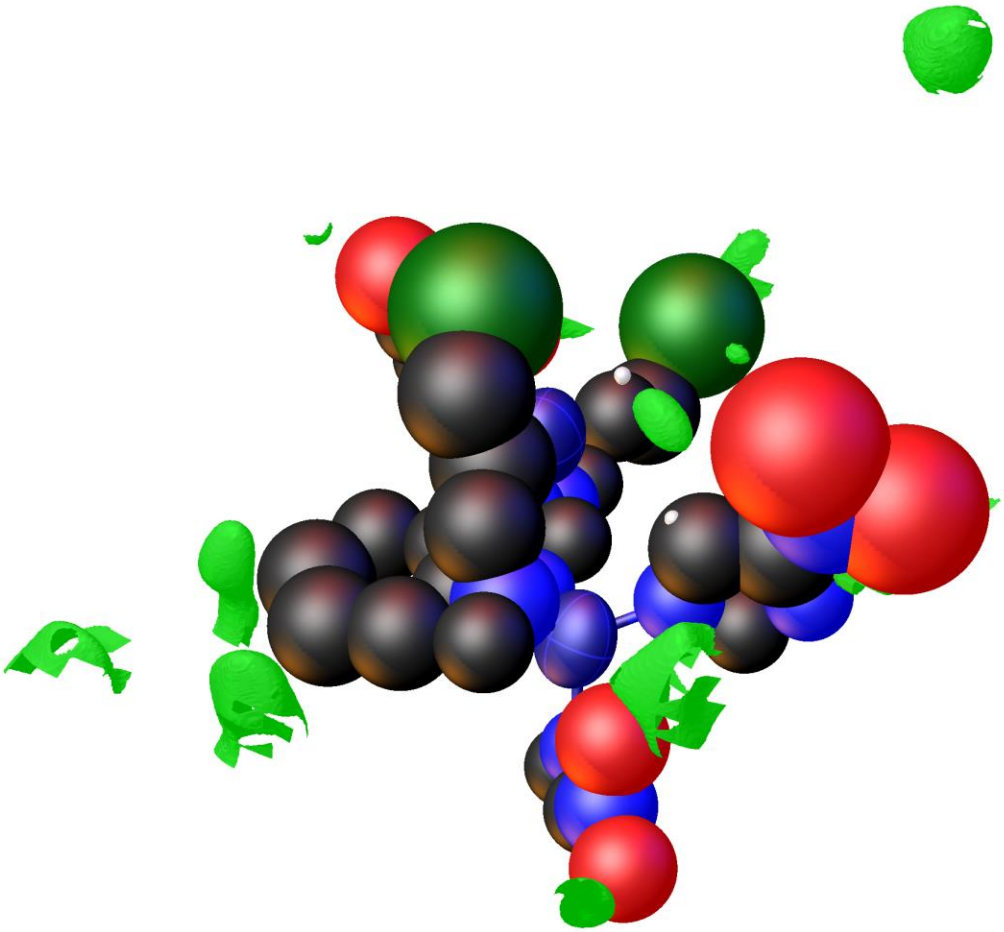

Figure 6.5. The asymmetric unit with the difference map during the structure refinement of ZIF-615 is depicted. This map was used during structure refinement to identify functional groups located on the imidazolate groups in order to distinguish the mixed linkers. The majority of electron density at this stage of the refinement is located within the cavities of the ZIF, or near disordered nitro functionalities. However, in the 5-position of the phenyl ring on the left of the figure shows electron density located around 1.7 Å from the carbon atom, confirming the presence of disordered chlorine atoms that make up 5-chlorobenzimidazole.

Conclusion

The work described herein describes how the structures of ZIFs can be modeled and refined from low resolution SXRD data, and the limitations associated with this compared to small molecule standards. In this case study, the low resolution was not an impediment to obtaining information on structural connectivity and topology, and permitted the location of imidazolate linkers of different steric hindrance. This provided a wealth of information that informed on the effect the combination of linkers has on the topology of the framework. This has the potential to inform on strategic design of ZIFs through synthetic methods. However, detailed bond lengths, angles and thermal ellipsoid information could not be reliably determined in some cases, since rigid body and other restraints were employed using external information.

Appendices and Notes

Acknowledgements. The synthesis and characterization beyond the structure of these ZIFs was performed by Jingjing Yang, who led the overall project. This work could not have been completed without his invaluable input. I also thank Qi Liu for the synthesis of ZIF-408, Yue-Biao Zhang, Enrique Gutierrez-Puebla and Angeles Monge-Bravo for helpful discussions on the crystallographic data, and Hengjiang Cong for collecting data for ZIF-365 and -408.

Chemicals used in this work. Imidazole (HIM), benzimidazole (HbIM), 5-chlorobenzimidazole (HcbIM), 5-methylbenzimidazole (HmbIM), 6-bromobenzimidazole (HbbIM), 6-nitrobenzimidazole (HnbIM), 2-methylbenzimidazole (2-HmbIM), 2-nitroimidazole (HnIM), Imidazole-2-carboxaldehyde (HaIM), 2-methylimidazole (HmIM), 4-nitroimidazole (4-HnIM), zinc(II) nitrate tetrahydrate [$Zn(NO_3)_2{\cdot}4H_2O$], zinc(II) trifluoromethanesulfonate [$Zn(CF_3SO_3)_2$], anhydrous *N*,*N*-dimethylformamide (DMF), anhydrous acetone were purchased from commercial source and were used directly without further purification. *N*,*N*-Diethylformamide (DEF) was obtained from BASF, which was stirred with activated carbon before treating with a solvent purification system.

All the synthetic procedures were conducted in open air. The ZIFs were activated by the following procedure: Firstly, the as-synthesized crystalline material was immersed in anhydrous DMF for three days, exchanged with fresh DMF three times per day; then immersed in anhydrous acetone for three days, exchange with fresh acetone three times per day. After that, the ZIFs were fully exchanged with liquid CO_2 for six times, and further kept under supercritical CO_2 atmosphere for 1 h before being bled using a Tousimis Samdri PVT-3D critical point dryer. The samples were finally evacuated to remove guest molecules under vacuum (0.01 Torr) at ambient temperature for 4 h, then at elaborated temperature of 50 °C for 4 h, 100 °C for 4 h, 150 °C for 4 h and finally 180 °C for 12 h to give the activated sample. The following measurements were all conducted using the activated samples for each ZIF unless otherwise noted.

Elemental analysis (EA) of activated ZIFs were performed using a Perkin Elmer 2400 Series II CHNS elemental analyzer; ^{1}H NMR spectra for digested solutions of ZIFs were acquired on a Bruker AVB-400 NMR spectrometer, with chemcial shifts of imidazoles identified by comparing with spectra for each pure linker, samples (*ca.* 10 mg for each) were dissolved in DMSO-d_6 (deuterated dimethyl sulfoxide, 580 μL) and 20% DCl in D_2O (20 μL) with sonications; attenuated-total-reflectance Fourier-transform infrared (ATR-FTIR) spectra of neat ZIFs were recorded on a Bruker ALPHA Platinum ATR-FTIR Spectrometer.

ZIF Syntheses

ZIF-303 (CHA), **$Zn(cbIM)_{0.70}(nIM)_{0.30}(IM)_{1.00}$.** A mixture of $Zn(NO_3)_2{\cdot}4H_2O$ (0.1 mmol, 0.5 mL of 0.2 M stock solution in DMF), HnIM (0.1 mmol, 0.5 mL of 0.2 M stock solution in DMF), HIM (0.2 mmol, 1.0 mL of 0.2 M stock solution in DMF), and HcbIM (0.1 mmol, 0.5 mL of 0.2 M stock solution in DMF) was sealed in a 4-mL glass vial and heated at 120 °C for 72 h. Yellow hexagonal plate crystals were collected and washed with anhydrous DMF (3 × 4 ml). (Yield: 49% based on Zn). EA: Calcd. for $Zn(C_3H_2N_3O_2)_{0.30}(C_3H_3N_2)(C_7H_4N_2Cl)_{0.70}$: C, 38.83; H, 2.37; N, 22.13%. Found: C, 37.86; H, 2.25; N, 23.11%. ATR-FTIR

(4000-400 cm^{-1}): 1608(w), 1574(w), 1539(w), 1494(s), 1472(s), 1435(m), 1365(s), 1341(m), 1321(w), 1288(m), 1238(m), 1192(m), 1171(s), 1126(w), 1088(s), 1062(m), 1013(w), 978(w), 953(s), 928(m), 832(m), 801(s), 756(s), 723(m), 669(s), 649(m), 598(m), 571(w), 482(m), 425(m).

ZIF-360 (KFI), $Zn(bIM)_{1.00}(nIM)_{0.70}(IM)_{0.30}$. A mixture of $Zn(NO_3)_2{\cdot}4H_2O$ (0.1 mmol, 0.5 mL of 0.2 M stock solution in DEF), HnIM (0.3 mmol, 1.5 mL of 0.2 M stock solution in DEF), HIM (0.1 mmol, 0.5 mL of 0.2 M stock solution in DEF), and HbIM (0.2 mmol, 1.0 mL of 0.2 M stock solution in DEF) was sealed in a 4-mL glass vial and heated at 100 °C for 72 h. Transparent trigonal prism crystals were collected from the wall and washed with anhydrous DEF (3 × 4 ml). (Yield: 38% based on Zn). EA: Calcd. for $Zn(C_3H_2N_3O_2)_{0.70}(C_3H_3N_2)_{0.30}(C_7H_5N_2)$: C, 42.73; H, 2.62; N, 23.42%. Found: C, 39.39; H, 2.48; N, 22.72%. ATR-FTIR (4000-400 cm^{-1}): 1611(m), 1539(m), 1476(s), 1364(s), 1301(m), 1278(m), 1244(s), 1198(w), 1173(s), 1118(w), 1091(s), 1005(w), 952(s), 908(s), 831(s), 793(m), 775(m), 740(s), 668(w), 651(s), 572(m), 552(m), 464(s), 427(s).

ZIF-365 (KFI), $Zn(cbIM)_{0.95}(nIM)_{0.60}(IM)_{0.45}$. A mixture of $Zn(NO_3)_2{\cdot}4H_2O$ (0.1 mmol, 0.5 mL of 0.2 M stock solution in DEF), HnIM (0.22 mmol, 1.1 mL of 0.2 M stock solution in DEF), HIM (0.1 mmol, 0.5 mL of 0.2 M stock solution in DEF), and HcbIM (0.2 mmol, 1.0 mL of 0.2 M stock solution in DEF) was sealed in a 4-mL glass vial and heated at 100 °C for 72 h. Transparent trigonal prism crystals were collected from the wall and washed with anhydrous DEF (3 × 4 ml). (Yield: 34% based on Zn). EA: Calcd. for

$Zn(C_3H_2N_3O_2)_{0.60}(C_3H_3N_2)_{0.45}(C_7H_4N_2Cl)_{0.95}$: C, 38.36; H, 2.09; N, 21.00%. Found: C, 35.90; H, 2.01; N, 20.67%. ATR-FTIR (4000-400 cm^{-1}): 1644(w), 1610(w), 1537(w), 1471(s), 1360(s), 1287(m), 1253(w), 1238(m), 1192(w), 1172(s), 1125(w), 1090(s), 1063(m), 951(s), 927(s), 852(w), 831(s), 800(s), 757(m), 723(s), 668(w), 650(s), 598(s), 571(m), 512(w), 481(s), 459(w), 425(s).

ZIF-376 (LTA), $Zn(nbIM)_{0.83}(mIM)_{0.25}(IM)_{0.92}$. A mixture of $Zn(NO_3)_2{\cdot}4H_2O$ (0.14 mmol, 0.7 mL of 0.2 M stock solution in DMF), HmIM (0.3 mmol, 1.5 mL of 0.2 M stock solution in DMF), HIM (0.1 mmol, 0.5 mL of 0.2 M stock solution in DMF), and HnbIM (0.2 mmol, 1.0 mL of 0.2 M stock solution in DMF) was sealed in a 4-mL glass vial and heated at 130 °C for 72 h, then cool down to room temperature. Transparent octahedral crystals (**ucb ZIF-414**) and brown cubic crystals were found on the wall, the cubic crystals were collected and analyzed by Single-crystal x-ray diffraction as **ZIF-376**. This ZIF was not purified or activated;, a few crops of crystals were picked up manually for powder x-ray and digested ^{1}H-NMR studies.

ZIF-386 (AFX), $Zn(nbIM)_{0.85}(nIM)_{0.70}(IM)_{0.45}$. A mixture of $Zn(NO_3)_2{\cdot}4H_2O$ (0.1 mmol, 0.5 mL of 0.2 M stock solution in DMF), HnIM (0.3 mmol, 1.5 mL of 0.2 M stock solution in DMF), HIM (0.1 mmol, 0.5 mL of 0.2 M stock solution in DMF), and HnbIM (0.2 mmol, 1.0 mL of 0.2 M stock solution in DMF) was sealed in a 4-mL glass vial and heated at 120 °C for 72 h. Yellow hexagonal plate crystals were collected and washed with anhydrous DMF (3 × 4 ml). (Yield: 38% based on Zn). EA: Calcd. for $Zn_2(C_3H_2N_3O_2)_{1.40}(C_3H_3N_2)_{0.90}(C_7H_4N_3O_2)_{1.70}$: C, 36.21; H, 1.99; N, 24.93%. Found: C, 35.33; H, 2.02; N, 24.37%. ATR-FTIR (4000-400 cm^{-1}): 1649(m), 1615(m), 1591(w), 1518(s), 1496(s), 1475(s), 1412(w), 1364(s), 1343(s), 1305(s), 1290(s), 1258(w), 1235(m), 1196(m), 1171(s),

1126(m), 1091(s), 1068(m), 1012(m), 981(w), 950(s), 885(m), 831(s), 795(s), 763(m), 736(s), 709(m), 668(m), 654(m), 623(w), 595(m), 573(m), 543(m), 503(w), 467(w), 450(m), 424(m).

ZIF-408, $Zn(cbIM)_{1.87}(mIM)_{0.08}(OH)_{0.05}$. A mixture of $Zn(NO_3)_2{\cdot}4H_2O$ (0.04 mmol, 0.2 mL of 0.2 M stock solution in DMF), HmIM (0.02 mmol, 0.1 mL of 0.2 M stock solution in DMF), and HcbIM (0.2 mmol, 1 mL of 0.2 M stock solution in DMF), and 0.6 mL DMF were sealed in a 4-mL glass vial and heated at 65 °C for 28 days, large cubic crystals were collected and washed with anhydrous DMF (3 × 4 ml). This ZIF was not activated, a few crops of crystals were picked up for powder x-ray and digested ^{1}H-NMR studies.

ZIF-410 (GME), $Zn(cbIM)_{1.10}(aIM)_{0.90}$. A mixture of $Zn(CF_3SO_3)_2$ (0.2 mmol, 1 mL of 0.2 M stock solution in DMF), HaIm (0.2 mmol, 1 mL of 0.2 M stock solution in DMF), and HcbIm (0.3 mmol, 1.5 mL of 0.2 M stock solution in DMF) was sealed in a 4-mL glass vial and heated at 85 °C for 96 h. Transparent hexagonal plate crystals were collected and washed with anhydrous DMF (3 × 4 ml). (Yield: 15% based on Zn).EA: Calcd. for $Zn(C_4H_3N_2O)_{0.90}(C_7H_4N_2Cl)_{1.10}$: C, 42.72; H, 2.25; N, 17.64%. Found: C, 41.92; H, 2.15; N, 17.60%. ATR-FTIR (4000-400 cm^{-1}): 1680(br), 1609(w), 1574(w), 1460(br), 1415(s), 1360(m), 1340(w), 1323(w), 1287(w), 1238(m), 1190(s), 1169(s), 1128(w), 1063(m), 953(m), 928(m), 852(w), 789(br), 758(w), 723(s), 700(w), 648(w), 598(s), 533(w), 481(s), 425(s)

ZIF-486 (GME), $Zn(nbIM)_{0.20}(mIM)_{0.65}(IM)_{1.15}$. A mixture of $Zn(NO_3)_2{\cdot}4H_2O$ (0.12 mmol, 0.6 mL of 0.2 M stock solution in DMF), HmIM (0.3 mmol, 1.5 mL of 0.2 M stock solution in DMF), HIM (0.24 mmol, 1.2 mL of 0.2 M stock solution in DMF), and HnbIM (0.06 mmol, 0.3 mL of 0.2 M stock solution in DMF) was sealed in a 4-mL glass vial and heated at 130 °C for 48 h. Transparent hexagonal crystals were collected by sonication and washed with anhydrous DMF (3 × 4 ml). (Yield: 38% based on Zn). EA: Calcd. for $Zn(C_4H_5N_2)_{0.65}(C_3H_3N_2)_{1.15}(C_7H_4N_3O_2)_{0.20}$: C, 39.30; H, 3.32; N, 25.84%. Found: C, 39.32; H, 3.09; N, 25.68%. ATR-FTIR (4000-400 cm^{-1}): 1614(w), 1591_w), 1514(w), 1500(w), 1476(m), 1462(w), 1422(w), 1379(w), 1346(m), 1307(w), 1292(w), 1243(m), 1198(w), 1173(m), 1144(m), 1088(s), 993(w), 954(s), 840(w), 797(w), 753(s), 737(m), 709(w), 691(w), 670(s), 594(w), 544(w), 484(w), 451(w), 422(s).

ZIF-412 (ucb), $Zn(bIM)_{1.13}(nIM)_{0.62}(IM)_{0.25}$. A mixture of $Zn(NO_3)_2{\cdot}4H_2O$ (0.1 mmol, 0.5 mL of 0.2 M stock solution in DMF), HnIM (0.3 mmol, 1.5 mL of 0.2 M stock solution in DMF), IM (0.1 mmol, 0.5 mL of 0.2 M stock solution in DMF), HbIM (0.2 mmol, 1.0 mL of 0.2 M stock solution in DMF) and 0.5 mL more DMF was sealed in a 4-mL glass vial and heated at 120 °C for 4 days, then cooled down at 1 °C/min. Polyhedral shaped crystals were collected from the wall (few impure large orange crystals at the bottom were removed) and washed with anhydrous DMF (3 × 4 mL) (Yield: 46% based on Zn). Single crystal suitable for single-crystal x-ray diffraction studies were grown in similar condition but with 1 mL DMF in 20-mL glass vial. EA: Calcd. for $Zn_3(C_3H_2N_3O_2)_{1.85}(C_3H_3N_2)_{0.75}(C_7H_5N_2)_{3.40}$: C, 44.55; H, 2.71; N, 22.77%. Found: C, 43.30; H, 2.62; N, 22.76%. ATR-FTIR (4000-400 cm^{-1}): 1612(w), 1541(w), 1476(s), 1367(s), 1301(m), 1278(m), 1244(s), 1198(s), 1175(w), 1119(m), 1092(w), 1005(m), 952(m), 909(m), 831(w), 794(w), 776(m), 740(s), 670(w), 650(m), 573(w), 552(w), 464(m), 425(m).

ZIF-413 (ucb), $Zn(mbIM)_{1.03}(nIM)_{0.64}(IM)_{0.33}$. A mixture of $Zn(NO_3)_2{\cdot}4H_2O$ (0.1 mmol, 0.5 mL of 0.2 M stock solution in DMF), HnIM (0.3 mmol, 1.5 mL of 0.2 M stock solution in DMF), HIM (0.1 mmol, 0.5 mL of 0.2 M stock solution in DMF), and HmbIM (0.2 mmol, 1.0 mL of 0.2 M stock solution in DMF) was sealed in a 4 mL glass vial and heated at 120 °C for 4 days, then cooled down at 1°C/min. Polyhedral shaped crystals were collected and washed with anhydrous DMF (3 × 4 mL). (Yield: 43% based on Zn). EA: Calcd. for $Zn_3(C_3H_2N_3O_2)_{1.90}(C_3H_3N_2)(C_8H_7N_2)_{3.10}$: C, 45.58; H, 3.25; N, 22.06%. Found: C, 44.83; H, 3.16; N, 21.80%. ATR-FTIR (4000-400 cm^{-1}): 1620(w), 1539(m), 1473(s), 1366(s), 1290(s), 1243(s), 1205(s), 1173(s), 1143(w), 1131(m), 1091(s), 1021(w), 950(s), 830(s), 824(s), 799(s), 761(s), 668(m), 652(s), 625(m), 604(m), 572(m), 495(m), 468(s), 427(s).

ZIF-414 (ucb), $Zn(nbIM)_{0.91}(mIM)_{0.62}(IM)_{0.47}$. A mixture of $Zn(NO_3)_2{\cdot}4H_2O$ (0.1 mmol, 0.5 mL of 0.2 M stock solution in DMF), HmIM (0.3 mmol, 1.5 mL of 0.2 M stock solution in DMF), HIM (0.075 mmol, 0.375 mL of 0.2 M stock solution in DMF), and HnbIM (0.225 mmol, 1.125 mL of 0.2 M stock solution in DMF) was sealed in a 4-mL glass vial and heated at 130 °C for 48 h, then cool down to room temperature at 0.1 °C/min . Transparent octahedral crystals were collected and washed with anhydrous DMF (3 × 4 ml). (Yield: 50% based on Zn). EA: Calcd. for $Zn_3(C_4H_5N_2)_{1.85}(C_3H_3N_2)_{1.40}(C_7H_4N_3O_2)_{2.75}$: C, 41.82; H, 2.78; N, 23.32%. Found: C, 40.98; H, 2.44; N, 22.91%. ATR-FTIR (4000-400 cm^{-1}): 1615(w), 1591(w), 1518(m), 1463(m), 1443(w), 1425(w), 1378(w), 1343(s), 1289(s), 1257(w), 1234(m), 1196(w), 1182(w), 1146(w), 1127(w), 1069(s), 994(w), 949(m), 886(w), .823(w), 796(s), 757(m), 736(s), 709(m), 689(w), 670(m), 648(w), 594(w), 544(w), 424(s).

ZIF-516 (ykh), $Zn(bbIM)_{0.77}(mbIM)_{1.23}(DMF)_{0.05}$. A mixture of $Zn(NO_3)_2{\cdot}4H_2O$ (0.04 mmol, 0.2 mL of 0.2 M stock solution in DMF), HmbIM (0.2 mmol, 1 mL of 0.2 M stock solution in DMF), HbbIM (0.2 mmol, 1 mL of 0.2 M stock solution in DMF) and 70 μL water was sealed in a 4-mL glass vial and heated at 130 °C for 4 days. Transparent crystals were collected and washed with anhydrous DMF (3 × 4 ml). (Yield: 72% based on Zn). EA: Calcd. for $Zn(C_8H_7N_2)_{1.23}(C_7H_4N_2Br)_{0.77}(C_3H_7NO)_{0.05}$: C, 48.45; H, 3.18; N, 14.88%. Found: C, 48.37; H, 3.20; N, 14.76%. ATR-FTIR (4000-400 cm^{-1}): 1603(w), 1469(s, br), 1340(m), 1286(m), 1240(s), 1203(m), 1180(m), 1141(w), 1130(m), 1052(w), 1017(w), 944(w), 917(m), 857(w), .822(w), 798(s), 760(m), 703(m), 648(s), 585(m), 468(s), 423(s).

ZIF-586 (ykh), $Zn(mbIM)_{1.72}(2\text{-}mbIM)_{0.28}$. A mixture of $Zn(NO_3)_2{\cdot}4H_2O$ (0.04 mmol, 0.2 mL of 0.2 M stock solution in DMF), 2-HmbIM (0.12 mmol, 0.6 mL of 0.2 M stock solution in DMF), and HmbIM (0.13 mmol, 0.65 mL of 0.2 M stock solution in DMF) was sealed in a 4-mL glass vial and heated at 130 °C for 3 days. Plate crystals were found along with powders. and washed with anhydrous DMF (3 × 4 ml). This ZIF was not activated, a few crops of crystals were picked up for powder x-ray and digested ^{1}H-NMR studies.

ZIF-615 (gcc), $Zn(cbIM)_{1.05}(4\text{-}nIM)_{0.95}$. A mixture of $Zn(NO_3)_2{\cdot}4H_2O$ (0.08 mmol, 0.4 mL of 0.2 M stock solution in DMF), 4-HnIM (0.12 mmol, 0.6 mL of 0.2 M stock solution in DMF), and HcbIM (0.08 mmol, 0.4 mL of 0.2 M stock solution in DMF) was sealed in a 4-mL glass vial and heated at 130 °C for 96 h. needle crystals were collected and washed with anhydrous DMF (3 × 4 ml). (Yield: 38% based on Zn). EA: Calcd. for $Zn(C_3H_2N_3O_2)_{0.95}(C_7H_4N_2Cl)_{1.05}$: C, 37.01; H, 1.86; N, 20.95%. Found: C, 34.85; H, 1.97; N, 19.58%. ATR-FTIR

(4000-400 cm^{-1}): 1610(w), 1575(w), 1534(m), 1513(m), 1470(s), 1381(s), 1368(s), 1340(m), 1287(m), 1245(s), 1219(w), 1191(m), 1107(s), 1064(m), 1036(m), 974(w), .928(m), 852(s), 824(s), 800(s), 752(m), 724(m), 665(s), 648(m), 598(m), 482(m), 424(m).

ZIF-725 (bam), $Zn(bbIM)_{1.35}(nIM)_{0.40}(IM)_{0.25}$. A mixture of $Zn(NO_3)_2{\cdot}4H_2O$ (0.1 mmol, 0.5 mL of 0.2 M stock solution in DMF), HnIM (0.085 mmol, 0.425 mL of 0.2 M stock solution in DMF), IM (0.1 mmol, 0.5 mL of 0.2 M stock solution in DMF), and HbbIM (0.4 mmol, 2.0 mL of 0.2 M stock solution in DMF) was sealed in a 4-mL glass vial and heated at 65 °C for 12 days. Colorless rod-shaped crystals were collected and washed with anhydrous DMF (3 × 4 ml). (Yield: 19% based on Zn). EA: Calcd. for $Zn_2(C_3H_2N_3O_2)_{0.80}(C_3H_3N_2)_{0.50}(C_7H_4N_2Br)_{2.70}$: C, 34.96; H, 1.79; N, 15.74%. Found C, 34.80; H, 1.57; N, 15.35%. ATR-FTIR (4000-400 cm-1): 1604(m), 1572(w), 1537(w), 1494(s), 1471(s), 1431(m), 1365(s), 1339(s), 1287(s), 1250(s), 1238(s), 1187(s), 1135(s), 1129(m), 1092(s), 1052(s), 1013(w), 952(m), 918(s), 852(m), 831(m), 793(s), 757(m), 705(s), 669(m), 648(s), 586(s), 478(s), 423(s).

Single-crystal X-ray diffraction. The resolution obtained for all samples was limited to varying degrees due to inherent disorder in the crystals. Data from NMR and elemental analysis were used as a starting point for the occupancies of functionalized imidazolates. For all structures except for **ZIF-516** and **-615**, all non-hydrogen atoms, in particular the positions of functional groups on the imidazole rings, were located using the difference map during refinement. Typically, the restraints and constraints used on the refined model include rigid group restraints such as restraining phenyl and imidazolate rings to be planar with the appropriate distances applied from other known structure models, and rigid-bond restraints which are derived from a sound chemical basis (*1*). In the case of the two exceptions, the coordinates of the zinc atoms were first located, then rigid body refinements of unfunctionalized imidazoles were first performed to improve phasing. The functional group positions were located using the difference map before being incorporated into the imidazolate rigid body. This process was iterated several times to ensure all functional groups were correctly located. See the individual description for each ZIF and their corresponding CIFs for further details. Samples were mounted on MiTeGen® kapton loops and placed in a 100(2) K nitrogen cold stream unless otherwise specified.

In all cases except ZIF-615, the data were processed with the Bruker APEX2 software package (*2*-*3*), integrated using SAINT v8.34A and corrected for the absorption by SADABS 2014/4 routines (no correction was made for extinction or decay). **ZIF-303** was processed as a two-domain twin using TWINABS. The structures were solved by intrinsic phasing (SHELXT) and refined by full-matrix least squares on F^2 (SHELXL-2014). The data reduction for **ZIF-615** was performed using the CrysAlisPro program (*4*) with a multiscan absorption correction using the ABSSCALE program incorporated in the software, and treated as a two-domain twin. All non-hydrogen atoms were refined anisotropically except for **ZIF-516** and **-615**, for which the low resolution precluded such treatment for non-zinc atoms. Hydrogen atoms were geometrically calculated and refined as riding atoms.

Single crystal X-ray diffraction analyses

Table 6.1. Crystal data and structure determination for **ZIF-303** (**CHA**)

Sample	**ZIF-303**
chemical formula	$C_{7.50}H_4Cl_{0.50}N_{4.25}O_{0.50}Zn$
formula mass	244.74
crystal system	trigonal
space group	$R\bar{3}$
λ (Å)	0.7749(1)
***a* (Å)**	26.9457(15)
***c* (Å)**	26.763(2)
Z	36
***V* (Å^3)**	16828(2)
temperature (K)	298(2)
size (mm^3)	0.150 × 0.100 × 0.100
density (g/cm^{-3})	0.869
measured reflections	2560
unique reflections	2560
parameters	284
restraints	283
R_{int}	0.1093
θ range (°)	2.08-18.34
R_1, wR_2	0.1247, 0.4031
***S* (GOF)**	1.189
max/min res. dens. (e/Å^3)	0.85/-0.62

$^a R_1 = \Sigma||F_o| - |F_c||/\Sigma|F_o|$; $^b wR_2 = [\Sigma w(F_o^2 - F_c^2)^2/\Sigma w(F_o^2)^2]^{1/2}$; $^c S = [\Sigma w(F_o^2 - F_c^2)^2/(N_{ref} - N_{par})]^{1/2}$.

ZIF-360 (KFI). A colorless block-shaped (120 μm × 130 μm × 150 μm) crystal of as-synthesized **ZIF-360** was quickly picked up from the mother liquor and mounted at beamline 11.3.1 at the ALS using radiation at λ = 1.2399(1) Å.

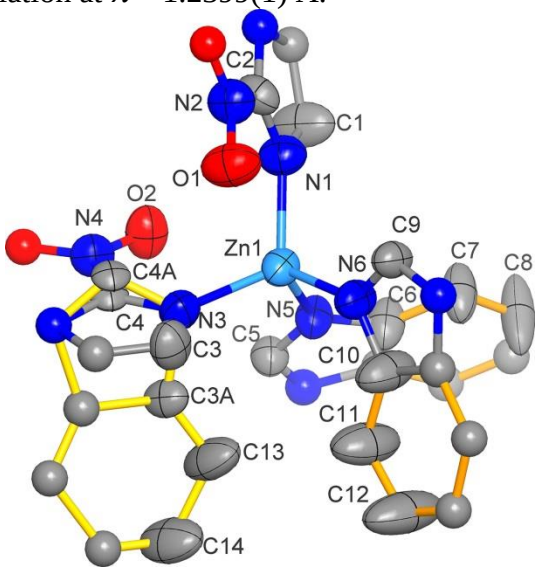

Figure 6.6. Asymmetric unit in the single-crystal structure of **ZIF-360** (thermal ellipsoids with 30% probability). Hydrogen atoms are omitted for clarity; orange bonds represent the disordering of bIM and IM. Symmetry-related atoms are not labeled and represented as spheres.

Table 6.2. Crystal data and structure determination for **ZIF-360** (**KFI**)

Sample	**ZIF-360**
chemical formula	$C_{18}H_{13}N_{10}O_4Zn_2$
formula mass	1217.24
crystal system	cubic
space group	$Im\bar{3}m$
λ **(Å)**	1.2399(1)
a **(Å)**	35.943(3)
Z	48
V **(Å^3)**	46436(13)
temperature (K)	100(2)
size (mm^3)	0.150 × 0.130 × 0.120
density (g/cm^{-3})	0.968
measured reflections	64698
unique reflections	1409
parameters	199
restraints	75
R_{int}	0.0919
θ **range (°)**	2.42-31.20
R_1, wR_2	0.0597, 0.1875
S **(GOF)**	1.095
max/min res. dens. (e/Å^3)	1.37/-0.31

$^a R_1 = \Sigma||F_o| - |F_c||/\Sigma|F_o|$; $^b wR_2 = [\Sigma w(F_o^2 - F_c^2)^2/\Sigma w(F_o^2)^2]^{1/2}$; $^c S = [\Sigma w(F_o^2 - F_c^2)^2/(N_{ref} - N_{par})]^{1/2}$.

ZIF-365 (KFI). A colorless block-shaped (110 μm × 130 μm × 140 μm) crystal of as-synthesized ZIF-365 was quickly picked up from the mother liquor and mounted at beamline 11.3.1 at the ALS using radiation at λ = 1.2399(1) Å.

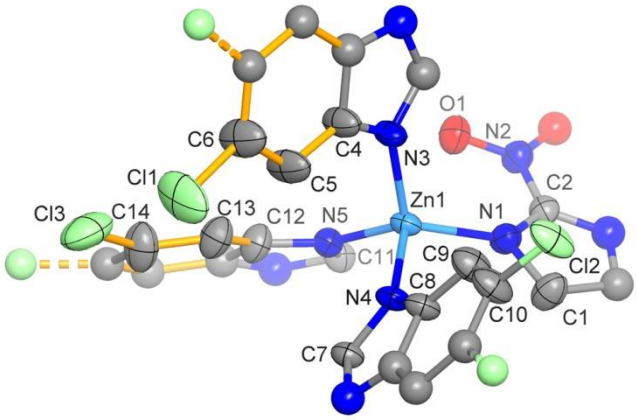

Figure 6.7. Asymmetric unit in the single-crystal structure of **ZIF-365** (thermal ellipsoids with 30% probability). Hydrogen atoms are omitted for clarity; orange bonds represent the disordering of cbIM and nIM and dashed bonds represent the disordering of the –Cl group. Symmetry-related atoms are not labeled and represented as spheres.

Table 6.3. Crystal data and structure determination for **ZIF-365** (**KFI**)

Sample	**ZIF-365**
chemical formula	$C_{20}H_{12}Cl_2N_9O_2Zn_2$
formula mass	612.054
crystal system	cubic
space group	$Im\bar{3}m$
λ **(Å)**	1.2399(1)
a **(Å)**	35.763(4)
Z	48
V **(Å^3)**	45739(13)
temperature (K)	100(2)
size (mm^3)	0.140 × 0.130 × 0.110
density (g/cm^{-3})	1.067
measured reflections	61149
unique reflections	1297
parameters	203
restraints	51
R_{int}	0.0688
θ **range (°)**	2.43-30.36
R_1, wR_2	0.0624, 0.2004
S **(GOF)**	1.110
max/min res. dens. (e/Å^3)	0.54/-0.29

[a] $R_1 = \Sigma||F_o| - |F_c||/\Sigma|F_o|$; [b] $wR_2 = [\Sigma w(F_o^2 - F_c^2)^2/\Sigma w(F_o^2)^2]^{1/2}$; [c] $S = [\Sigma w(F_o^2 - F_c^2)^2/(N_{ref} - N_{par})]^{1/2}$.

ZIF-376 (LTA). A colorless block-shaped (100 μm × 100 μm × 100 μm) crystal of as-synthesized **ZIF-376** was quickly picked up from the mother liquor and mounted on a Bruker D8 Venture diffractometer with the Cu target selected (λ = 1.54178 Å). Due to significant intrinsic disorder in the crystal, imidazolate and phenyl rings were treated with rigid bond constraints, and to keep the groups planar. The geometry of the functionalized imidazoles was modeled using the known geometry from other reported ZIFs.

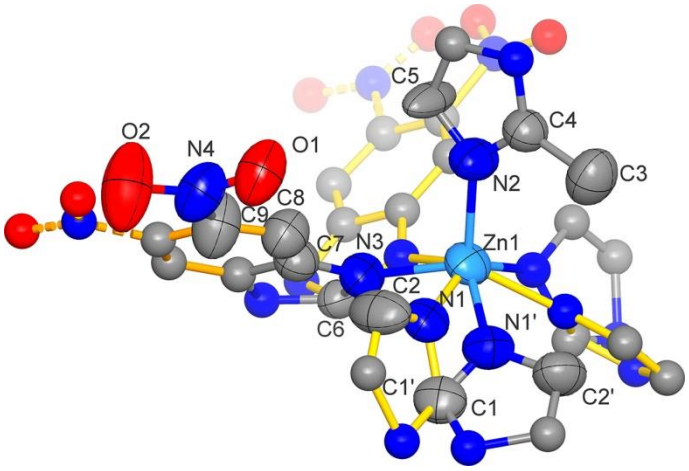

Figure 6.8. Asymmetric unit in the single-crystal structure of **ZIF-376** (thermal ellipsoids with 30% probability). Hydrogen atoms are omitted for clarity; orange bonds represent the disordering of nbIm and Im and dashed bonds represent the disordering of the $–NO_2$ group. The dashed double-colored sets represent the disordering of Im and nbIm. Symmetry-related atoms are not labeled and represented as spheres.

Table 6.4. Crystal data and structure determination for **ZIF-376** (**LTA**)

Sample	**ZIF-376**
chemical formula	$C_{3.625}H_{2.875}N_{2.125}O_{0.25}Zn$
formula mass	225.78
crystal system	cubic
space group	$Pm\bar{3}m$
λ **(Å)**	1.54178
a **(Å)**	22.688(3)
Z	24
V **(Å^3)**	11679(4)
temperature (K)	100(2)
size (mm^3)	0.100 × 0.100 × 0.100
density (g/cm^{-3})	0.770
measured reflections	7779
unique reflections	765
parameters	132
restraints	148
R_{int}	0.0634
θ **range (°)**	3.37-39.94
R_1, wR_2	0.01189, 0.3415
S **(GOF)**	1.092
max/min res. dens. (e/Å^3)	0.64/-0.38

$^a R_1 = \Sigma||F_o| - |F_c||/\Sigma|F_o|$; $^b wR_2 = [\Sigma w(F_o^2 - F_c^2)^2/\Sigma w(F_o^2)^2]^{1/2}$; $^c S = [\Sigma w(F_o^2 - F_c^2)^2/(N_{ref} - N_{par})]^{1/2}$.

ZIF-386 (AFX). A colorless block-shaped (200 μm × 200 μm × 80 μm) crystal of as-synthesized **ZIF-386** was quickly picked up from the mother liquor and on a Bruker MicroSTAR-H APEX II diffractometer with λ = 0.71073 Å.

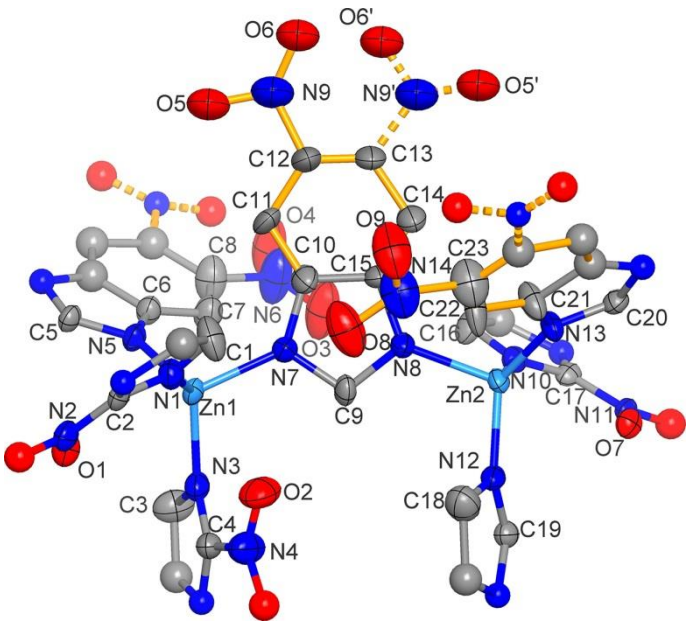

Figure 6.9. Asymmetric unit in the single-crystal structure of **ZIF-386** (thermal ellipsoids with 15% probability). Hydrogen atoms are omitted for clarity; orange bonds represent the disordering of nbIM and IM and dashed bonds represent the disordering of the $–NO_2$ group. Symmetry-related atoms are not labeled and represented as spheres.

Table 6.5. Crystal data and structure determination for **ZIF-386** (**AFX**)

Sample	**ZIF-386**
chemical formula	$C_{36}H_{23}N_{22}O_{12}Zn_4$
formula mass	1217.24
crystal system	hexagonal
space group	$P6_3/mmc$
λ **(Å)**	1.54178
a **(Å)**	27.1315(7)
c **(Å)**	34.4505(12)
Z	12
V **(Å^3)**	21962.1(14)
temperature (K)	100(2)
size /mm^3	0.200 × 0.200 × 0.080
density (g/cm^{-3})	1.104
measured reflections	78188
unique reflections	2908
parameters	380
restraints	95
R_{int}	0.0505
θ **range (°)**	1.88-43.00
R_1, wR_2	0.0792, 0.2850
S **(GOF)**	1.143
max/min res. dens. (e/Å^3)	0.79/-0.39

[a] $R_1 = \Sigma||F_o| - |F_c||/\Sigma|F_o|$; [b] $wR_2 = [\Sigma w(F_o^2 - F_c^2)^2/\Sigma w(F_o^2)^2]^{1/2}$; [c] $S = [\Sigma w(F_o^2 - F_c^2)^2/(N_{ref} - N_{par})]^{1/2}$.

ZIF-408 (moz). A colorless block-shaped (40 μm × 60 μm × 80 μm) crystal of as-synthesized **ZIF-408** was quickly picked up from the mother liquor and mounted at beamline BL17U1 at the SSRF using radiation at λ = 0.7292(9) Å. Due to the poor resolution of 1.36 Å as a result of weak diffraction from significant intrinsic disorder in the crystal, imidazolate and phenyl rings were treated with rigid group and bond constraints. The geometry of the functionalized imidazoles was modeled using the known geometry from other reported ZIFs.

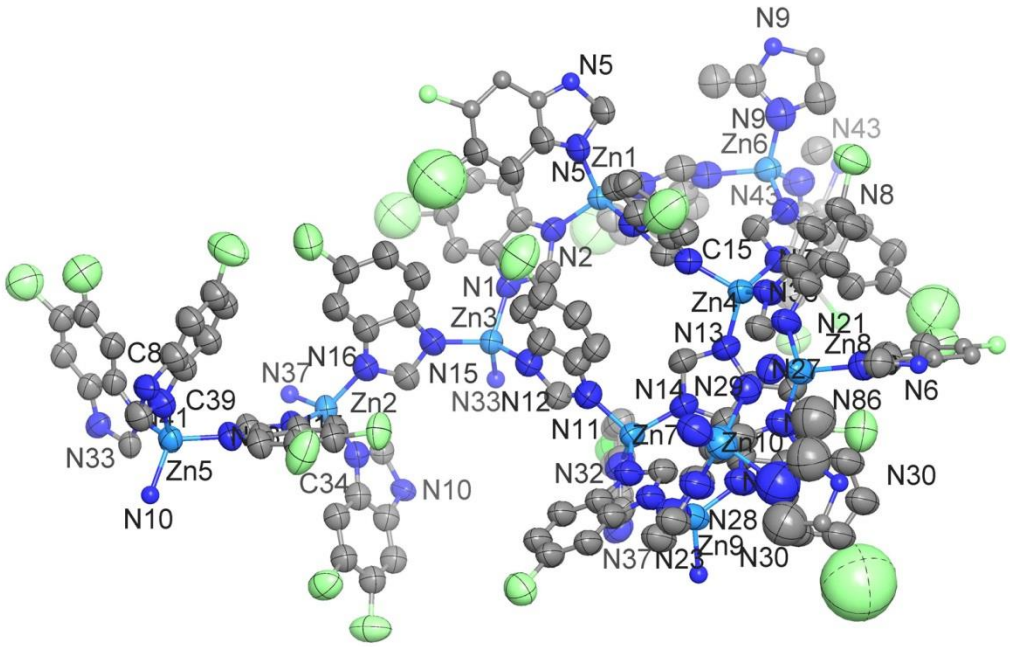

Figure 6.10. Asymmetric unit in the single-crystal structure of **ZIF-408** (thermal ellipsoids with 15% probability). Hydrogen atoms are omitted for clarity. Symmetry-related atoms are not labeled and represented as spheres.

Table 6.6. Crystal data and structure determination for **ZIF-408** (**moz**)

Sample	**ZIF-408**
chemical formula	$C_{273}H_{149}Cl_{39}N_{78}O_2Zn_{20}$
formula mass	7243
crystal system	Cubic
space group	$Im\bar{3}$
λ (Å)	0.72929(1)
***a* (Å)**	70.593(8)
Z	24
***V* (Å^3)**	351791(122)
temperature (K)	100(2)
size (mm^3)	0.04 × 0.06 × 0.08
density (g/cm^{-3})	0.821
measured reflections	26180
unique reflections	14490
parameters	453
restraints	87
R_{int}	0.0141
θ range (°)	0.7-16.3
R_1, wR_2	0.1863, 0.5573
***S* (GOF)**	1.697
max/min res. dens. (e/Å^3)	0.99/-0.70

[a] $R_1 = \Sigma||F_o| - |F_c||/\Sigma|F_o|$; [b] $wR_2 = [\Sigma w(F_o^2 - F_c^2)^2/\Sigma w(F_o^2)^2]^{1/2}$; [c] $S = [\Sigma w(F_o^2 - F_c^2)^2/(N_{ref} - N_{par})]^{1/2}$.

ZIF-410 (GME). A colorless block-shaped (80 μm × 85 μm × 120 μm) crystal of as-synthesized **ZIF-410** was quickly picked up from the mother liquor and mounted on a Bruker MicroSTAR-H APEX II diffractometer with λ = 0.71073 Å.

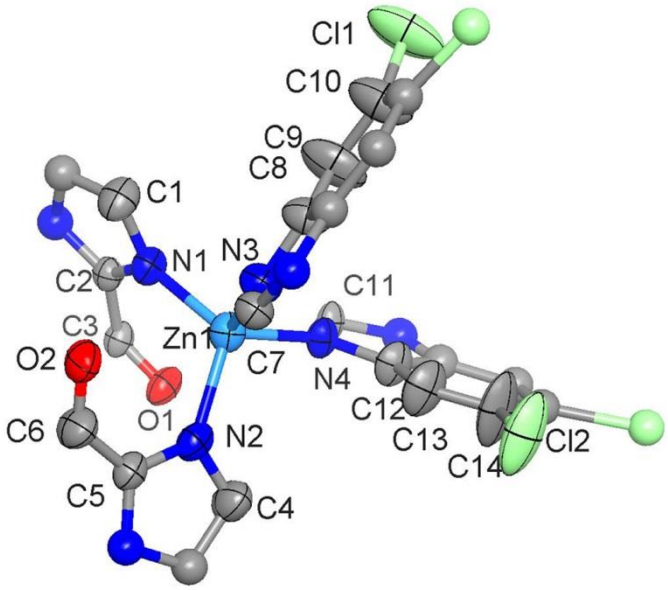

Figure 6.11. Asymmetric unit in the single crystal structure of **ZIF-410** (thermal ellipsoids with 15% probability). Hydrogen atoms are omitted for clarity; the dashed bonds represent the disordering of the –Cl group and the disordering of O on the –CHO group of the aIM. Symmetry-related atoms are not labeled and represented as spheres.

Table 6.7. Crystal data and structure determination for **ZIF-410** (**GME**)

Sample	**ZIF-410**
chemical formula	$C_{11}H_7ClN_4OZn_3$
formula mass	312.03
crystal system	hexagonal
space group	$P6_3/mmc$
λ **(Å)**	1.54178
a **(Å)**	25.9453(6)
c **(Å)**	19.5015(6)
Z	24
V **(Å^3)**	11368.8(6)
temperature (K)	100(2)
size (mm^3)	0.120 × 0.085 × 0.080
density (g/cm^{-3})	1.094
measured reflections	19478
unique reflections	1335
parameters	189
restraints	35
R_{int}	0.0502
θ **range (°)**	1.97-40.06
R_1, wR_2	0.0692, 0.2506
S **(GOF)**	1.138
max/min res. dens. (e/Å^3)	0.63/-0.28

[a] $R_1 = \Sigma||F_o| - |F_c||/\Sigma|F_o|$; [b] $wR_2 = [\Sigma w(F_o^2 - F_c^2)^2/\Sigma w(F_o^2)^2]^{1/2}$; [c] $S = [\Sigma w(F_o^2 - F_c^2)^2/(N_{ref} - N_{par})]^{1/2}$.

ZIF-486 (GME). A colorless block-shaped (100 μm × 100 μm × 200 μm) crystal of as-synthesized **ZIF-486** was quickly picked up from the mother liquor and mounted at beamline 11.3.1 at the ALS using radiation at λ = 0.7749(1) Å. Due to weak diffraction from significant intrinsic disorder in the crystal, imidazolate and phenyl rings were treated with rigid group and bond constraints. The geometry of the functionalized imidazoles was modeled using the known geometry from other reported ZIFs.

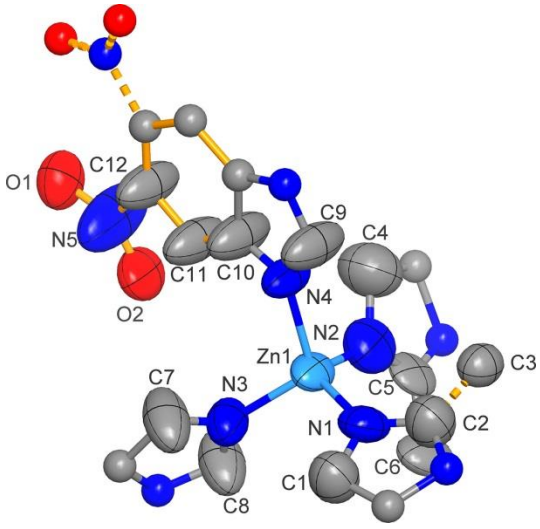

Figure 6.12. Asymmetric unit in the single-crystal structure of **ZIF-486** (thermal ellipsoids with 30% probability). Hydrogen atoms are omitted for clarity; orange bonds represent the disordering of nbIM and IM and dashed bonds represent the disordering of the $–NO_2$ group. Symmetry-related atoms are not labeled and represented as spheres.

Table 6.8. Crystal data and structure determination for **ZIF-486** (**GME**)

Sample	**ZIF-486**
chemical formula	$C_{7.50}H_{7.40}N_{4.20}O_{0.40}Zn$
formula mass	228.15
crystal system	hexagonal
space group	*P6₃/mmc*
λ (Å)	0.7749(1)
***a* (Å)**	27.0807(16)
***c* (Å)**	16.7619(16)
Z	24
***V* (Å^3)**	10645.7(16)
temperature (K)	100(2)
size (mm^3)	0.200 × 0.200 × 0.100
density (g/cm^{-3})	0.854
measured reflections	15269
unique reflections	1469
parameters	132
restraints	136
R_{int}	0.0534
θ range (°)	2.31-20.04
R_1, wR_2	0.1153, 0.3525
***S* (GOF)**	1.020
max/min res. dens. (e/Å^3)	1.09/-0.52

$^a R_1 = \Sigma||F_o| - |F_c||/\Sigma|F_o|$; $^b wR_2 = [\Sigma w(F_o^2 - F_c^2)^2/\Sigma w(F_o^2)^2]^{1/2}$; $^c S = [\Sigma w(F_o^2 - F_c^2)^2/(N_{ref} - N_{par})]^{1/2}$.

ZIF-412 (ucb). A colorless block-shaped (100 μm × 120 μm × 130 μm) crystal of as-synthesized **ZIF-412** was quickly picked up from mother liquor and mounted at beamline 11.3.1 at the ALS using radiation at λ = 0.8265(1) Å.

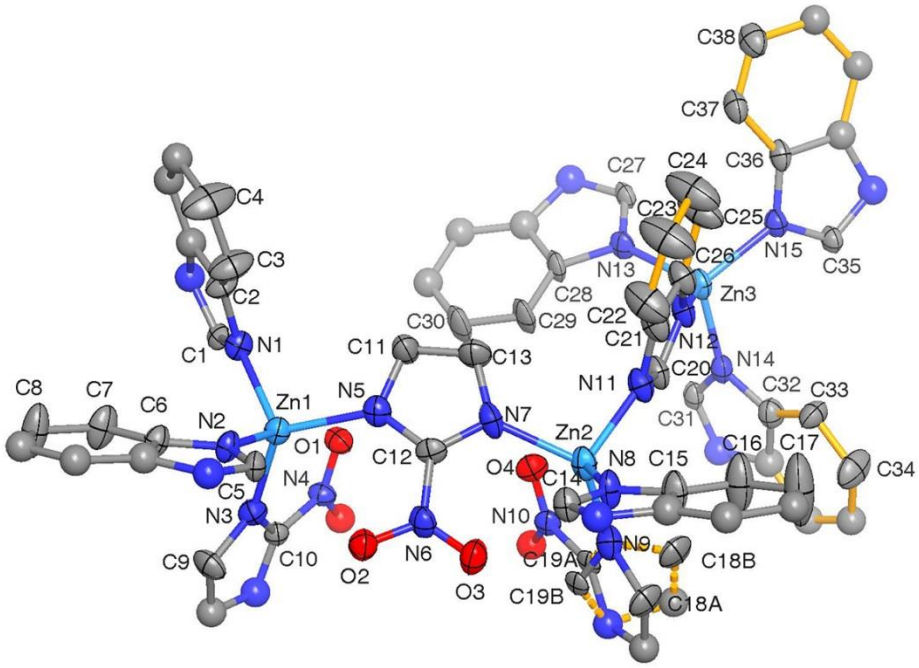

Figure 6.13. Asymmetric unit in the single crystal structure of **ZIF-412** (thermal ellipsoids with 15% probability). Hydrogen atoms are omitted for clarity; orange bonds represent the disordering of bIm and Im. Symmetry-related atoms are not labeled and represented as spheres.

Table 6.9. Crystal data and structure determination for **ZIF-412** (**ucb**)

Sample	**ZIF-412**
chemical formula	$C_{31.6}H_{22.95}N_{13.85}O_{3.7}Zn_3$
formula mass	852.03
crystal system	cubic
space group	$Fm\bar{3}m$
λ **(Å)**	0.8265(1)
a **(Å)**	72.205(2)
Z	192
V **(Å^3)**	376445(31)
temperature (K)	100(2)
size (mm^3)	0.100 × 0.120 × 0.130
density (g/cm^{-3})	0.722
measured reflections	270972
unique reflections	4845
parameters	516
restraints	137
R_{int}	0.1418
θ **range (°)**	1.70-19.30
R_1, wR_2	0.0434, 0.1503
S **(GOF)**	1.081
max/min res. dens. (e/Å^3)	0.32/-0.29

$^a R_1 = \Sigma||F_o| - |F_c||/\Sigma|F_o|$; $^b wR_2 = [\Sigma w(F_o^2 - F_c^2)^2/\Sigma w(F_o^2)^2]^{1/2}$; $^c S = [\Sigma w(F_o^2 - F_c^2)^2/(N_{ref} - N_{par})]^{1/2}$.

ZIF-413 (ucb). A yellow block-shaped (100 μm × 100 μm × 100 μm) crystal of as-synthesized **ZIF-413** was quickly picked up from the mother liquor and mounted at beamline 11.3.1 at the ALS using radiation at λ = 1.2399(1) Å.

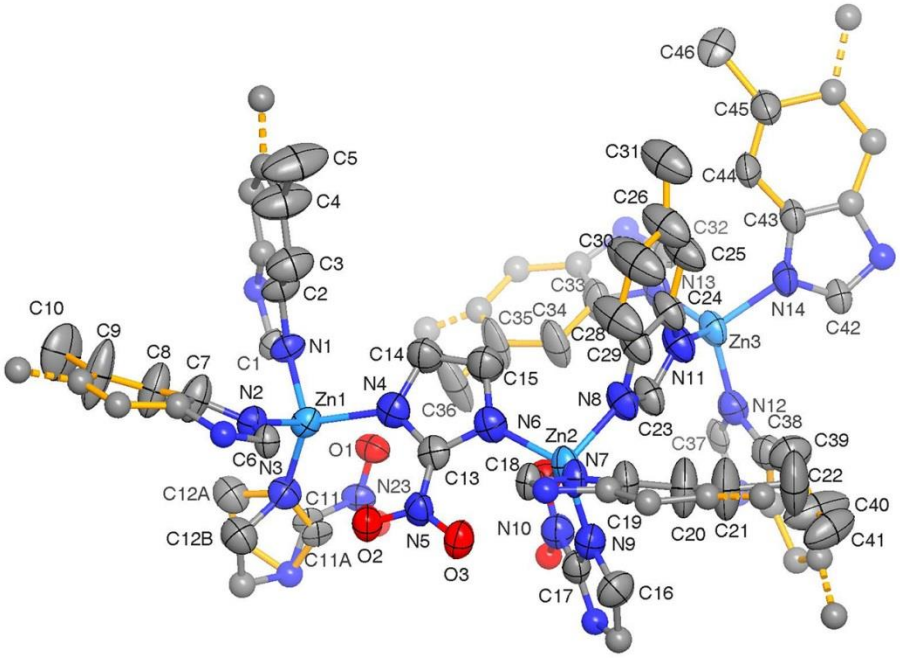

Figure 6.14. Asymmetric unit in the single crystal structure of **ZIF-413** (thermal ellipsoids with 15% probability). Hydrogen atoms are omitted for clarity; orange bonds represent the disordering of mbIm and Im and dashed bonds represent the disordering of the $–CH_3$ group. Symmetry-related atoms are not labeled and represented as spheres.

Table 6.10. Crystal data and structure determination for **ZIF-413** (**ucb**)

Sample	**ZIF-413**
chemical formula	$C_{33.5}H_{26.49}N_{13.81}O_{3.63}Zn_3$
formula mass	876.74
crystal system	cubic
space group	$Fm\bar{3}m$
λ **(Å)**	1.2399(1)
a **(Å)**	72.3673(14)
Z	192
V **(Å^3)**	378989(22)
temperature (K)	100(2)
size (mm^3)	0.100 × 0.100 × 0.100
density (g/cm^{-3})	0.737
measured reflections	168049
unique reflections	5478
parameters	561
restraints	362
R_{int}	0.0295
θ **range (°)**	1.96-31.06
R_1, wR_2	0.1032, 0.3434
S **(GOF)**	1.050
max/min res. dens. (e/Å^3)	1.11/-0.32

$^a R_1 = \Sigma||F_o| - |F_c||/\Sigma|F_o|$; $^b wR_2 = [\Sigma w(F_o^2 - F_c^2)^2/\Sigma w(F_o^2)^2]^{1/2}$; $^c S = [\Sigma w(F_o^2 - F_c^2)^2/(N_{ref} - N_{par})]^{1/2}$.

ZIF-414 (ucb). A colorless block-shaped (90 μm × 90 μm × 90 μm) crystal of as-synthesized **ZIF-414** was quickly picked up from the mother liquor and mounted at beamline 11.3.1 at the ALS using radiation at λ = 0.7749(1) Å. Due to the poor resolution of 1.33 Å as a result of weak diffraction from significant intrinsic disorder in the crystal, imidazolate and phenyl rings were treated with rigid group and bond constraints. The geometry of the functionalized imidazolate linkers was modeled using the known geometry from other reported ZIFs.

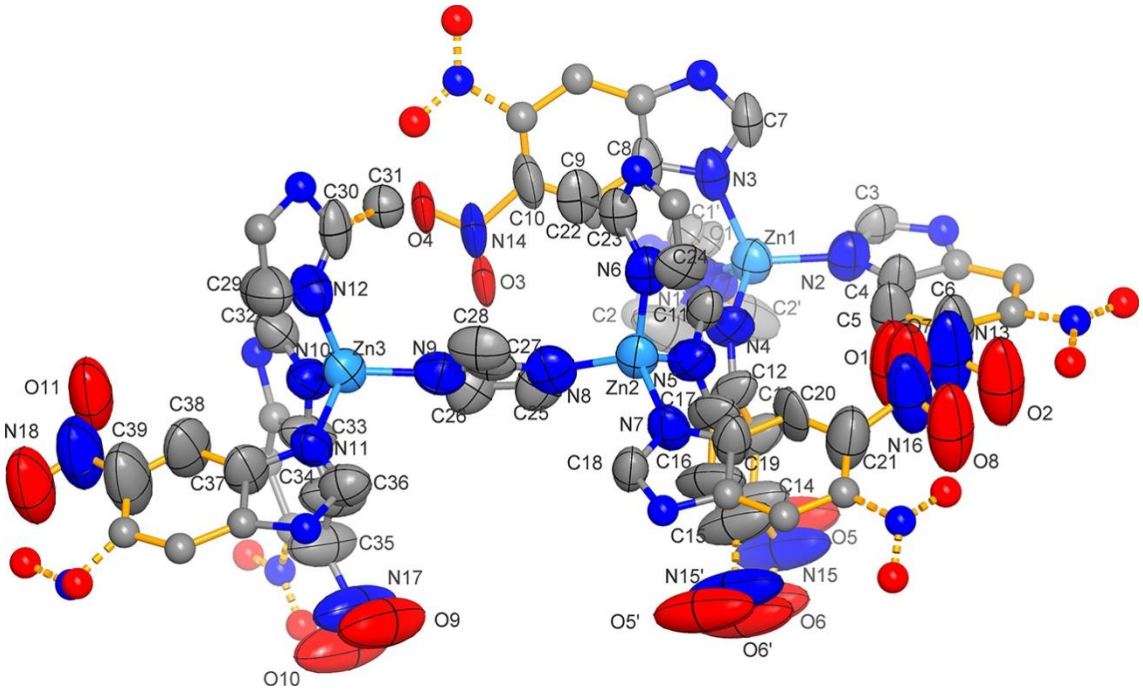

Figure 6.15. Asymmetric unit in the single-crystal structure of **ZIF-414** (thermal ellipsoids with 15% probability). Hydrogen atoms are omitted for clarity; orange bonds represent the disordering of nbIm and Im and dashed bonds represent the disordering of the $–NO_2$ group. Symmetry-related atoms are not labeled and represented as spheres.

Table 6.11. Crystal data and structure determination for **ZIF-414** (**ucb**)

Sample	**ZIF-414**
chemical formula	$C_{29.08}H_{24.45}N_{14.30}O_{4.60}Zn_3$
formula mass	843.95
crystal system	cubic
space group	$Fm\bar{3}m$
λ **(Å)**	0.7749(1)
a **(Å)**	72.2609(18)
Z	192
V **(Å^3)**	377320(28)
temperature (K)	100(2)
size (mm^3)	0.090 × 0.090 × 0.090
density (g/cm^{-3})	0.713
measured reflections	285177
unique reflections	4062
parameters	600
restraints	500
R_{int}	0.0928
θ **range (°)**	2.04-16.93
R_1, wR_2	0.0932, 0.2491
S **(GOF)**	1.157
max/min res. dens. (e/Å^3)	0.37/-0.29

$^a R_1 = \Sigma||F_o| - |F_c||/\Sigma|F_o|$; $^b wR_2 = [\Sigma w(F_o^2 - F_c^2)^2/\Sigma w(F_o^2)^2]^{1/2}$; $^c S = [\Sigma w(F_o^2 - F_c^2)^2/(N_{ref} - N_{par})]^{1/2}$.

ZIF-516 (ykh). A colorless block-shaped (80 μm × 40 μm × 40 μm) crystal of as-synthesized **ZIF-516** was quickly picked up from mother liquor and mounted at beamline 11.3.1 at the ALS using radiation at λ = 0.7749(1) Å. Only 1.33 Å resolution could be obtained for this sample, which precluded anisotropic refinement and individual atomic positions except for zinc atoms. Considering the geometry of imidazolate and its functionalized derivatives are known, a rigid body refinement was used to aid structure refinement by first modeling benzimidazolate groups, using Materials Studio 7.0, to improve phasing, then refining and inspecting Fourier difference map to locate the bromo- and methyl- functional groups. However, there were no clear crystallographically independent positions for either functional group, which may in part be due to the low resolution of the data and disordered nature of these groups, but also that 5-bromobenzimidazole and 5-methylbenzimidazole may occupy the same crystallographic sites due to their similar size and shape. Thus, although the NMR ratio is 0.77:1.23 5-bromobenzimidazole:5-methylbenzimidazole, the functional groups were modeled as equally disordered across all sites, thus being modeled in a 1:1 ratio.

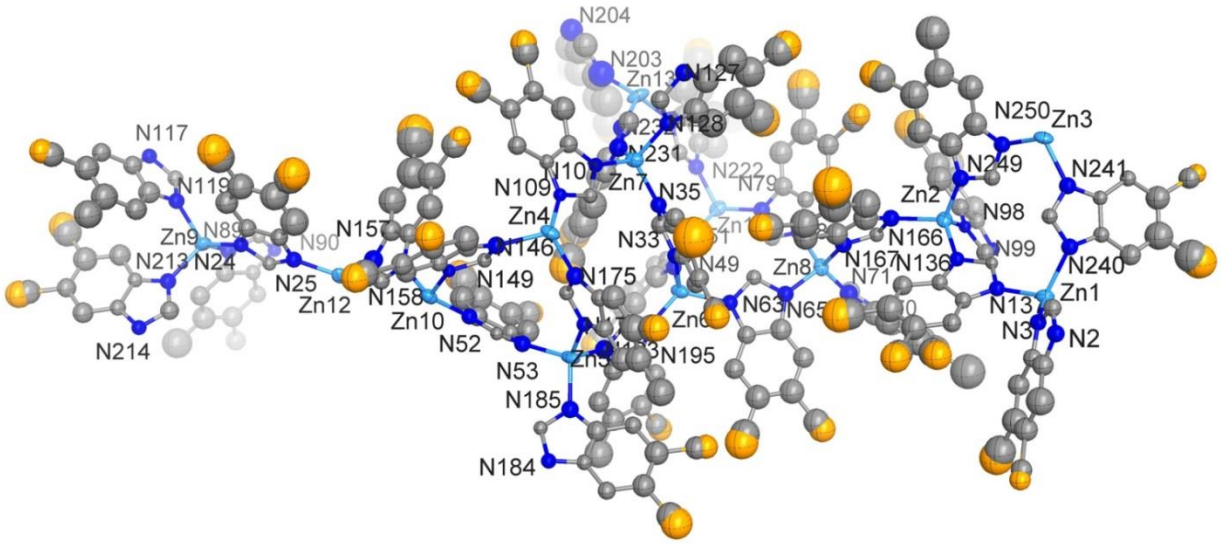

Figure 6.16. Asymmetric unit in the single-crystal structure of **ZIF-516** (thermal ellipsoids with 15% probability). Hydrogen atoms are omitted for clarity. Symmetry-related atoms are not labeled and represented as spheres.

Table 6.12. Crystal data and structure determination for **ZIF-516**

Sample	**ZIF-516**
chemical formula	$C_{195}H_{77}Br_{13}N_{52}Zn_{13}$
formula mass	5036.72
crystal system	tetragonal
space group	*P4₃2₁2*
λ (Å)	0.7749(1)
***a* (Å)**	29.157(3)
***c* (Å)**	69.955(9)
Z	8
***V* (Å^3)**	59470(15)
temperature (K)	100(2)
size (mm^3)	0.080 × 0.040 × 0.040
density (g/cm^{-3})	1.125
measured reflections	94423
unique reflections	13193
parameters	609
restraints	271
***R*$_{int}$**	0.1308
θ range (°)	1.95-16.95
***R*$_1$, *wR*$_2$**	0.0972, 0.2730
***S* (GOF)**	1.047
Flack parameter	0.498(6)*
max/min res. dens. (e/Å^3)	0.61/-0.65

$^a R_1 = \Sigma||F_o| - |F_c||/\Sigma|F_o|$; $^b wR_2 = [\Sigma w(F_o^2 - F_c^2)^2/\Sigma w(F_o^2)^2]^{1/2}$; $^c S = [\Sigma w(F_o^2 - F_c^2)^2/(N_{ref} - N_{par})]^{1/2}$.

*Note that the low resolution precludes determining the framework chirality.

ZIF-586 (ykh). A colorless plate-shaped (10 μm × 30 μm × 30 μm) crystal of as-synthesized **ZIF-586** was quickly picked up from the mother liquor and mounted at beamline BL17U1 at the SSRF using radiation at λ = 0. 7292(9) Å. Due to the poor resolution of 1.55 Å as a result of weak diffraction from significant intrinsic disorder in the crystal, imidazolate and phenyl rings were treated with rigid group and bond constraints. The functional groups were not determined due to the poor resolution of crystals.

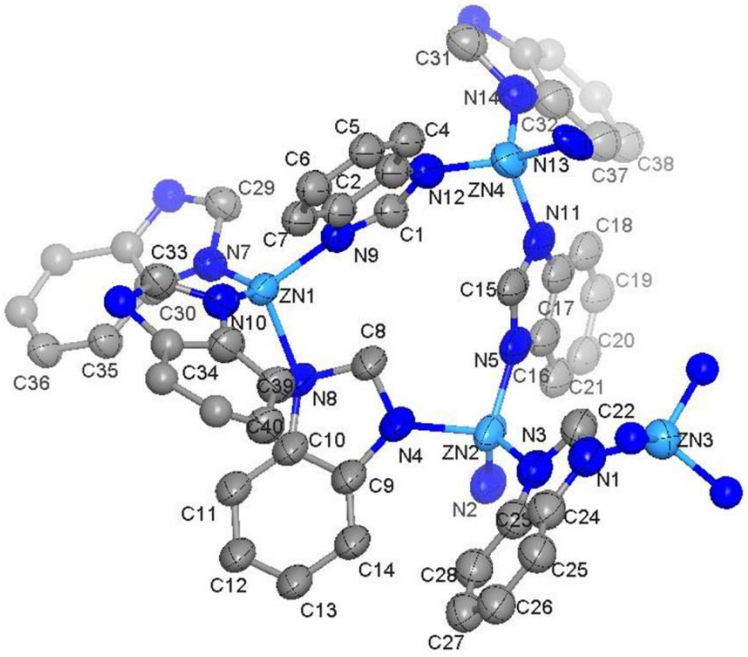

Figure 6.17. Asymmetric unit in the single-crystal structure of **ZIF-586** (thermal ellipsoids with 30% probability). Hydrogen atoms are omitted for clarity. Symmetry-related atoms are not labeled and represented as spheres.

Table 6.13. Crystal data and structure determination for **ZIF-586** (**ykh**)

Sample	**ZIF-586**
chemical formula	$C_{304}\ N_{104}\ Zn_{26}$
formula mass	6807.70
crystal system	tetragonal
space group	*P4₂/ncm*
λ (Å)	0.72929(1)
***a* (Å)**	29.744(4)
***c* (Å)**	34.550(7)
Z	4
***V* (Å^3)**	30567(11)
temperature (K)	100(2)
size (mm^3)	0.03× 0.03 × 0.01
density (g/cm^{-3})	0.846
measured reflections	2255
unique reflections	2255
parameters	161
restraints	185
R_{int}	0.0496
θ range (°)	1.399-13.605
R_1, wR_2	0.2256, 0.5573
***S* (GOF)**	1.021
max/min res. dens. (e/Å^3)	0.56/-0.40

$^a R_1 = \Sigma||F_o| - |F_c||/\Sigma|F_o|$; $^b wR_2 = [\Sigma w(F_o^2 - F_c^2)^2/\Sigma w(F_o^2)^2]^{1/2}$; $^c S = [\Sigma w(F_o^2 - F_c^2)^2/(N_{ref} - N_{par})]^{1/2}$.

ZIF-615 (gcc). A colorless rod-shaped (50 μm × 15 μm × 15 μm) crystal of as-synthesized **ZIF-615** was quickly picked up from mother liquor and mounted at beamline 5.0.2 at the ALS using radiation at λ = 0.8999(1) Å. Only 1.4 Å resolution could be obtained for this sample, which precluded anisotropic refinement and individual atomic positions except for zinc atoms. Considering the geometry of imidazolate and its functionalized derivatives are known, a rigid body refinement was used to aid structure refinement by first modeling imidazolate groups with Materials Studio 7.0, since these groups are common to both linkers present in this framework to improve phasing, then refining these rigid bodies and inspecting Fourier difference map to locate the phenyl rings and disordered bromine groups 5-bromobenzimidazole in order to distinguish this linker's position from that of 4-nitroimidazole. When the position of 5-bromobenzimidazole was found, this moiety was incorporated into the rigid body refinement and the refinement and difference map inspection process was iterated with further improved phasing as more of the structure is modeled until all 5-bromobenzimidazole positions were located. The 4-nitroimidazole groups were then modeled, with the nitro group constrained as a 1:1 split occupancy between the 4- and 5-positions on the imidazole except in one case where the thermal ellipsoids failed to converge on the 5-position. Checking the framework confirmed that the nitro group would clash with a fully-occupied 5-bromobenzimidazole, thus the 4-position on nitroimidazole was modeled with the nitro group at full occupancy.

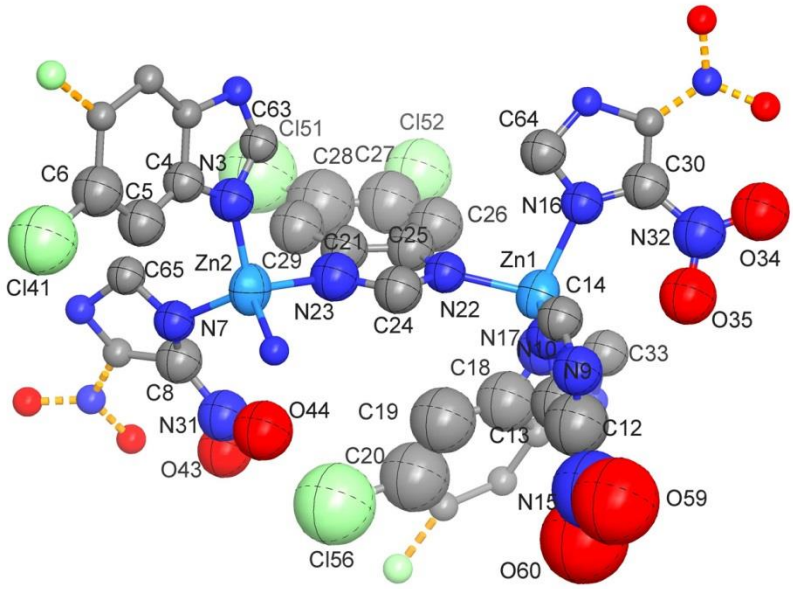

Figure 6.18. Asymmetric unit in the single crystal structure of **ZIF-615** (thermal ellipsoids with 15% probability). Hydrogen atoms are omitted for clarity; orange bonds represent the disordering of 4-nIm. Symmetry-related atoms are not labeled and represented as spheres.

Table 6.14. Crystal data and structure determination for **ZIF-615** (**gcc**)

Sample	**ZIF-615**
chemical formula	$C_{20}H_{11}Cl_2N_{10}O_4Zn_2$
formula mass	657.03
crystal system	hexagonal
space group	*P6₃/mmc*
λ (Å)	0.8999(1)
***a* (Å)**	31.731(6)
***c* (Å)**	28.412(6)
Z	12
***V* (Å^3)**	24774(11)
temperature (K)	100(2)
size (mm^3)	0.050 × 0.015 × 0.015
density (g/cm^{-3})	1.058
measured reflections	15250
unique reflections	4924
parameters	95
restraints	28
R_{int}	0.208
θ range (°)	1.63-18.74
R_1, wR_2	0.1933, 0.5500
***S* (GOF)**	1.084
max/min res. dens. (e/Å^3)	0.47/-0.57

$^a R_1 = \Sigma||F_o| - |F_c||/\Sigma|F_o|$; $^b wR_2 = [\Sigma w(F_o^2 - F_c^2)^2/\Sigma w(F_o^2)^2]^{1/2}$; $^c S = [\Sigma w(F_o^2 - F_c^2)^2/(N_{ref} - N_{par})]^{1/2}$.

ZIF-725 (bam). A colorless block-shaped (80 μm × 100 μm × 100 μm) crystal of as-synthesized **ZIF-725** was quickly picked up from the mother liquor and mounted at beamline 11.3.1 at the ALS using radiation at λ = 0.7749(1) Å. Due to the poor resolution of 1.38 Å as a result of weak diffraction from significant intrinsic disorder in the crystal, imidazolate and phenyl rings were treated with rigid group and bond constraints. The geometry of the functionalized imidazolate linkers were modeled using the known geometry from other reported ZIFs.

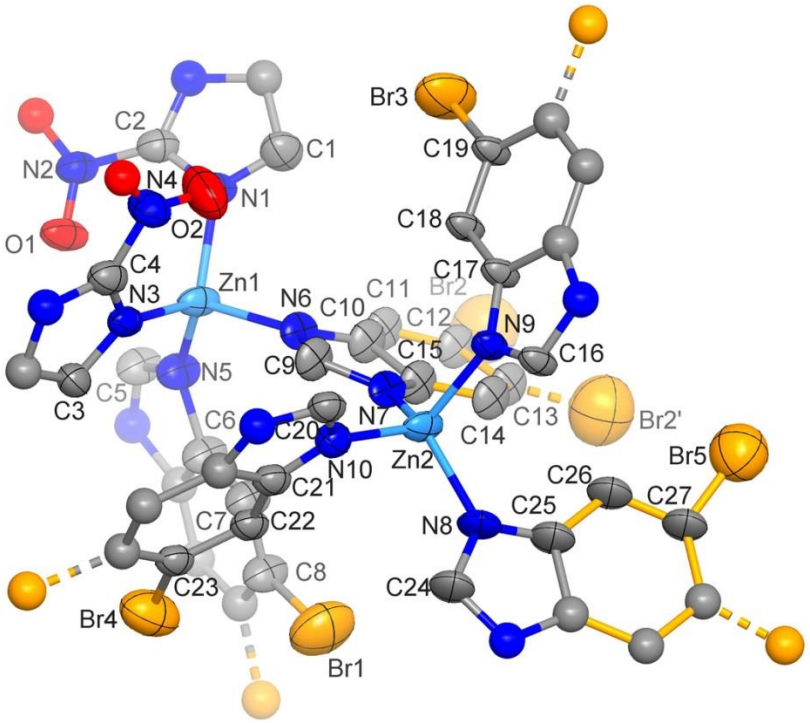

Figure 6.19. Asymmetric unit in the single-crystal structure of **ZIF-725** (thermal ellipsoids with 30% probability). Hydrogen atoms are omitted for clarity, orange bonds represent the disordering of bbIM and IM and dashed bonds represent the disordering of the –Br group. Symmetry-related atoms are not labeled and represented as spheres.

Table 15. Crystal data and structure determination for **ZIF-725** (**bam**)

Sample	**ZIF-725**
chemical formula	$C_{22}H_{13.50}Br_{2.50}N_9O_2Zn_2$
formula mass	766.43
crystal system	hexagonal
space group	*P*6/*mmm*
λ **(Å)**	1.0332(1)
a **(Å)**	42.586(3)
c **(Å)**	19.8692(13)
Z	24
V **(Å^3)**	31206(4)
temperature (K)	100(2)
size (mm^3)	0.100 × 0.100 × 0.080
density (g/cm^{-3})	0.979
measured reflections	90065
unique reflections	2411
parameters	348
restraints	473
R_{int}	0.2655
θ **range (°)**	2.12-21.97
R_1, wR_2	0.1621, 0.4377
S **(GOF)**	1.152
max/min res. dens. (e/Å^3)	0.72/-0.57

$^a R_1 = \Sigma||F_o| - |F_c||/\Sigma|F_o|$; $^b wR_2 = [\Sigma w(F_o^2 - F_c^2)^2/\Sigma w(F_o^2)^2]^{1/2}$; $^c S = [\Sigma w(F_o^2 - F_c^2)^2/(N_{ref} - N_{par})]^{1/2}$.

Bibliography

(1) Müller, P. *Crystallogr. Rev.* **2009**, *15* (1), 57–83.

(2) Wlodawer, A.; Minor, W.; Dauter, Z.; Jaskolski, M. *FEBS J.* **2008**, *275* (1), 1–21.

(3) Wang, J.; Dauter, M.; Alkire, R.; Joachimiak, A.; Dauter, Z. *Acta Crystallogr. Sect. D Biol. Crystallogr.* **2007**, *63* (12), 1254–1268.

(4) Yang, J.; Zhang, Y.-B.; Liu, Q.; Trickett, C. A.; Gutierrez-Puebla, E.; Monge, M. Á.; Cong, H.; Aldossary, A.; Deng, H.; Yaghi, O. M. *J. Am. Chem. Soc.* **2017**, *Just Accepted*, DOI:10.1021/jacs.7b02272.

(5) Palatinus, L.; Chapuis, G. *J. Appl. Crystallogr.* **2007**, *40* (4), 786–790.

(6) Thorn, A.; Dittrich, B.; Sheldrick, G. M. *Acta Crystallogr. Sect. A Found. Crystallogr.* **2012**, *68* (4), 448–451.

(7) Bruker. In *APEX2 (Bruker AXS Inc., Madison, Wisconsin, U.S.A)*; 2010.

(8) Sheldrick, G. M. *Acta Crystallogr. Sect. A Found. Crystallogr.* **2007**, *64* (1), 112–122.

(9) Oxford Diffraction/Agilent Technologies UK Ltd, Yarnton, E. .

(10) Dolomanov, O. V.; Bourhis, L. J.; Gildea, R. J.; Howard, J. A. K.; Puschmann, H. *J. Appl. Crystallogr.* **2009**, *42* (2), 339–341.

(11) Rees, B.; Jenner, L.; Yusupov, M. *Acta Crystallogr. Sect. D Biol. Crystallogr.* **2005**, *61* (9), 1299–1301.

(12) Spek, A. L. *Acta Crystallogr. Sect. D Biol. Crystallogr.* **2009**, *65* (2), 148–155.

(13) Eddaoudi, M.; Kim, J.; Rosi, N.; Vodak, D.; Wachter, J.; O'Keeffe, M.; Yaghi, O. M. *Science* **2002**, *295* (5554), 469–472.

(14) Pettersen, E. F.; Goddard, T. D.; Huang, C. C.; Couch, G. S.; Greenblatt, D. M.; Meng, E. C.; Ferrin, T. E. *J. Comput. Chem.* **2004**, *25* (13), 1605–1612.

(15) Wang, B.; Côté, A. P.; Furukawa, H.; O'Keeffe, M.; Yaghi, O. M. *Nature* **2008**, *453* (7192), 207–211.

Chapter 7: Conclusion and Outlook

The chemical and structural makeup, along with their influence on the properties of MOFs, is a rich field of study that continues to push the boundaries of scientific knowledge the deeper it is explored. Chapters 2 and 3 are testament to this, with key structural features in UiO-66 and sulfated MOF-808 identified and manipulated to drastically alter the properties of the MOF. Indeed, in both of these cases, simply adding moisture leads to dramatic changes in the physical characteristics of the MOFs, yet by the average unit cell very little has changed. This should serve simultaneously as a caution, but also as encouragement that solid-state materials are much more complex than they outwardly appear. This offers the potential to invent and discover far more than meets the eye. Further, identification and an understanding of the dominant underlying chemical features that dictate the properties of a given material could lead to the next functional material or billion-dollar catalyst. This is not only limited to MOFs, but applies throughout solid-state and materials chemistry. Besides their own value, MOFs offer a way to probe solid-state chemistry through their crystalline nature and extremely large internal surface area. This cannot be replicated for materials that are only active on their external surface, as is evidenced with sulfated MOF-808 and sulfated zirconia.

Much remains to be investigated however, even with MOFs that appear fairly similar at first glance. For instance, even the coordination mode of the chemically comparable sulfate and selenate groups when coordinated to MOF-808 have some differences in aqueous phase. It was also quite unexpected that the dominant, or in the case of selenate, exclusively bridging mode is converted to chelating only upon removal of solvent molecules from the cavities. Indeed, much of MOF chemistry that is studied, in particular related to gas uptake and storage, occurs at the solid-gas phase interface of the internal surface of the MOF, and not at the solid-liquid interface that exists when MOFs are immersed in solution. However, the vast majority of MOF structures are reported in the as-synthesized form, or without first removing the mother liquor. This standard practice is for both ease of characterization as well as to prevent damage to the crystals, which can occur upon solvent removal. It should be noted that rather different conclusions would have been drawn had the crystal structure of S- and Se-MOF-808 been investigated solely in aqueous solution.

Later chapters showcase the potential that MOFs have in developing materials with precisely-defined chemical functionality that can be exploited through knowledge of the molecular chemistry of the building blocks. These include the linkers containing both disulfide and carboxylate groups that have the potential to be cleaved under reducing and acidic conditions respectively, the use of a high density of chelating moieties with the L-aspartate-based linkers, and the complexity arising from phosphonate-based coordinating groups that offer many different binding modes. Even with what may be considered poor quality crystals that diffract to low resolution by small molecule standards, a vast array of information can still be obtained and utilized by combining with other informative spectroscopic and materials characterization techniques. This is exemplified in the systematic study of the ordered linker arrangement of the ZIFs identified in Chapter 6.

In many ways, the chemistry of MOFs is a culmination of the marriage between molecular and solid-state framework chemistry, and this paves the way for the advantages and previously attained knowledge in these fields to be exploited for the advancement of humanity. A strong understanding of all structural and chemical aspects of this is a crucial component to the development of the field.